이학박사학위논문

Development of novel bioprobes and target identification method, and their application to discovery of bioactive small molecules

새로운 바이오 프로브와 표적 단백질 동정 방법의 개발 그리고 생리활성 저분자 화합물들의 발굴에의 응용

2012년 8월

서울대학교 대학원

화학부 유기화학전공

박 종 민

Table of Contents

Abstract

Development of novel approaches in drug discovery has got attention because of the recent withdrawal of marketed drugs developed by conventional target based medicinal chemistry. In addition, the identification of small molecules that control nonconventional drug targets has become increasingly important for curing diseases that are resistant to existing drugs, developing regenerative medicine, and treating incurable diseases. Therefore, we have focused on development of novel bioprobes to monitor biological system, screening systems to discover bioactive small molecules, and a new target identification method to reveal the mechanism of action of the bioactive small molecules.

In **Part I**, development of glucose bioprobe (Chapter 1- 4), a fluoride probe (Chapter 5), and a zidovudine probe (Chapter 6) are described. We designed and completed the asymmetric synthesis of novel fluorescent glucose analogues. The first chiral bioprobe of our choice, namely Cy3-Glc-α, showed superior properties as a glucose-uptake tracer compared to the previously reported 2-NBDG. We also developed a novel system for the screening of anticancer agents through the detection of metabolic perturbation by measuring glucose uptake in cancer cells with our bioprobe Cy3-Glc-α. (Chapter 1) Based on the success of Cy3-Glc-α, we synthesized a series of fluorescent glucose analogues by adding Cy3 fluorophore to the α-anomeric position of D-glucose with various linkers. The resulting seven Cy3-labeled glucose analogues (GBs-Cy3) were evaluated by flow cytometry for their GLUT-specific translocation and competitiveness with D-glucose in the medium, along with image-based analysis using fluorescence microscopy. Systematic and quantitative evaluation of these GBs-Cy3 led to the identification of GB2-Cy3 as a GLUT-specific fluorescent glucose

bioprobe. GB2-Cy3 was ten times more sensitive than 2-NBDG, a leading fluorescent glucose bioprobe, as was confirmed by flow cytometry and fluorescence microscopy analyses. GB2-Cy3 was successfully utilized in three different systems to quantitatively monitor changes of glucose uptake in metabolically active C2C12 myocytes under various treatment conditions. (Chapter 2) GB2-Cy3 was used to evaluate a small molecule activator of AMPK, Ampkinone (AKN). AMPK is an important energy sensor in mammalian cells and an attractive target molecule for the treatment of metabolic disorders, including obesity and type 2 diabetes. It has been well established that activation of AMPK stimulates glucose uptake by increasing GLUT4 translocation to the cell surface. Therefore, we observed glucose uptake perturbation by AKN with our own glucose bioprobe, GB2-Cy3. The detailed mechanism of AKN action was also studied with GB2-Cy3. (Chapter 3) The great success of one photon glucose bioprobe made us to extend our research area to two photon microscopy for tissue imaging. Based on the GB2-Cy3 structure, we have developed a new TP tracer, AG2, that can be easily taken up by cancer cells and tissues through glucose-specific translocation. It can monitor glucose uptake in normal and colon-cancer tissues from human patients and can visualize the efficacy of anticancer agents in cancer cells and colon-cancer tissues. (Chapter 4) Besides glucose bioprobes, we have successfully developed TBPCA as a fluoride ion probe for fluorescence cell bioimaging. We also demonstrated fluorescence cell bioimaging using TBPCA for the detection of NaF in A549 human epithelial lung cancer cells under physiological conditions. Moreover, TBPCA can be utilized for the quantification of fluoride ions in living systems. (Chapter 5) In Chapter 6,

development of a zidovudine (ZDV) probe (ZP) is described. ZDV has been used for AIDS treatment worldwide. Therefore, researches about ZDV side effects are very important. In order to provide the quantitative measurement tool for the side effect studies of ZDV therapy, we accomplished the bio-orthogonal tracing of ZDV-incorporated DNA in the in-gel fluorescence imaging system as well as cellular imaging of ZDV-incorporated mammalian chromosomes. Most importantly, unlike other existing methods such as autoradiography or immunostaining, we were able to quantify the incorporation efficiency of ZDV by different kinds of DNA-synthesizing enzymes on the basis of our unique observation of band shifts induced by specific labeling of cationic Cy3-labeled ZP.

In Part II, screening bioactive small molecules (Chapter 1) and development of a new target identification method (Chapter 2) are described. Based on our research of bioprobe development, we discovered a novel nonsteroidal androgen receptor(AR) antagonist using a cell-based reporter gene assay, along with our small-molecule library constructed using a diversity-oriented synthetic pathway. A novel benzopyran-fused tetracyclic core imbeded compound 6 f was identified as having an excellent antagonistic activity confirmed by western blot analysis, RT-PCR, and in vitro cellular proliferation assay. We also demonstrated that compound 6 f is active against not only WT AR but also mutant AR, such as T877A or W741L (bicalutamide-resistant AR mutant). This new molecular framework might provide valuable insight for the development of therapeutics able to treat advanced prostate cancer. (Chapter 1) To understand the mechanism of action of the bioactive small molecules, we have developed a new target identification method, FITGE, which aims to observe

interactions between proteins and small molecules in an intact cellular environment. After a series of failures using conventional target identification methods, we successfully identified the protein target of anti-proliferative compound with FITGE only in live cells, and observed the environment-dependent binding events of a functional small molecule by direct comparison between live cells and cell lysates. The FITGE method can address the current limitations of conventional target identification methods and can significantly enhance the possibility of target identification through the combination of the covalent capturing of target proteins in an intact cellular environment and the efficient exclusion of nonspecific protein labeling using two-color 2DGE. We believe our FITGE method provides a unique means of target identification in live cells.

Keywords : Glucose Bioprobe, AMPK, Diabetes, Obesity, Two-Photon Glucose Bioprobe, Fluoride, Zidovudine, Androgen Receptor, Anticancer Agent, Target Identification.

Student Number : 2005-23208

Part I

Development of Novel Bioprobes and Its Applications in Biological Systems

Chapter 1. Development of a Cy3-Labeled Glucose Bioprobe and Its Application in Bioimaging and Screening for Anticancer Agents

- *Angew. Chem. Int. Ed.* **2007**, *46*, 2018.

Introduction

Glucose is the most important energy source for cell growth; therefore, a fast-growing cancer cell requires more glucose than a normal cell. One of the biochemical marker in tumor malignancy is enhanced tumor glycolysis primarily due to the overexpression of glucose transporters (GLUTs) and the increased activity of mitochondria-bound hexokinases in tumors.[1] The *in vitro* and *in vivo* assessment of glucose utilization has been of considerable interest to scientific communities, especially those in the biological and biomedical fields. One of the successful applications of this assessment is tumor diagnosis using [^{18}F] 2-fluoro-2-deoxyglucose (^{18}FDG)-based positron emission tomography (PET).[2a-b] PET with ^{18}FDG is a molecular imaging modality that monitors metabolic perturbation in tumor cells and allows the imaging of the exact positions of tumors in the human body; therefore, it is widely applied in the diagnosis of various tumors.[2c-d] A fluorescent 2-deoxyglucose analog, i.e., 2-[*N*-(7-nitrobenz-2-oxa-1,3-diazol-4-yl)amino]-2-deoxy-D-glucose (2-NBDG), was developed and extensively studied, primarily by Yoshioka et al.[3] 2-NBDG has been widely applied in various studies, especially for tumor imaging and examination of GLUT-related cell metabolism.[3–8] In addition, some 2-deoxyglucose analogs have been reported.[9-10] However, these analogs have several limitations; therefore, we designed and synthesized a novel fluorescent-labeled

glucose analog—Cy3 linked *O*-1-glycosylated glucose—not a *N*-2-glycosylated one like the previous analogs (**Scheme 1**)

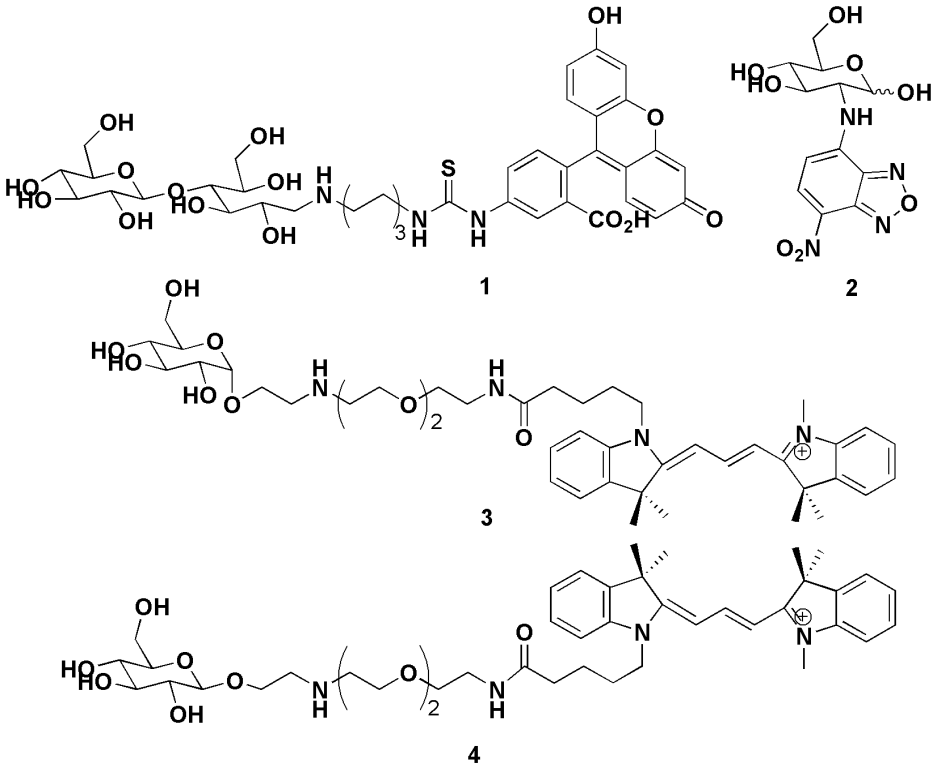

Scheme 1. Structure of fluorescence labeled glucose bioprobes. FITC-labeled cellobiose (**1**); 2-NBDG (**2**); Cy3-labeled α-glucose (**3**); Cy3-labeled β-Glucose (**4**)

Results and Discussion

In our initial approach, the natural disaccharide, cellobiose, was directly labeled with fluorescence isothiocyanate (FITC) by reductive amination[11] using sodium borohydride. However, this approach has several disadvantages: first, the yield is low, and the purification process is tedious; second, only the β anomer form of bioprobes was prepared using this procedure. In addition, FITC was not the appropriate fluorescent dye for this study due to its photochemical properties and fast photobleaching during experimentation with a confocal laser scanning microscope (CLSM) or fluorescent microscope. Due to these limitations, a second approach was

pursued to improve the reaction yields by using simple purification steps and to synthesize both anomers (α and β) of D-glucose labeled with photo resistant dye.

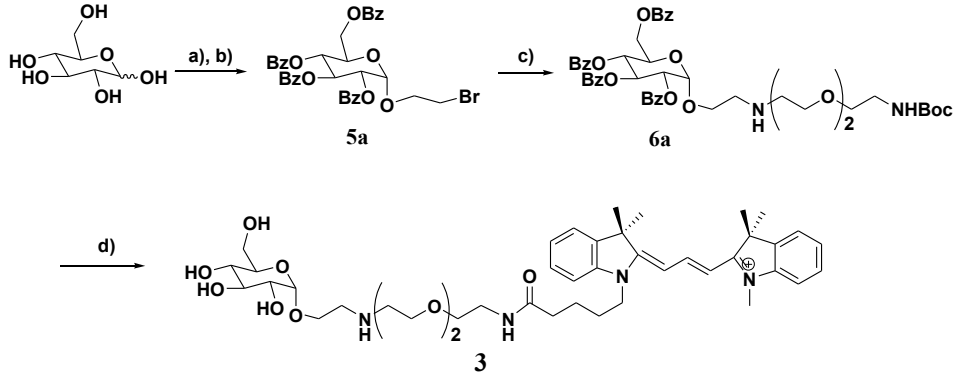

a) 2-bromoethanol, Dowex 50WX8-400 ion exchange resin, 70°C reflux; b) benzoyl chloride, pyridine, DMAP; c) *N*-Boc-3,6-dioxaoctane-1,8-diamine, triethylamine, DMF, 50°C; d) (i) NaOMe , MeOH; (ii) 50% TFA /DCM; (iii) Cy3-OH , EDC, DIPEA , DMF

Scheme 2. Synthetic scheme of Cy3-labeled glucose analogs

The conformation of D-glucose is recognized to be pyranose, a hemiacetal ring. Due to the special reactivity of the anomeric hydroxyl group, 2-bromoethanol can be regioselectively introduced into the anomeric position by acid-catalyzed Fischer glycosylation with a 2:1 (α:β) ratio as confirmed by NMR.[12] The resulting reaction mixture was benzoylated for isolation of the α and β anomers (**5a** and **5b**, respectively).[13] After the separate coupling of PEG-amine linker (*N*-Boc-3,6-dioxaoctane-1,8-diamine)[14] with the both anomers (**5a** and **5b**), the obtained sugar (**6a**) was treated for debenzoylation and de-boc protection (**Scheme 2, 6b** not shown). After basification of the deprotected products with DIPEA in order to remove any residual TFA, the resulting chiral glucoside with primary amine can be coupled with any probes such as fluorescent dyes or biotin. Our choice in the final modification was Cy3 fluorescent dye instead of FITC because the former is tolerant to intense light sources and compatible with various bioassay systems. We used in-house Cy3 carboxylic acid synthesized at high yields based on well-documented procedures.[15] EDC coupling of Cy3 carboxylic acid with the resulting glucosides yielded the

desired Cy3-labeled D-glucoses after prep HPLC purification. Both anomers of Cy3-labeled D-glucose were prepared using identical procedures with complete control over the stereochemistry on the glucosides, and the final products were completely characterized by ^{1}H, ^{13}C NMR, MALDI-TOF MS, and HRMS.

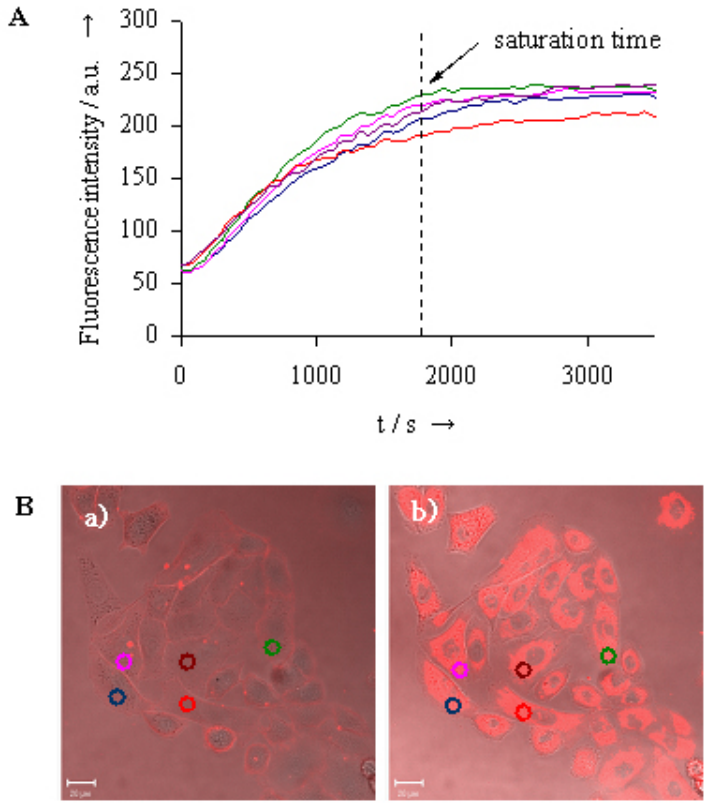

Figure 1. (A) Cy3-Glc-α uptake by A549 cells. Fluorescence intensities were expressed as arbitrary unit (a.u.) determined by continuous measurement from ROIs (Regions of Interest) in five independent cells marked on B based on unbiased selection. (B) Merged phase-contrast image and fluorescence images in A549 cells captured by live-cell imaging with a CLSM. (a) A549 cells after 0 min. (b) A549 cells after 60 min. *Scale bar* is 20 μm.

After completion of chiral Cy3-labeled D-glucose synthesis, we proceeded to evaluate the bioapplicability of our bioprobes in a bioassay system. First, we measured the efficiency of Cy3-Glc-α (**3**) uptake into cells by using a CLSM. To decide the optimum concentration of Cy3-Glc-α, we allowed A549 cells (human lung carcinoma cell line) to incorporate our bioprobe at Cy3-Glc-α concentration of 100

μM, 50 μM, 25 μM, 12.5 μM and 6 μM. Based on the repeated tests, we selected 12.5 μM as the optimum concentration in cellular uptake experiments (see supporting information). With an optimized concentration for live cell imaging, we used a CLSM to measure the optimum incubation time required to achieve the maximum uptake of our bioprobe. As shown in **Figure 1**, the uptake of our bioprobe by A549 cells reaches the maximum within 35 min. Previous work with 2-NBDG (NBD-labeled 2-aminoglucoside) (**2**) reported that an apparent maximum uptake of 2-NBDG was reached within 30 min, which is consistent with our observation.[16] Under these optimized conditions, we tested whether or not our bioprobe acts as a glucose analog.

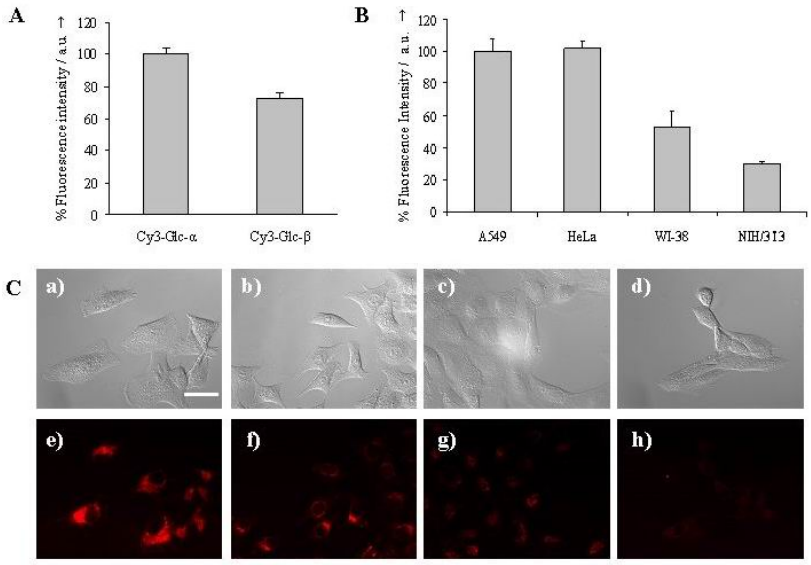

Figure 2. (A) Cy3-Glc-α and Cy3-Glc-β uptake by A549 cells. Fluorescence intensities were expressed as an arbitrary unit (a.u.) determined by fluorometry, and data are the mean of 35–50 cells from an experimental representative of at least two independent experiments. (B) Efficiency of Cy3-Glc-α uptake in cancer cells (A549, HeLa) vs. normal cells (WI-38, NIH/3T3). (C) Comparison of Cy3-Glc-α uptake by A549 cells (a, e), HeLa cells (b, f), WI-38 cells (c, g) and NIH/3T3 cells (d, h); (a–d) Phase-contrast images; (e–h) Fluorescence images. *Scale bar* in (a) is 40 μm.

Compared to 2-NBDG, our bioprobe is an *O*-glycosylated glucose analog at the C-1 position; therefore, we asymmetrically synthesized both anomers simultaneously under the assumption that the behavior of these anomers could be different, because the molecular conformation of Cy3-Glc-α and Cy3-Glc-β would be

quite distinct. To confirm our hypothesis, we performed real-time uptake measurement of Cy3-Glc-α and compared the findings with those of Cy3-Glc-β by live imaging of A549 cells by using inverted fluorescent microscope. As shown in **Figure 2A**, the uptake of Cy3-Glc-α was 40% superior to that of Cy3-Glc-β; this led us to the conclusion that the stereochemistry at the C-1 anomeric position definitely influences the efficiency of mimicking glucose, and this might be due to the binding orientation of D-glucose in GLUTs.[17] Based on this observation, further studies in bioimaging and bioapplication were performed only with the α anomer of the Cy3-glucose analog as our choice of the bioprobe. We also measured the efficiency of Cy3-Glc-α uptake, in particular, we focused our attention on the differentiation of GLUT-overexpressing cancer cells (A549; lung carcinoma cell line, HeLa; cervical carcinoma cell line) instead of normal cells (WI-38; lung normal cell line, NIH/3T3; murine fibroblast cell line). Cy3-Glc-α uptake in NIH/3T3 was only 30% that of A549 cells. Interestingly, Cy3-Glc-α uptake in HeLa cells was almost identical, which confirms the selective uptake of Cy3-Glc-α in cancer cells with enhanced glucose-metabolism (**Figure 2B**). This data demonstrated that the cellular uptake of Cy3-Glc-α depends on the higher glucose metabolism in cancer cells, which in turn relies on the ATP generated from glycolysis in order to meet the energy requirements of rapid replicating tissue. Therefore, glucose metabolism is strongly correlated with the GLUT/hexokinase expression levels. This data led us to the application of Cy3-Glc-α in bioimaging and bioassay in cancer studies.

To confirm whether the intracellular uptake pathway of glucose analogs is relevant to that of D-glucose, the direct competition experiment has been utilized in many studies.[1,8,9,16] If the cellular uptake of a certain glucose analog depends on the

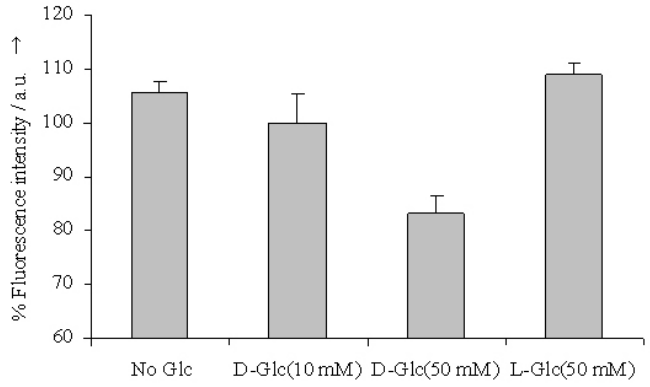

Figure 3. Dose-dependent Cy3-Glc-α uptake inhibition in A549 cells in the absence or presence of 10, 50 mM D-glucose. To demonstrate specific inhibition by D-glucose, an identical experiment was performed in the presence of 50 mM L-glucose, and this resulted in no uptake inhibition. Fluorescence intensities were expressed as arbitrary units (a.u.) determined by fluorometry, and the data are the mean of 35–50 cells from an experimental representative of at least two independent experiments.

concentration of D-glucose but not on that of L-glucose, then that particular glucose analog would enter the cell via a GLUT-mediated glucose uptake system. Based on prior experiments, we tested the process of the cellular uptake of Cy3-Glc-α by measuring the efficiency of Cy3-Glc-α uptake by A549 cells at 37°C in RPMI1640 lacking glucose or containing 10 mM D-glucose, 50 mM D-glucose, and 50 mM L-glucose. As shown in Figure 3, the uptake of Cy3-Glc-α decreased as the concentration of D-glucose in the medium increased. However, the uptake of Cy3-Glc-α was not influenced by the concentration of L-glucose in the medium. In addition, we measured the uptake of Cy3-Glc-α using A549 cells in media containing 55 mM alanine in order to ensure that the osmotic pressure in the medium does not affect Cy3-Glc-α uptake, and we observed no difference in the uptake efficiency under the media with or without 55 mM alanine (see supporting information). The uptake of Cy3-Glc-α by A549 cells is inhibited by D-glucose but not by L-glucose; this suggests that Cy3-Glc-α is taken up by the cell through a glucose-specific transport system, not by passive diffusion. Therefore, Cy3-Glc-α can function as a D-

glucose mimic and can be applied as a research tool in the study of glucose metabolism.

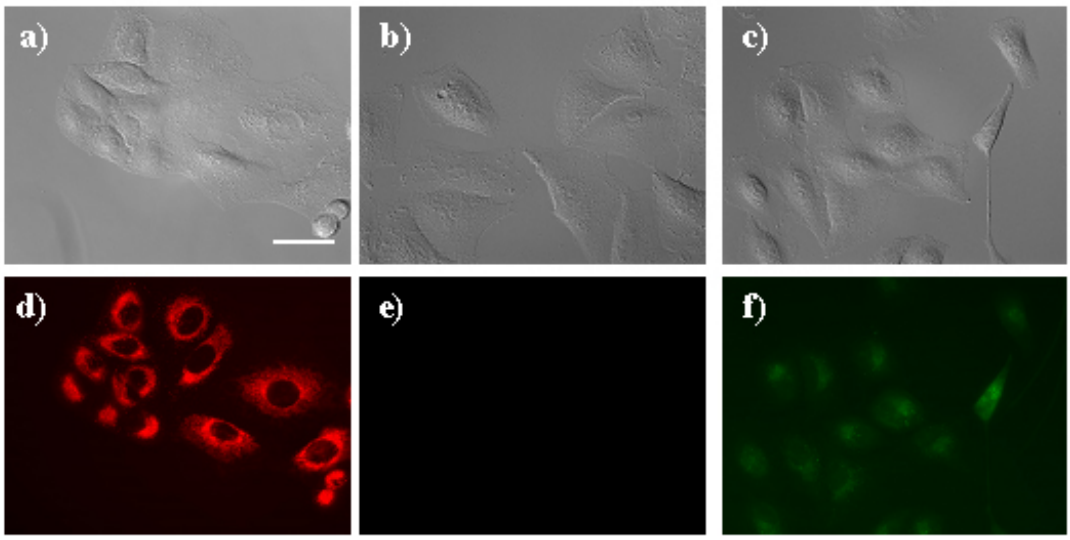

Figure 4. Uptake image of 2-NBDG and Cy3-Glc-α by A549 cells with different conditions: (a, d) 12.5 μM of Cy3-Glc-α with lens exposure of CCD camera for 500 ms; (b, e) 12.5 μM of 2-NBDG with lens exposure of CCD camera for 500 ms (c, f) 125μM of 2-NBDG with lens exposure of CCD camera for 11000 ms; (a, b, c) Phase-contrast image in A549 cells; (d, e, f) Fluorescence image in A549 cells. Fluorescence of 2-NBDG cannot be detected in same condition with Cy3-Glc-α case. Even 125 μM of 2-NBDG can not be detected with lens exposure of CCD camera for 500 ms. 10 fold increase of concentration and 20 fold increase of lens exposure time was needed to get measurable fluorescence intensity with 2-NBDG than with Cy3-Glc-α. *Scale bar* in (a) is 40 μm.

We confirmed that Cy3-Glc-α acts as a D-glucose analog, and we compared Cy3-Glc-α with a fluorescent analog of 2-deoxyglucose, i.e., 2-NBDG.[1,3-8] The cellular uptake of 2-NBDG cannot be detected under the identical experimental condition of Cy3-Glc-α. To achieve fluorescence intensity with 2-NBDG up to 80% that of Cy3-Glc-α, 10 fold increase of 2-NBDG concentration and 20 fold increase of lens exposure time in D-glucose-depleted medium were needed with identical experimental setups. In addition, the cellular uptake of 2-NBDG in normal media (containing 10 mM D-glucose) is extremely low (>60% uptake reduction in normal media) and can be hardly detected using fluorescent based imaging methods.[16] It is detectable only in glucose-depleted media, and this is a critical limitation of its

bioapplication in the biologically significant environments. In comparison with 2-NBDG, the reduction of Cy3-Glc-α uptake in glucose-containing media is 5% compared to that in glucose-depleted media (**Figure 4**). Therefore, Cy3-Glc-α can be applied in a bioassay system without glucose starvation.

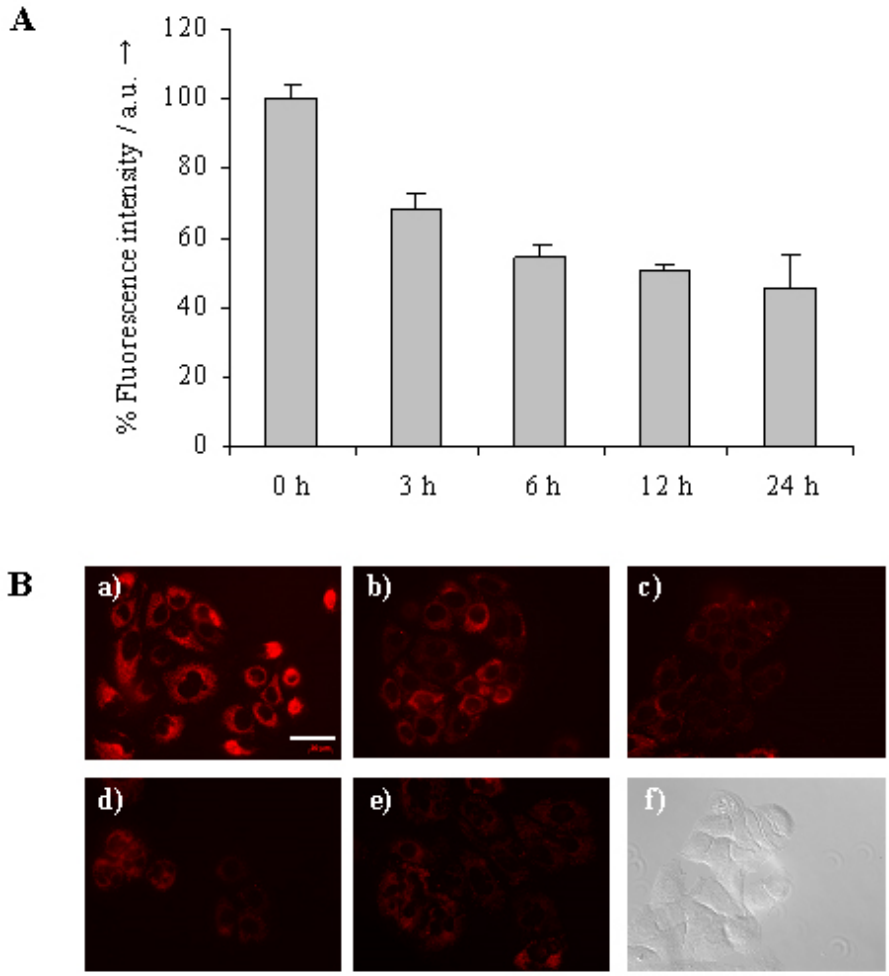

Figure 5. (A) Cy3-Glc-α uptake by A549cells is measured after 0, 3, 6, 12, and 24 h of treatment with taxol (9.8 μM) at 37°C. Fluorescence intensities were expressed as an arbitrary unit (a.u.) determined by fluorometry and the data are the mean of 35–50 cells from an experimental representative of at least two independent experiments. (B) Comparison of Cy3-Glc-α uptake by A549 cells after treatment with taxol (9.8 μM) at 37°C for the following durations: (a) 0 (b) 3 (c) 6 (d) 12, and (e) 24 h. (f) phase-contrast image after 6 h incubation. After incubation with taxol, each image was captured with a fluorescent microscope after 30 min of Cy3-Glc-α treatment as described in the supplementary information. Fluorescence intensity decreased as the incubation time with taxol was increased. *Scale bar* in (a) is 40 μm.

Based on the fact that Cy3-Glc-α could be taken up by cells as a D-glucose analog through a D-glucose specific transport mechanism in normal glucose-containing medium, we applied Cy3-Glc-α to the screening of small molecule modulators involved in cellular metabolism. We postulated that the depression of cellular metabolism in cancer cells can be caused by anticancer agents, which is closely related to the reduction of glucose uptake. We intended to monitor this phenomenon by our fluorescent bioprobe Cy3-Glc-α. As a proof-of-principle experiment, we treated A549 cancer cells with taxol, an anticancer agent, and we measured the uptake of Cy3-Glc-α at 3, 6, 12, and 24 h after treatment. When we treated the cells with 9.8 μM taxol, the cellular uptake of our bioprobe reduced as the incubation time increased (**Figure 5**); this clearly demonstrates the potential of Cy3-Glc-α for evaluation of the metabolic perturbation caused by bioactive small molecules in live cells under physiological conditions. Therefore, Cy3-Glc-α should not affect cell viability. By measuring the viability of cells treated with Cy3-Glc-α (12.5 μM) by using a CCK-8 kit [Dojindo, Japan], we concluded that Cy3-Glc-α treatment does not affect cell viability under our incubation conditions (see supporting information). We also observed the dose dependency of Cy3-Glc-α uptake by changing the taxol concentration from 490 nM to 49 nM (Table 1). Another anticancer agent, i.e., combretastatin, also prohibited cellular proliferation by disturbing cellular metabolism, as indicated by a reduction in the cellular uptake of Cy3-Glc-α. Based on these proof-of-principle experiments, we are confident that Cy3-Glc-α can be used to evaluate the behavior of bioactive small molecules in cells in a manner similar to the MTT assay, which measures the mitochondrial function.[18] The advantages of a screening system with Cy3-Glc-α over an MTT assay are as follows: first, the measurement time is short. MTT assays usually take 24 h and up to 72 h in

many cases, i.e. when taxol and combretastatin are used; however, the screening system with Cy3-Glc-α showed significant differences in 6 h and maximum difference in 12 h. Second, the observation channel of a screening system with Cy3-Glc-α is quite different from that of a cell-viability assay; the former involves measuring glucose-uptake efficiency, and the latter involves measuring mitochondria function. Therefore, we envision that the two assay systems will compensate for each others limitations.

Table 1. Dose dependence of Cy3-Glc-α uptake by A549 cells in the presence of various concentrations of anticancer agents.

	After 6 h	After 12 h
Taxol (9.8 μM)	54.8%	50.2%
Taxol (490 nM)	88.4%	61.8%
Taxol (49 nM)	96.5%	86.9%
Combretastatin (2 μM)	57.4%	45.0%

Conclusion

We designed and completed the asymmetric synthesis of novel fluorescent glucose analogs, and we demonstrated the importance of stereochemistry at the anomeric C-1 position of glucose in the efficiency of cellular uptake in A549 lung carcinoma cells. The chiral bioprobe of our choice, namely Cy3-Glc-α, showed superior properties as a glucose uptake tracer compared to the previously reported 2-NBDG. We also developed the novel system for the screening of anticancer agents via the detection of metabolic perturbation by measuring glucose uptake in cancer cells with our bioprobe Cy3-Glc-α. The development of the high throughput screen (HTS) system using Cy3-Glc-α is currently underway, not only for the discovery of

novel anticancer gents but also for that of glucose-uptake regulating agents for the treatment of obesity or diabetes.[16]

Supporting Information

D-(+)-Cellobiose, and D-(+)-glucose, acetic anhydride, sodium borohydride, sodium methoxide (0.5 M solution in methanol), fluorescein isothiocyanate (FITC), benzoyl chloride, pyridine, DMF, DMSO and trifluoroacetic acid (TFA) were purchased from Sigma-Aldrich (St. Louis, MO, USA). 1,6diaminohexane was purchased from Fluka (Switzerland). *N,N*-Diisopropylethylamine, triethylamine, and 2-bromoethanol were purchased from TCI (Japan). The ^{1}H and ^{13}C NMR spectra were recorded on a Bruker DRX-300 (Bruker Biospin, Germany) and Varian Inova-500 (Varian Assoc., Palo Alto, USA), and chemical shifts were measured in ppm downfield from internal tetramethylsilane (TMS) standard. The desired products were identified with MALDI-TOF MS analysis using Bruker Daltonics(Germany). The identity of final compounds was confirmed by high-resolution mass spectrometry (HRMS). HRMS analysis was performed at the Mass spectrometry facility of the National Center for Inter-university Research Facilities, Seoul National University. Reverse phase HPLC analysis was performed on a VP-ODS C-18 column (150 x 4.6 mm) at a flow rate of 1.0 mL/min for analysis, and PRC-ODS C-18 column (250 x 20 mm) at a flow rate of 10.0 mL/min for preparation, Shimadzu LC-6AD pump, SPD10A detector (Japan). HPLC solvents consist of water containing 0.1% TFA (solvent A) and acetonitrile containing 0.1% TFA (solvent B).

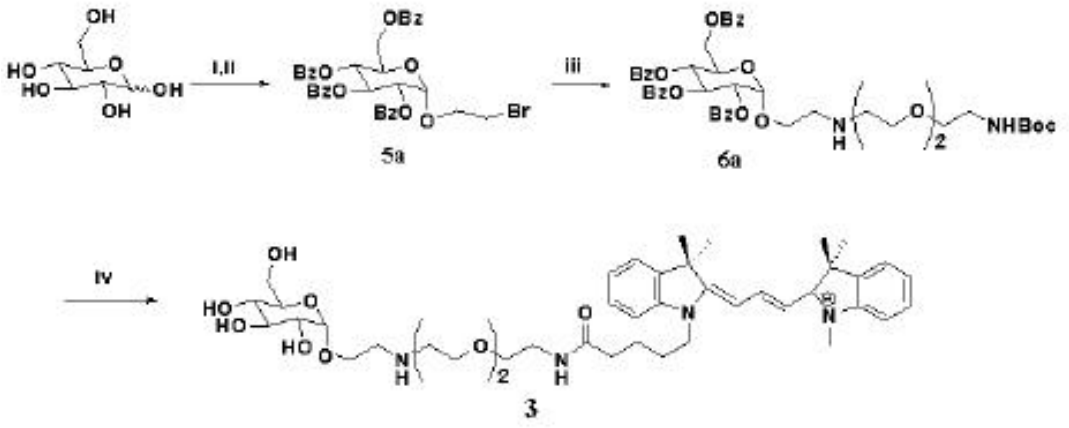

i. 2-bromoethanol, Dowex 50WX8-400 ion exchange resin, 70°C reflux ii. Benzoyl chloride, pyridine, DMAP iii. N-Boc-3,6-dioxaoctane-1,8-diamine, triethylamine, DMF, 50°C iv. (i) NaOMe , MeOH (ii) 50% TFA /DCM (iii) Cy3-OH , EDC, DIPEA , DMF

Supporting Scheme 1. Synthetic scheme of Cy3-labeled glucose analogs

(2-Bromoethyl)-2,3,4,6-tetra-O-benzyl-a-D-glucoside (5a) Glucose (1 g, 5.55 mmol) was dissolved in 2-bromoethanol (6 mL, 85 mmol) with Dowex 50WX8-400 ion exchange resin (1 g). The reaction mixture was refluxed at 70 °C overnight and the reaction completion was monitored by TLC.[12] The reaction mixture was filtered to remove the resin and concentrated in vacuo. After the purification of glycosylated compound by silica-gel flash column chromatography (ethyl acetate : MeOH = 10 : 1 to 5 : 1), the desired compound was achieved as a mixture of a and ß anomers in 2:1 ratio (total yield 74%) confirmed by NMR. For further modification, free hydroxyl groups on resulting (2-bromoethyl)-D-glucoside (2.7 g, 9.5 mmol) were benzoylated in pyridine (60 mL) by drop-wise addition of benzoyl chloride (8.8 mL, 76 mmol) over 10 min at 0 °C, followed by stirring at room temperature for overnight in the presence of DMAP (116 mg, 0.952 mmol).[13] The mixture was quenched with the addition of MeOH (10 mL) and the reaction mixture was diluted with ethyl acetate. The organic layer was washed with 1H HCl and sat. NaHCO3, and dried over anhydrous MgSO4. Then, organic layer was filtered and condensed under reduced pressure, and the desired each anomer was successfully isolated by silica-gel flash

column chromatography (ethyl acetate : n-hexane = 1:3) in 2:1 (a:ß) ratio. ^{1}H NMR (300 MHz, $CDCl_3$) 8.09–7.89 (m, 8H), 7.54–7.31 (m, 12H), 6.23 (t, *J* = 9.9 Hz, 1H), 5.70 (t, *J* = 9.9 Hz, 1H), 5.44 (d, *J* = 3.6 Hz, 1H), 5.33 (dd, *J* = 10.1, 3.7 Hz, 1H), 4.64–4.56 (m, 2H), 4.48 (dd, *J* = 11.9, 5.1 Hz, 1H), 4.16–4.03 (m, 1H), 3.94–3.85 (m, 1H), 3.76–3.70 (m, 2H); ^{13}C NMR (75 MHz, $CDCl_3$) 166.20, 165.88, 165.78, 165.30, 133.48, 133.19, 129.98, 129.91, 129.76, 129.72, 129.63, 129.10, 128.93, 128.79, 128.45, 128.32, 96.31, 71.83, 70.30, 69.34, 68.92, 68.31, 62.95, 29.80; MALDI TOF MS calcd for C36H43O12 $[M+H]^+$ 703.11; found: 703.05.

(2-Bromoethyl)-2,3,4,6-tetra-*O*-benzyl-ß-D-glucoside (5b) ^{1}H NMR (300 MHz, $CDCl_3$) 8.04–7.81 (m, 8H), 7.44–7.28 (m, 12H), 5.91 (t, *J* = 9.6 Hz, 1H), 5.67 (t, *J* = 9.7 Hz, 1H), 5.54 (dd, *J* = 7.9, 1.7 Hz, 1H), 4.93 (d, *J* = 7.8 Hz, 1H), 4.66 (dd, *J* = 9.1, 3.0 Hz, 1H), 4.48 (dd, *J* = 6.8, 5.3 Hz, 1H), 4.24–4.07 (m, 2H), 3.94–3.83 (m, 1H), 3.49–3.36 (m, 2H); ^{13}C NMR (75 MHz, $CDCl_3$) 166.15, 165.82, 165.22, 133.56, 133.34, 129.86, 129.78, 129.55, 129.26, 129.09, 128.75, 128.49, 128.40, 128.37, 128.29, 101.54, 72.81, 72.40, 71.69, 69.89, 69.64, 63.03, 29.74; MALDI TOF MS calcd for C36H43O12 $[M+H]^+$: 703.11 ; found : 703.16.

[2-(*N*-boc-3,6-dioxaoctane-1,8-diaminoethyl)]-2,3,4,6-tetra-O-benzyl-a-D-glucoside (6a) To a solution of (2-bromoethyl)-2,3,4,6-tetra-O-benzyl-a -D-glucoside **5a** (120 mg, 0.170 mmol) in 1 mL anhydrous DMF was added *N*-Boc-3,6-dioxaoctane-1,8-diamine[14] (127 mg, 0.512 mmol) and TEA(71 µL, 0.512 mmol), and the reaction mixture was stirred at 50°C. After the reaction completion monitored by TLC, the resulting solution was diluted with ddH2O, then extracted with ethyl acetate. The combined organic layer was washed with brine and condensed under reduced pressure. The desired product **6a** was purified by silica-gel flash column chromatography (chloroform: ethanol: TEA= 87:8:5) as a yellowish oily compound

(114 mg, 76%). ^{1}H NMR (300 MHz, $CDCl_3$) 8.06–7.86 (m, 8H), 7.52–7.28 (m, 12H), 6.19 (t, *J* = 9.8 Hz, 1H), 5.71 (t, *J* = 9.6 Hz, 1H), 5.40 (d, *J* = 3.5 Hz, 1H), 5.33 (dd, *J* = 10.1, 3.7Hz, 1H), 4.62 (d, *J* = 9.5 Hz, 1H), 4.50–4.47 (m, 2H), 3.99–3.94 (m , 1H), 3.72–3.60 (m, 2H), 3.54–3.50 (m, 6H), 3.44 (t, *J* = 5.1 Hz, 2H), 3.29 (d, *J* = 4.5 Hz, 2H), 2.92–2.86 (m, 2H), 2.78–2.73 (m, 2H), 2.32 (s, 2H), 2.20 (s, 1H), 1.42 (s, 9H); ^{13}C NMR (75 MHz , $CDCl_3$) 166.17, 165.83, 165.69, 165.27, 156.03, 133.44, 133.13, 129.88, 129.85, 129.73, 129.67, 129.10, 128.97, 128.86, 128.49, 128.41, 128.30, 96.26, 79.09, 71.96, 70.47, 70.44, 70.18, 69.48, 68.41, 67.86, 67.08, 62.93, 49.00, 48.66, 40.35, 28.42; MALDI TOF MS calcd for $C_{47}H_{55}N_2O_{14}$ $[M+H]^+$: 871.36; found : 871.51.

[2-(*N*-boc-3,6-dioxaoctane-1,8-diaminoethyl)]-2,3,4,6-tetra-O-benzyl-ß-D-glucoside (6b) We used a similar procedure described for **6a** above to prepare **6b** from **5b**. The crude product was purified by silica-gel flash column chromatography to afford 104 mg (70 %) of **6b**: ^{1}H NMR (300 MHz, $CDCl_3$) 8.19–7.81 (m, 8H), 7.54–7.25 (m, 12H), 5.90 (t, *J* = 9.6 Hz, 1H), 5.68 (t, *J* = 9.7 Hz, 1H), 5.52 (t, *J* = 8.0Hz, 1H), 4.89 (d, *J* = 7.8 Hz, 1H), 4.65 (dd, *J* = 12.1, 2.9 Hz, 1H), 4.50 (dd, *J* = 12.1, 4.9 Hz, 1H), 4.18–4.15 (m, 1H), 4.06–4.00 (m, 1H), 3.75–3.68 (m, 1H), 3.50–3.46 (m, 6H), 3.36(t, *J* = 5.2 Hz, 2H), 3.29 (d, *J* = 4.7 Hz, 2H), 2.82–2.66 (m, 4H), 1.98 (s, 2H), 1.42 (s, 9H); ^{13}C NMR (75 MHz, $CDCl_3$) 191.84, 166.14, 165.80, 165.19, 165.10, 133.45, 133.29, 133.25, 133.15, 129.81, 129.75, 129.56, 129.22, 128.76, 128.41, 128.30, 101.43, 79.11, 72.89, 72.24, 71.92, 70.52, 70.19, 70.09, 69.90, 69.69, 63.12, 48.92, 40.34, 28.43; MALDI TOF MS calcd for $C_{47}H_{55}N_2O_{14}$ $[M+H]^+$: 871.36; found : 871.59.

[2-(*N*-Cy3-3,6-dioxaoctane-1,8-diaminoethyl)]-a-D-glucose (3) To a solution of **6a** (20 mg, 0.023 mmol) in 1 mL of MeOH was added sodium methoxide (0.5 M in

MeOH, 368 μL, 0.184 mmol) for debenzoylation of **6a**. After reaction was completed, the mixture was neutralized with methanolic HCl, and then concentrated in vacuo. For the deprotection of Boc group on primary amine, 50% TFA in dichloromethane was added to the residue, followed by concentration by N2 purging. The resulting fully deprotected compound in DMF (300 uL) was slightly basified with DIPEA and added with Cy3-OH[15] (10 mg, 0.022 mmol) and EDC (7 mg, 0.046 mmol) in 50 uL DMF. The reaction mixture was stirred at room temperature and the reaction was monitored by HPLC analysis. The elution protocol for analytical HPLC starts with 95% A for 5 min, followed by a linear gradient to 5% A over 35 min, continued to 0% A over 5 min, held at 0% A for 15 min, and finally returned to 95% A over 10 min. Purification by prep HPLC affords 5.2 mg (30 %) of **3** (retention time: 25 min). The desired product was confirmed by ^{1}H, ^{13}C NMR, MALDI-TOF MS, and HRMS: ^{1}H NMR (500 MHz, MeOD) 8.55 (t, *J* = 13 Hz, 1H), 7.54 (d, *J* = 7.5 Hz, 2H), 7.45 (q, *J* = 7 Hz, 2H), 7.37–7.29 (m, 5H), 6.43 (d, *J* = 13.5 Hz, 2H), 4.16 (t, *J* = 7.5 Hz, 2H), 4.03–3.99 (m, 1H), 3.82 (dd, *J* = 11.5, 2.0 Hz, 1H), 3.75 (t, *J* = 4.5 Hz, 2H), 3.69 (s, 5H), 3.66–3.59 (m, 7H), 3.53(t, *J* = 6.0 Hz, 3H), 3.48 (dd, *J* = 9.5, 3.5 Hz, 1H), 3.36 (t, *J* = 6.0 Hz, 4H), 3.28–3.26 (m, 4H), 2.30 (t, *J* = 7.0 Hz, 2H), 1.80 (s, 17H); ^{13}C NMR (125 MHz, MeOD) 175.56, 174.77, 174.36, 150.96, 142.84, 142.13, 140.97, 128.77, 125.61, 125.52, 122.33, 122.17, 111.17, 111.00, 102.60, 102.39, 99.05, 73.71, 73.11, 72.03, 70.35, 70.20, 70.01, 69.35, 65.63, 62.48, 61.43, 49.42, 43.71, 38.98, 35.04, 30.55, 27.11, 26.93, 26.73, 22.79; HRMS(FAB^{+}): calcd for $C_{43}H_{63}N_4O_9$ $[M]^{+}$: 779.4595; found, 779.4601.

[2-(*N*-Cy3-3,6-dioxaoctane-1,8-diaminoethyl)]-ß-D-glucose (4) We used a similar procedure described for **3** above to prepare **4** from **6b**. The crude product was purified by prep HPLC to afford 7.6 mg (42 %) of **4**: ^{1}H NMR (500 MHz, MeOD) 8.58 (t, *J* =

13.5 Hz, 1H), 7.57 (d, *J* = 7.0 Hz, 2H), 7.48 (d, *J* = 4.5 Hz, 2H), 7.39–7.34 (m, 4H), 6.46 (d, *J* = 13.5 Hz, 2H), 4.38 (d, *J* = 7.5 Hz, 1H), 4.19 (t, *J* = 7.0 Hz, 2H), 4.14–4.11 (m, 1H), 3.97–3.91 (m, 2H), 3.77 (t, *J* = 5.0 Hz, 2H), 3.72–3.66 (m, 9H), 3.56 (t, *J* = 5.5 Hz, 2H), 3.40–3.24 (m, 11H), 2.33 (t, *J* = 6.5 Hz, 2H), 1.79 (s, 17H); ^{13}C NMR (125 MHz, MeOD) 175.56, 174.77, 174.36, 150.96, 142.83, 142.13, 140.97, 128.78, 125.62, 125.53, 122.33, 122.17, 111.18, 111.09, 102.97, 102.61, 102.39, 77.02, 76.71, 73.69, 70.33, 70.16, 70.01, 69.36, 65.53, 64.49, 61.36, 49.42, 43.71, 38.97, 35.05, 30.51, 27.11, 26.93, 26.73, 22.79; HRMS(FAB$^+$) calcd for $C_{43}H_{63}N_4O_9[M]^+$: 779.4589; found, 779.4609.

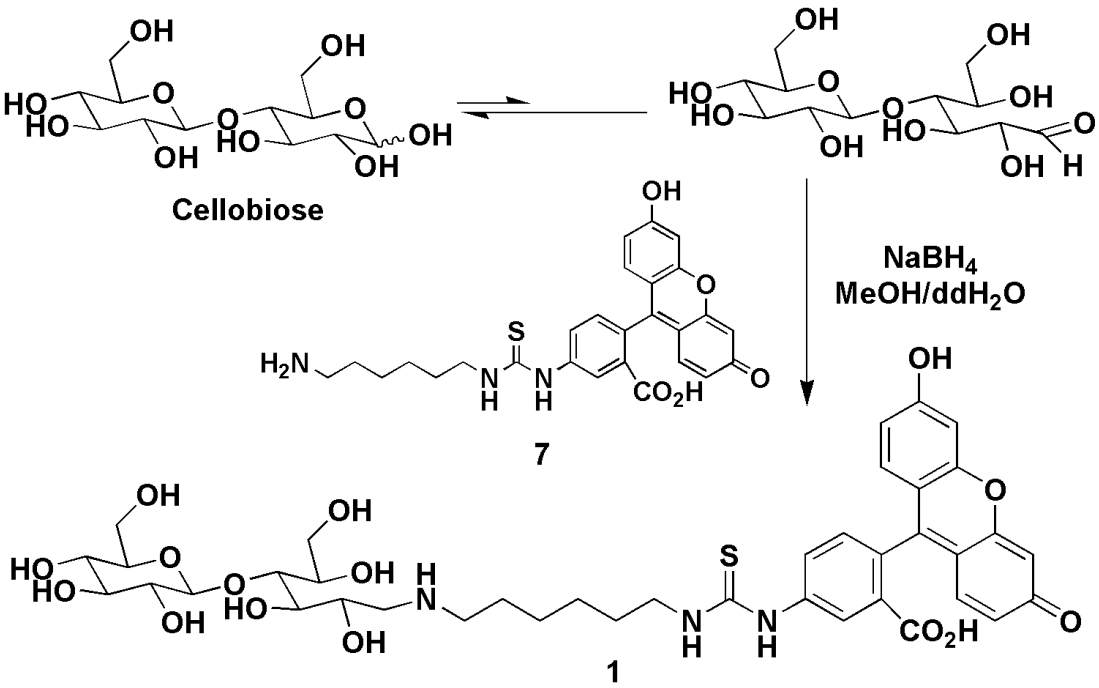

Supporting Scheme 2. First synthetic approach of fluorescent glucose analog by reductive amination from cellobiose

5-(3-(6-aminohexyl)thioureido)-2-(3-hydroxy-6-oxo-6H-xanthen-9-yl)benzoic acid (7) To a cooled solution of 1,6-diaminohexane (4.8 g, 41 mmol) in 20 mL of MeOH was slowly added FITC (400 mg, 1 mmol) in 40 mL of anhydrous DMF. The reaction mixture was added with TEA (0.17 mL, 1.23 mmol), and stirred at room temperature for 6 h. The reaction was monitored by TLC. After completion, the

resulting solution was concentrated under reduced pressure. The desired compound was obtained by recrystallization with methanol/dichloromethane as a scarlet solid (520 mg, quantitative yield).

2-(3-hydroxy-6-oxo-6H-xanthen-9-yl)-5-(3-(6-((4R,5S)-2,3,5,6-tetrahydroxy-4-((2S,3S,4S,5S)-3,4,5-trihydroxy-6-(hydroxymethyl)-tetrahydro-2H-pyran-2-yloxy)hexylamino)hexyl)thioureido) benzoic acid (1) To a solution of 5-(3-(6-aminohexyl)thioureido)-2-(3-hydroxy-6-oxo-6H-xanthen-9-yl)benzoic acid (315 mg, 62,4 mmol) in a minimal amount of methanol was added cellobiose (1 g, 3 mmol) in a minimal amount of ddH2O. The reaction mixture was stirred at room temperature for 10 h and heated for 6 h at 55oC. The resulting solution was added with NaBH4 (0.1 g, 2.8 mmol) in MeOH, and then stirred at room temperature overnight. The solvent was removed under reduced pressure and the residue was freeze-dried. The desired product was purified by gradient reverse-phase prep HPLC as a scarlet solid (70 mg, 13.5%). ES-MS calcd for $C_{39}H_{50}N_3O_{15}S$ $[M+H]^+$: 832.29. Found: 832.2.

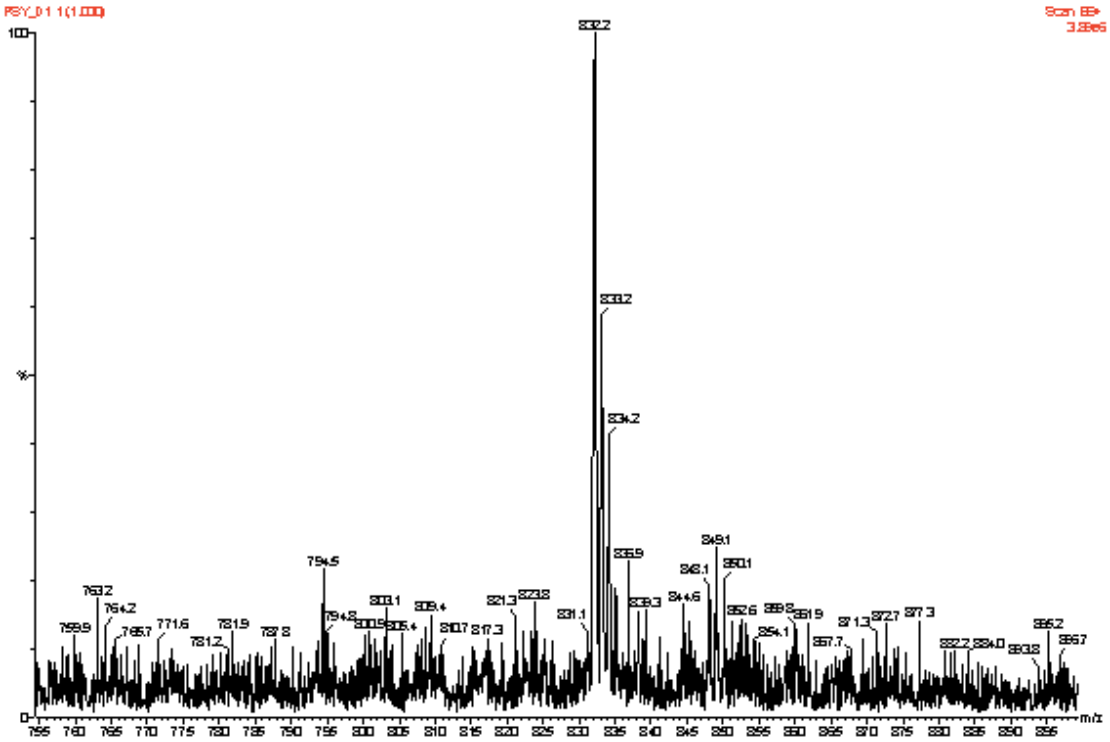

Cell culture: A549 human lung melanoma cells, HeLa human cervical carcinoma cells, NIH/3T3 murine fibroblast cells, WI-38 human lung fibroblast cells were obtained from American Type Culture Collection (ATCC, Manassas, VA, USA). A549 cells, HeLa cells and WI-38 cells were cultured in RPMI 1640 (United Search Partners, Austin, TX, USA) supplemented with heat-inactivated 10% (v/v) fetal bovine serum (FBS, United Search Partners, Austin, TX, USA) and 1 % (v/v) Antibiotic-Antimycotic solution(United Search Partners, Austin, TX, USA). NIH/3T3 were cultured in DMEM (United Search Partners, Austin, TX, USA) supplemented with heat-inactivated 10% (v/v) fetal bovine serum (FBS, United Search Partners, Austin, TX, USA) and 1 % (v/v) antibiotic-antimycotic solution(United Search Partners, Austin, TX, USA). All the cell lines were maintained in a humidified atmosphere of 5% CO2 and 95% air at 37°C, and cultured in T75 Flask (Nalge Nunc International, Naperville, IN, USA) in order to observe fluorescence emission by confocal laser scanning microscopy (CLSM).

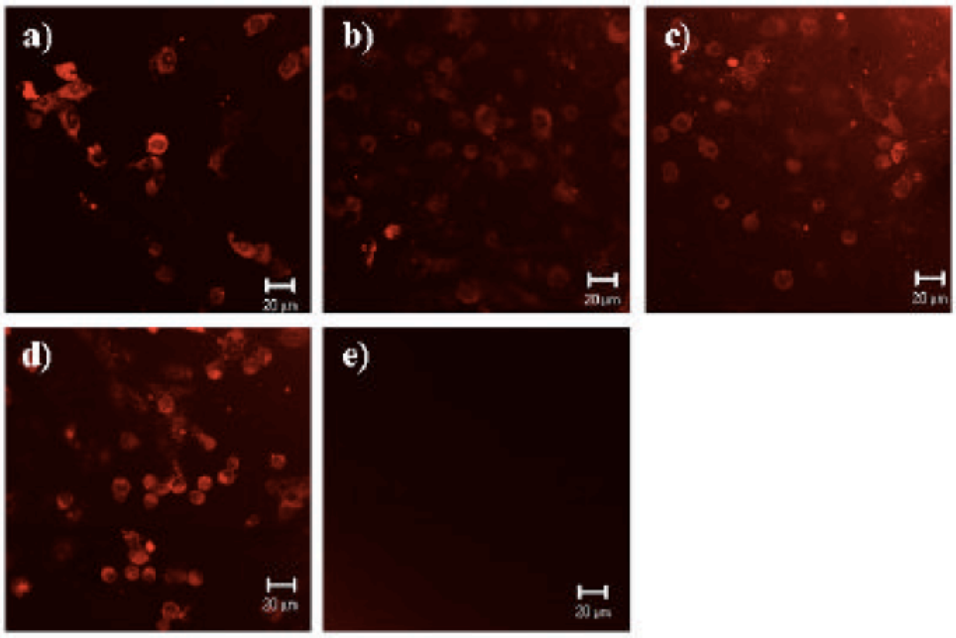

Supporting Figure 1. Determination of the optimum concentration of Cy3-Glc-a in A549 cells a) 100 μM; b) 50 μM; c) 25 μM; d) 12.5 μM; e) 6 μM.

Protocol of Confocal Laser Scanning Microscope: 1 x 10^4 Cells were cultured on a Lab-Tek glass chamber slide (Nalge Nunc International, Naperville, IN, USA) in 35 mm cell culture dish. After 24 h, the glass chamber slide was taken from culture dish and loaded on chamber. Then, the chamber is attached to the microscope. The temperature of the chamber is maintained at 37°C. After Injection of 12.5 μM of Cy3-Glc-α in RPMI 1640 in chamber, the fluorescent image was taken every 60s, digitalized, and saved on the computer for later analysis. To decide the optimum concentration of Cy3-Glc-α, we allowed A549 cells (human lung carcinoma cell line) to incorporate our bioprobe at Cy3-Glc-α concentration of 100 μM, 50 μM, 25 μM, 12.5 μM and 6 μM (See **Supporting Figure 1**). Based on the repeated tests, we selected 12.5 μM as the optimum concentration in cellular uptake experiments.

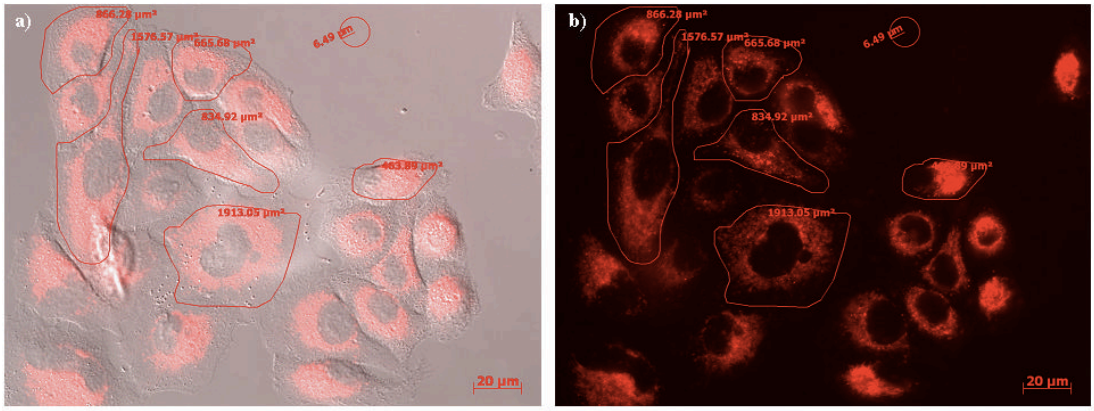

Supporting Figure 2. a) Merged image of phase contrast image and fluorescence image in A549 cells after 30 min of Cy3-Glc-a incubation. b) Fluorescence image of a). Boundary with red line is for measurement of Cy3 intensity.

Protocol of Inverted Fluorescent Microscope: 1? 104 Cells were cultured on a Lab-Tek glass chamber slide (Nalge Nunc International, Naperville, IN, USA) in 35 mm cell culture dish. After 24 h, cells were treated for each experimental purpose. Then, 12.5 μM of Cy3-Glc-a containing RPMI 1640 is replaced with media. Cells were exposed to Cy3-Glc-a for 40 min, then washed with PBS (phosphate buffered saline) 3 times. Finally, the glass chamber slide was taken from culture dish and loaded on

the fluorescence microscope (Axiovert 200, Carl Zeiss, Germany). Fluorescence images of 35–50 cells were taken by CCD camera (Axiocam MRm, Germany) and fluorescence intensity of each cells was measured by Axiovision (program for data analysis). With Axiovision, we draw an area as ROIs (regions of interest) which contains a cell in phase-contrast image. Axiovision analyses CCD camera images and let us know the digitalized mean of fluorescence intensity in the ROIs that we determined. We subtract the background intensity from the fluorescence intensity to get the fluorescence intensity value that a cell contains. (See **Supporting Figure 2**) With the method which is described above, we digitalized fluorescence intensity and perform various experiments.

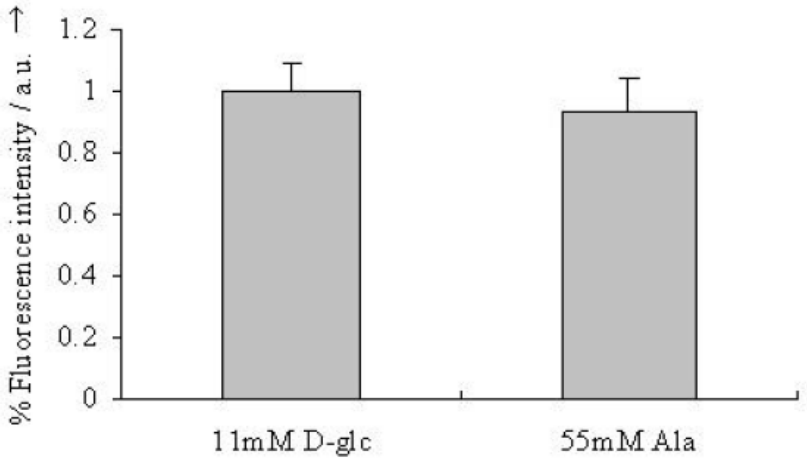

Supporting Figure 3. Cy3-Glc-α uptake by A549 in the absence or presence of 55 mM alanine. There are no differences of uptake efficiency in media with or without 55 mM alanine.

To perform the direct competition experiment, we measure uptake of Cy3-Glc-α by A549 with media containing 55 mM alanine to make sure that osmotic pressure in media does not affect the uptake of Cy3-Glc-α. There were no differences of uptake efficiency in media with or without 55 mM alanine. (See **Supporting**

Figure 3) This result makes sure that osmotic pressure does not affect uptake of Cy3-Glc-α by A549.

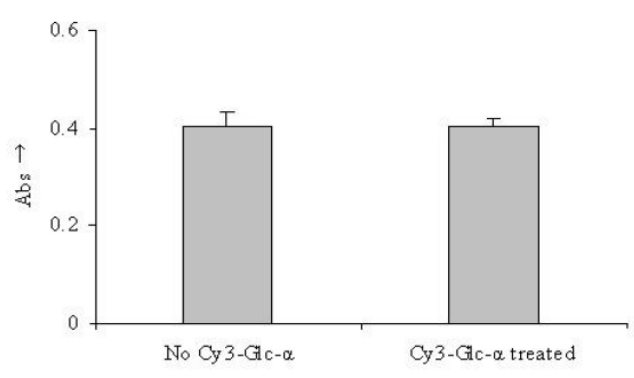

Supporting Figure 4. Cell viability is measured using CCK-8 kit after treatment with Cy3-Glc-α (12.5 μM). Cy3-Glc-α treatment does not affect cell viability in our incubation condition.

We assume that the perturbed cellular metabolism of cancer cells by anticancer agents would be depressed, which is closely related to the reduction of glucose uptake. We intended to monitor this phenomenon by our fluorescent bioprobe, Cy3-Glc-α. For this purpose, Cy3-Glc-α should not affect cell viability. The viability measurement of cells treated with Cy3-Glc-α (12.5 μM) using CCK-8 kit (Cell Counting Kit-8, Dojindo, Japan) is measured by ELISA plate reader (ELx800™, BioTek, USA). CCK-8 is a colorimetric assay for determining the number of viable cells in cell proliferation and cytotoxicity assays. The principle of measuring cell viability of CCK-8 is same with that of MTT. However, CCK-8 is more sensitive than MTT, Hence we chose CCK-8 for cell viability test. With the result by CCK-8, we could conclude that Cy3-Glc-α treatment does not affect cell viability in our incubation condition. (See **Supporting Figure 4**)

Reference

[1] M. Zhang, Z. Zhang, D. Blessington, H. Li, T. M. Busch, V. Madrak, J. Miles, B. Chance, J. D. Glickson, G. Zheng, *Bioconjugate Chem.* **2003**, *14*, 709.

[2] a) P. Som, H. L. Atkins, D. Bandoypadhyay, J. S. Fowler, R. R. MacGregor, K. Matsui, Z. H. Oster, D. F. Sacker, C. Y Shiue, H. Turner, C. N. Wan, A. P. Wolf, S. V. Zabinski, *J. Nucl. Med.* **1980**, *21*, 670; b) H. Yorimitsu, Y. Murakami, H. Takamatsu, S. Nishimura, E. Nakamura, *Angew. Chem. Int. Ed.* **2005**, *44*, 2708. c) P. S. Conti, D. L. Lilien, K. Hawley, J. Keppler, S. T. Grafton, J. R. Bading, *Nucl. Med. Biol*. **1996**, *23*, 717; d) J. Czernin, M. E. Phelps, *Annu. Rev. Med.* **2002**, *53*, 89.

[3] K. Yoshioka, H. Takahashi, T. Homma, M. Saito, K. B. Oh, Y. Nemoto, H. Matsuoka, *Biochim. Biophys. Acta.* **1996**, *1289*, 5.

[4] K. Yoshioka, M. Saito, K. B. Oh, Y. Nemoto, H. Matsuoka, M. Natsume, H. Abe, *Biosci. Biotech. Biochem.* **1996**, *60*, 1899.

[5] A. Natarajan, F. Srienc, *J. Microbiol. Methods.* **2000**, *42,* 87.

[6] K. B. Oh, H. Matsuoka, *Int. J. Food Microbiol.* **2002**, *76*, 47.

[7] P. G. Lloyd, C. D. Hardin, M. Sturek, *Phdysiol. Res.* **1999**, *48*, 401.

[8] K. Yamada, M. Nakata, N. Horimoto, M. Saito, H. Matsuoka, N. Inagaki, *J. Biol. Chem.* **2000**, *275*, 22278.

[9] Z. Cheng, J. Levi, Z. Xiong, O. Gheysens, S. Keren, X. Chen, S.S. Gambhir, *Bioconjugate Chem.* **2006**, *17*, 662.

[10] a) Z. Zhang, H. Li, Q. Liu, L. Zhou, M. Zhang, Q. Luo, J. Glickson, B. Chance, G. Zheng, *Biosensors and Bioelectronics.* **2004**, *20*, 643. b) Y. Ye, S. Bloch, S. Achilefu, *J. Am. Chem. Soc*, **2004**, *126*, 7740.

[11] K. D. McReynolds, A. Bhat, J. C. Conboy, S. S. Saavedra, J. Gervay-Hague, *Bioorg. Med. Chem*. **2002**, *10*, 625.

[12] F. Fazio, M. C. Bryan, O. Blixt, J. C. Paulson, C.-H. Wong, *J. Am. Chem. Soc,* **2002***, 124,* 14397.

[13] a) M. A. Maier, C. G. Yannopoulos, N. Mohamed, A. Roland, H. Fritz, V. Mohan, G. Just, M. Manoharan, *Bioconjugate Chem.* **2003***, 14,* 18; b) R. E. Campbell, M. E. Tanner, *J. Org. Chem.* **1999***, 64,* 9487.

[14] a) M. Trester-Zedlitz, K. Kamada, S. K. Burley, D. Fenyo, B. T. Chait, T. W. Muir, *J. Am. Chem. Soc.* **2003***,125,* 2416; b) Y. Li, Y.-M. Zhu, H.-J. Jiang, J.-P. Pan, G.-S. Wu, J.-M. Wu, Y.-L. Shi, J.-D. Yang, B.-A. Wu, *J. Med. Chem.* **2000***, 43,* 1635.

[15] G. A. Korbel, G. Lalic, M. D. Shair, *J. Am. Chem. Soc.* **2001,** *123***,** 361.

[16] R. G. O'Neil, L. Wu, N. Mullani, *Mol. Imaging Biol.* **2005**, *7*, 388.

[17] P. W. Hruz, M.M. Mueckler, *Mole. Memb. Biol.* **2001**, *18*, 183.

[18] T. Mosmann, *J. Immunol. Methods.* **1983**, *65*, 55.

Chapter 2. Development of a New Series of Fluorescent Glucose Bioprobes and Their Application on Real-Time and Quantitative Monitoring of Glucose Uptake in Living Cells

- *Chem. Eur. J.* **2012**, *17*, 143.

Introduction

After the successful application of our novel fluorescent glucose bioprobe, Cy3-Glc-α, in cancer research[1], we focused on the monitoring of glucose uptake for the study of metabolic diseases, particularly diabetes mellitus, in which the maintenance of cellular glucose homeostasis is a key event that must be monitored. In this Chapter, we report the development and optimization of an image-based real-time monitoring system of glucose uptake in metabolically active cells, such as adipocytes and muscle cells. Furthermore, we applied our monitoring system in flow cytometry analysis for the quantitiative evaluation of cellular events in order to overcome the limitations associated with image-based analysis; Flow cytometry analysis allows for simultaneous multiparametric analysis of the characteristics of single cells by using an optical detection apparatus.[2]

Results and Discussion

To develop an efficient glucose monitoring system, we designed and synthesized various fluorescence-labeled analogues of D-glucose. On the basis of our previous study on Cy3-Glc-α, we expanded our panel of fluorescent glucose bioprobes through the incorporation of three different organic fluorophores Cy3, fluorescein isothiocyanate (FITC), and rhodamine B isothiocyanate (RITC) through linker molecules connected at the α-anomeric position of D-glucose. However, FITC-based glucose analogues are not suitable for use in real-time cellular monitoring, because of the FITC's susceptibility to photobleaching under the fluorescence microscopy measurement. In the case of RITC-based D-glucose analogues, we failed to observe either competitive cellular influx under the increased concentration of D-glucose in the medium or a significant deterioration of cellular influx in the presence

of high concentrations of D-glucose, which was systematically evaluated in NIH/3T3 fibroblast cells.

This implies that RITC-based glucose bioprobes are taken up not by GLUT-specific cellular translocation, but by passive diffusion. Therefore, we synthesized a new series of Cy3-labeled glucose analogues with diverse linkers connected at the a-anomeric position of D-glucose. Seven Cy3-labeled glucose analogues were synthesized and subjected to biological evaluation tests for studying the competitive cellular uptake of these analogues in the presence of D-glucose through glucose transporters.

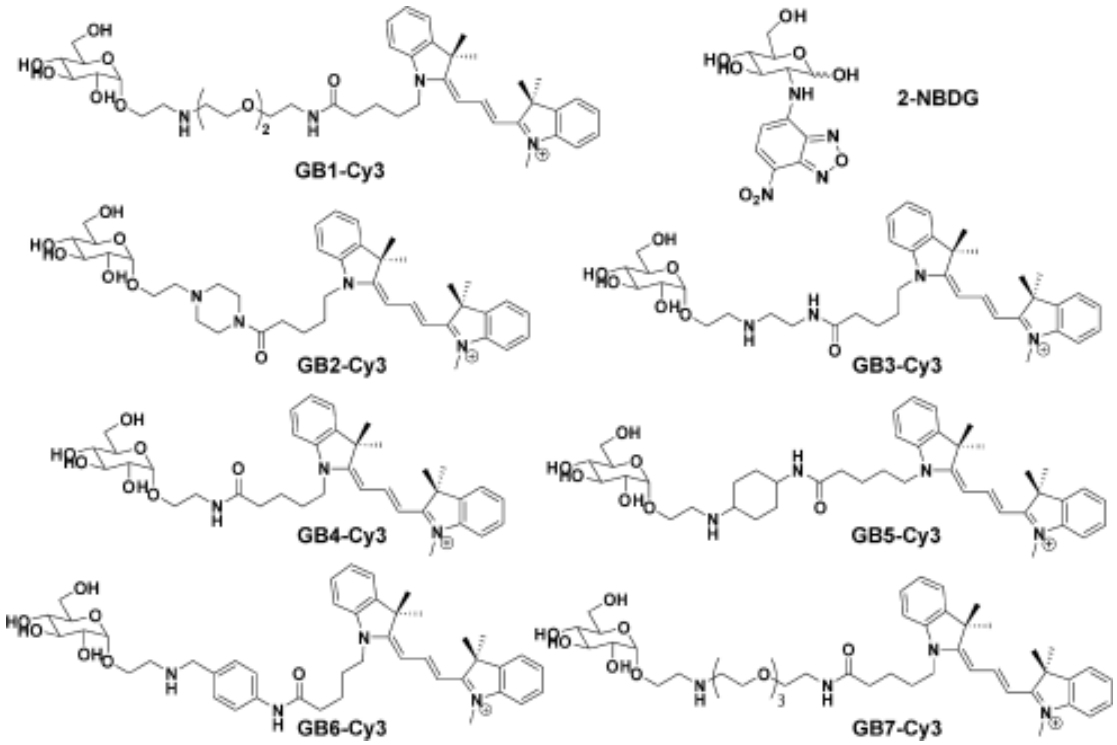

After synthesizing the aforementioned seven Cy3-labeled glucose analogues (GBs-Cy3), we performed a competition assay of these bioprobes using flow cytometry for the systematic and quantitative evaluation of various GBs-Cy3 with different linkers. To measure the competitive cellular uptake of GBs-Cy3, NIH/3T3 fibroblast cells were incubated for 30 min with each GB-Cy3 analogue in the absence or presence of 11 mM D-glucose or 11 mM L-glucose. As shown in Figure 1 A, the

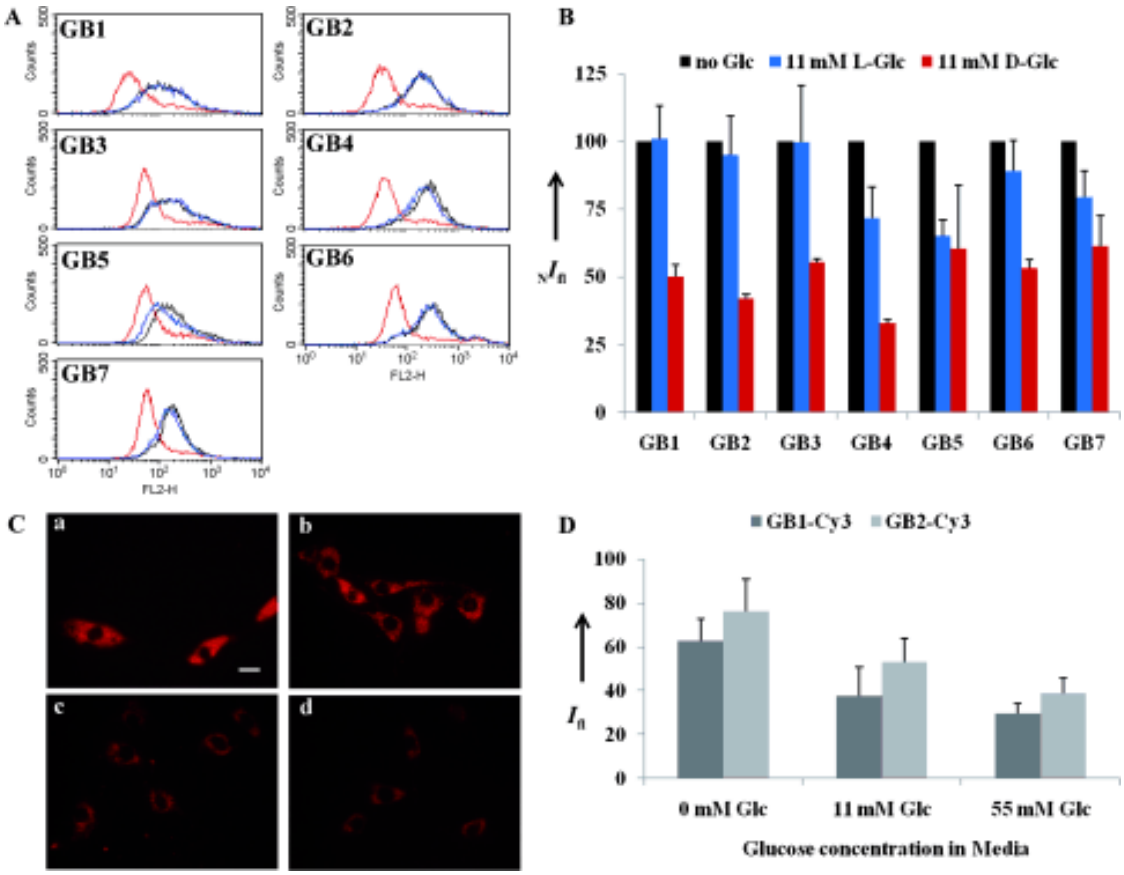

Figure 1. Glucose competition test in NIH/3T3 using flow cytometry. A) NIH/3T3 was treated with 5 μM GBs-Cy3 for 30 min and washed with cold PBS; the cells were finally analyzed by flow cytometry. Black line: no glucose, blue line: 11 mM L-glucose; red line: 11 mM D-glucose. B) Normalized fluorescence intensities $_{N}I_{fl}$. of GBs-Cy3 under three different conditions. The signal intensity recorded under each condition was normalized to 100 with the fluorescence intensity observed under glucose-deficient condition. C) Image-based analysis of glucose competition by fluorescence microscopy. NIH/3T3 fibroblast cells were incubated with 5 μM of GB1-Cy3 (a, c) and 5 μM of GB2-Cy3 (b, d) in the absence (a, b) or presence (c, d) of 11 mM D-glucose in the DMEM media. The scale bar represents 20 μm. D) Fluorescence intensities I_{fl} were determined by fluorometry: the data are the average of the values obtained in measurements performed on 35–50 cells in an experiment that is representative of at least two independent experiments.

peaks in the flow cytometry histogram of the GBs-Cy3-treated cells shifted more to the left in the presence of 11 mM D-glucose (red line) in comparison with the peaks obtained in the absence of glucose (black line) or in the presence of 11 mM L-glucose (blue line).[3-5] The fluorescence intensity was reduced to approximately 40–60 % in the presence of 11 mM D-glucose in all GBs-Cy3 treatments. Although we observed different fluorescence intensities of GBs-Cy3 in the cellular experiments, we focused

on the reduction of fluorescence intensity in the presence of D-glucose. Therefore, the mean cellular fluorescence intensity values obtained in the absence of D-glucose were normalized to 100 % and compared with the reduction in the intensity under three different conditions (Figure 1 B). Among the seven GBs-Cy3 derivatives, only GB1-Cy3 and GB2-Cy3 were found to be suitable for further studies. Upon the uptake of GB1-Cy3 and GB2-Cy3 in the D-glucose-containing medium, the cellular fluorescence intensity was reduced by approximately 50 and 42 %, respectively, as compared to that in the glucose-depleted medium; on the other hand, the fluorescence intensity was unaffected in the L-glucose-containing medium. This drastic reduction in the fluorescence intensity confirmed that GB1-Cy3 and GB2-Cy3 translocate to the cytoplasm through GLUTs by competing with D-glucose, but not with L-glucose. To validate this flow-cytometry-based analysis, we carried out a fluorescence-image-based analysis of GB1-Cy3 and GB2-Cy3. As shown in Figure 1 C and 1D, the fluorescence intensity was significantly decreased upon incubation in a medium containing 11 mM and 55 mM D-glucose as compared to that in the glucose-deficient medium. The direct comparison of these fluorescence images in NIH/3T3 fibroblasts confirms that flow cytometry analysis with our fluorescent glucose bioprobes, GB1-Cy3 and GB2-Cy3, allows the unbiased and reliable evaluation of cellular glucose uptake under specific conditions.

After the identification of GLUT-specific fluorescent glucose bioprobes, we compared GB1-Cy3 and GB2-Cy3 with 2-NBDG, a well-known fluorescent glucose bioprobe. 2-NBDG, originally reported by Yoshioka, has been widely used in various studies, especially for tumor imaging and examination of GLUT-related cell metabolism.[4,6,7] For direct comparison of these glucose bioprobes with flow cytometry analysis, NIH/3T3 cells were treated with 5 μM of three different glucose

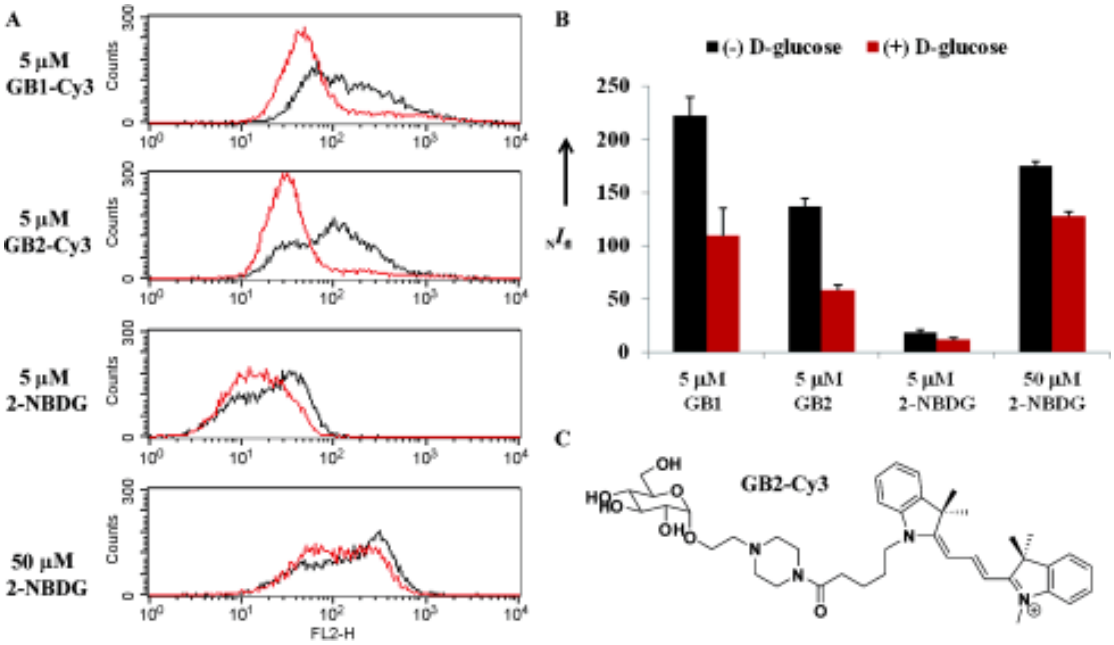

Figure 2. Glucose competition test in NIH/3T3 fibroblast cells by flow cytometry analysis. A) NIH/3T3 cells were incubated with GB1-Cy3 (5 μM), GB2-Cy3 (5 μM) or 2-NBDG (5 μM and 50 μM) for 30 min in the absence (black line) and presence (red line) of 11 mM D-glucose in the media. After washing with cold PBS, individual cells were analyzed by flow cytometry. B) Mean fluorescence intensities I_{fl} were determined by flow cytometry. C) Structure of GB2-Cy3, a new fluorescent glucose bioprobe.

bioprobes (GB1-Cy3, GB2-Cy3, and 2-NBDG) in the presence or absence of 11 mM D-glucose. As shown in Figure 2, the fluorescence intensity of 2-NBDG-treated cells in flow cytometry histograms was very weak and differed slightly in the absence and presence of D-glucose, confirming that 2-NBDG does not compete with D-glucose in GLUT-mediated cellular uptake. However, the fluorescence intensity decreased by approximately 50 and 60 % upon the cellular uptake of GB1-Cy3 and GB2-Cy3, respectively, as revealed by flow cytometry analysis. When the concentration of 2-NBDG was ten times of GB1-Cy3 and GB2-Cy3, fluorescence intensities from 2-NBDG-treated cells were comparable to one another. Moreover, a small decrease (30 %) of the fluorescence intensity was observed upon treatment with 2-NBDG (50 μM) in the presence and absence of 11 mM D-glucose. In fact, 2-NBDG has been widely used as a fluorescent 2-deoxyglucose analogue that is transported into the cells

in a GLUT-specific manner. However, the sensitivity of our fluorescent glucose bioprobes GB1-Cy3 and GB2-Cy3 is ten times higher than that of 2-NBDG. In addition, both GB1-Cy3 and GB2-Cy3 effectively compete with D-glucose in the media and translocate into the cytoplasm in a GLUT-specific manner, which was confirmed by fluorescence microscopy and flow cytometry. Taken together, especially its effective competition with d-glucose, we chose GB2-Cy3 as a selected fluorescent glucose bioprobe.

In continuation of our research on type-2 diabetes, we applied our glucose bioprobe GB2-Cy3 for the study of energy homeostasis in metabolically active cells such as adipocytes and muscle cells, in which high influx of D-glucose was mediated by overexpression of GLUT4. Initially, we pursued the fluorescent-image-based analysis of GB2-Cy3 cellular uptake in two cell lines; 3T3 L1 adipocytes and C2C12 mouse skeletal muscle cells. However, 3T3 L1 cells were not suitable for image-based analysis due to the lipid droplets and multilayered growth—the consequence of adipocyte differentiation (data not shown). Therefore, we focused on studying the homeostasis of cellular glucose influx in C2C12 muscle cells that were effectively differentiated with proper size and morphology.

Therefore, we selected C2C12 mouse skeletal muscle cells as in vitro platform for further studies on bioimaging and flow cytometry analysis. To confirm GLUT-specific cellular translocation of GB2-Cy3, we investigated the competitive inhibition of GB2-Cy3 uptake in C2C12 myocytes in the presence of d-glucose, which was continuously monitored by confocal laser scanning microscopy (CLSM). As shown in Figure 3, the fluorescence intensity of GB2-Cy3-treated C2C12 cells was 50 % greater in the absence of D-glucose than that in the presence of 5.5 mM D-glucose, as evident from the continuous monitoring of individual cells over a 20 min period after

incubation with GB2-Cy3 (10 μM) in the medium. Real-time monitoring of glucose uptake in NIH/3T3 fibroblast cells also revealed a similar pattern, indicating that GB2-Cy3 translocates into the cytoplasm in a GLUT-specific manner.

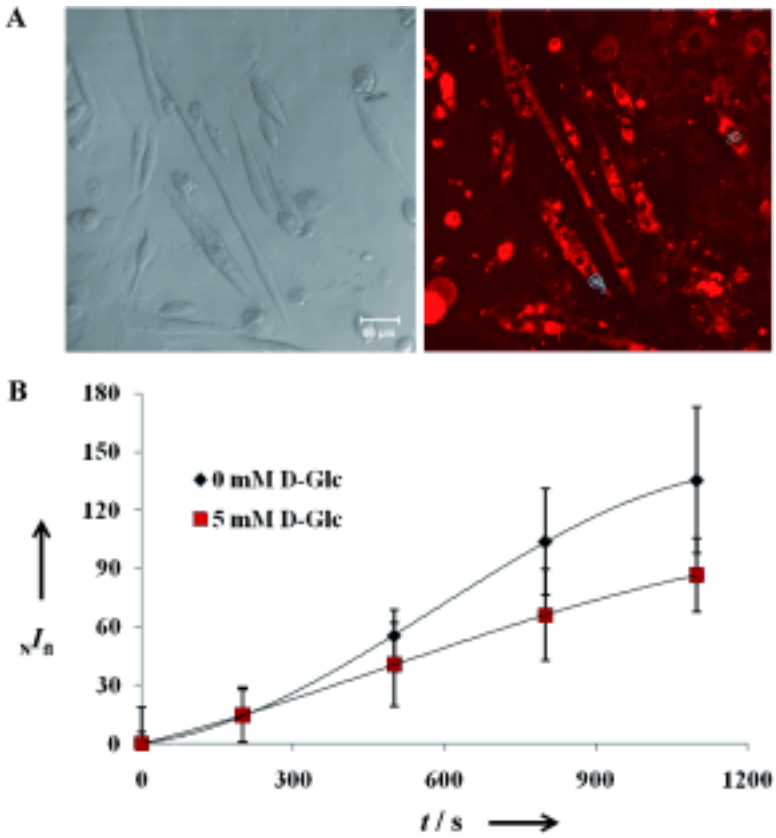

Figure 3. A) Images showing GB2-Cy3 cellular uptake by C2C12 myocytes. The scale bar represents 50 μm. B) Normalized fluorescence intensities $_NI_{fl.}$ were determined by continuous CLSM measurements performed on the region of interest (ROI) in five independent C2C12 cells marked in A) and were based on unbiased selection. Real-time monitoring of the competitive cellular uptake of GB2-Cy3 was carried out by using a confocal laser scan microscope in the absence or presence of 5.5 mM D-glucose in the media.

As mentioned above, GB2-Cy3 can visualize the level of glucose uptake in C2C12 myocytes by means of a GLUT-specific translocation in competition with D-glucose. Glucose transporters (GLUTs) are a family of membrane proteins, and 13 members of this family have been identified thus far.[8,9] Among them, GLUT1 and GLUT4 are well-characterized transporters that are expressed in various tissues.[10,11] In particular, GLUT1 is expressed in the plasma membrane and is

responsible for the basal level of glucose uptake in metabolically active adipocytes and muscle cells as well as in many other cell types. In contrast, GLUT4 is found in adipose tissues and skeletal/cardiac muscles and is known to be responsible for the regulation of cellular glucose uptake upon stimulation caused by external factors, such as insulin and exercise.[12,13] The level of cellular glucose uptake can be controlled by the translocation of GLUT4 from its intracellular storage sites to the plasma membrane and this translocation is controlled by two different signalling pathways: the insulin-dependent PI3 K/Akt signalling pathway[14,15] and the insulin-independent AMPK signalling pathway.[16,17] The former pathway is triggered by the binding event of insulin receptors with secreted insulin, and the subsequent activation of downstream signalling proteins, such as PI3 K and Akt, leads to the GLUT4 translocation to the plasma membrane. In contrast, muscle contraction and exercise cause the increase of cellular AMP/ATP ratio, and the subsequent phosphorylation at Thr172 of AMP kinase (AMPK) can trigger the insulin-independent signalling pathway. AMPK plays a crucial role as an energy sensor in metabolic tissues and stimulates glucose uptake in skeletal muscles. Upon treatment with a synthetic analogue of AMP, 5-aminoimidazole-4-carboxamide ribonucleoside (AICAR),[18,19] AMPK can be directly activated by the phosphorylation at Thr172 and readjust the balance of AMP to ATP ratio by the increased production of ATP; this increase is due to the enhanced glucose uptake through GLUT4 translocation to plasma membrane and subsequently metabolized by the TCA cycle. The insulin-dependent PI3 K/Akt signalling pathway and the insulin-independent AMPK signalling pathway enhance cellular glucose uptake through GLUT4 translocation. Therefore, we envisioned CLSM-based continuous monitoring and flow-cytometry-based quantitative monitoring of cellular glucose influx with GB2-Cy3 upon the

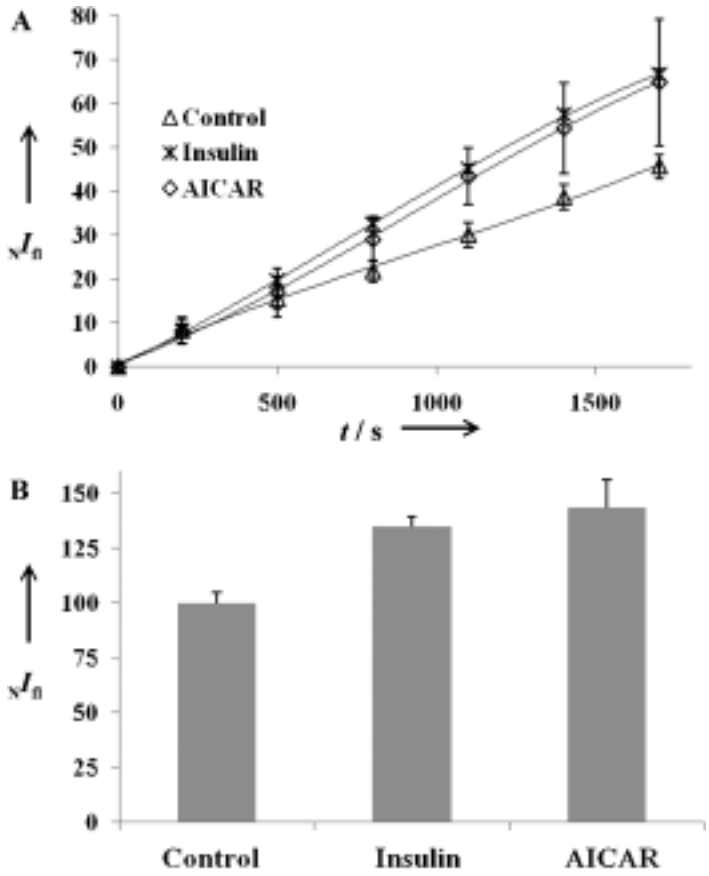

Figure 4. A) Normalized fluorescence intensities $_{N}I_{fl}$ were determined by continuous CLSM measurements of cellular GB2-Cy3 from the region of interest (ROI) in five independent C2C12 cells. Glucose uptake in C2C12 myocytes was stimulated by treatment with insulin (100 nM) and AICAR (1 mM) through insulin-dependent and insulin-independent signaling pathways. B) C2C12 myocytes were incubated with GB2-Cy3 (5 μM) for 30 min in the absence or presence of insulin (100 nM) and AICAR (1 mM). After washing with cold PBS, individual cells were analyzed by flow cytometry. Mean fluorescence intensities were determined by flow cytometry; the signal intensity was normalized to 100 by using a control.

stimulation of above-mentioned signalling pathways. As shown in Figure 4, CLSM and flow cytometry analysis revealed a 52 and 38 % increase, respectively, in the fluorescence intensity of GB2-Cy3 upon the treatment of C2C12 myocytes with insulin (100 nM), which is consistent with previous reports on 1.39-fold enhancement of glucose uptake in C2C12 cells upon stimulation with insulin.[20] We also observed the enhanced glucose uptake in C2C12 myocytes upon stimulation of insulin-independent AMPK signalling pathway by the treatment of AICAR (1 mM), a

synthetic AMP mimetic; 50 and 42 % increase of fluorescent intensity was observed using GB2-Cy3-based CLSM and flow cytometry analysis, respectively. Taken together, GB2-Cy3 can be utilized for the real-time and quantitative monitoring (CLSM and flow cytometry analysis) of cellular glucose uptake upon the perturbation of insulin-dependent PI3 K/Akt signalling and insulin-independent AMPK signaling pathways.

We then monitored the changes in cellular glucose uptake upon the inhibition of the insulin-dependent signalling pathway. Wortmannin is a specific inhibitor of PI3 K, which plays an important role in the insulin-dependent signalling pathway for GLUT4 translocation.[21,22] Therefore, the inhibition of PI3 K by wortmannin resulted in the desensitization of insulin stimulation, and the enhanced glucose uptake pattern in the insulin-treated cells might be reversed upon pre-treatment with wortmannin. Recent studies have demonstrated that the incubation of C2C12 muscle cells with 200 nM wortmannin for 1 h causes a 50 and 67 % reduction in the cellular glucose uptake monitored by radioisotope-labeled 2-deoxyglucose (2-DG), compared to the basal level and the insulin-stimulated condition, respectively.[23]As shown in Figure 5, GB2-Cy3 can differentiate the enhanced cellular glucose uptake in the presence of insulin (100 nM) from the reduced glucose uptake in insulin-treated C2C12 myocytes after pre-treatment with wortmannin (1 μM) using in three different monitoring systems: image-based analysis using fluorescence microscopy (Figure 5 A and B), quantitative analysis using flow cytometry (Figure 5 C), and real-time analysis by CLSM measurements (Figure 5 D). All these results were consistent with those reported previously.[23,24] Thus, we are confident that our fluorescent glucose bioprobe, GB2-Cy3, can monitor changes of cellular glucose uptake under the external stimulation with three distinct and complementary detection systems.

Conclusion

In this chapter, we describe the discovery and application of a novel fluorescent glucose bioprobe, GB2-Cy3, for the real-time and quantitative monitoring of glucose uptake in living cells. We synthesized a series of fluorescent glucose analogues by adding Cy3 fluorophore to the α-anomeric position of D-glucose with various linkers. The resulting seven Cy3-labeled glucose analogues (GBs-Cy3) were evaluated by flow cytometry for their GLUT-specific translocation and competitiveness with D-glucose in the medium, along with image-based analysis using fluorescence microscopy. Systematic and quantitative evaluation of these GBs-Cy3 led to the identification of GB2-Cy3 as a GLUT-specific fluorescent glucose bioprobe. GB2-Cy3 was ten times more sensitive than 2-NBDG, a leading fluorescent glucose bioprobe, as was confirmed by flow cytometry and fluorescence microscopy analyses. GB2-Cy3 was successfully utilized in three different systems to quantitatively monitor changes of glucose uptake in metabolically active C2C12 myocytes under various treatment conditions. As opposed to the standard glucose uptake assay performed using radioisotope-labeled deoxy-D-glucose and a scintillation counter, GB2-Cy3 allows the real-time monitoring of glucose uptake in living cells under different experimental conditions, which provides a powerful research tool for chemical biology and biomedical science. In addition, GB2-Cy3 can be further utilized in high-content screening (HCS), which is a drug discovery method with image-based analysis of living cells in a high-throughput manner as the basic unit for the discovery of novel therapeutic agents. Overall, our results demonstrate that GB2-Cy3 is a novel fluorescent glucose bioprobe to monitor cellular glucose uptake in a real-time and quantitative manner and has a potential for making

significant advances in biomedical studies and the diagnosis of various diseases, especially metabolic diseases.

Supporting Information

D-(+)-Glucose, acetic anhydride, sodium borohydride, fluorescein isothiocyanate (FITC), rhodamine B isothiocyanate (RITC), sodium methoxide (0.5 M solution in methanol), benzoyl chloride, piperazine, ethylene diamine, cyclohexane-1,4-diamine, 4-aminobenzylamine, 4,7,10-trioxa-1,13-tridecanediamine, 3,6-dioxaoctane-1,8-diamine, dimethylformamide (DMF), dichloromethane (DCM), dimethylsulfoxide (DMSO), pyridine, and trifluoroacetic acid (TFA) were purchased from Sigma-Aldrich [St. Louis, MO, USA]. *N,N*-Diisopropylethylamine, triethylamine, and 2-bromoethanol were purchased from TCI [JAPAN]. (7-Azabenztriazol-1-yloxy)tripyrrolidinophosphonium hexaflurophosphate (PyAOP) was purchased from PerSeptive Biosystems [Germany]. The ^{1}H and ^{13}C NMR spectra were recorded on a Bruker DRX-300 MHz and Varian 500MHz instrument using tetramethylsilane as references. High resolution mass spectrometry (HRMS) analysis was performed at the Mass Spectrometry Facility of the National Center for Inter-university Research facilities, Seoul National University. The desired products were identified with LC/MS analysis using Finnigan MSQ LC/MS system by direct injection for electron spray ionization (ESI) or atmosphere pressure chemical ionization (APCI). Gradient reverse phase HPLC analysis was performed using VP-ODS C18 column for analysis, PRC-ODS C18 column for preparation, LC-6AD pump, SPD-10A detector [Shimadau, Japan]. Eluent A is the deionized water containing 0.1 % TFA [HPLC grade, B&J, USA] and eluent B is the acetonitrile containing 0.1 % TFA [HPLC grade, B&J, USA].

NIH/3T3 (mouse fibroblast cells) and C2C12 (mouse myoblast cells) were obtained from ATCC [American Type Culture Collection, USA]. High glucose DMEM, low glucose DMEM, glucose-depleted DMEM, fetal bovine serum (FBS), horse serum, antibiotic antimycotic solution were purchased from GIBCO [Carlsbad, CA, USA]. Phosphate-buffered saline (PBS) and glucose solution were purchased from Welgene Inc. [Seoul, South Korea]. Insulin and wortmannin were purchased from SIGMA [USA]. AICAR was purchased from Toronto Research Chemicals, Inc. [Canada]. Microscope cover glasses were purchased from Marienfeld GmbH & Co., KG [Germany]. Fluorescence microscope images were obtained by using a confocal laser scanning microscope (CLSM) [Carl Zeiss-LSM510, Germany] and fluorescence optical microscope [Olympus IX71, Japan]. Fluorescence image analysis and quantification was performed using Image-Pro software [Media Cybernetics, USA]. FACS tubes were purchased from BD Biociences [USA]. Flow cytometry analysis was performed with FACSCalibur [BD Biosciences, USA].

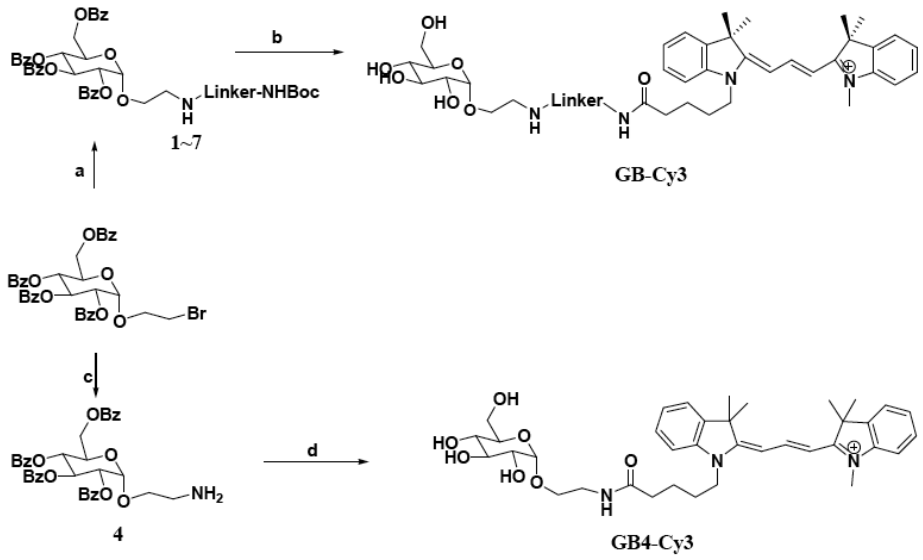

a. Mono Boc-diamine linker, triethylamine, DMF, 80℃ ; b. (i)50% TFA /DCM (ii) Cy3-COOH , PyAOP, DIPEA , DMF (iii) NaOMe , MeOH ; c. (i) NaN_3, DMF, 80℃ (ii) PPh_3, THF (iii) dH_2O;d. (i) Cy3-COOH,PyAOP, DIPEA, DMF (ii) NaOMe, MeOH

Supplementary Scheme 1. Synthetic scheme of Cy3-GBs

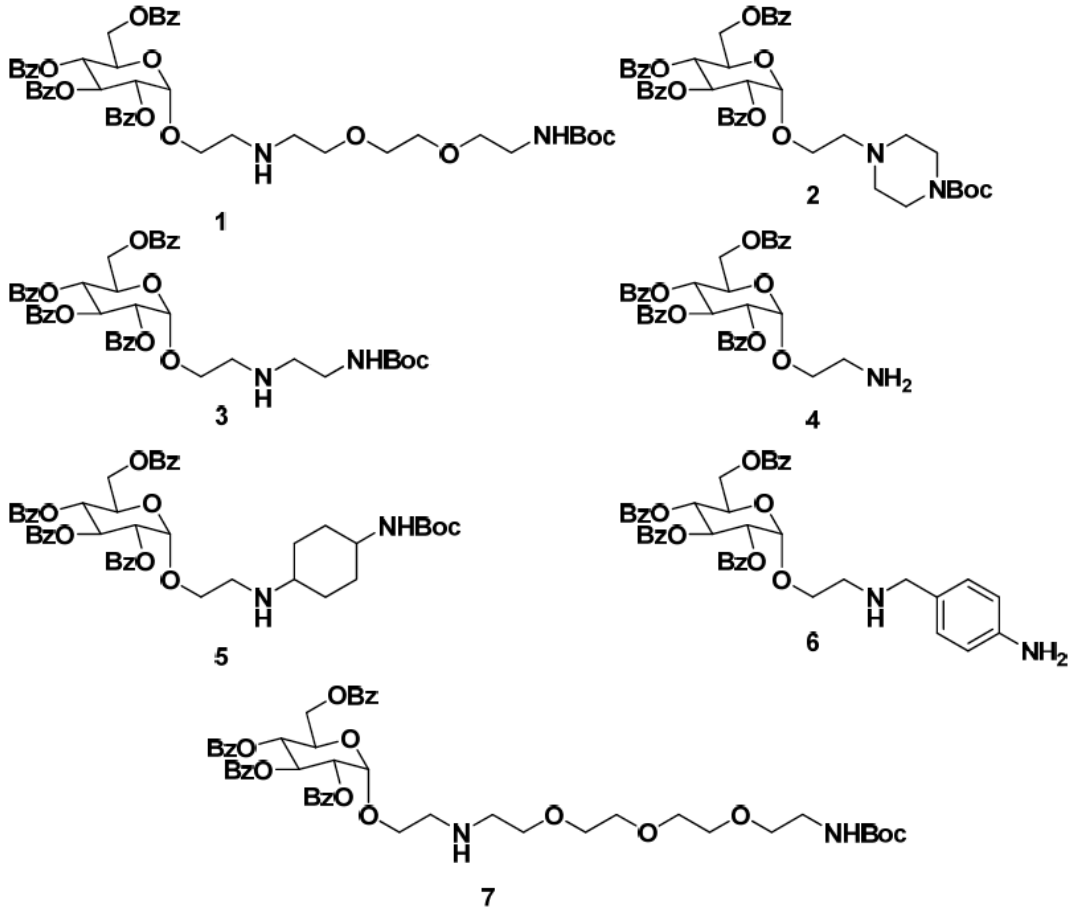

Supplementary Figure 1. Structures of glucose analogues with various linkers

[2-(*N*-boc-3,6-dioxaoctane-1,8-diaminoethyl)]-2,3,4,6-tetra-O-benzoyl-α-D-glucoside (1):

To a solution of (2-bromoethyl)-2,3,4,6-tetra-O-benzoyl-α-D-glucoside (800 mg, 1.137 mmol) in 10 mL anhydrous DMF was added *N*-Boc-3,6-dioxaoctane-1,8-diamine (1.188 g, 3.411 mmol), potassium iodide (377 mg, 2.274 mmol) and TEA (475 μL, 3.411 mmol). The reaction mixture was stirred at 80 °C for 10 h. After the reaction completion monitored by TLC, the resulting solution was diluted with ddH2O, then extracted three times with ethyl acetate. The combined organic layer was washed with brine, dried over anhydrous $MgSO_4$, and condensed under reduced pressure. The desired product **1** was purified by silica-gel flash column chromatography (hexane:ethyl acetate = 1:1 → DCM:MeOH = 10:1) as a yellow oil

(980 mg, quantitative yield). ^{1}H NMR (500 MHz, $CDCl_3$) δ 8.06–7.86 (m, 8H), 7.52–7.28 (m, 12H), 6.19 (dd, *J* = 9.8, 9.8 Hz, 1H), 5.71 (dd, *J* = 9.6, 9.5 Hz, 1H), 5.40 (d, *J* = 3.5 Hz, 1H), 5.33 (dd, *J* = 10.1, 3.5 Hz, 1H), 4.62 (d, *J* = 9.5 Hz, 1H), 4.50–4.47 (m, 2H), 3.99–3.94 (m, 1H), 3.72–3.60 (m, 2H), 3.54–3.50 (m, 6H), 3.44 (t, *J* = 5.1 Hz, 2H), 3.29 (d, *J* = 4.5 Hz, 2H), 2.92–2.86 (m, 2H), 2.78–2.73 (m, 1H), 2.32 (bs, 2H), 1.42 (s, 9H); ^{13}C NMR (125 MHz, $CDCl_3$) δ 166.17, 165.83, 165.69, 165.27, 156.03, 133.44, 133.13, 129.88, 129.85, 129.73, 129.67, 129.10, 128.97, 128.86, 128.49, 128.41, 128.30, 96.26, 79.09, 71.96, 70.47, 70.44, 70.18, 69.48, 68.41, 67.86, 67.08, 62.93, 49.00, 48.66, 40.35, 28.42; LC/MS calcd for $C_{47}H_{55}N_2O_{14}$ $[M+H]^+$: 871; found: 871.

[2-(*N*-boc-piperazynoethyl)]-2,3,4,6-tetra-O-benzoyl-α-D-glucoside (2) General procedure for the synthesis of **1** was applied for the preparation of **2**. The crude product was purified by silica-gel flash column chromatography to afford the desired compound **2** in 70 % yield (185 mg). ^{1}H NMR (500 MHz, $CDCl_3$) δ 8.05–7.86 (m, 8H), 7.57–7.28 (m, 12H), 6.18 (dd, *J* = 10.5, 9.5 Hz, 1H), 5.68 (dd, *J* = 9.5, 9.5 Hz, 1H), 5.43 (d, *J* = 3.5 Hz, 1H), 5.29 (dd, *J* = 10.5, 3.5 Hz, 1H), 4.63–4.59 (m, 1H), 4.49–4.45 (m, 2H), 3.89 (ddd, *J* = 11.0, 5.5, 5.0 Hz, 1H), 3.67 (ddd, *J* = 11.0, 6.0, 5.0 Hz, 1H), 3.23 (bs, 4H), 2.65–2.58 (m, 2H), 2.35 (bs, 4H), 1.44 (s, 9H); ^{13}C NMR (125 MHz, CDCl3) δ 166.62, 166.30, 166.16, 165.78, 155.11, 133.99, 133.92, 133.64, 130.33, 130.20, 130.16, 130.13, 129.62, 129.44, 129.34, 128.97, 128.90, 128.78, 96.38, 96.32, 80.01, 72.42, 70.88, 70.00, 68.73, 66.73, 63.51, 57.92, 53.87, 28.91; LC/MS calcd for $C_{45}H_{49}N_2O_{12}$ $[M+H]^+$: 809; found: 809.

[2-(*N*-boc-ethylenediaminoethyl)]-2,3,4,6-tetra-O-benzoyl-α-D-glucoside (3): General procedure for the synthesis of **1** was applied for the preparation of **3**. The crude product was purified by silica-gel flash column chromatography to afford the desired product **3** in 97 % yield (54 mg). ^{1}H NMR (500 MHz, $CDCl_3$) δ 8.05–7.87 (m, 8H), 7.57–7.29 (m, 12H), 6.18 (dd, *J* = 10.5, 9.5 Hz, 1H), 5.69 (dd, *J* = 10.0, 9.5 Hz, 1H), 5.39 (d, *J* = 5 Hz, 1H), 5.30 (dd, *J* = 10.5, 5 Hz, 1H), 4.87 (bs, 1H), 4.62–4.60 (m, 1H), 4.50–4.45 (m, 2H), 3.93–3.90 (m, 1H), 3.60–3.59 (m, 1H), 3.00–2.96 (m, 2H), 2.87–2.83(m, 1H), 2.79–2.76 (m, 1H), 2.64–2.55 (m, 2H), 1.43 (s, 9H); ^{13}C NMR (75 MHz, $CDCl_3$) δ 166.16, 165.83, 165.67, 165.29, 155.99, 133.59, 133.43, 133.15, 129.87, 129.79, 129.72, 129.13, 128.93, 128.87, 128.56, 128.41, 128.31, 96.17, 79.13, 72.07, 70.45, 69.54, 68.37, 67.89, 63.00, 48.81, 48.37, 45.61, 30.16, 29.70, 28.42 ; LC/MS calcd for $C_{43}H_{47}N_2O_{12}$ $[M+H]^+$: 783; found: 783.

[2-aminoethyl]-2,3,4,6-tetra-O-benzoyl-α-D-glucoside (4): To a solution of (2-bromoethyl)-2,3,4,6-tetra-O-benzoyl-α-D-glucoside (100 mg, 0.142 mmol) in 1.5 mL anhydrous DMF was added NaN_3 (28 mg, 0.426 mmol) and the reaction mixture was stirred at 80 °C for 10 h. After the reaction completion monitored by TLC, the resulting solution was diluted with ddH2O, then extracted three times with ethyl acetate. The combined organic layer was washed with brine, dried over anhydrous $MgSO_4$, and condensed under reduced pressure. To a solution of resulting azidoglucoside (94 mg) in 5 mL anhydrous THF, PPh_3 (96 mg, 0.366 mmol) was added and the reaction mixture was stirred at room temperature. After the reaction completion monitored by TLC, 500 μL of ddH2O was added. After the filtration and condensation of crude product, the desired product **4** was purified by silica-gel flash column chromatography (hexane:ethyl acetate = 1:1 → DCM:MeOH = 5:1) as a

white solid in 71 % yield (64 mg). ^{1}H NMR (500 MHz, $CDCl_3$) δ 8.05–7.87 (m, 8H), 7.54–7.30 (m, 12H), 6.21 (dd, *J* = 10.5, 9.5 Hz, 1H), 5.71 (dd, *J* = 9.5, 9.5 Hz, 1H), 5.39 (d, *J* = 3.5 Hz, 1H), 5.33 (dd, *J* = 10.5, 3.5Hz, 1H), 4.63–4.60 (m, 1H), 4.50–4.48 (m, 2H), 3.88–3.86 (m, 1H), 3.54–3.52 (m, 1H), 2.93–2.91 (m, 2H), 2.67 (bs, 2H); ^{13}C NMR (125 MHz, $CDCl_3$) δ 166.41, 166.19,165.98, 165.52, 133.72, 133.66, 133.41, 133.38, 130.10, 130.05, 129.95, 129.92, 129.88, 129.35, 129.15, 129.08, 128.74, 128.65, 128.53, 96.55, 72.24, 71.14, 70.71, 69.78, 68.14, 63.24, 41.62; LC/MS calcd for $C_{36}H_{34}NO_{10}$ $[M+H]^+$: 640; found: 640.

[2-(*N*-boc-cyclohexane-1,4-diaminoethyl)]-2,3,4,6-tetra-O-benzoyl-α-D-glucoside (5):

General procedure for the synthesis of **1** was applied for the preparation of **5**. The crude product was purified by silica-gel flash column chromatography to afford the desired product **5** in 50% yield (45 mg). ^{1}H NMR (500 MHz, $CDCl_3$) δ 8.10–7.87 (m, 8H), 7.57–7.28 (m, 12H), 6.19 (dd, *J* = 10.0, 10.0 Hz, 1H), 5.69 (dd, *J* = 10.0, 9.5 Hz, 1H), 5.38 (d, *J* = 3.5 Hz, 1H), 5.30 (dd, *J* = 10.0, 3.5Hz, 1H), 4.61–4.59 (m, 1H), 4.99–4.43 (m , 2H), 3.95–3.93 (m, 1H), 3.62–3.59 (m, 1H), 2.87–2.78 (m, 2H), 2.33–2.31 (m, 1H), 2.03–2.02 (m, 2H), 1.96–1.87 (m, 2H), 1.73–1.68 (m, 2H), 1.44 (s, 9H), 1.30–1.21(m, 3H), 1.05–0.96 (m, 3H); ^{13}C NMR (125 MHz, $CDCl_3$) δ 166.34, 166.06, 165.79, 165.44, 160.12, 155.99, 133.78, 133.63, 133.34, 130.04, 129.91, 129.89, 129.83, 129.28, 129.10, 129.04, 128.70, 128.60, 128.50, 96.23, 74.07, 71.21, 69.67, 68.05, 63.15, 56.14, 49.98, 46.10, 32.10, 31.85, 31.79, 28.62; LC/MS calcd for $C_{47}H_{53}N_2O_{12}$ $[M+H]^+$: 837; found: 837.

[2-(4-amino benzylaminoethyl)]-2,3,4,6-tetra-O-benzoyl-α-D-glucoside (6):

General procedure for the synthesis of **1** was applied for the preparation of **6**. The

crude product was purified by silica-gel flash column chromatography to afford the desired product **6** in 56 % yield (30 mg). ^{1}H NMR (500 MHz, $CDCl_3$) δ 8.05–7.86 (m, 8H), 7.56–7.28 (m, 12H), 7.03–7.01 (m, 2H), 6.59–6.57(m, 2H), 6.19 (dd, *J* = 10.0, 10.0 Hz, 1H), 5.69 (dd, *J* = 10.5, 10.0 Hz, 1H), 5.39–5.32 (m, 2H), 4.58 (d, *J* = 11.0 Hz, 1H), 4.48–4.43 (m, 2H), 3.97–3.95 (m, 1H), 3.65–3.63 (m, 3H), 2.92–2.82 (m, 2H); ^{13}C NMR (125 MHz, $CDCl_3$) δ 167.77, 166.42, 166.08, 165.96, 165.50, 133.91, 133.65, 133.36, 130.52, 130.26, 130.13, 130.08, 129.98, 129.94, 129.89, 129.63, 129.36, 129.13, 129.11, 128.72, 128.66, 115.38, 96.49, 72.12, 70.72, 69.68, 68.12, 63.14, 53.07, 47.76; LC/MS calcd for $C_{43}H_{40}N_2O_{10}$ $[M+H]^+$: 745; found: 745.

[2-(*N*-boc-4,7,10-trioxa-1,13-tridecanediaminoethyl)]-2,3,4,6-tetra-O-benzoyl-α-D-glucoside (7): General procedure for the synthesis of **1** was applied for the preparation of **7**. The crude product was purified by silica-gel flash column chromatography to afford the desired product **7** in 86% yield (58 mg). ^{1}H NMR (500 MHz, $CDCl_3$) δ 8.05–7.88 (m, 8H), 7.57–7.28 (m, 12H), 6.18 (dd, *J* = 10.0, 10.0 Hz, 1H), 5.70 (dd, *J* = 9.5, 9.0 Hz, 1H), 5.39 (d, *J* = 3.0 Hz, 1H), 5.31 (dd, *J* = 10.0, 2.5Hz, 1H), 5.03 (bs, 1H), 4.61 (d, *J* = 10.5 Hz, 1H), 4.47 (d, *J* = 10.0 Hz, 2H), 3.97–3.95 (m, 1H), 3.63–3.57 (m , 12H), 3.38 (s, 2H), 3.22–3.21 (m, 2H), 2.89–2.85 (m, 2H), 2.66–2.65 (m, 2H), 1.75 (t, *J* = 6.0 Hz, 2H), 1.63–1.55 (m, 2H), 1.43 (s, 9H); ^{13}C NMR (125 MHz, $CDCl_3$) δ 166.38, 166.06, 165.88, 165.48, 156.28, 133.73, 133.66, 133.40, 133.39, 130.07, 129.97, 129.92, 129.88, 129.35, 129.18, 129.10, 128.74, 128.65, 128.54, 96.44, 72.21, 70.79, 70.71, 70.42, 70.31, 69.83, 69.72, 69.66, 68.13, 68.16, 48.75, 47.28, 38.75, 29.93, 28.70; LC/MS calcd for $C_{51}H_{63}N_2O_{15}$ $[M+H]^+$: 943; found: 943.

General Procedure for the Synthesis of GB1-Cy3: For the deprotection of Boc group on the primary amine of **1** (100 mg, 0.131 mmol), 50% TFA in dichloromethane was added to compound **1**, followed by N2 purging to remove residual DCM and TFA in the reaction mixture. The resulting deprotected residue in DMF (200 μL) was slightly basified with DIPEA (100 μL, 0.57 mmol) and added to a solution of Cy3-COOH (29 mg, 0.065 mmol) and PyAOP (101 mg, 0.19 mmol) in 200 μL DMF. The reaction mixture was stirred at room temperature for 1 h and the reaction completion was monitored by HPLC analysis. After purification using reverse-phase HPLC charged with C18 column, sodium methoxide (0.5 M in MeOH, 520 μL, 0.26 mmol) was added for debenzoylation and the reaction mixture was stirred at room temperature. After the reaction completion monitored by HPLC analysis, the reaction mixture was neutralized with methanolic HCl (1 mL). The elution protocol for analytical HPLC is following: (1) 95% eluent A for 1 min, (2) a linear gradient to 60% eluent A over 4 min, (3) a linear gradient to 50% eluent A over 10 min, (4) a linear gradient to 5% eluent A over 10 min, (5) a linear gradient to 0% eluent A over 5 min, (6) a constant flow with 0% eluent A for 10 min, and (6) a linear gradient from 0% to 95% eluent A over 10 min for the regeneration and washing. The purification of crude mixture using prep HPLC affords the desired product **GB1-Cy3** in 26% three-step yield (13.5 mg; retention time at 12 min). ^{1}H NMR (500 MHz, CD_3OD) δ 8.55 (dd, *J* = 14.0, 13.0 Hz, 1H), 7.54 (d, *J* = 7.5 Hz, 2H), 7.47–7.43 (m, 2H), 7.37–7.29 (m, 4H), 6.44 (dd, *J* = 13.5, 1.5 Hz, 2H), 4.16 (t, *J* = 7.5 Hz, 2H), 4.03–3.99 (m, 1H), 3.82 (dd, *J* = 11.5, 2.0 Hz, 1H), 3.76–3.74 (m, 2H), 3.69–3.59 (m, 12H), 3.57–3.47 (m, 5H), 3.49–3.37 (m, 4H), 3.28–3.25 (m, 4H), 2.30 (t, *J* = 7.0 Hz, 2H), 1.80 (s, 12H); ^{13}C NMR (125 MHz, CD_3OD) δ 175.56, 174.77, 174.36, 150.96, 142.84, 142.13, 140.97, 128.77, 125.61, 125.52, 122.33, 122.17, 111.17, 111.00,

102.60, 102.39, 99.05, 73.71, 73.11, 72.03, 70.35, 70.20, 70.01, 69.35, 65.63, 62.48, 61.43, 49.42, 43.71, 38.98, 35.04, 30.55, 27.11, 26.93, 26.73, 22.79; HRMS (FAB^+): calcd for $C_{43}H_{63}N_4O_9$ $[M]^+$: 779.4595; found: 779.4601.

GB2-Cy3: General procedure for the synthesis of **GB1-Cy3** was applied for the preparation of **GB2-Cy3**. The crude product was purified by using prep HPLC with same elution protocol to afford the desired product **GB2-Cy3** in 85% three-step yield (22 mg; retention time at 12 min). ^1H NMR (500 MHz, CD_3OD) δ 8.55 (t, J = 13.5 Hz, 1H), 7.54 (d, J = 7.5 Hz, 2H), 7.47–7.30 (m, 6H), 6.45 (dd, J = 13.4, 9.0 Hz, 2H), 4.20–4.17 (m, 2H), 4.08–4.05 (m, 1H), 3.83–3.80 (m, 3H), 3.67 (s, 3H) 3.63–3.42 (m, 12H), 2.57–2.54 (m, 2H), 1.97–1.79 (m, 6H), 1.78 (s, 6H), 1.77 (s, 6H); ^{13}C NMR (125 MHz, CD_3OD) δ 175.56, 174.86, 172.06, 151.01, 142.88, 142.20, 141.03, 140.90, 128.80, 125.64, 125.58, 122.35, 122.21, 111.28, 111.11, 102.60, 102.51, 99.20, 73.71, 73.32, 71.96, 70.35, 61.46, 60.82, 56.16, 55.35, 49.48, 49.45, 43.87, 38.37, 31.68, 30.57, 27.14, 26.98, 26.98, 26.90, 21.91; HRMS (FAB^+): calcd for $C_{41}H_{57}N_4O_7$ $[M]^+$: 717.4227; found: 717.4235.

GB3-Cy3: General procedure for the synthesis of **GB1-Cy3** was applied for the preparation of **GB3-Cy3**. The crude product was purified by using prep HPLC with same elution protocol to afford the desired product **GB2-Cy3** in 22% three-step yield (8 mg; retention time at 11 min). ^1H NMR (300 MHz, CD_3OD) δ 8.57 (t, J = 13.4 Hz, 1H), 7.56 (d, J = 7.3 Hz, 2H), 7.49–7.45 (m, 2H), 7.40–7.31 (m, 4H), 6.47 (dd, J = 13.4, 3.0 Hz, 2H), 4.22–4.17 (m, 2H), 4.05–4.01 (m, 1H), 3.87–3.84 (m, 2H), 3.71–3.59 (m, 6H), 3.53–3.49 (m, 5H), 3.28–3.21 (m, 2H), 2.40–2.00 (m, 2H), 1.97–1.80 (m, 6H), 1.79 (bs, 12H); ^{13}C NMR (75 MHz, CD_3OD) δ 175.59, 175.34, 174.59, 150.78, 142.64, 141.93, 140.77, 140.67, 128.56, 125.41, 125.32, 122.12, 121.97,

111.02, 110.88, 102.42, 102.22, 98.88, 73.53, 72.92, 71.94, 70.27, 62.28, 61.24, 49.23, 43.55, 35.76, 34.66, 30.37, 26.91, 26.74, 26.67, 22.25; HRMS(FAB^+): calcd for $C_{39}H_{55}N_4O_7$ $[M]^+$: 691.4075; found: 691.4073.

GB4-Cy3: General procedure for the synthesis of **GB1-Cy3** was applied for the preparation of **GB4-Cy3**. The crude product was purified by using prep HPLC with same elution protocol to afford the desired product **GB4-Cy3** in 57% three-step yield (8 mg; retention time at 12 min). ^1H NMR (300 MHz, CD_3OD) δ 8.57 (t, J = 13.4 Hz, 1H), 7.55 (d, J = 7.4 Hz, 2H), 7.49–7.44 (m, 2H), 7.39–7.30 (m, 4H), 6.47 (d, J = 13.4 Hz, 2H), 4.77 (d, J = 3.7 Hz, 1H), 4.21–4.16 (m, 2H), 3.83–3.79 (m, 2H), 3.71 (s, 3H), 3.71–3.52 (m, 7H), 3.42–3.33 (m, 2H), 3.27–3.25 (m, 1H), 2.35–2.31 (m, 2H), 1.98–1.67 (m, 14H) ; ^{13}C NMR (75 MHz, CD_3OD) δ 175.32, 174.61, 174.10, 150.75, 142.67, 141.98, 140.78, 140.69, 128.60, 128.54, 125.38, 125.31, 122.11, 121.96, 111.04, 110.88, 102.45, 102.27, 98.89, 73.73, 72.51, 72.12, 70.43, 66.62, 61.35, 49.24, 49.21, 43.53, 38.85, 34.93, 30.40, 26.93, 26.76, 26.54, 22.67; HRMS (FAB^+): calcd for $C_{37}H_{50}N_3O_7$ $[M]^+$: 648.3649; found: 648.3660.

GB5-Cy3: General procedure for the synthesis of **GB1-Cy3** was applied for the preparation of **GB5-Cy3**. The crude product was purified by using prep HPLC with same elution protocol to afford the desired product **GB5-Cy3** in 16% three-step yield (3 mg; retention time at 12 min). ^1H NMR (300 MHz, CD_3OD) δ 8.58 (t, J = 13.4 Hz, 1H), 7.57 (d, J = 7.3 Hz, 2H), 7.51–7.44 (m, 2H), 7.40–7.31 (m, 4H), 6.47 (dd, J = 13.4, 2.0 Hz, 2H), 4.22–4.17 (m, 2H), 4.05–4.01 (m, 1H), 3.88–3.83 (m, 1H), 3.71 (s, 3H), 3.71–3.50 (m, 7H), 3.28–3.21 (m, 2H), 2.32–2.27 (m, 2H), 2.21–2.20 (m, 2H), 2.05–2.01 (m, 3H), 1.97–1.79 (m, 14H), 1.58–1.31 (m, 6H); ^{13}C NMR (75 MHz, CD_3OD) δ 175.36, 174.65, 173.32, 150.78, 142.64, 141.93, 140.79, 140.68, 128.57,

125.43, 125.34, 122.14, 121.98, 111.00, 110.88, 102.38, 102.23, 98.77, 73.49, 72.92, 71.79, 70.11, 62.56, 61.23, 55.85, 44.46, 43.51, 42.75, 34.86, 31.64, 30.35, 29.78, 27.62, 27.50, 26.91, 26.75, 26.54, 22.64; HRMS (FAB^+): calcd for $C_{43}H_{61}N_4O_7$ $[M]^+$: 745.4540; found: 745.4545.

GB6-Cy3: General procedure for the synthesis of **GB1-Cy3** was applied for the preparation of **GB6-Cy3**. The crude product was purified by using prep HPLC with same elution protocol to afford the desired product **GB6-Cy3** in 35% three-step yield (6 mg; retention time at 12 min). ^1H NMR (300 MHz, CD_3OD) δ 8.58 (t, J = 13.4 Hz, 1H), 7.53 (d, J = 7.1 Hz, 2H), 7.47–7.28 (m, 10H), 6.48–6.43 (m, 2H), 4.80–4.67 (m, 3H), 4.20–4.17 (m, 2H), 3.96–3.92 (m, 1H), 3.83–3.76 (m, 2H), 3.71–3.67 (m, 4H), 3.65–3.54 (m, 5H), 3.48–3.43 (m, 3H), 2.73–2.70 (m, 1H), 1.93–1.77 (m, 2H), 1.77 (bs, 12H); ^{13}C NMR (75 MHz, CD_3OD) δ 175.18, 174.59, 174.19, 174.02, 150.73, 142.67, 141.97, 140.67, 128.89, 128.64, 128.54, 128.24, 127.67, 127.22, 125.32, 122.09, 121.97, 121.16, 119.97, 111.16, 110.82, 102.43, 98.94, 73.76, 72.76, 72.56, 72.01, 71.88, 70.38, 65.13, 61.39, 61.28, 49.24, 46.47, 43.80, 39.05, 32.09, 30.37, 29.36, 26.95, 26.76, 22.20; HRMS (FAB^+): calcd for $C_{44}H_{57}N_4O_7$ $[M]^+$: 753.4227; found: 753.4209.

GB7-Cy3: General procedure for the synthesis of **GB1-Cy3** was applied for the preparation of **GB7-Cy3**. The crude product was purified by using prep HPLC with same elution protocol to afford the desired product **GB7-Cy3** in 25% three-step yield (10 mg; retention time at 12min). ^1H NMR (300 MHz, CD_3OD) δ 8.55 (t, J = 13.4 Hz, 1H), 7.55 (d, J = 7.3 Hz, 2H), 7.48–7.42 (m, 2H), 7.37–7.28 (m, 4H), 6.44 (d, J = 13.4 Hz, 2H), 4.19–4.14 (m, 2H), 4.03–3.97 (m, 1H), 3.85–3.81 (m, 2H), 3.69 (s, 3H),

3.69–3.62 (m, 12H), 3.56–3.53 (m, 4H), 3.51–3.46 (m, 4H), 3.26–3.20 (m, 6H), 2.31–2.27 (m, 2H), 2.02–1.94 (m, 3H), 1.90–1.69 (m, 14H); ^{13}C NMR (75 MHz, CD_3OD) δ 175.35, 174.58, 173.94, 150.76, 142.64, 141.94, 140.77, 140.68, 128.56, 125.42, 125.33, 122.14, 121.98, 110.99, 110.89, 102.42, 102.23, 102.22, 98.89, 73.52, 72.93, 71.84, 70.17, 70.04, 69.87, 69.77, 69.73, 68.38, 68.25, 62.39, 61.24, 49.23, 46.04, 43.51, 36.35, 34.96, 30.37, 29.13, 26.92, 26.75, 26.54, 25.76, 22.68; HRMS (FAB^+): calcd for $C_{47}H_{71}N_4O_{10}$ $[M]^+$: 851.5170; found: 851.5193.

Cell Culture and Differentiation

NIH/3T3 (mouse fibroblast cells) and C2C12 (mouse myoblast cells) were obtained from ATCC [American Type Culture Collection, USA]. All cell lines were cultured in Dulbecco's modified Eagle medium (DMEM) containing 10% fetal bovine serum (FBS) and 1% antibiotic-antimycotic solution at 37 °C in an atmosphere of 5% CO_2. For the differentiation to mature muscle cells, the C2C12 mouse myoblast cells were maintained in DMEM supplemented with 10% FBS and 1% antibiotic-antimycotic solution [GIBCO]. When the cells reached 100% confluence, the medium was changed to DMEM containing 2% horse serum and supplemented in every other day. Flow cytometry and fluorescence microscopy imaging experiments were carried out on the cells 3 to 5 days after differentiation.

Competition Test in NIH/3T3 by Flow Cytometry Analysis

To measure the competitive cellular uptake of GBs-Cy3, NIH/3T3 fibroblast cells were washed once with cold PBS and incubated for 30 min at 37 °C in the presence of individual fluorescent glucose bioprobes (GBs-Cy3) in PBS containing 11 mM D-glucose, 11 mM Lglucose, and no glucose. The final concentration of the analog in

the system was adjusted to 5 μM. After washing with cold phosphate-buffered saline (PBS), individual cells were harvested, and transferred to individual FACS tubes. NIH/3T3 cells (1 x 10^4 cells) were analyzed using a flow cytometer (FACS CaliburTM) at an excitation wavelength of 488 nm. Fluorescence emission from the GBs-Cy3 in individual cells was observed by the FL2 channel in the range 564–606 nm; the fluorescence intensity data were analyzed by plotting one- or two-dimensional histograms. Specific gating protocols were used to eliminate the artifacts caused by cell debris or dead cells, and subsequently, the regions of the histogram were converted to the corresponding numerical values.

Antidiabetic Agent Tests in C2C12 Myocytes by Flow Cytometry Analysis

C2C12 myoblast cells were cultured in a 6-well plate. After the cells reached 100% confluence, differentiation was started. After differentiation proceeded to a sufficiently high level, the cell culture medium was changed to a low-glucose medium (without FBS), and the cells were retained in the new medium for 4 h. The cells were then incubated for 1 h in a glucose-depleted DMEM medium (without FBS) in the presence of 100 nM insulin or 1 mM AICAR. Next, the medium was replaced with a glucose-depleted DMEM medium containing 5 mM GB2-Cy3, and the cells were retained in the latter for 30 min. Then, the cells were washed with cold PBS, harvested, and transferred to each FACS tube. C2C12 myocytes (1 x 10^4 cells) were analyzed with a flow cytometer (FACS Calibur^{TM}) at an excitation wavelength of 488 nm. Fluorescence emission from the GBs-Cy3 in individual cells was observed by the FL2 channel in the range 564–606 nm; the fluorescence intensity data were analyzed by plotting one- or two-dimensional histograms. Specific gating protocols were used to eliminate the artifacts caused by cell debris or dead cells, and subsequently, the

regions of the histogram were converted to the corresponding numerical values. For the inhibition test of the insulin-dependent signaling pathway, the cells were incubated with insulin (100 nM) after pretreatment with wortmannin (1 μM) for 1 h.

Glucose Uptake Assay in C2C12 myocytes with Fluorescence Microscope.

C2C12 myoblasts were cultured on a microscope cover glass in a 35-mm cell culture dish. After differentiation, the cell culture medium was changed to a low-glucose medium (without FBS), and the cells were retained in the new medium for 4 h. The cells were then incubated for 1 h in a glucose-deficient DMEM medium (without FBS) in the presence of 100 nM insulin or 1 mM AICAR. Next, the medium was changed to a glucose-deficient DMEM medium containing 5 mM GB2-Cy3, and the cells were retained in the latter for 30 min. After washing three times with ice-cold PBS, the cover slip was loaded on the caster of a fluorescence microscope (Olympus IX71). During microscopy observations, the cells were placed in a chamber that was maintained at 37 °C. For continuous CLSM (Carl Zeiss-LSM510) monitoring of cellular glucose uptake, the cover glass was loaded on the caster of the microscope after pretreatment with the appropriate bioactive small molecules for 1 h. After the introduction of a glucose-depleted DMEM medium containing 5 mM Cy3-Glc-α into the chamber, fluorescence images were recorded every 7 s; the obtained image were digitized and saved in a computer for further analysis. The temperature of the chamber was maintained at 37 °C.

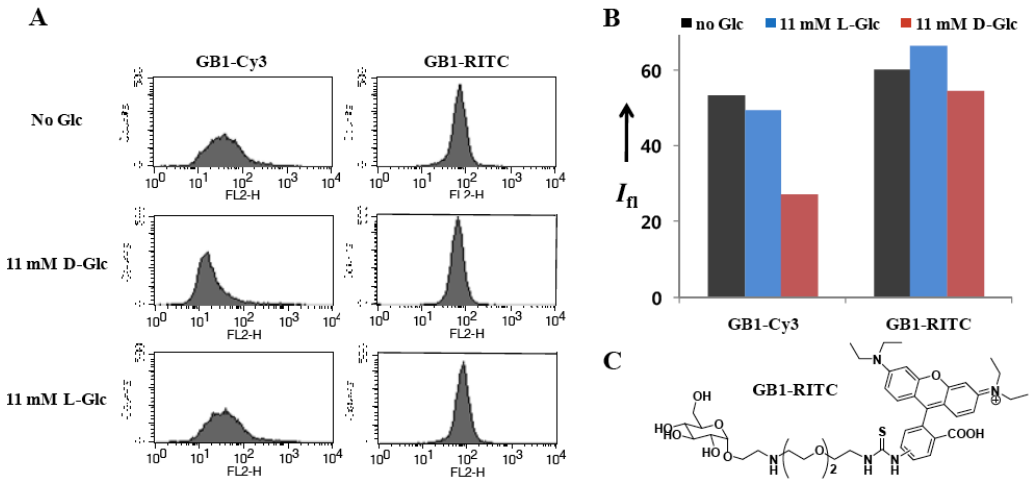

Supplementary Figure 2. Competitive inhibition of glucose uptake in NIH/3T3 fibroblast cells as determined by flow cytometry analysis: A) 3 x 10^5 NIH/3T3 cells were incubated with 5 μM **GB1-Cy3** or **GB1-RITC** bioprobes at 37°C for 30 min in the absence and presence of 11 mM D-glucose or 11 mM L-glucose, respectively. After washing with cold PBS, 1 x 10^4 NIH/3T3 cells were analyzed with a flow cytometry. Black line: no glucose, blue line: 11 mM L-glucose; red line: 11 mM D-glucose. B) The fluorescence intensities I_{fl} were observed under three different conditions. The cellular uptake of **GB1-Cy3** in the presence of 11 mM D-glucose in the medium was decreased down to about 50% of glucose depleted condition. In In contrast, competitive cellular influx of RITC-based glucose analogs is not observed even when there is an increase in the concentration of D-glucose in the medium; further, there is no significant deterioration of cellular influx in the presence of high concentrations of D-glucose. C) Structures of **GB1-RITC**

Reference

[1] J. Park, H. Y. Lee, M.-H. Cho, S. B. Park, *Angew. Chem.* **2007**, *119*, 2064; *Angew. Chem. Int. Ed.* **2007**, *46*, 2018.

[2] H. M. Davey, D. B. Kell, *Microbiol. Rev.* **1996**, *60*, 641.

[3] K. Yoshioka, H. Takahashi, T. Homma, M. Saito, K. B. Oh, Y. Nemoto, H. Matsuoka, *Biochim. Biophys. Acta Gen. Subj.* **1996**, *1289*, 5.

[4] R. G. O'Neil, L. Wu, N. Mullani, *Mol. Imaging Biol.* **2005**, *7*, 388.

[5] Z. Cheng, J. Levi, Z. Xiong, O. Gheysens, S. Keren, X. Chen, S. S. Gambhir, *Bioconjugate Chem.* **2006**, *17*, 662.

[6] S. W. Ball, J. R. Bailey, J. M. Stewart, C. M. Vogels, S. A. Westcott, *Can. J. Physiol. Pharmacol.* **2002**, *80*, 205.

[7] C. Zou, Y. Wang, Z. Shen, *J. Biochem. Biophys. Methods* **2005**, *64*, 207.

[8] A. L. Olson, J. E. Pessin, *Annu. Rev. Nutr.* **1996**, *16*, 235.

[9] J. E. Pessin, G. I. Bell, *Annu. Rev. Physiol*. **1992**, *54*, 911.

[10] M. J. Charron, F. C. Brosius III, S. L. Alper, H. F. Lodish, *Proc. Natl. Acad. Sci. USA* **1989**, *86*, 2535.

[11] G. W. Gould, G. D. Holman, *Biochem. J.* **1993**, *295*, 329.

[12] K. Dawson, A. Aviles-Hernandez, S. W. Cushman, D. Malide, *Biochem. Biophys. Res. Commun.* **2001**, *287*, 445.

[13] Y. Mitsumoto, A. Klip, *J. Biol. Chem.* **1992**, *267*, 4957.

[14] H. Cho, J. Mu, J. K. Kim, J. L. Thorvaldsen, Q. Chu, E. B. Crenshaw III, K. H. Kaestner, M. S. Bartolomei, G. I. Shulman, M. J. Birnbaum, *Science* **2001**, *292*, 1728.

[15] A. R. Saltiel, C. R. Kahn, *Nature* **2001**, *414*, 799.

[16] G. A. Rutter, G. da Silva Xavier, I. Leclerc, *Biochem. J.* **2003**, *375*, 1.

[17] W. W. Winder, *J. Appl. Physiol*. **2001**, *91*, 1017.

[18] E. J. Kurth-Kraczek, M. F. Hirshman, L. J. Goodyear, W. W. Winder, *Diabetes* **1999**, *48*, 1667.

[19] H. Sakoda, T. Ogihara, M. Anai, M. Fujishiro, H. Ono, Y. Onishi, H. Katagiri, M. Abe, Y. Fukushima, N. Shojima, K. Inukai, M. Kikuchi, Y. Oka, T. Asano, *Am. J. Physiol. Endocrinol. Metab.* **2002**, *282*, E1239.

[20] V. Sarabia, T. Ramlal, A. Klip, *Biochem. Cell Biol*. **1990**, *68*, 536.

[21] J. F. Clarke, P. W. Young, K. Yonezawa, M. Kasuga, G. D. Holman, *Biochem. J.* **1994**, *300*, 631.

[22] S. Egert, N. Nguyen, F. C. Brosius III, M. Schwaiger, *Cardiovasc. Res*. **1997**, *35*, 283.

[23] T. Nedachi, M. Kanzaki, *Am. J. Physiol. Endocrinol. Metab*. **2006**, *291*, E817.

[24] J. L. Smith, P. B. Patil, J. S. Fisher, *J. Appl. Physiol*. **2005**, *99*, 877.

Chapter 3. Discovery and Evaluation of a Novel Small Molecule Activator of AMP-Activated Protein Kinase

- *J. Med. Chem.* **2010**, *53*, 7405.

Introduction

The global incidence of type 2 diabetes is increasing rapidly, with higher rates of morbidity and mortality, resulting in a significant financial and social burden worldwide.[1] Type 2 diabetes is characterized by insulin resistance and hyperglycemia, which lead to chronic complications in both small and large blood vessels.[2,3] Therefore, numerous studies have focused on the development of therapeutics able to maintain normal levels of blood glucose by increasing glucose clearance in peripheral tissues such as skeletal muscle and adipose tissue.[4,5] Recent studies have shown that impaired handling of cellular energy homeostasis is closely associated with insulin resistance, resulting in type 2 diabetes, metabolic syndrome, hypertension, and increased cardiovascular risk.[6] Therefore, molecules that regulate cellular energy metabolism hold promise as drug targets for the development of therapeutics for diabetes and obesity.[7]

AMP-activated protein kinase (AMPK) is a heterotrimeric complex comprising catalytic α and regulatory β/γ subunits that senses low energy status by monitoring the ratio of ATP to AMP.[8] AMPK is activated during muscle contraction and exercise by the phosphorylation of threonine 172 by LKB1[9] and Ca^{2+}/calmodulin-dependent kinase kinase (CaMKK).[10] Once AMPK is activated, it stimulates glucose uptake in skeletal muscle through independent pathways in insulin-resistant conditions.[11] Enhanced glucose uptake induced by AMPK is achieved, as least in part, by enhanced GLUT4 translocation to the plasma membrane for fusion

and docking.[12] Several studies have reported that the AMP analogue, 5-aminoimidazole-4-carboxamide-1-β-d-ribofuranoside (AICAR), and other small-molecule activators of AMPK increase glucose uptake in vitro[13] and in vivo.[14] Although their mechanisms of action are still incompletely understood, evidence indicates that metformin[15] and thiazolidinediones (TZDs)[16] act through activation of AMPK in type 2 diabetes. Furthermore, AMPK is the target molecule of two adipose tissue-derived hormones, leptin[17] and adiponectin,[18] which are major regulators of energy metabolism and glucose homeostasis. These accumulated findings have made AMPK an attractive therapeutic target for the treatment of type 2 diabetes and obesity.

In this study, we identified a small-molecule activator of AMPK, ampkinone (**6f**), as an effective therapeutic agent for the treatment of obesity and type 2 diabetes. This novel skeleton (**6**) is a tetracyclic structure embedded with a privileged benzopyran substructure, derived from 2500-member small molecules library constructed in-house using diversity-oriented synthesis strategy to prepare skeletally diverse small molecules to mimic natural product-like or druglike chemical structures.[19] This collection of druglike small molecules containing more than 40 unique molecular frameworks can increase the possibility of identifying a novel modulator of biological system such as AMPK.[20] Ampkinone, a small molecule with this molecular framework (**6**), stimulated the activation and phosphorylation of AMPK in cell lines originating from muscle, fat, and liver. Phosphorylation of acetyl-CoA carboxylase (ACC), a major downstream target molecule of AMPK, confirmed that ampkinone stimulates functional activation of AMPK via the phosphorylation at Thr172 in cultured cells. We also demonstrated the enhanced cellular glucose uptake monitored by fluorescent glucose bioprobe, Cy3-Glc-α,[21] and cross-checked with ^{3}H-labeled 2-deoxy-d-glucose. Consistent with the in vitro data presented here,

administration of ampkinone to diet-induced obese (DIO) mice up-regulated the activity of AMPK in the liver and muscle and enhanced insulin sensitivity. Furthermore, histological analysis confirmed that ampkinone treatment accelerated the consumption of lipids via increased oxidation in the liver and adipose tissues, similar to other small molecule activators of AMPK.[22] Collectively, the results demonstrate that ampkinone is a new small-molecule activator of AMPK that may be effective for the treatment of type 2 diabetes and obesity.

Results and Discussion

We previously reported synthetic methods for the concise and efficient library construction using diversity-oriented synthesis (DOS) strategy, which generated novel scaffolds embedded with privileged substructures via various chemical transformations.[20] To identify a novel small-molecule activator of AMPK, we

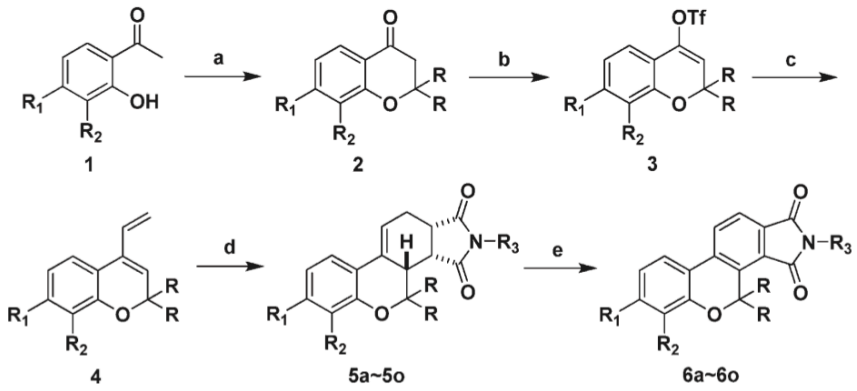

Scheme 1. Synthetic Scheme of Benzopyran-Embedded Molecular Framework (6)[a]
[a]Reagents and conditions: (a) cyclopentanone or acetone, pyrrolidine, EtOH, reflux; (b) trifluoromethanesulfonic anhydride, 2,6-di-*tert*-butyl-4-methylpyridine, CH_2Cl_2, 0 °C; (c) vinylboronic acid dibutyl ester, $Pd(PPh_3)_4$, Na_2CO_3, EtOH/toluene/H_2O, 70 °C; (d) maleimide derivatives, toluene, reflux; (e) DDQ, toluene, reflux.

evaluated an in-house small molecule collection constructed by these DOS pathways. After extensive bioassays using Western blot analysis, we identified a new molecular framework (**6**) that stimulates the phosphorylation of AMPK. The aromatized

benzopyran moiety in **6** was shown to be essential for AMPK activation because other types of benzopyran-fused tetracycles such as monoene (**5**), hydrogenated compound (**S7**), and allylic alcohol (**S8**) were inactive toward AMPK (Figure S1 in the Supporting Information). On the basis of initial screening results, a focused small molecule library was constructed by a series of reactions designed to produce **6**: [1] the cyclization of hydroxyacetophenones (**1**) with acetone or cyclopentanone, [2] triflation of carbonyl moiety on substituted chroman-4-ones (**2**), [3] palladium-mediated vinylation of vinyl triflate intermediates (**3**), [4] Diels−Alder reaction of bicyclic dienes (**4**) with substituted maleimides, and [5] subsequent aromatization of benzopyran-containing tetracyclic monoenes (**5**) with 2,3-dichloro-5,6-dicyanobenzoquinone (DDQ) (Scheme 1).

Cpd.	R	R^1	R^2	R^3	% activity[a]	
					AMPK	ACC
6a	Me	OMe	OH	H	158	123
6b	Me	OMe	OH	Me	205	145
6c	Me	OMe	OH	Ph	273	254
6d	Me	OMe	OH	Bn	165	194
6e	Me	OMe	OH	*p*-Acetylphenyl	264	384
6f	Me	OMe	OH	4-Benzoylphenyl	322	295
6g	Me	OMe	OH	Biphenyl-4-yl	160	114
6h	Me	OMe	OH	9-Oxo-9*H*-fluoren-3-yl	249	154
6i	Me	OMe	OH	Biphenyl-3-yl	175	201
6j	Me	OMe	OH	4-Benzylphenyl	169	129
6k	Me	OMe	OH	4-(Benzo[*d*]oxazol-2-yl)phenyl	92	91
6l	Me	OMe	H	4-Benzoylphenyl	159	154
6m	Me	F	H	4-Benzoylphenyl	186	156
6n	Me	H	H	4-Benzoylphenyl	203	92
6o	$-(CH_2)_4-$	OMe	OH	4-Benzoylphenyl	113	51

Table 1. Activation of AMPK (pT172) and ACC (pS79) phosphorylation induced by individual compounds in the focused library
[a]Relative phosphorylation activity induced by the treatment of individual compounds at 10 μM in the Western blot analysis.

Using a 15-member focused library (**6a**−**o**) with various structural modifications, we conducted a structure−activity relationship (SAR) study via

Western blot analysis (see Table 1). On the basis of our SAR study, 2-(4-benzoylphenyl)-6-hydroxy-7-methoxy-4,4-dimethylchromeno[3,4-*e*]isoindole-1,3-dione (**6f**) demonstrated the most efficient activation of AMPK and subsequent functional phosphorylation of ACC (Figure S2 in the Supporting Information). The compound activity on AMPK phosphorylation was slightly attenuated when benzophenone moiety at the R^3position of molecular framework **6** was replaced with simpler moieties such as acetylphenyl group (**6e**) and phenyl (**6c**), but it was completely abolished when hydrogen (**6a**), methyl (**6b**), and benzyl group (**6d**) were introduced at the R^3 position. The introduction of bulky substituents such as biphenyl-4-yl (**6g**), biphenyl-3-yl (**6i**), and 4-benzylphenyl group (**6j**) diminished the activity in Western blot analysis; however, 9-oxo-9*H*-fluoren-3-yl moiety (**6h**) somewhat preserved its activity because of its structural similarity to benzophenone. In addition, cyclopentyl moiety at the R position (**6o**) or various substituents at the R^1 and R^2positions (**6l**−**n**) caused a significant reduction in the compound activity on AMPK phosphorylation. On the basis of this screening result, we classified **6f** as a novel small molecule activator of AMPK and designated this compound ampkinone (AKN) (Figure 1A).

To investigate the effect of AKN on AMPK activation, we utilized cell lines originating from cardiac and skeletal muscle, adipose tissue, and liver. Immunoblot analysis of a time course assay conducted in L6 skeletal muscle cells revealed that the AKN-mediated phosphorylation of AMPK (Thr172) was increased at 10 min, reached a maximum at 1 h, and persisted for 6 h (Figure 1B). Phosphorylation of ACC (Ser79), an intracellular substrate of AMPK, was also increased by treatment with AKN on a timeline similar to that of AMPK. Immunocomplex kinase assays with the SAMS peptide revealed a 2.7-fold increase in AMPK activity upon treatment with 10 μM

AKN. Treatment with 1 mM AICAR as a positive control for AMPK activation induced a 3.2-fold increase in AMPK activity (Figure 1C). We next examined the dose-dependent effect of AKN on AMPK activation. The phosphorylation of AMPK and ACC was dose-dependently increased in various cell lines, such as C2C12 skeletal muscle cells, 3T3-L1 adipose-like mouse embryonic fibroblasts, and HepG2 human hepatoma cells as well as L6 cells (Figure 1D). These data indicate that AKN stimulates the phosphorylation and activity of AMPK in multiple cell lines originating from muscle, fat, and liver. The estimated EC_{50} of AKN is 4.3 μM in L6 cells (Figure1E and Figure S3 in the Supporting information).

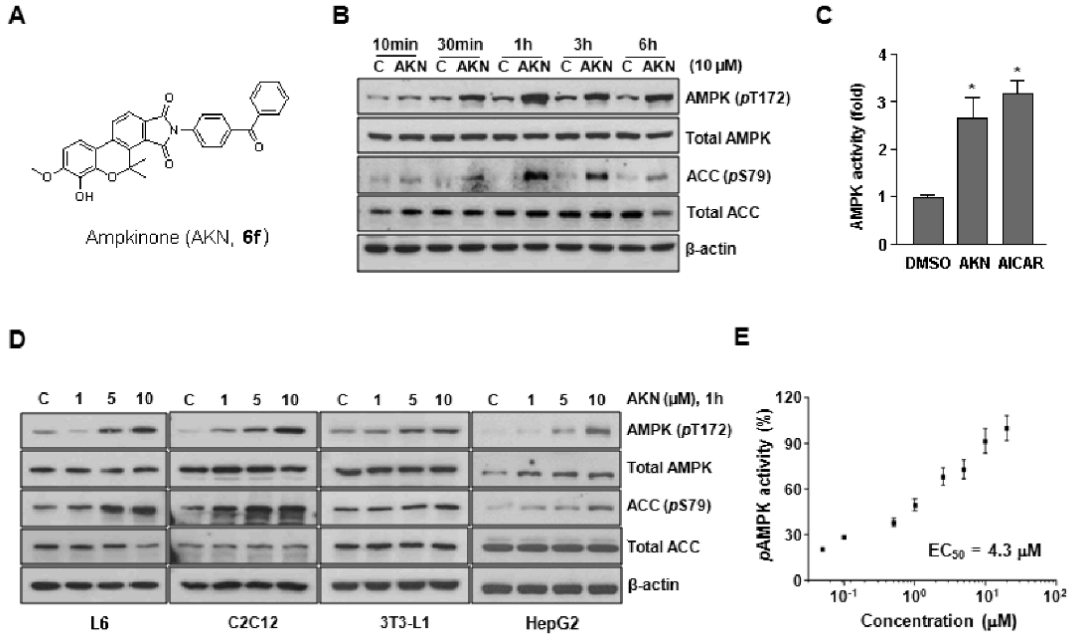

Figure 1. AKN stimulates the phosphorylation of AMPK (pT172) and ACC (pS79) in a time- and dose-dependent manner. (A) Chemical structure of AKN (**6f**). (B) AKN-induced phosphorylation of AMPK (pT172) and ACC (pS79). Western blot analysis of lysates from L6 cells treated with AKN (10 μM) for the indicated times was performed with antibodies against the indicated proteins. (C) Total AMPK activity in cells treated with AKN or DMSO was measured using a synthetic SAMS peptide substrate and [γ-^{32}P]ATP. (D) L6 cells, C2C12 myocytes, 3T3-L1 preadipocytes, and HepG2 hepatic cells were incubated for 1 h with the indicated concentrations of AKN. (E) EC_{50} was determined by Western blotting in various concentrations (0−20 μM) and data analysis with PRISM3 program. Immunoblots were performed using anti-AMPK (pT172), anti-AMPK, anti-ACC (pS79), and anti-ACC antibodies. (*) $P <$ 0.05 vs corresponding control.

We next determined whether AKN could directly activate AMPK. ^{32}P incorporation by isolated AMPK into the SAMS peptide was not different in AKN-treated samples compared to the DMSO control (data not shown). This suggests that AKN does not directly activate purified AMPK in a cell-free condition. Then we investigated whether the cellular levels of AMP, ADP, or ATP can be perturbed upon treatment with AKN. As shown in Figure 2A, the treatment with AKN at 10 μM caused no significant alteration in AMP to ATP ratio in L6 cells (Figure S4 in the Supporting Information).

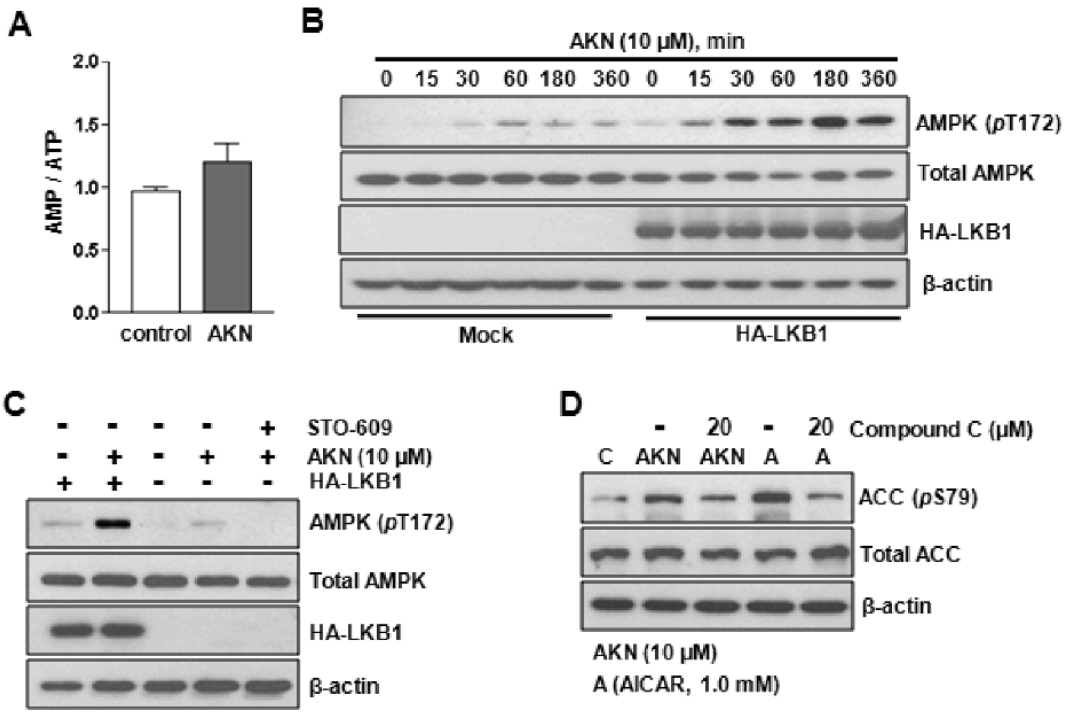

Figure 2. AKN predominantly stimulates AMPK activation via the LKB1 pathway. (A) AMP to ATP ratio was not significantly changed upon treatment with AKN. (B) LKB1-deficient HeLa cells and HeLa cells transfected with a pcDNA3.1 plasmid encoding LKB1-tagged hemagglutinin (HA) were exposed to AKN (10 μM) for the indicated time periods after 6 h of serum starvation. Immunoblot analysis was then performed with antibodies against AMPK (pT172), AMPK, and HA. (C) The effect of the CaMKK inhibitor, STO-609, on AKN-mediated AMPK activation following 1 h of treatment in Hela cells. (D) L6 cells were exposed to AKN (10 μM) or AICAR (1 mM) for 1 h in the presence or absence of compound **C** (20 μM), and immunoblots were performed with anti-ACC (pS79), anti-ACC, and anti-actin as a loading control.

Consequently, we hypothesized that AKN might stimulate AMPK phosphorylation through the activation of upstream signaling pathway. LKB1 and CaMKK are two primary AMPK kinases.[9,10] For the mechanistic understanding, we investigated whether one or both of these kinases were required for the activation of AMPK by AKN. As confirmed by the data shown in Figure 2B, HeLa cells do not express LKB1.[23] Therefore, HeLa cells were transfected with hemagglutinin (HA)-tagged LKB1 for 24 h to induce the expression of exogenous LKB1 and then treated with AKN for the indicated time. In mock-transfected cells, treatment with AKN slightly increased AMPK phosphorylation from 60 to 360 min, while AMPK phosphorylation in LKB1-transfected cells was noticeably higher. These data indicate that LKB1 activity is required for robust AKN-mediated AMPK phosphorylation, though the slight increase in AMPK phosphorylation in mock-transfected cells suggested the involvement of another upstream kinase. Accordingly, HeLa cells were preincubated with STO-609, a specific inhibitor of CaMKK.[24] Treatment of STO-609 in mock-transfected HeLa cells completely suppressed the phosphorylation of AMPK induced by AKN (Figure 2C), indicating that LKB1 and CaMKK mediate the activation of AMPK by AKN. Finally, to determine whether phosphorylation of ACC upon treatment with AKN is associated with AMPK, L6 cells were preincubated with the AMPK-specific inhibitor, compound **C**, followed by treatment with AKN for 1 h. As shown in Figure 2D, AKN-induced ACC phosphorylation was significantly diminished through the specific inhibition of AMPK with compound **C**. Taken together, these data confirm that AKN stimulates the phosphorylation of AMPK neither by direct activation as in the case of AICAR, an AMP analogue, nor by the consequence of altered cellular AMP/ATP ratio. In addition, it was also confirmed

that both kinases, LKB1 and CaMKK, are required for full activation of AKN-stimulated phosphorylation of AMPK.

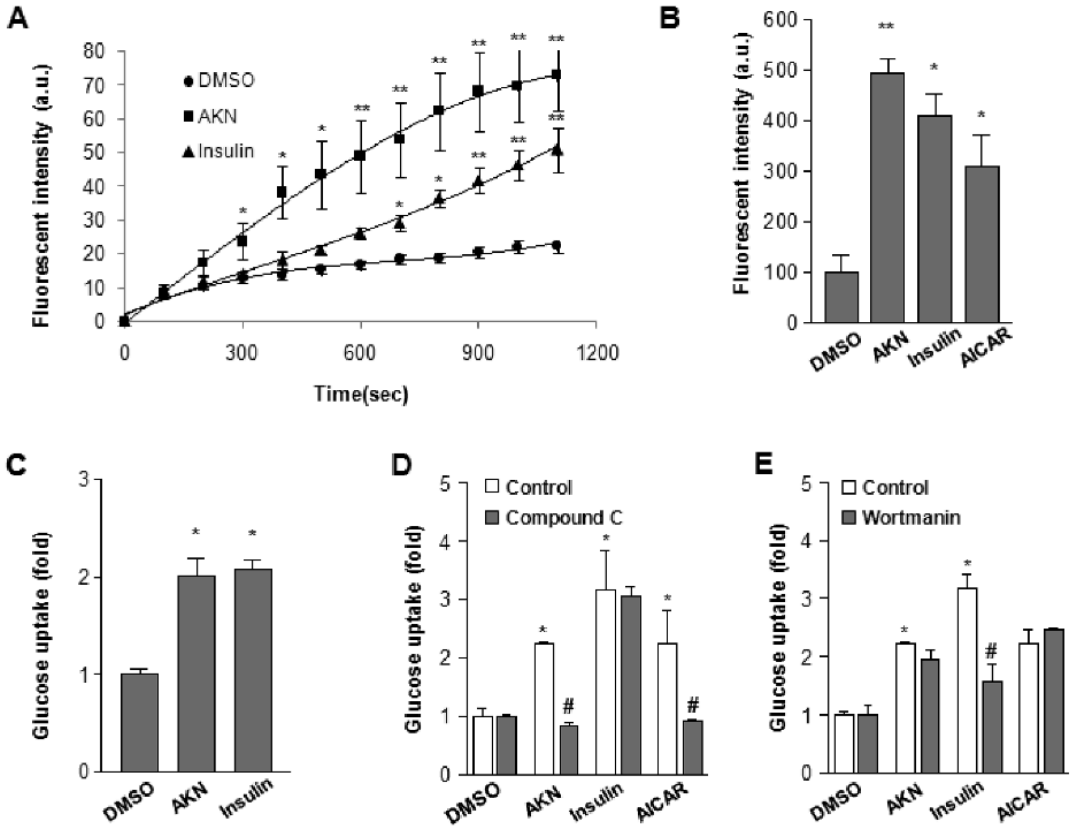

Figure 3. AKN stimulates glucose uptake through AMPK but not Akt. (A) C2C12 and (B) L6 myocytes were incubated for 1 h with AKN (10 μM) or insulin (100 nM). Next, (A, B) Cy3-Glc-α (DMSO-treated = closed circles; AKN-treated = closed squares; insulin-treated = closed triangles) or (C) 2-deoxy-D-glucose-1,2-^{3}H(N) was added to culture media for the indicated time periods (A) or 10 min (B, C), and glucose uptake was measured. (D) The effect of the AMPK inhibitor compound **C** (20 μM, 30 min preincubation) and (E) the PI3K inhibitor wortmannin (1 μM, 30 min preincubation) on AKN- (10 μM), insulin- (100 nM), or AICAR (1 mM)-mediated glucose uptake following 1 h of treatment in L6 myocytes: (*) $P < 0.05$; (**)$P < 0.01$ vs corresponding control; (#) $P < 0.05$ vs corresponding treated groups (AKN, insulin, and AICAR).

AMPK plays a crucial role as an energy sensor in metabolic tissues and stimulates glucose uptake in skeletal muscle.[8] To determine the effect of AKN on cellular glucose uptake, we utilized the fluorescent glucose bioprobe, Cy3-Glc-α, which enters the cell through competition with D-glucose via glucose transporters

(GLUTs).[21] Compared to glucose uptake assay with radioisotope-labeled deoxy-D-glucose using scintillation counter, this method allows the real-time monitoring of cellular glucose uptake under experimental conditions using fluorescent microscopy or confocal laser scanning microscopy (CLSM). As shown in Figure 3A, a 2.3-fold enhancement in cellular glucose uptake was observed by CLSM in C2C12 myocytes treated with insulin. Under identical experimental settings, we measured a 3.2-fold enhancement in cellular glucose uptake upon treatment with AKN. Enhanced cellular glucose uptake was also monitored by fluorescent microscopy following treatment with AKN, insulin, and AICAR (Figure 3B and Figure S5 in the Supporting Information), and a dose-dependent enhancement of fluorescent intensity was observed in cells treated with AKN (Figure S6 in the Supporting Information). These data were confirmed by the conventional glucose uptake assay with 2-deoxy-D-glucose-1,2-^{3}H(N) using scintillation counter (Figure 3C).

Insulin-dependent PI3K/Akt signaling and insulin-independent AMPK signaling are two of the pathways that regulate cellular glucose uptake.[25] To understand the cellular mechanisms underlying this process, we investigated the involvement of both pathways in AKN-enhanced glucose uptake by inhibiting either the AMPK pathway or the PI3K/Akt pathway with compound**C** and wortmannin, respectively. Cellular glucose uptake was stimulated by AKN, AICAR, and insulin in C2C12 myocytes. The inhibition of AMPK with compound **C** resulted in a complete inhibition of enhanced glucose uptake in cells treated with AKN and AICAR (Figure 3D). However, the enhanced glucose uptake induced by insulin was not affected by the inhibition of AMPK. In contrast, the glucose uptake pattern in insulin-treated cells was reversed only after pretreatment with wortmannin (Figure 3E). Consistent with this data, immunoblot analysis revealed that Akt phosphorylation was

not increased above basal levels by treatment with AKN (Figure S7 in the Supporting Information). This demonstrates that AKN-stimulated glucose uptake results primarily from increased AMPK activation and not via PI3K/Akt signaling.

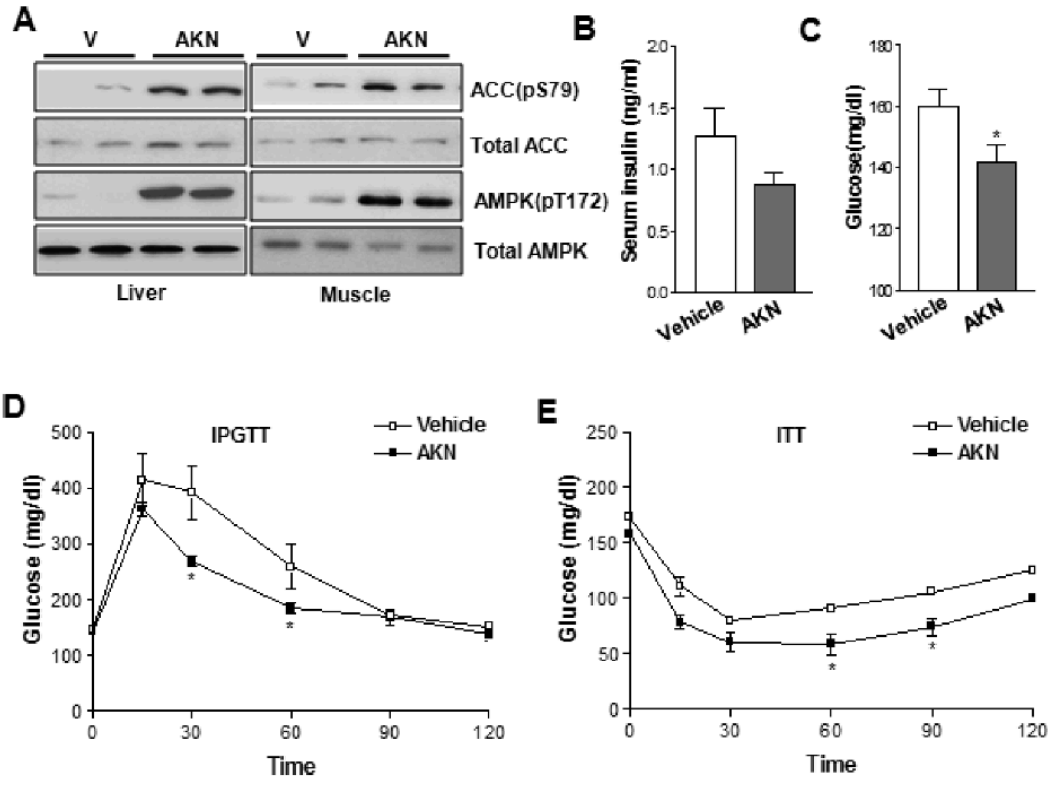

Figure 4. AKN activates the AMPK signaling pathway and enhances glucose homeostasis in vivo. (A) The effect of AKN on the phosphorylation of AMPK and ACC in vivo. Vehicle (PEG400, n = 7) or 10 (mg/kg)/d AKN (n = 7) were administered subcutaneously to DIO mice. After administration of AKN for 1 month, immunoblot analysis of tissue lysates from liver and muscles was performed with antibodies against the indicated proteins after fasting for 24 h. (B) Serum insulin and (C) blood glucose levels were determined using the ALPCO insulin EIA kit and a glucometer (Accu Check, Roche), respectively. (D) The intraperitoneal glucose tolerance test (IPGTT) and (E) insulin tolerance test (ITT) were performed in DIO mice treated with vehicle (□, n = 7) or 10 (mg/kg)/d AKN (■, n = 7) for 3 weeks and 4 weeks, respectively: (*) $P < 0.05$; (**) $P < 0.01$ vs the corresponding vehicle control group.

We next examined the in vivo effect of AKN in DIO mice fed a diet containing 60% fat for 8 weeks after microsomal stability test of this compound (Figure S8 in the Supporting Information). DIO mice were injected subcutaneously

for 4 weeks with 10 (mg/kg)/d of AKN in PEG400. Phosphorylation of AMPK was confirmed by immunoblot analysis of proteins from the liver and muscle of DIO mice treated with vehicle or AKN. Consistent with our in vitro data, AKN-treated DIO mice had increased levels of phosphorylated AMPK/ACC, suggesting that AKN is an effective activator of AMPK in liver and muscle (Figure 4A). Interestingly, we observed that serum insulin and glucose levels in AKN-treated DIO mice were lower than those in the control groups (Figure 4B and Figure 4C). Therefore, we investigated the glucose dispersal rates in both groups. As shown in Figure 4D, elevated blood glucose induced by intraperitoneal injection was more rapidly lowered in AKN-treated DIO mice than control mice. These findings indicate that AKN effectively enhanced insulin sensitivity in animal models (Figure 4E). Taken together, these data support that AKN is a novel small-molecule AMPK activator with antidiabetic effects.

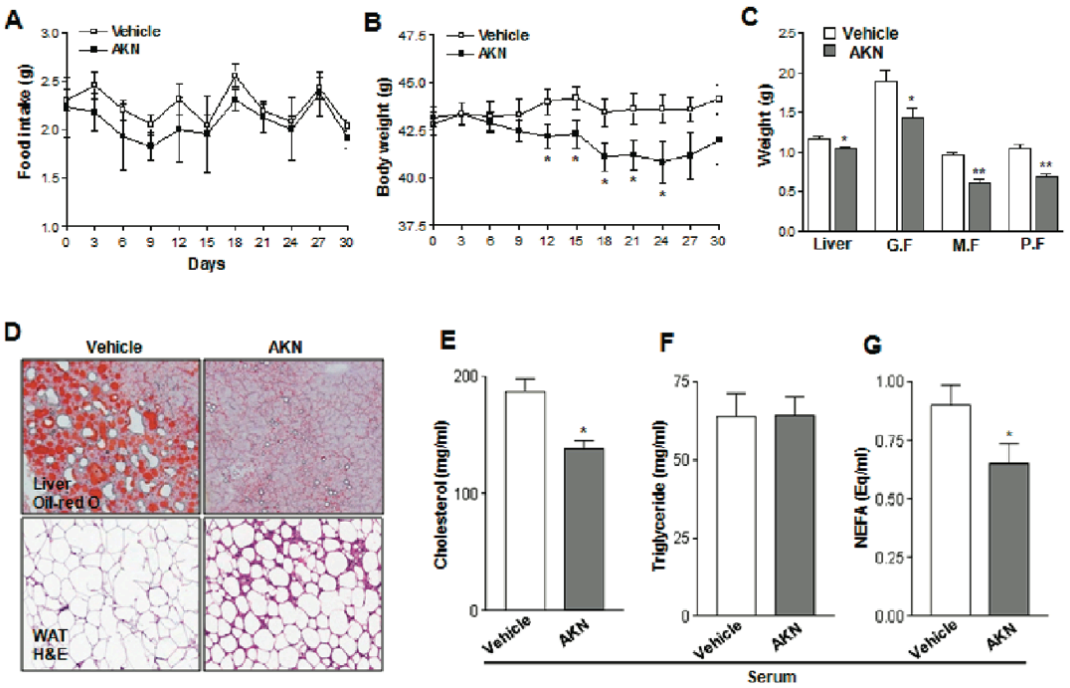

Figure 5. AKN treatment ameliorates metabolic symptoms in DIO mice. (A) Food intake and (B) the body weight of DIO mice groups, either vehicle-treated (□, $n = 7$) or AKN-treated (■, $n = 7$), were monitored during the subcutaneous administration of 10 (mg/kg)/d AKN for 1 month. (C) The weights of adipose tissues (GF, gonadal

fat; MF, mesenteric fat; PF, perirenal fat) and other organs were compared between DIO mice treated with vehicle (□, $n = 7$) and those treated with 10 (mg/kg)/d AKN (■, $n = 7$) for 1 month. (D) Oil-red O staining of liver cells from DIO mice treated with vehicle (upper, left) or 10 (mg/kg)/d AKN (upper, right) and H & E staining of gonadal fat from DIO mice treated with vehicle (lower, left) or 10 (mg/kg)/d AKN (lower, right). (E−G) Lipid parameters of serum from DIO mice after subcutaneous administration of vehicle (□, $n = 7$) or 10 (mg/kg)/d AKN (■, $n = 7$) for 1 month: (*) $P < 0.05$; (**) $P < 0.01$ vs the corresponding vehicle control group.

We next sought to investigate the potential antiobesity effects of AKN. AKN (10 (mg/kg)/d) was administered to DIO mice for 30 days via subcutaneous injection, and food intake and body weight were monitored every 3 days. No significant difference in food intake was observed between the groups (Figure 5A). Interestingly, by week 3, the body weights of AKN-treated DIO mice were significantly decreased, resulting in a ~5% decrease compared to the initial weight. Conversely, the weights of vehicle-treated DIO mice increased slightly over the study period (Figure 5B). The changes in body weight were the result of changes in fat mass, which were significantly decreased in AKN-treated mice compared to vehicle-treated mice (Figure 5C). In agreement with this observation, Oil-red O staining of liver and H & E staining of gonadal fat revealed dramatic differences between AKN- and vehicle-treated mice in terms of fat mass and fat area, respectively (Figure 5D). Finally, although triglyceride levels in serum were not affected upon treatment with either AKN or vehicle (Figure 5F), other lipid parameters such as cholesterol and nonesterified fatty acids (NEFA) were significantly decreased in AKN-treated DIO mice compared to control groups (Figure 5E and 5G). These data indicate that AKN also has antiobesity effects.

Conclusion

In this Chapter, we have described ampkinone, a novel small-molecule activator of AMPK with potential antidiabetic and antiobesity effects. Through extensive immunoblotting assays using a 2500-member small molecule collection constructed by diversity-oriented synthesis strategy,[20] we identified a novel molecular framework (**6**) with a privileged benzopyranyl substructure. We then conducted a structure−activity relationship (SAR) study using a 15-member focused library with a tetracyclic skeleton (**6**) and identified **6f** as the best candidate for further in vitro and in vivo evaluation. This compound, which we designated ampkinone (AKN), is an effective small-molecule activator of AMPK. We confirmed the in vitro effects of AKN on the functional activation of AMPK through active phosphorylation of ACC, its specific substrate, in multiple cell lines derived from metabolic tissues.

AMPK is an important energy sensor in mammalian cells. Its activity is induced in response to high levels of AMP and/or low ATP. Under these conditions, AMP binds to the γ-subunit of AMPK and induces a conformational change that allows Thr172 of the α-subunit to be phosphorylated by AMPK kinases.[8] AMPK is activated by upstream kinases, including LKB1[9] and CaMKK.[10] We determined that both kinases, LKB1 and CaMKK, are required for full activation of AKN-stimulated phosphorylation of AMPK. On the basis of our findings in LKB1- and mock-transfected HeLa cells, AKN-mediated AMPK activation was induced mainly via the up-regulation of LKB1. Although AKN-mediated AMPK phosphorylation is primarily mediated by LKB1, the activation of AMPK is also slightly stimulated by CaMKK upon treatment of AKN evidenced by immunoblot analysis with specific inhibitors. Both LKB1 and CaMKK function as AMPK kinases in different cell lines and tissues, suggesting that they play different roles in the regulation of AMPK.

However, the molecular mechanism of AKN-mediated AMPK activation remains to be elucidated.

It has been well established that activation of AMPK stimulates glucose uptake by increasing GLUT4 translocation to the cell surface.[26] Interestingly, AMPK-mediated glucose uptake occurs through a different mechanism than in the insulin-signaling pathway.[27] As shown in Figure 3, AKN strongly increased glucose uptake in C2C12 myocytes. This effect was completely eliminated by the inhibition of AMPK with compound **C** but not by the inhibition of PI3K via wortmannin. In addition, AKN treatment did not induce phosphorylation of Akt in L6 cells. These data suggest that AKN-mediated glucose uptake is dependent on AMPK, not Akt. In addition, our results demonstrated that AKN does not induce cell cycle arrest or associated cell apoptosis even after strong activation of AMPK for 6 h, which was confirmed by cell viability assays (Figures S9 and S10 in the Supporting Information). Furthermore, OXPHOS activity in L6 myocytes was not affected by treatment with AKN, indicating that AKN-mediated AMPK activation did not result from inhibition of the respiratory chain.[28] Therefore, AKN could be ideal for investigating the physiological effects of AMPK up-regulation without causing oxidative stress.

Abnormal AMPK activity has been implicated in the progression of obesity and diabetes.[8] Several reports suggest that activation of AMPK enhances insulin sensitivity and increases glucose cellular uptake in vitro and in vivo.[4,5,7] In this study, activation of AMPK by AKN enhanced insulin sensitivity and induced glucose uptake in various cultured cell lines and DIO mice, resulting in a reduction in serum insulin and glucose levels (Figure 4). Moreover, the activity of ACC, a key enzyme in lipid accumulation and synthesis, is negatively regulated by activation of AMPK. Similar to other AMPK stimulators,[16,29] AKN treatment resulted in a mild reduction in body

weight and a concomitant reduction in adipose tissue weight. Furthermore, hepatic steatosis can result from abnormal activity of 3-hydroxy-3-methylglutaryl coenzyme A reductase (HMG-CoA reductase) and ACC. These two enzymes are regulated by AMPK and primarily responsible for hepatic cholesterol and fatty acid synthesis.[30] Our data suggested that AKN-mediated AMPK activation in DIO mice leads to a reduction in hepatic steatosis and decreased cholesterol and free fatty acids in the serum. However, we need to identify the real target protein regulating AKN-mediated AMPK activation in order to understand the exact regulating mechanism of these antidiabetic and antiobesity effects found in vitro and in vivo. Overall, our results demonstrate that the small-molecule AKN indirectly stimulates the activation of AMPK and has a potential as a therapeutic agent for the treatment of diabetes and obesity.

Supporting Information

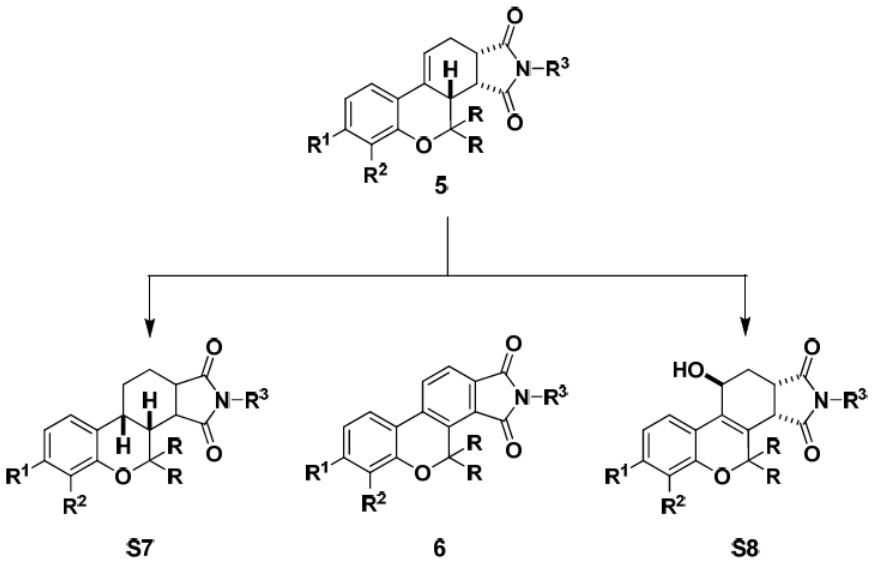

Figure S1. Chemical structures of scaffold **S7** and **S8**.

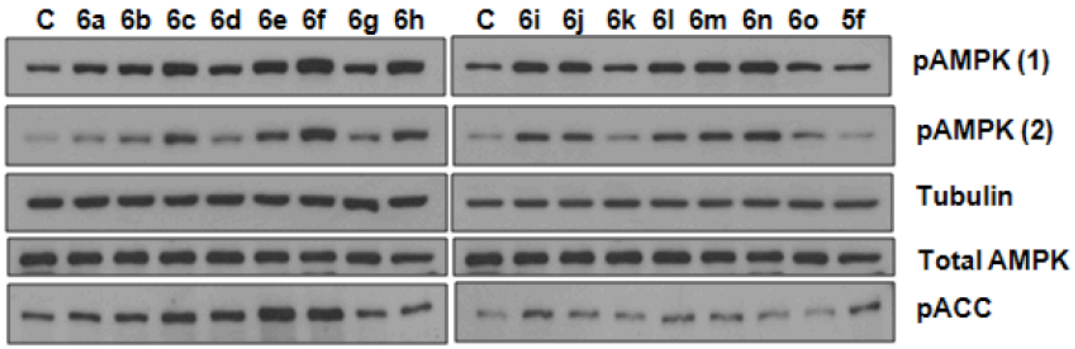

Figure S2. Immunoblot analysis of 16-membered focused library. Phosphorylation of AMPK(pT172) and ACC (pS79) were induced upon treatment with small molecules (10 μM) in L6 cells and detected with antibodies against the indicated proteins.

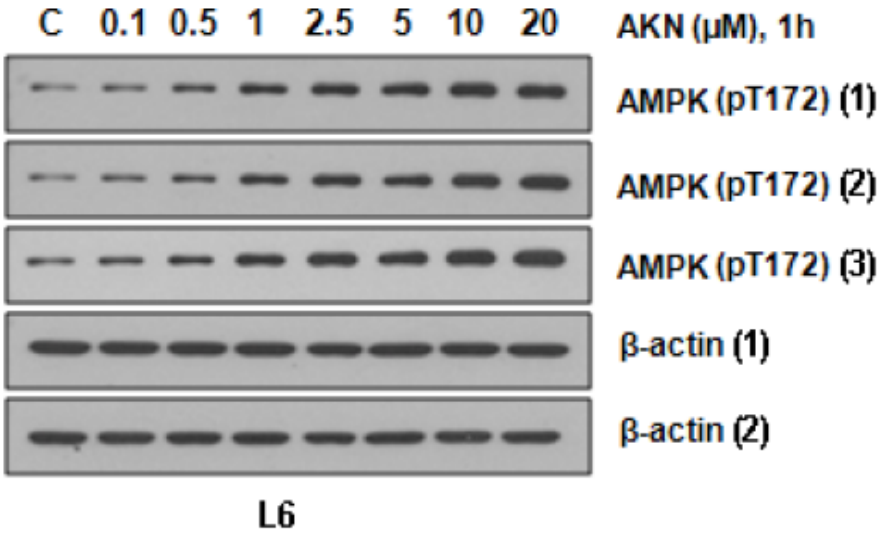

Figure S3. AKN stimulates the phosphorylation of AMPK (pT172) in a dose-dependent manner. L6 cells were incubated for 1 h with the indicated concentrations of AKN.

A

	AMP	ADP	ATP	AMP/ATP
WT_1	1024.2	1676.4	5609.0	0.18
WT_2	1230.6	1853.2	6095.3	0.20
WT_3	1005.1	1644.0	5209.8	0.19
WT_4	1100.3	1713.9	5368.0	0.20
E5_1	1319.6	2127.5	5038.0	0.26
E5_2	1857.2	2531.4	3931.9	0.47
E5_3	1179.3	2079.6	4226.2	0.28
E5_4	855.3	1745.8	5048.4	0.17

B

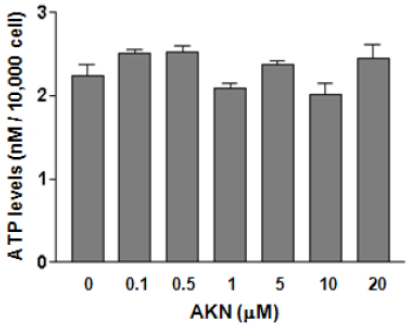

Figure S4. (A) Quantitative analysis of ATP, ADP and AMP concentration using HPLC MS/MS system and (B) the measurement of ATP levels performed by ATPlite 1step kit upon treatment with AKN in L6 cells.

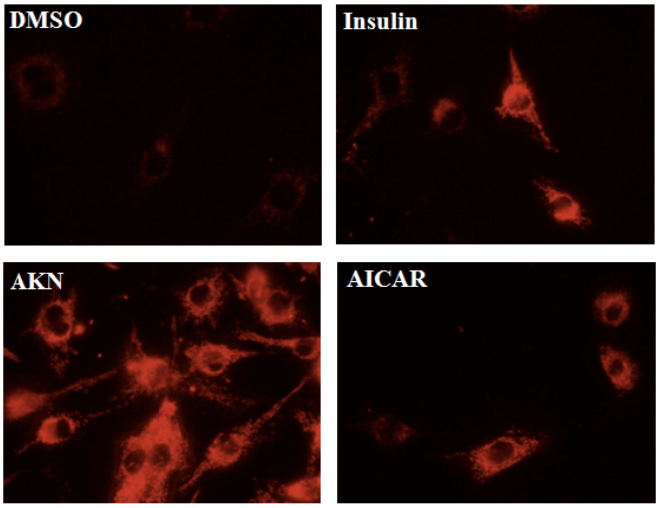

Figure S5. Cellular glucose uptake was monitored in C2C12 myocytes by using fluorescence microscopy. C2C12 myocytes were incubated with ampkinone (AKN, 10 μM), insulin (100 nM) or AICAR (1 mM) for 1 h. Then, Cy3-Glc-α (5 μM) was added to the culture media and the fluorescence image was captured after 30 min incubation.

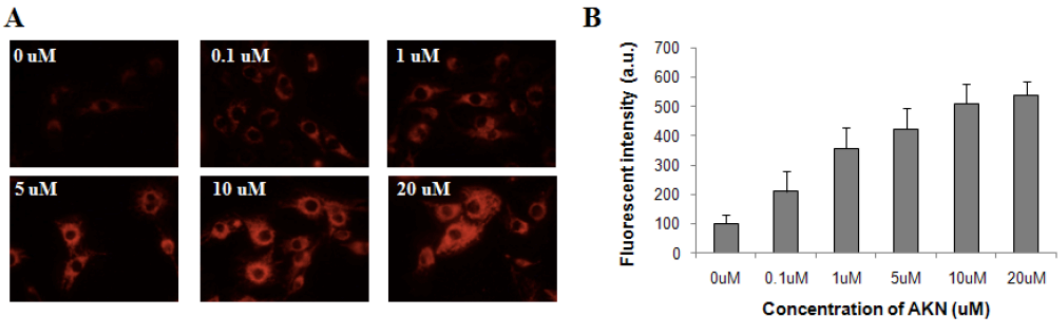

Figure S6. The enhanced cellular glucose uptake upon treatment with ampkinone was monitored by using fluorescence microscope in dose-dependent manners. After C2C12 skeletal muscle cells were incubated with ampkinone (AKN) at various concentrations for 1 h, Cy3-Glc-a (5 μM) was added to these culture media and the fluorescence image was captured after 30 min incubation.

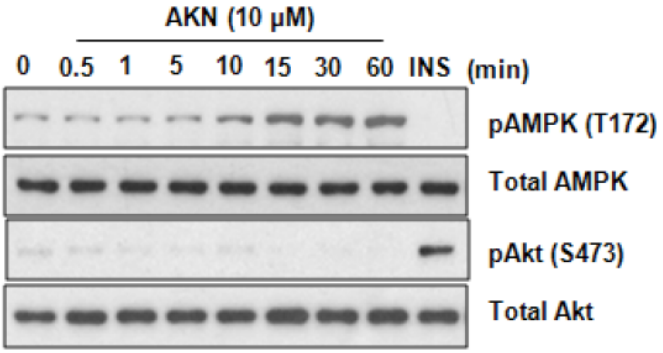

Figure S7. Immunoblot analysis of ampkinone (AKN)-induced phosphorylation of AMPK and Akt in time-dependent manners in L6 muscle cells. AKN selectively stimulates the phosphorylation/activation of AMPK but not that of Akt.

A

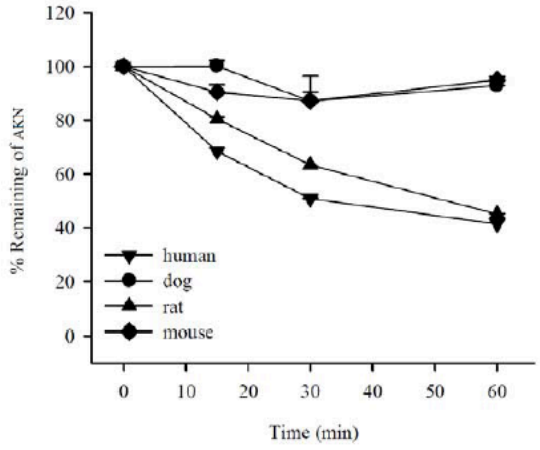

B

compounds	Half-life ($t_{1/2}$, min)			
	Human	Dog	Rat	Mouse
AKN	31	[a] √	52	√
Verapamil (P.C.)	12	10	8	4

[a] √ ; Mean percent value is confirmed over 89% at 60minute.

C

compounds	Remaining % of Parent molecule at 60 min.			
	Human	Dog	Rat	Mouse
AKN	41	93	45	95
Verapamil (P.C.)	6	*ND	ND	ND

*ND; No-peaks detection

Figure S8. Ampkinone (AKN) is stable in liver metabolism of all species, human, dog, rat, and mouse. (A) Mean ± SD of remaining percent of AKN in the liver microsome of human, dog, rat, and mouse (n = 2). (B) Half-life time and (C) Microsomal stability of AKN in four different species.

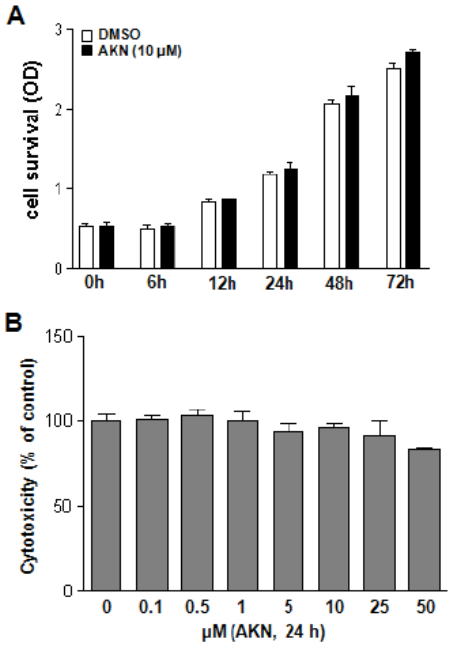

Figure S9. Ampkinone (AKN) does not affect the cell viability in L6 cell lines monitored by mitochondrial activity using MTT assay at the varied incubation time upto 72 h at 10 µM concentration or and at the varied concentration upto 50 µM for 24 h incubation.

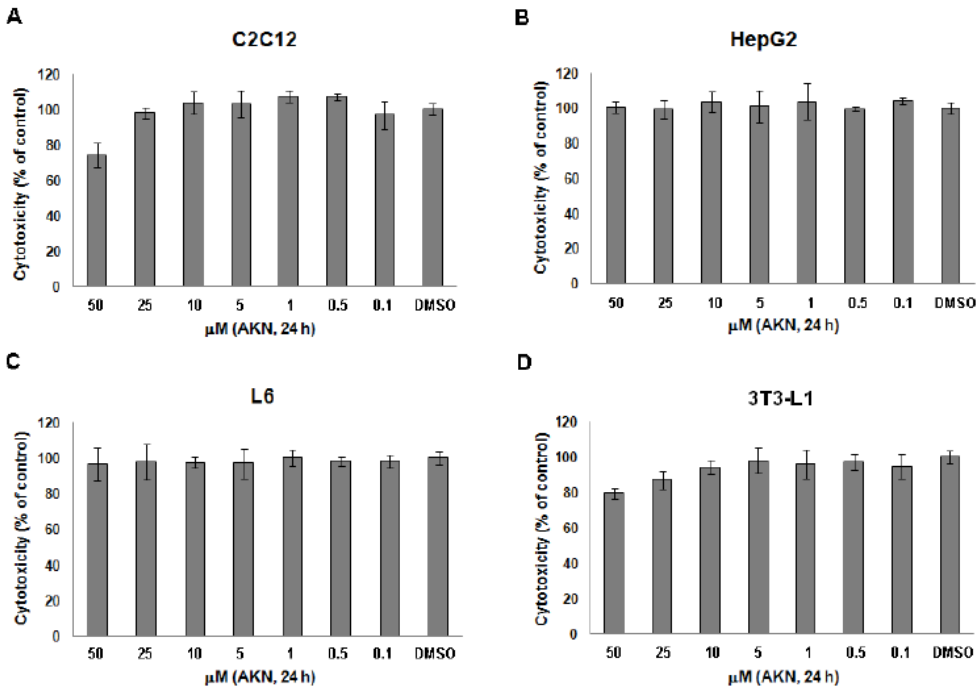

Figure S10. Ampkinone (AKN) does not affect the cell viability in various cell lines monitored by mitochondrial activity using WST-1 assay at the varied concentration for 24 h incubation.

Reference

[1] P. Zimmet, *J. Intern. Med.* **2000**, *247*, 301.

[2] C. F. Semenkovich, *J. Clin. Invest.* **2006**, *116*, 1813.

[3] E. Cohen, A. Dillin, *Nat. Rev. Neurosci.* **2008**, *9*, 759.

[4] R. J. Shaw, K. A. Lamia, D. Vasquez, S.-H. Koo, N. Bardeesy, R. A. Depinho, M. Montminy, L. C. Cantley, *Science* **2005**, *310*, 1642.

[5] J. A. Baur, K. J. Pearson, N. L. Price, H. A. Jamieson, C. Lerin, A. Kalra, V. V. Prabhu, J. S. Allard, G. Lopez-Lluch, K. Lewis, P. J. Pistell, S. Poosala, K. G. Becker, O. Boss, D. Gwinn, M. Wang, S. Ramaswamy, K. W. Fishbein, R. G. Spencer, E. G. Lakatta, D. Le Couteur, R. J. Shaw, P. Navas, P. Puigserver, D. K. Ingram, R. de Cabo, D. A. Sinclair, *Nature* **2006**, *444*, 337.

[6] R. R. Wing, M. G. Goldstein, K. J. Acton, L. L. Birch, J. M. Jakicic, J. F. Sallis Jr., D. Smith-West, R. W. Jeffery, R. S. Surwit, *Diabetes Care* **2001**, *24*, 117.

[7] J. H. Hwang, D. W. Kim, E. J. Jo, Y. K. Kim, Y. S. Jo, J. H. Park, S. K. Yoo, M. K. Park, T. H. Kwak, Y. L. Kho, J. Han, H.-S. Choi, S.-H. Lee, J. M. Kim, I. Lee, T. Kyung, C. Jang, J. Chung, G. R. Kweon, M. Shong, *Diabetes* **2009**, *58*, 965.

[8] a) D. Carling, *Trends Biochem. Sci.* **2004**, *29*, 18; b) D. G. Hardie, *Annu. Rev. Pharmacol. Toxicol.* **2007**, *47*, 185; c) D. G. Hardie, *FEBS Lett.* **2008**, *582*, 81.

[9] R. J. Shaw, M. Kosmatka, N. Bardeesy, R. L. Hurley, L. A. Witters, R. A. DePinho, L. C. Cantley, *Proc. Natl. Acad. Sci. USA.* **2004**, *101*, 3329.

[10] R. L. Hurley, K. A. Anderson, J. M. Franzone, B. E. Kemp, A. R. Means, L. A. Witters, *J. Biol. Chem.* **2005**, *280*, 29060.

[11] W. W. Winder, D. G. Hardie, *Am. J. Physiol.* **1999**, *277*, E1.

[12] J. T. Treebak, S. Glund, A. Deshmukh, D. K. Klein, Y. C. Long, T. E. Jensen, S. B. Jørgensen, B. Viollet, L. Andersson, D. Neumann, T. Wallimann, E. A. Richter, A. V. Chibalin, J. R. Zierath, J. F. P. Wojtaszewski, *Diabetes* **2006**, *55*, 2051.

[13] T. Hayashi, M. F. Hirshman, E. J. Kurth, W. W. Winder, L. J. Goodyear, *Diabetes* **1998**, *47*, 1369.

[14] B. Cool, B. Zinker, W. Chiou, L. Kifle, N. Cao, M. Perham, R. Dickinson, A. Adler, G. Gagne, R. Iyengar, G. Zhao, K. Marsh, P. Kym, P. Jung, H. S. Camp, E. Frevert, *Cell Metab.* **2006**, *3*, 403.

[15] M. Stumvoll, N. Nurjhan, G. Perriello, G. Dailey, J. E. Gerich, *N. Engl. J. Med.* **1995**, *333*, 550.

[16] A. R. Nawrocki, M. W. Rajala, E. Tomas, U. B. Pajvani, A. K. Saha, M. E. Trumbauer, Z. Pang, A. S. Chen, N. B. Ruderman, H. Chen, L. Rossetti, P. E. Scherer, *J. Biol. Chem.* **2006**, *281*, 2654.

[17] Y. Minokoshi, Y. -B. Kim, O. D. Peroni, L.G.D. Fryer, C. Muller, D. Carling, B. B. Kahn, *Nature* **2002**, *415*, 339.

[18] T. Yamauchi, J. Kamon, Y. Minokoshi, Y. Ito, H. Waki, S. Uchida, S. Yamashita, M. Noda, S. Kita, K. Ueki, K. Eto, Y. Akanuma, P. Froguel, F. Foufelle, P. Ferre, D. Carling, S. Kimura, R. Nagai, B. B. Kahn, T. Kadowaki, *Nat. Med.* **2002**, *8*, 1288.

[19] a) S. L. Schreiber, *Science* **2000**, *287*, 1964; b) M. D. Bruke, S. L. Schreiber, *Angew. Chem., Int. Ed.* **2004**, *43*, 46; c) D. S. Tan, *Nat. Chem. Biol.* **2005**, *1*, 74.

[20] a) S. K. Ko, H. J. Jang, E. Kim, S. B. Park, *Chem. Commun.* **2006**, 2962; b) S. -C. Lee, S. B. Park, *Chem. Commun.* **2007**, 3714; c) H. An, S. J. Eum, M. Koh, S. K. Lee, S. B. Park, *J. Org. Chem.* **2008**, *73*, 1752; d) Y. Kim, J. Kim, S. B. Park, *Org. Lett.* **2009**, *11*, 17; e) S. Lee, S. B. Park, *Org. Lett.* **2009**, *11*, 5214.

[21] a) J. Park, H. Y. Lee, M. -H. Cho, S. B. Park, *Angew. Chem. Int. Ed.* **2007**, *46*, 2018; b) Y. S. Tian, H. Y. Lee, C. S. Lim, J. Park, H. M. Kim, Y. N. Shin, E. S. Kim, H. J. Jeon, S. B. Park, B. R. Cho, *Angew. Chem. Int. Ed.* **2009**, *48*, 8027.

[22] B. Cool, B. Zinker, W. Chiou, L. Kifle, N. Cao, M. Perham, R. Dickinson, A. Adler, G. Gagne, R. Iyengar, G. Zhao, K. Marsh, P. Kym, P. Jung, H. S. Camp, E. Frevert, *Cell Metab.* **2006**, *3*, 403.

[23] S. -Y. Kim, N. H. Jeoung, C. J. Oh, Y. -K. Choi, H. -J. Lee, H. -J. Kim, J. -Y. Kim, J. H. Hwang, S. Tadi, Y. -H. Yim, K. -U. Lee, K. -G. Park, S. Huh, K. -N. Min, K. -H. Jeong, M. G. Park, T. H. Kwak, G. R. Kweon, K. Inukai, M. Shong, I. -K. Lee, *Circ. Res.* **2009**, *104*, 842.

[24] H. Tokumitsu, H. Inuzuka, Y. Ishikawa, M. Ikeda, I. Saji, R. Kobayashi, *J. Biol. Chem.* **2002**, *277*, 15813.

[25] G. D. Cartee, J. F. P. Wojtaszewski, *Appl. Physiol. Nutr. Metab.* **2007**, *32*, 557.

[26] E. J. Kurth-Kraczek, M. F. Hirshman, L. J. Goodyear, W. W. Winder, *Diabetes* **1999**, *48*, 1667.

[27] H. A. Koistinen, D. Galuska, A. V. Chibalin, J. Yang, J. R. Zierath, G. D. Holman, H. Wallberg-Henriksson, *Diabetes* **2003**, *52*, 1066.

[28] D. A. Hildeman, T. Mitchell, J. Kappler, P. Marrack, *J. Clin. Invest.* **2003**, *111*, 575.

[29] G. Perriello, R. Jorde, N. Nurjhan, M. Stumvoll, G. Dailey, T. Jenssen, D. M. Bier, J. E. Gerich, *Am. J. Physiol.* **1995**, *269*, E443.

[30] J. L. Goldstein, M. S. Brown, *Nature* **1990**, *343*, 425.

[31] T. Hayashi, M. F. Hirshman, N. Fujii, S. A. Habinowski, L. A. Witters, L. J. Goodyear, *Diabetes* **2000**, *49*, 527.

[32] M. Lee, J. -T. Hwang, H. -J. Lee, S. -N. Jung, I. Kang, S. -G. Chi, S. -S. Kim, J. Ha, *J. Biol. Chem.* **2003**, *278*, 39653.

[33] E. D. Abel, H. C. Kaulbach, R. Tian, J. C. A. Hopkins, J. Duffy, T. Doetschman, T. Minnemann, M. -E. Boers, E. Hadro, C. Oberste-Berghaus, W. Quist, B. B. Lowell, J. S. Ingwall, B. B. Kahn, *J. Clin. Invest.* **1999**, *104*, 1703.

[34] A. Zisman, O. D. Peroni, E. D. Abel, M. D. Michael, F. Mauvais- Jarvis, B. B. Lowell, J. F. P. Wojtaszewski, M. F. Hirshman, A. Virkamaki, L. J. Goodyear, C. R. Kahn, B. B. Kahn, *Nat. Med.* **2000**, *6*, 924.

==========

Abbreviations: AMP, adenosine 5'-monophosphate; AMPK, adenosine 5'-monophosphate activated protein kinase; AKN, ampkinone; CaMKK, Ca^{2+}/calmodulin-dependent kinase kinase; DIO, diet-induced obese; GLUT4, glucose transporter 4; AICAR, 5-aminoimidazole-4-carboxamide-1-β-d-ribofuranoside; TZDs, thiazolidinediones; ACC, acetyl-CoA carboxylase; DOS, diversity-oriented synthesis; DDQ, 2,3-dichloro-5,6-dicyanobenzoquinone; SAR, structure−activity relationship; CLSM, confocal laser scanning microscopy; IPGTT, intraperitoneal glucose tolerance test; ITT, insulin tolerance test; NEFA, nonesterified fatty acids; HMG-CoA, 3-hydroxy-3-methylglutaryl coenzyme A.

Chapter 4. Development of a Two-Photon Tracer for Glucose Uptake and its application in live tissues

- *Angew. Chem. Int. Ed.* **2009**, *48*, 8027.

Introduction

In one-photon microscopy (OPM), the probes are excited with short-wavelength light (≈350–550 nm); this, however, limits their application in tissue imaging, owing to inherent problems such as shallow penetration depth (<80 μm), interference by cellular autofluorescence, photobleaching, and photodamage.[1,2] To overcome these problems, it is crucial to use two-photon microscopy (TPM), which utilizes two near-infrared photons for excitation. TPM offers a number of advantages over OPM, including greater penetration depth (>500 μm), localized excitation, and longer observation times.[3,4] In particular, the extra penetration depth afforded by TPM is an essential element for application in tissue-imaging studies because the artifacts arising from surface preparation, such as damaged cells, can extend over 70 μm into the tissue interior.[5] However, visualization of glucose uptake by live cells and tissues with two-photon (TP) tracers has not been reported so far.

Results and Discussion

The requirements for a TP tracer to visualize glucose uptake include sufficient water solubility for staining cells and tissues, preferential uptake by cancer cells, a large TP cross-section for a bright TPM image, pH resistance, and high photostability. Our strategy was to link α-D-glucose with the fluorophore 2-acetyl-6-dimethylaminonaphthalene (acedan) through 3,6-dioxaoctane-1,8-diamine or a

piperazine linkage (in AG1 and AG2, respectively; Scheme 1), so that the tracers are transported into the cells through the glucose-specific mechanism. Acedan is a polarity-sensitive fluorophore that has been successfully employed in the development of TP probes for the cell membrane,[6] metal ions,[7-9] and acidic vesicles.[10] We now report that these tracers facilitate the visualization of glucose uptake in cancer cells and live tissues at a depth of 75–150 μm for more than 3000 s and can be used for screening anticancer agents.

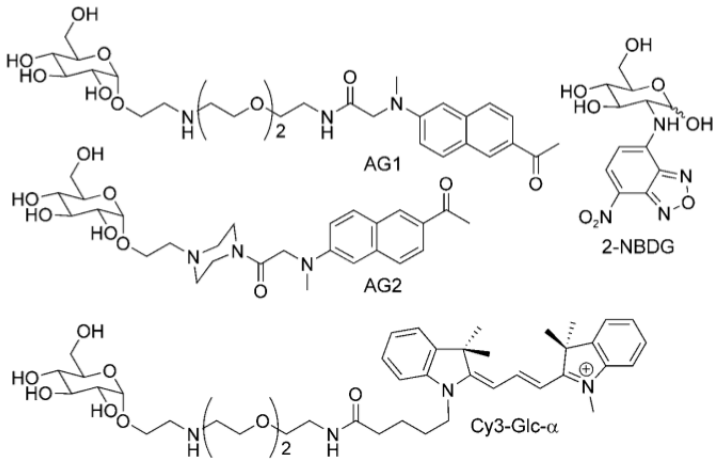

Scheme 1. Structures of fluorescent tracers AG1, AG2, 2-NBDG, and Cy3-Gly-α.

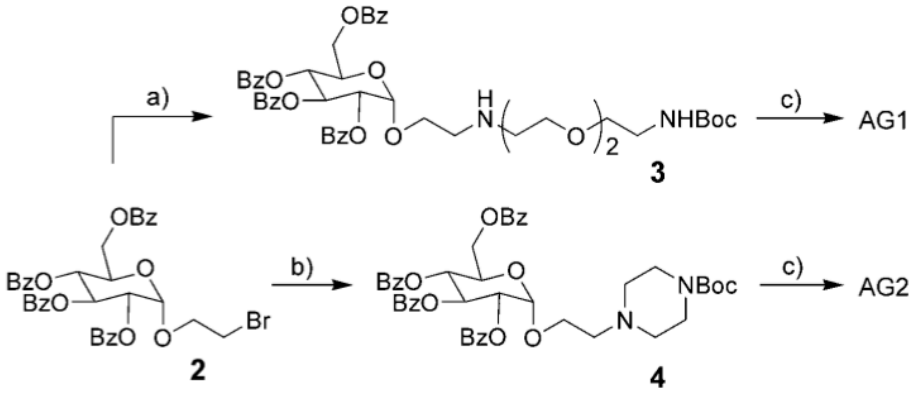

Scheme 2. a) *N*-Boc-3,6-dioxaoctane-1,8-diamine, Et_3N, DMF, 50 °C; b) *N*-Boc-piperazine, Et_3N, DMF, 50 °C; c) 1. NaOMe, MeOH; 2. 50 % TFA/CH_2Cl_2; 3. **1**, EDC, DIPEA, DMF. Boc: *tert*-butoxycarbonyl; DMF: *N*,*N*-dimethylformamide; TFA: trifluoracetic acid; EDC: 3-(3-dimethylaminopropyl)-1-ethylcarbodiimide; DIPEA: *N*,*N*-diisopropylethylamine.

The preparation of AG1 and AG2 is shown in Scheme 2. 6-Acetyl-2-[*N*-methyl-*N*-(carboxymethyl)amino]naphthalene (**1**), **2**, and **3** were prepared by the method used in our previous studies.[6-11] The reaction of **2** with *N*-Boc-piperazine afforded **4** in 70 % yield. AG1 and AG2 were prepared in 26 and 86 % yields, respectively, by treating **3** and **4** with **1**.

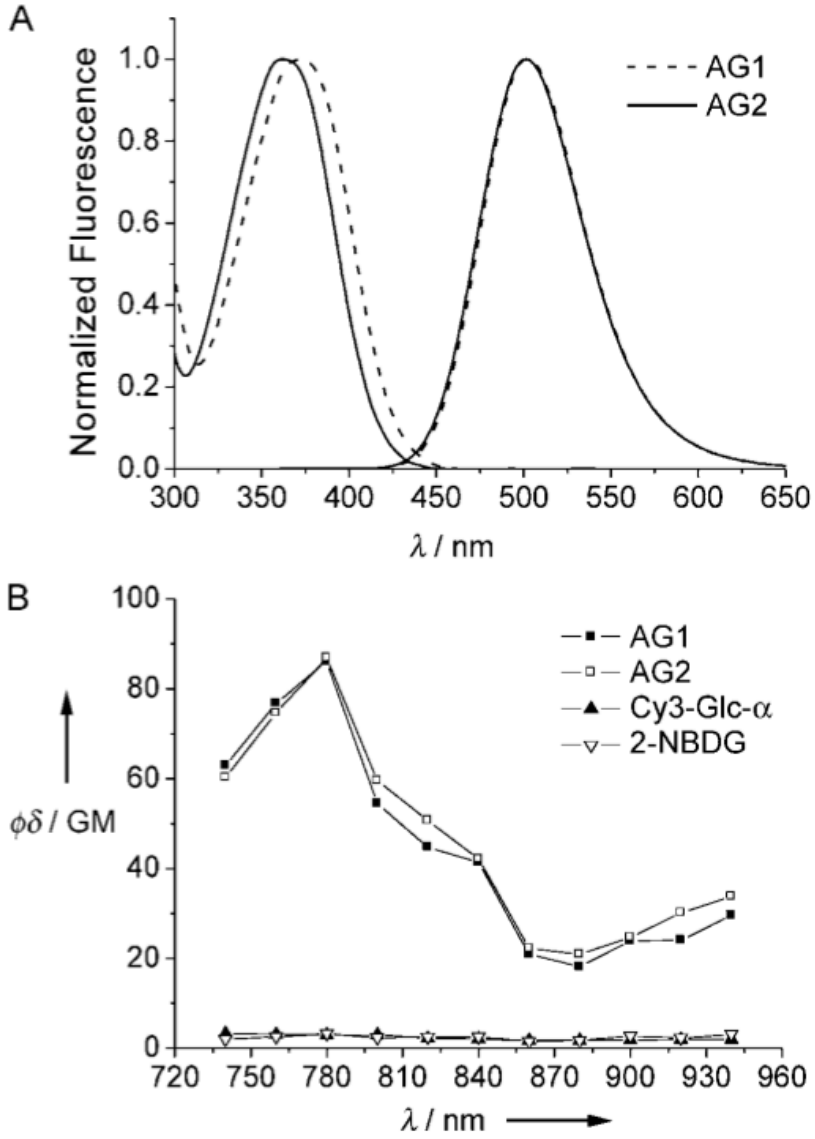

Figure 1. A) One-photon absorption and emission spectra of AG1 and AG2 in phosphate-buffered saline (PBS) buffer (137 mM NaCl, 3 mM KCl, 10 mMNa_2HPO_4, 2 mM KH_2PO_4, pH 7.4). B) Two-photon action spectra for AG1, AG2, Cy3-Glc-α, and 2-NBDG in PBS buffer.

The fluorescence spectra of AG1 and AG2 showed gradual bathochromic shifts with increases in the solvent polarity (E_T^N) with the following order of solvents: 1,4-dioxane<DMF<EtOH<H_2O (Figure S1 and Table S1 in the Supporting Information). The large bathochromic shifts upon increases in the solvent polarity indicate the utility of these molecules as polarity probes. Both compounds show strong fluorescence in all of the solvents. Moreover, they are pH insensitive in the biologically relevant pH range (Figure S1 c and S1 f in the Supporting Information). The TP action spectrum of AG1 determined by the two-photon-excited fluorescence (TPEF) method[12] indicated a $\Phi\delta$ value of ≈90 GM at 780 nm, which is much larger than those observed for Cy3-Glc-α and 2-NBDG (Figure 1 and Table 1). Hence, the TPM images of the samples stained with AG1 or AG2 would appear much brighter than those stained with Cy3-Glc-α or 2-NBDG.

Compound	$\lambda_{max}^{(1)}/\lambda_{max}^{(fl)}$ [b]	Φ[c]	$\lambda_{max}^{(2)}$ [d]	δ_{max} [e]	$\Phi\delta_{max}$ [f]
AG1	373/501	0.90	780	95	86
AG2	375/501	0.56	780	155	88
Cy3-Glc-α	545/555	0.01	n.d.[g]	n.d.[g, h]	n.d.[g, h]
2-NBDG	465/540[i]	n.d.[g]	n.d.[g]	n.d.[g, h]	n.d.[g, h]

Table 1. Photophysical data for AG1, AG2, Cy3-Glc-α, and 2-NBDG.[a]

[a] All measurements were performed in PBS buffer. [b] λ_{max} values of the one-photon absorption and emission spectra in nm. [c] Fluorescence quantum yield, ±15 %. [d] λ_{max} value of the two-photon absorption spectrum in nm. [e] The peak two-photon action cross-section in 10^{-50} cm^4/photon (GM), ±15 %. [f] Two-photon action cross-section in GM. [g] n.d.: not determined. [h] The two-photon-excited fluorescence intensity was too weak to allow accurate measurement of the cross-section. [i] Reference 20.

The optimum concentration of these probes for the cellular uptake experiments was determined by comparing the TPM images of A549 cells treated with 6, 12.5, 25, 50, and 100 μM of AG1 and AG2 for 30 min. The TPM images appeared brighter as the probe concentration was increased up to 50 μM; however, at

100 μM concentrations, some cell death was observed (Figure S2 in the Supporting Information). Moreover, a higher uptake rate and a brighter TPM image were obtained when the cells were treated with AG2 than when they were treated with AG1 (see Figure 3 A and Figure S3 in the Supporting Information). Furthermore, the effect of AG2 on the viability of cells was studied by using the CCK-8 kit: AG2 showed negligible toxicity, which indicates that it could be applied for live-cell imaging (Figure S4 in the Supporting Information). Therefore, we used 50 μM AG2 as the optimum concentration in further cellular uptake experiments.

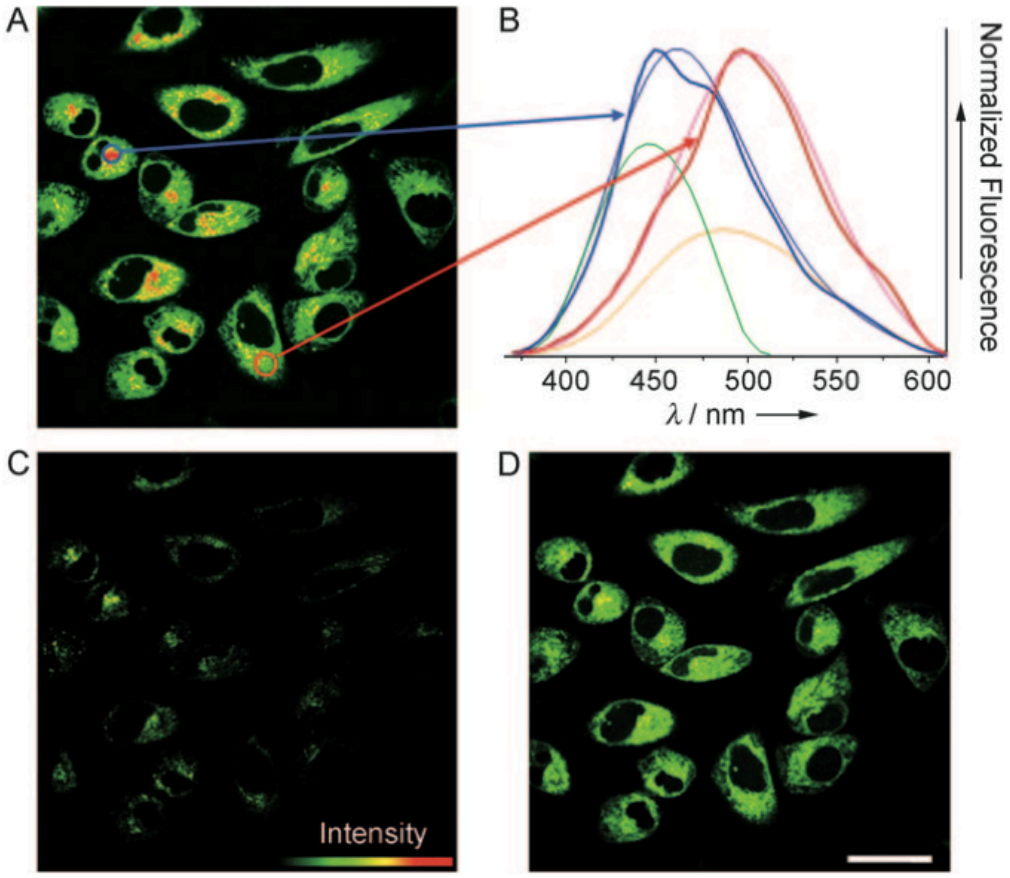

Figure 2. Pseudocolored TPM images of A549 cells incubated with 50 μM AG2 for 10 min, collected at A) 360–620, C) 360–460, and D) 520–620 nm. B) Two-photon-excited fluorescence spectra from the hydrophobic (marked in blue) and hydrophilic (marked in red) regions of the AG2-labeled A549 cells. The thin pale blue and pink curves represent the dissected Gaussian functions for the blue and red bands, respectively. The orange and green lines are discussed in the text. The excitation wavelength was 780 nm. The images shown are representative of the images obtained in the repeat experiments (n=5). Scale bar: 30 μm.

The pseudocolored TPM images of cultured A549 cells treated with 50 μM AG2 showed intense spots and homogeneous domains with two-photon emission maxima at 461 (marked in blue in Figure 2 A and B) and 497 nm (marked in red), respectively. The TPEF spectrum of the intense spots was asymmetrical and could be fitted to two Gaussian functions with emission maxima at 445 (green line in Figure 2 B) and 488 nm (orange line), whereas the TPEF spectrum of the homogeneous domain could be fitted to a single Gaussian function (pink line) with an emission maximum at 497 nm. The longer wavelength band of the dissected Gaussian function (orange line in Figure 2 B) is similar to the band of the single Gaussian function (pink line). This result suggests that the probe is located in two regions of different polarity: a more polar one that is likely to be cytosol and a less polar one that is likely to be membrane associated. Moreover, the shorter wavelength band (green in Figure 2 B) in the dissected Gaussian functions decreases to the baseline at wavelengths of less than 520 nm. Consistently, the TPM image collected at 520–620 nm is homogeneous without intense spots (Figure 2 D), whereas the one collected at 360–460 nm clearly shows them (Figure 2 C). Similar results were reported for acedan-derived TP probes for Mg^{2+} (AMg1)[7] and Ca^{2+} ions (ACa1).[8] Therefore, cytosolic AG2 can be selectively detected by using the detection window of 520–620 nm, with minimal interference from the membrane-bound probes. Furthermore, the TPM images of A549 cells costained with AG2 and MitoTracker, a well-known one-photon fluorescent (OPF) probe for mitochondria,[13] merged well with the OPM image (Figure S5 in the Supporting Information), which indicates that the probes are predominantly located in the mitochondria.

To assess whether AG2 is selectively taken up by cancer cells, the efficiencies of AG2 uptake by A549 (lung carcinoma cell line), HeLa (cervical cancer cell line),

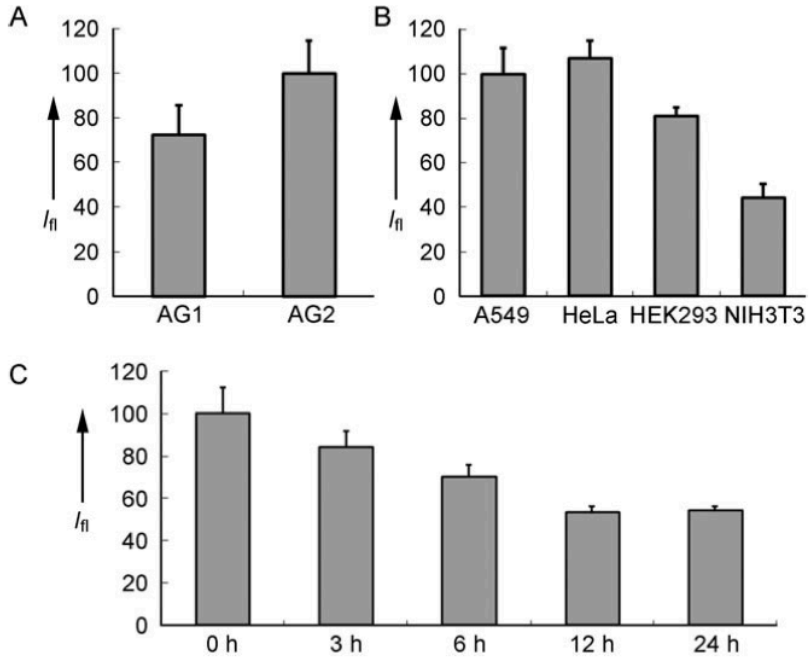

Figure 3. A) Relative AG1 and AG2 uptake by A549 cells. B) Relative AG2 uptake in cancer cells (A549, HeLa) and normal cells (HEK293, NIH/3T3). C) Relative AG2 uptake by A549 cells after treatment with taxol (9.8 μM) for 0, 3, 6, 12, and 24 h. Cells were incubated with AG1 or AG2 (50 μM) for 10 min, either before (A and B) or after (C) treating the cells with taxol (9.8 μM) for the designated period of time, and TPEF intensities from 40–60 cells were determined by photomultiplier tube. The data are the average of at least five independent experiments.

HEK293 (human embryonic kidney 293 cell line), and NIH/3T3 (murine fibroblast cell line) cells were compared. AG2 uptake was most efficient in A549 and HeLa cells, followed by HEK293 and NIH/3T3 cells (Figure 3 B and Figure S7A in the Supporting Information); this result is similar to that obtained in the case of Cy3-Glc-α[14] and confirms the selective uptake of AG2 by cancer cells with enhanced glucose metabolism. The cellular uptake experiment showed that AG2 effectively competes with D-glucose in the media for cellular uptake; the fluorescence intensities of AG2 in A549 cells inoculated with media containing 10 mM or 50 mM D-glucose were reduced by about 16 and 74 %, respectively, as compared to that with glucose-depleted medium, and the fluorescence intensity was not affected by medium containing L-glucose (50 mM; Figure S6 in the Supporting Information). Furthermore,

AG2 uptake was not influenced by the presence of 55 mM D,L-alanine, which indicates that osmotic pressure does not have an impact on AG2 uptake. These results suggest that AG2 is a glucose analogue that is taken up by the cells through a glucose-specific transport system and not by passive diffusion.[14-17] Therefore, AG2 can be used for visualizing glucose uptake in living cells by TPM, without subjecting the cells to glucose starvation.

To demonstrate the utility of this probe, we investigated the effects of taxol on AG2 uptake by A549 cells. It was expected that the anticancer agent would depress the cellular metabolism and thereby reduce glucose uptake in the cancer cells.[14] The cells were incubated with the anticancer agent for 1, 3, 6, 12, and 24 h, washed with PBS, treated with AG2, and then imaged. The cellular uptake of AG2 was lower with longer incubation times (Figure 3 C and Figure S7B in the Supporting Information). Dose-dependent uptake of AG2 was also observed with taxol concentrations of 49 nM, 490 nM, and 9.8 μM (Table 2). Another anticancer agent, combretastatin, also inhibited AG2 uptake in a similar manner (Table 2). Hence, AG2 can be used for screening anticancer agents in live cells by TPM.

	AG2 uptake [%]	
	after 6 h	after 12 h
taxol (9.8 μM)	69.5	50.7
taxol (490 nM)	89.6	69.5
taxol (49 nM)	97.6	81.8
combretastatin (2 μM)	70.2	53.2

Table 2. Dose dependence of AG2 uptake by A549 cells in the presence of various concentrations of anticancer agents

We further assessed the utility of AG2 in tissue imaging for the diagnosis of colon cancer, for which we used images of normal- and cancer-tissue slices from colon-cancer patients. The bright-field image of the normal tissue clearly revealed the

presence of glands on the tissue surface. However, the cancer tissue appeared almost amorphous and did not have a definite structure (Figure 4 A and Figure S8A in the Supporting Information). The tissues were incubated in artificial cerebrospinal fluid (ACSF) for 4 h at 37 °C in the absence and presence of taxol (50 μM), after which the AG2 uptake was monitored by TPM by following the change in TPEF at a depth of 100 μm. The result shows that AG2 uptake in the cancer tissue is much faster than that in the normal tissue and that the cancer tissue pretreated with taxol for 4 h exhibits much slower AG2 uptake than the untreated one (Figure 4 A and B). A similar result was observed from the normal- and cancer-tissue slices obtained immediately after colonoscopic biopsy, which indicates that incubation of the tissue slices in ACSF for 4 h did not significantly influence the relative uptake rate (Figure S8B in the Supporting Information). Furthermore, the uptake could be monitored for more than 3000 s without noticeable decay. These results strongly support the applicability of AG2 in deep-tissue imaging for the diagnosis of colon cancer, in addition to its useful properties for in vivo imaging, namely high photostability and low toxicity.

Colon cancer is known to originate from the mucosa in the intestinal glands and spread into the interior of the tissue,[18] so we have obtained TPM images at different depths from the tissue surface. The TPEF intensities appear scattered at shallow depths due to different degrees of dye adsorption at tissue surfaces that are very different, as shown in the bright-field images (Figure 4 A and Figure S8A in the Supporting Information). However, we were able to obtain reliable results at a depth of ≥75 μm from the tissue surface. TPM images of the tissue sections obtained for 4000 s revealed the AG2 distribution at depths of 75, 100, 125, and 150 μm, and each

image exclusively represents the distribution in a given plane (Figure S8D and S9 in the Supporting Information).

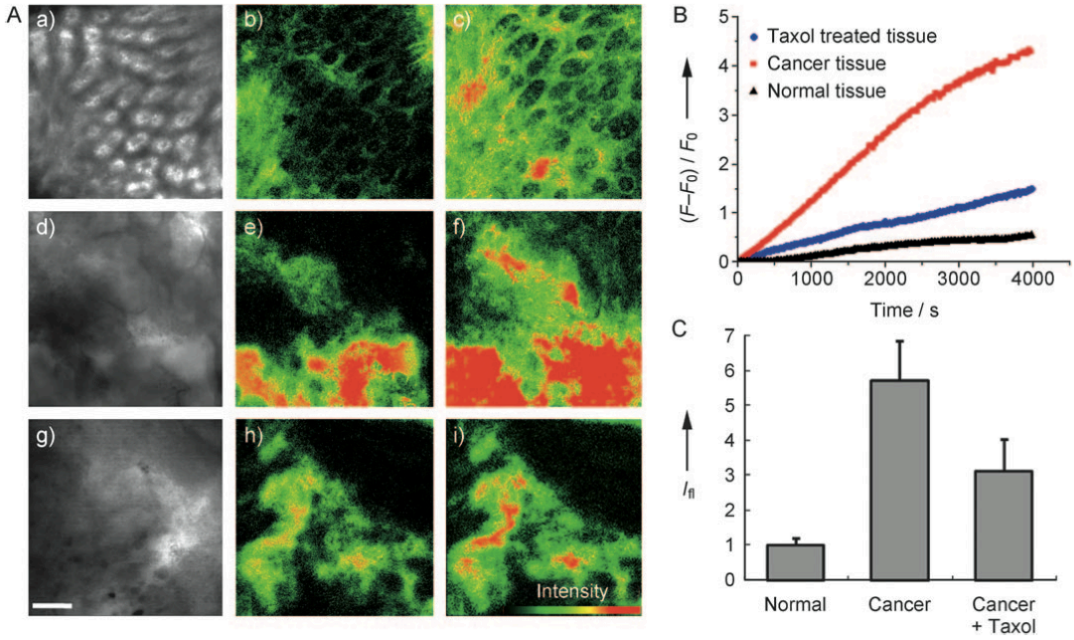

Figure 4. A) Images of normal tissue (a–c), cancer tissue (d–f), and cancer tissue treated with taxol (g–i). Normal tissues were incubated in ACSF for 4 h, and cancer tissues were incubated in the absence and presence of taxol (50 μM) in ACSF for 4 h, after which AG2 uptake was monitored. a, d, and g are bright-field images; b, e, and h are pseudocolored TPM images obtained after incubation with AG2 for 4000 s; and c, f, and i are pseudocolored TPM images obtained after incubation with AG2 for 4 h. The TPM images were obtained at a depth of 100 μm by collecting the TPEF spectra in the range of 520–620 nm on excitation with fs pulses at 780 nm. Scale bar: 30 μm. B) Time course of AG2 uptake by normal tissue, cancer tissue, and cancer tissue treated with taxol (50 μM) at 100 μm depth as a function of time. C) Relative AG2 uptake by normal tissue, cancer tissue, and cancer tissue treated with taxol (50 μM) for 4000 s. The columns indicate the sum of the TPEF intensities measured by photomultiplier tube at depths of 75, 100, 125, and 150 μm from the tissue surface, relative to that of normal tissue. The data are the average of three independent experiments.

TPM images were obtained up to a depth of 150 μm due to the limited penetration of AG2 into the tissues during the incubation; TPM images at deeper depths could be obtained if the tissues were incubated for a longer period of time. As expected, the uptake was most efficient near the tissue surface; it decreased with

larger imaging depths and was negligible at a depth of >150 μm. In addition, the uptake rate was much slower than that in the cells, probably because of the extracellular matrix, which is more abundant in aged tissues. The sum of the TPEF intensities measured at depths ranging from 75 to 150 μm was largest in the case of cancer tissue, followed by cancer tissue treated with taxol, and then normal tissue (Figure 4 C). This result once again clearly demonstrates the preferential uptake of AG2 by cancer tissue and emphasizes the usefulness of AG2 in the diagnosis of colon cancer.

Finally, it is worthwhile to compare the near-infrared (NIR) imaging with the IR dye 800CW-2DG[19] and the TPM imaging with AG2. Both methods are capable of imaging deep inside live tissues because of the long excitation wavelengths (≈800 nm). However, the two methods are entirely different. Whereas the former is useful for imaging big objects such as a whole mouse, the latter is suitable for imaging microlevel objects such as cells and tissue slices with high resolution. Due to the localized excitation inherent in the two-photon process and the capability of imaging the pixels (focal point of the laser), TPM images can be obtained at different depths with a few hundred nm resolution (Figure S8 and S9 in the Supporting Information). This is not possible with NIR imaging.

Conclusion

To conclude, we have developed a new TP tracer, AG2, that can be excited by 780 nm fs laser pulses and can be easily taken up by cancer cells and tissues through glucose-specific translocation. AG2 is pH independent at a wide range of physiological pH values (pH 4.0–10) and shows negligible cytotoxicity and high photostability. It can monitor glucose uptake in normal and colon-cancer tissues from

human patients for more than 3000 s and can visualize the efficacy of anticancer agents in cancer cells and colon-cancer tissues at depth of 75–150 mm by TPM. This compound may be useful in diagonizing the early stages of cancer and in the development of customized cancer therapy for a patient by comparing the uptake rates of AG2 in normal and cancerous tissues treated with different anticancer drugs at different depths.

Supporting Information

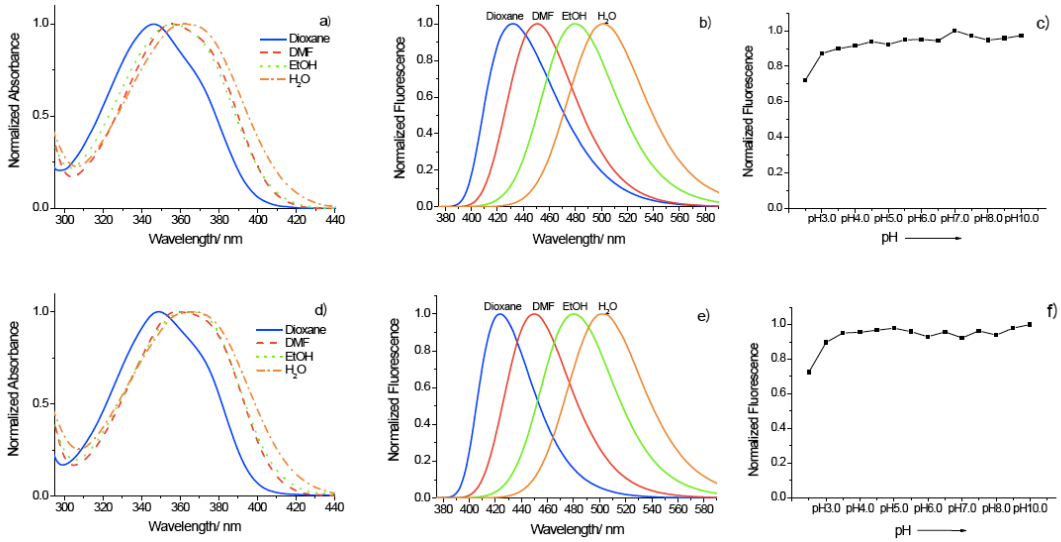

Figure S1. (a, d) Normalized absorption (b, e) emission spectra and (c, f) pH dependency of (a, b, c) AG1, (d, e, f) AG2 in 1,4-dioxane, DMF, EtOH, and H2O.

Solvent (E_T^N)[a]	$\lambda_{max}^{(1)}$ [b]		λ_{max}^{fl} [b]		Φ[c]	
	AG1	AG2	AG1	AG2	AG1	AG2
Dioxane (0.164)	360	362	434	425	0.59	0.72
DMF (0.386)	366	369	451	449	1.00	1.00
EtOH (0.654)	364	370	479	480	1.00	0.97
H_2O (1.00)	373	375	501	501	0.90	0.56

Table S1. Photophysical properties of AG1, AG2 in various solvents.

[a] The numbers in the parenthesis are normalized empirical parameter of solvent polarity.[5] [b] λ_{max} of the one-photon absorption and emission spectra in nm. [c] Fluorescence quantum yield, ± 15 %.

Spectroscopic measurements : Absorption spectra were recorded on a Hewlett-Packard 8453 diode array spectrophotometer, and fluorescence spectra were obtained with Amico-Bowman series 2 luminescence spectrometer with a 1-cm standard quartz cell. The fluorescence quantum yield was determined by using Coumarin 307 and Rhodamine B as the reference. The spectral data obtained under various conditions are summarized in Figure S1 and Table S1.

Two-photon fluorescence microscopy : Two-photon fluorescence microscopy images of probelabeled cells and tissues were obtained with spectral confocal and multiphoton microscopes (Leica TCS SP2) with a x 100 (NA = 1.30 OIL) and x 20 (NA = 0.30 DRY) objective lens, respectively. The twophoton fluorescence microscopy images were obtained with a DM IRE2 Microscope (Leica) by exciting the probes with a mode-locked titanium-sapphire laser source (Coherent Chameleon, 90 MHz, 200 fs) set at wavelength 780 nm and output power 1230 mW, which corresponded to approximately 10 mW average power in the focal plane. To obtain images at 360–460 nm and 520–620 nm range, internal PMTs were used to collect the signals in an 8 bit unsigned 512 x 512 pixels at 400 Hz scan speed.

Cell culture and imaging : A549 human lung carcinoma cells, HeLa human cervical carcinoma cells, NIH/3T3 murine fibroblast cells, HEK293 human embryonic kidney cells were obtained from American Type Culture Collection (ATCC, Manassas, VA, USA). A549 cells were cultured in RPMI 1640 (WelGene) supplemented with heat-inactivated 10% FBS (WelGene), penicillin (100 units/mL), and streptomycin (100 ug/mL). NIH/3T3 cells, HeLa cells, and HEK293 cells were cultured in DMEM (WelGene) supplemented with heat-inactivated 10% FBS (WelGene), penicillin (100

units/mL), and streptomycin (100 ug/mL). All the cell lines were maintained in a humidified atmosphere of 5% CO2 and 95% air at 37 °C. Two days before imaging, the cells were detached and $10^4/mm^2$ cells were plated on glass-bottomed dishes (MatTek). For labeling, the growth medium was removed and replaced with RPMI 1640 (without D-glucose) (United Search Partners, Austin, TX, USA) without serum. The cells were treated and incubated with required concentration of tracker at 37 °C for 10 min. The cells were washed three times with phosphate buffered saline (PBS; Gibco) and then imaged. To compare the relative uptake of AG1 and AG2 per unit cell, the TPEF intensities from regions of interest chosen without bias among 46-60 cells were determined by the photomultiplier tube (PMT) and the data were digitalized by Histogram (program for data analysis). The relative uptake in tissues was determined by the same method except that TPM images of the tissue sample were obtained at different depths. The effects of taxol and combretastatin on the AG2 uptake were determined by adding appropriate amount of the DMSO solution (10 mM) of the anti cancer agents to the cells and tissues. In all cases the DMSO content was maintained to be 1 %.

Optimum concentration of AG1 and AG2 for the uptake experiment : To determine the optimum concentration for the uptake experiment, the TPM images of A549 cells labeled with 6, 12.5, 25, 50, and 100 μM of AG1 and AG2 for 30 min were compared. The image became brighter as the probe concentration was increased up to 50 μM; however, at higher concentration than this, the cell death was observed (Figure S2). Moreover, the uptake rate was faster (600 vs 800 s) and the TPM image was brighter when the cells were labeled with AG2 than when they were treated with AG1 (Figure S3). Therefore, we used 50 μM of AG2 for the uptake experiments.

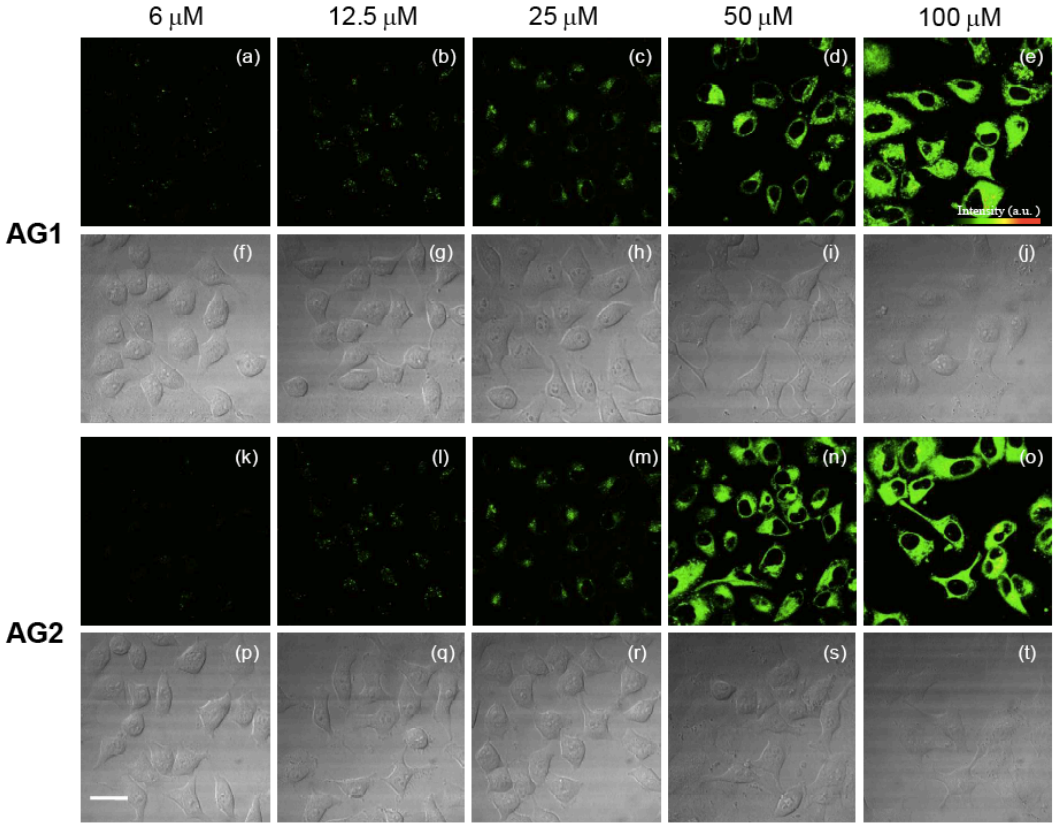

Figure S2. Images of A549 cells incubated with 6-100 μM of AG1 (a-j) and AG2 (k-t) for 30 min. f-j and p-t are bright field images; a-e and k-o are TPM images. TPM images were obtained by collecting TPEF at 520-620 nm upon excitation with fs pulses at 780 nm. The images shown are representative of the images obtained in the replicate experiments (n = 5). Scale bar, 30 μm.

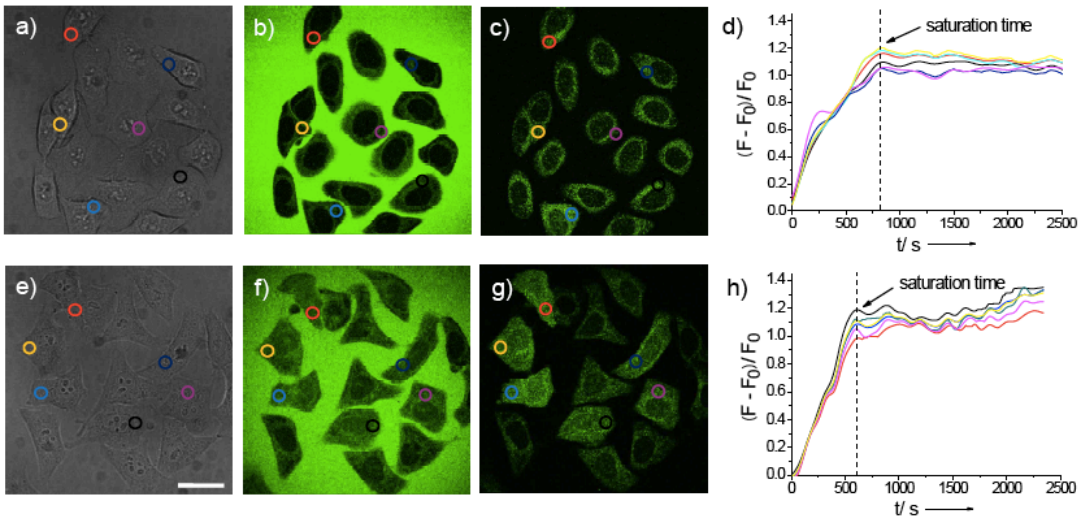

Figure S3. Images of A549 cells incubated with AG1 (a-d) and AG2 (e-h). a and e are bright-field images; b and f are TPM images obtained immediately after incubation; and c and g are TPM images obtained 40 min after incubation. (d, h) Changes of the relative fluorescence intensity with time at the regions of six independent cells marked in (a, e), which are chosen without bias. TPM images were obtained by collecting TPEF at 520–620 nm upon excitation with fs pulses at 780 nm. Scale bars, 30 μm.

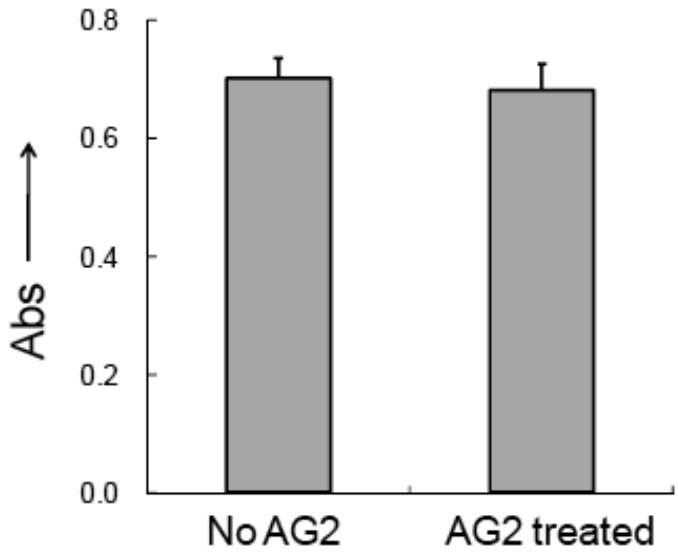

Figure S4. Viability of A549 cells in the presence of AG2 as measured by using CCK-8 kit. The cells were incubated with 50 μM AG2 for 10 min.

Colocalization experiment : To determine where AG2 is predominantly located inside the cells, a colocalization experiment was conducted with A549 cells by co-staining with AG2 and MitoTracker, a well known one-photon fluorescent (OPF) probe for the mitochondria. The TPM image was well merged with the OPM image (Figure S6), indicating that the probes are predominantly located in the mitochondria.

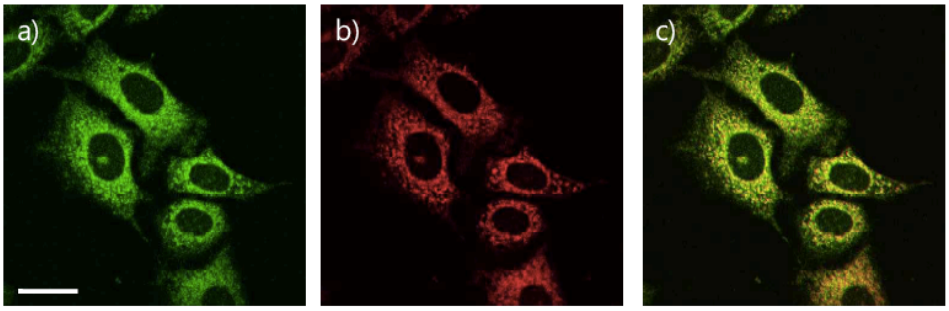

Figure S5. (a) TPM image of A549 cells incubated with 50 μM AG2 for 10 min, (b) one-photon fluorescence image of the A549 cells labeled with Mito-Tracker for 10 min, and (c) merged image. Exitation wavelengths are 780 nm (a) and 488 nm (b), respectively. The images shown are representative of the images obtained in the replicate experiments (n = 5). Scale bars, 30 μm.

Competition experiment : To determine whether the intracellular uptake pathway of AG2 is relevant to that of D-glucose, a competition experiment was conducted. For this purpose, A549 cells were incubated with AG2 (50 μM) for 10 min in the presence of 0, 10, and 50 mM D-glucose, and 50 mM L-glucose and relative AG2 uptake was determined by TPM. To assess whether the osmotic pressure does not have an impact on the uptake, the same experiment was conducted in the presence of 55 mM D,L-alanine. The results are shown in Figure S7.

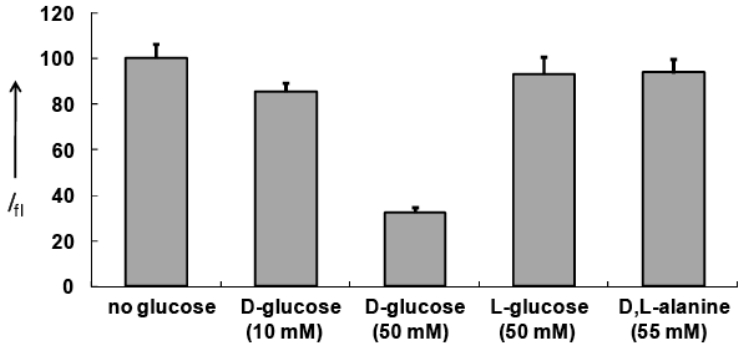

Figure S6. Dose-dependent inhibition of AG2 uptake by A549 cells in the presence of D- and L-glucose and D,L-alanine. TPEF intensities from 40-60 cells were measured by PMT. The data are the average of at least five independent experiments. The TPEF was collected upon excitation at 780 nm with fs pulses.

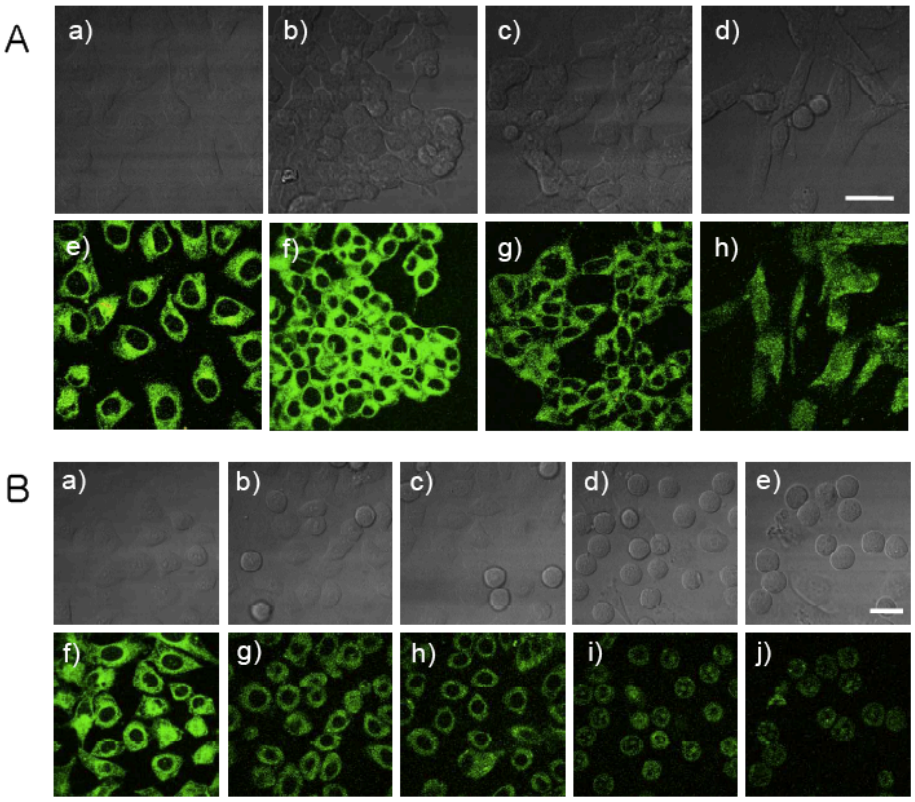

Figure S7. (A) TPM images of A549 cells (a, e), HeLa cells (b, f), HEK293 cells (c, g), and NIH/3T3 cells (d, h) after AG2 (50 μM) uptake for 10 min, a–d are bright-field images and e–j are TPM images. (B) TPM images of A549 cells after treatment with taxol (9.8 μM) for 0 h (a, f), 3 h (b, g), 6 h (c, h), 12 h (d, i), and 24 h (e, j). a–e are bright field images and f–j are TPM images. Each image was obtained after treating the cells with taxol (9.8 μM) for the designated period of time, after which they were incubated with AG2 (50 μM) for 10 min. The images were obtained by collecting the TPEF in the range of 520–620 nm upon excitation with fs pulses at 780 nm. The images shown are representative of the images obtained in the replicate experiments (n = 5). Scale bar, 30 μm.

Preparation and TPM imaging of human cancer tissue slices : Human colon cancer tissues and normal tissues were obtained from colon cancer patients during colonoscopic examination, according to an approved institutional review board protocol. Normal tissues, cancer tissues, and cancer tissues containing 50 μM taxol were incubated in artificial cerebrospinal fluid (ACSF) bubbled with 95% O2 and 5% CO2 for 4 hrs at 37 °C. Tissues were then washed three times with ACSF, transferred to glassbottomed dishes (MatTek), added with 50 μM AG2, and observed by TPM (Figure 4 in the text). To determine whether the relative uptake was influenced by the incubation in ACSF, the same experiment was conducted using normal tissues and colon cancer tissues obtained immediately after colonoscopic biopsy. The result is similar to that obtained with tissues incubated in ACSF for 4 h, indicating that the relative uptake is not influenced by the incubation (Figure S8).

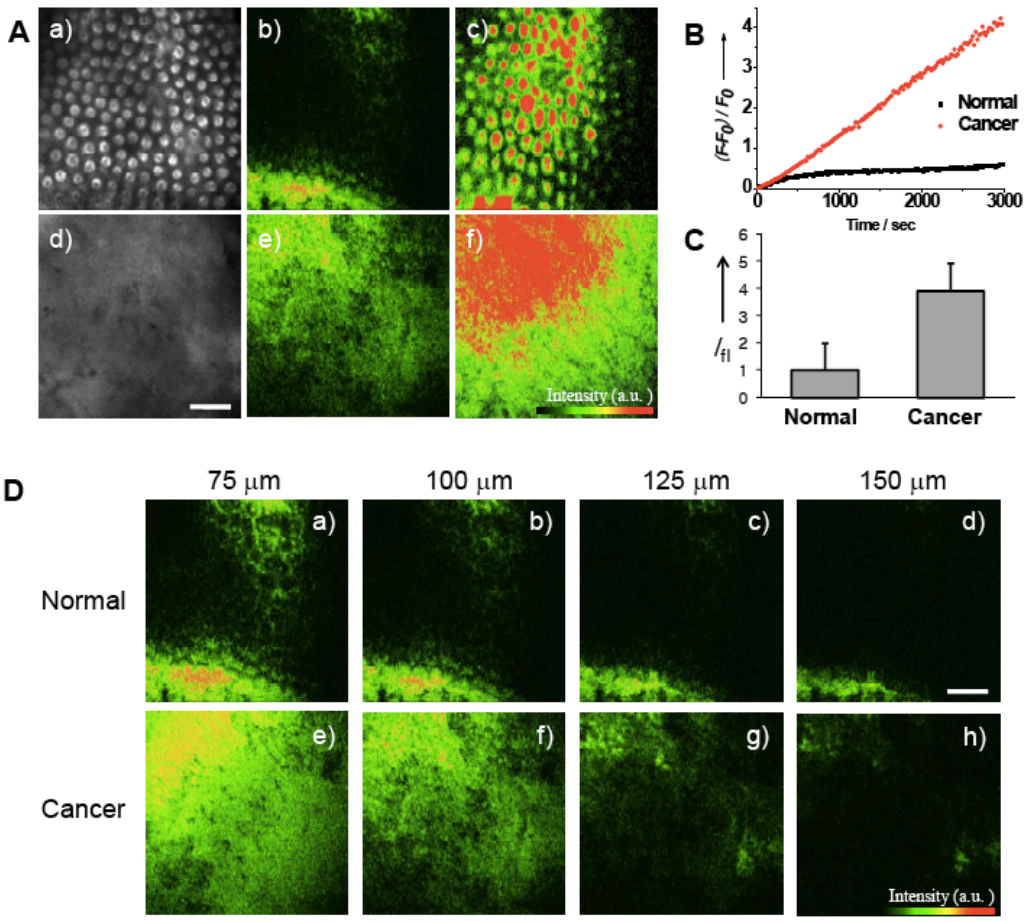

Figure S8. (A) Images of normal tissues (a,b,c) and cancer tissues (d,e,f) from a colon cancer patient. a and b are bright field images; b and e are pseudo-colored TPM images obtained after incubation with AG2 (50 μM) for 3,000 s; and c and f are pseudo-colored TPM images obtained after incubation with AG2 (50 μM) for 5 h. (B) Time course of AG2 uptake by normal and cancer tissues obtained immediately after colonoscopic biopsy at 100 μm depth. (C) The columns indicate the sum of the TPEF intensities measured by PMT at depths of 75, 100, 125, and 150 μm from the tissue surface, relative to that of normal tissue. The data are the average of 3 independent experiments. (D) TPM images of normal and cancer tissues obtained at depths of 75, 100, 125, and 150 μm from the tissue surface. TPM images were obtained by collecting the TPEF at 520–620 nm upon excitation at 780 nm with fs pulse. Scale bar, 300 μm.

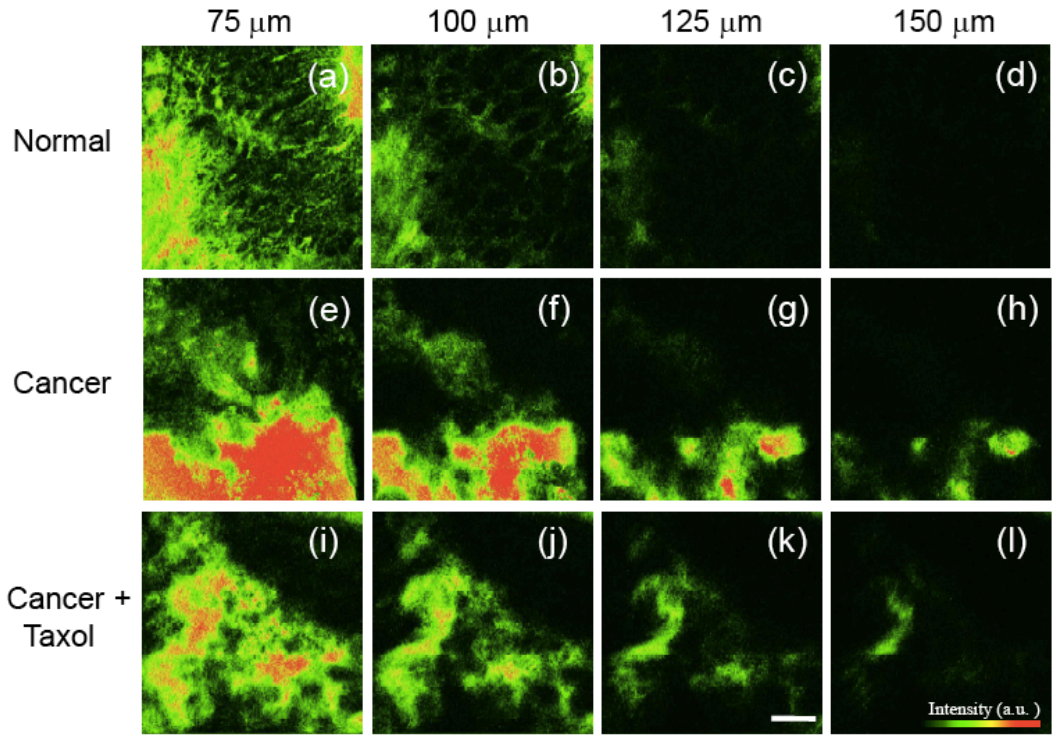

Figure S9. TPM images of normal tissue (a, b, c, d), cancer tissue (e, f, g, h), and cancer tissue treated with taxol (50 μM) (i, j, k, l) for 4,000 s at depths of 75, 100, 125, and 150 μm from the tissue surface. Normal tissues were incubated in ACSF for 4 h, and cancer tissues were incubated in the absence and presence of taxol (50 μM) in ACSF for 4 h, after which AG2 uptake was monitored. The TPM images were obtained by collecting the TPEF at 520–620 nm upon excitation at 780 nm with fs pulse. Scale bar, 150 mm.

Synthesis of AG1 and AG2. The synthetic procedures for 6-Acetyl-2-[*N*-methyl-*N*-(carboxymethyl)amino]naphthalene (**1**), (2-bromoethyl)-2,3,4,6-tetra-*O*-benzoyl-α-D-glucoside (**2**) and [2-(*N*-boc-3,6-dioxaoctane-1,8-diaminoethyl)]-2,3,4,6-tetra-*O*-benzoyl-α-D-glucoside (**3**) are available in our previous publication.[9] Syntheses of compounds **AG1**, **AG2**, and **4** are described below.

Synthesis of AG1. To a solution of **3** (130 mg, 0.17 mmol) in MeOH (1 mM), sodium methoxide (0.5 M in MeOH, 1.1 mL, 0.56 mmol) was added for debenzoylation of **3**. After the reaction was completed, the reaction mixture was neutralized with methanolic HCl, and then concentrated under reduced pressure. For the deprotection of Boc group, 50 % TFA in dichloromethane was added to the resulting residue of

previous reaction. The resulting fully-deprotected compound was condensed by N_2 purging, redissolved in DMF (1 mL), slightly basified with TEA (0.58 mL, 0.42 mmol), and added with **1** (36 mg, 0.14 mmol) and EDC (40 mg, 0.21 mmol) in DMF (500 mL) for amide coupling. The reaction mixture was stirred at room temperature and the reaction completion was monitored by HPLC analysis. The elution protocol for analytical HPLC starts with 95% eluent A (deionized water containing 0.1 % TFA) and 5% eluent B (HPLC-grade acetonitrile containing 0.1% TFA) for 1 min, followed by a linear gradient to 60, 50, 5, and 0% of eluent A over the period of 4, 10, 10, and 5 min, respectively. The elution was continued with 0% eluent A for 5 min and returned back to 95% eluent A over 10 min period for regeneration. Purification by prep-HPLC afforded 22 mg (26 %) of **AG1** (retention time: 11 min). The desired product was confirmed by ^{1}H, ^{13}C NMR, MALDI-TOF MS, and HRMS. ^{1}H NMR (300 MHz, CD_3OD) δ 8.40 (s, 1H), 7.89 (s, 1H), 7.86 (s, 1H), 7.66 (d, J = 8.7 Hz, 1H), 7.18 (dd, J = 6.6, 2.4 Hz, 1H), 6.97 (d, J = 2.1 Hz, 1H), 4.82 (d, J = 3.6 Hz, 1H), 4.10 (s, 2H), 4.00–3.93 (m, 1H), 3.81 (dd, J = 11.7, 2.0 Hz, 1H), 3.70–3.58 (m, 5H), 3.57–3.47 (m, 8H), 3.45–3.35 (m, 3H), 3.32–3.27 (m, 3H), 3.25–3.22 (m, 2H), 3.15–3.12 (m, 2H), 2.64 (s, 3H); ^{13}C NMR (75 MHz, CD_3OD) δ 198.94, 171.66, 149.45, 137.66, 130.84, 130.64, 130.49, 126.16, 125.68, 123.94, 116.04, 105.69, 98.84, 73.53, 72.89, 71.83, 70.14, 69.97, 69.84, 69.20, 65.36, 62.26, 61.23, 56.32, 46.92, 46.87, 38.80, 38.70, 25.08; HRMS(FAB^+) calcd for $C_{29}H_{44}N_3O_{10}$ $[M+H]^+$: 594.3021; found: 594.3020.

[2-(*N*-Boc-piperazinyl)]-2,3,4,6-tetra-*O*-benzoyl-a-D-glucoside (4): Compound **4** was prepared by a similar procedure used for the synthesis of **3** from **2**.[9] To a solution of (2-bromoethyl)-2,3,4,6-tetra-O-benzoyl-α-D-glucoside **2** (230 mg, 0.327

mmol) in 2 mL anhydrous DMF, *N*-Boc-piperazine (183 mg, 0.981 mmol) and TEA (182 μL, 1.308 mmol) were added, and the reaction mixture was stirred at 50 °C. After the completion of reaction monitored by thin-layered chromatography (TLC), the resulting solution was diluted with ddH_2O, and extracted trice with ethyl acetate. The combined organic layer was washed with brine and dried under anhydrous $MgSO_4$. The filtrate was condensed under reduced pressure and the desired product **4** was purified by silica-gel flash column chromatography (n-hexane : ethyl acetate = 2 : 1 gradually changed to 1 : 2) as a yellowish oil (185 mg, 70%): ^{1}H NMR (500 MHz, $CDCl_3$) δ 8.05–7.86 (m, 8H), 7.57–7.28 (m, 12H), 6.18 (t, *J* = 10 Hz, 1H), 5.68 (t, *J* = 9.5 Hz, 1H), 5.43 (d, *J* = 3.5 Hz, 1H), 5.29 (dd, *J* = 10.0, 3.5 Hz, 1H), 4.63–4.59 (m, 1H), 4.49–4.45 (m, 2H), 3.89 (ddd, *J* = 11.0, 5.5, 5.0 Hz, 1H), 3.67 (ddd, *J* = 11.0, 6.0, 5.0 Hz, 1H), 3.23 (bs, 4H), 2.65–2.58 (m, 2H), 2.35 (bs, 4H), 1.44 (s, 9H); ^{13}C NMR (125 MHz, $CDCl_3$) δ 166.62, 166.30, 166.16, 165.78, 155.11, 133.99, 133.92, 133.64, 130.33, 130.20, 130.16, 130.13, 129.62, 129.44, 129.34, 128.97, 128.90, 128.78, 96.38, 96.32, 80.01, 72.42, 70.88, 70.00, 68.73, 66.73, 63.51, 57.92, 53.87, 28.91; LC/MS calcd for $C_{45}H_{49}N_2O_{12}$ $[M+H]^+$: 809; found: 809.

Synthesis of AG2. AG2 was prepared by a similar procedure used for the synthesis of **AG1**. The crude product was purified by prep-HPLC to afford 13 mg (86 %) of **AG2**. ^{1}H NMR (300 MHz, CD_3OD) δ 8.41 (s, 1H), 7.89–7.83 (m, 2H), 7.64 (d, *J* = 8.0 Hz, 1H), 7.21 (dd, *J* = 9.3, 2.3 Hz, 1H), 6.98 (s, 1H), 4.92 (d, *J* = 3.6 Hz, 1H), 4.54 (s, 2H), 4.18–4.07 (m, 2H), 3.88–3.83 (m, 3H), 3.71–3.43 (m, 10H), 3.35–3.32 (m, 2H), 3.17 (s, 4H), 2.65 (s, 3H); ^{13}C NMR (75 MHz, CD_3OD) δ 198.96, 168.82, 149.77, 137.84, 130.54, 130.47, 125.98, 125.38, 123.76, 115.87, 105.28, 98.93, 73.49, 73.10, 71.72, 70.01, 61.23, 60.47, 56.01, 52.92, 38.41, 25.01; HRMS(FAB$^+$) calcd for

$C_{27}H_{38}N_3O_8[M+H]^+$: 532.2653; found, 532.2652.

Reference

[1] D. Thomas, S. C. Tovey, T. J. Collins, M. D. Bootman, M. J. Berridge, P. Lipp, *Cell Calcium* **2000**, *28*, 213.

[2] R. Rudolf, M. Mongillo, R. Rizzuto, T. Pozzan, *Nat. Rev. Mol. Cell Biol.* **2003**, *4*, 579.

[3] W. R. Zipfel, R. M. Williams, W. W. Webb, *Nat. Biotechnol.* **2003**, *21*, 1369.

[4] F. Helmchen, W. Denk, *Nat. Methods* **2005**, *2*, 932.

[5] R. M. Williams, W. R. Zipfel, W. W. Webb, *Curr. Opin. Chem. Biol.* **2001**, *5*, 603.

[6] H. M. Kim, B. H. Jeong, J. Y. Hyon, M. J. An, M. S. Seo, J. H. Hong, K. J. Lee, C. H. Kim, T. Joo, S. C. Hong, B. R. Cho, *J. Am. Chem. Soc.* **2008**, *130*, 4246.

[7] H. M. Kim, C. Jung, B. R. Kim, S. Y. Jung, J. H. Hong, Y. G. Ko, K. J. Lee, B. R. Cho, *Angew. Chem. Int. Ed.* **2007**, *46*, 3460.

[8] H. M. Kim, B. R. Kim, J. H. Hong, J. S. Park, K. J. Lee, B. R. Cho, *Angew. Chem. Int. Ed.* **2007**, *46*, 7445.

[9] H. M. Kim, M. S. Seo, M. J. An, J. H. Hong, Y. S. Tian, J. H. Choi, O. Kwon, K. J. Lee, B. R. Cho, *Angew. Chem. Int. Ed.* **2008**, *47*, 5167.

[10] H. M. Kim, M. J. An, J. H. Hong, B. H. Jeong, O. Kwon, J. Y. Hyon, S. C. Hong, K. J. Lee, B. R. Cho, *Angew. Chem. Int. Ed.* **2008**, *47*, 2231.

[11] J. Czernin, M. E. Phelps, *Annu. Rev. Med.* **2002**, *53*, 89.

[12] C. Xu, W. W. Webb, *J. Opt. Soc. Am. B* **1996**, *13*, 481.

[13] M. Murata, M. Akao, B. O'Rourke, E. Marban, *Circ. Res.* **2001**, *89*, 891.

[14] J. Park, H. Y. Lee, M. H. Cho, S. B. Park, *Angew. Chem. Int. Ed.* **2007**, *46*, 2018.

[15] M. Zhang, Z. Zhang, D. Blessington, H. Li, T. M. Busch, V. Madrak, J. Miles, B. Chance, J. D. Glickson, G. Zheng, *Bioconjugate Chem.* **2003**, *14*, 709.

[16] K. Yamada, M. Nakata, N. Horimoto, M. Saito, H. Matsuoka, N. Inagaki, *J. Biol. Chem.* **2000**, *275*, 22278.

[17] R. G. O'Neil, L. Wu, N. Mullani, *Mol. Imaging Biol.* **2005**, *7*, 388.

[18] L. D. Zinkin, *Dis. Colon Rectum* **1983**, *26*, 37.

[19] J. L. Kovar, W. Volcheck, E. Sevick-Muraca, M. A. Simpson, D. M. Olve, *Anal. Biochem.* **2009**, *384*, 254.

[20] *The Handbooks—A Guide to Fluorescent Probes and Labeling Techonologies* (Ed.: R. P. Haugland), 10th ed., Molecular Probes, Eugene, OR, 2005.

Chapter 5. Fluorescent Probe for Detection of Fluoride in Water and Bioimaging in A549 Human Lung Carcinoma Cells

- *Chem. Commun*. **2009**, 4735

Introduction

Fluoride ions are widely used as an essential ingredient in toothpaste and pharmaceutical agents and are even added to drinking water owing to their tendency to prevent dental caries[1] and enamel demineralization resulting from wearing orthodontic appliances; they are also used for the treatment of osteoporosis.[2] However, a high intake of fluoride may cause fluorosis,[3] and also lead to nephrotoxic changes[4] and urolithiasis in humans.[5] In molecular and cell biology, NaF is known to influence various cell signaling processes [6] and to induce apoptosis at high concentrations for 24 h in mammalian cells.[7] For these reasons, considerable effort has been devoted to the development of novel methods for the detection of fluorides, particularly NaF.[8,9] In fact, the development of receptor -based sensors for the detection of fluoride ions is challenging owing to the small size, high electronegativity, and high hydration enthalpy of fluoride ion. Therefore, while most chemosensors recognizefluoride ions in a tetrabutylammonium fluoride (TBAF) salt in organic solvents,[8] only a few can detect fluoride ions, as in NaF, in aqueous solutions.[9] Recently, Gabbaï successfully demonstrated a borane-based fluoride receptor working in DMSO–H_2O (4 : 6, v/v).[9a] Swager, Yang and their co-workers also developed fluoride-detecting systems based on a coumarin moiety performing in organic solvents such as THF, CH_2Cl_2 or in acetone–water (7 : 3, v/v) through Si–O bond cleavage.[8e,9d] However, none of the fluoride chemosensors meet the requirements for biological applications, which are as

follows; (1) to be able to selectively detect fluoride ions in 100% water, (2) to be capable of permeating the cell membrane , (3) to be non-toxic and display fluorescence upon the detection of fluoride ions in cellular systems. To the best of our knowledge, no fluoride chemosensors or probes satisfying the above-mentioned requirements have been reported.

Results and Discussion

In an effort to address these issues for biological applications, we have explored the possibility of developing a novel fluoride chemodosimeter in water. As part of previous contributions to the development of chemodosimeters,[8b,e,f,9] we recently demonstrated a resorufin-based chemodosimeter incorporating a *tert*-butyldiphenylsilyl (TBDPS) moiety for the detection of fluoride anions, with high selectivity in aqueous solution.[9b] However, our initial attempt to apply the resorufin -based system for the detection of fluoride ion in 100% water failed due to its poor solubility in water.

In our endeavour to develop a fluoride sensor in water, we moved forward to design a new fluoride detection system working under physiological conditions. In order to improve the water solubility, we planned to downsize our sensor system and introduce hydrophilic moieties. This analysis led us to design a 7-hydroxycoumarin-based system containing a *tert*-butyldimethylsilyl (TBDMS) moiety, TBMCA (1, *tert*-butyldimethylsilyl 7-hydroxycourmarin-4-acetic acid methyl ester), based on a previous approach.[9b] In addition, we introduced a methyl ester group to 4-acetic acid on the fluorescent coumarin moiety to increase water solubility and to enhance cell permeability as well as to detain the fluorophore inside the cell after hydrolysis by using a negatively charged carboxylate group.[10] TBMCA was prepared

by silyl protection of 7-hydroxycoumarin-4-acetic acid methyl ester with TBDMSCl and imidazole in anhydrous DMF.[11] 7-Hydroxycoumarin-4-acetic acid methyl ester was synthesized in accordance with a known procedure.[12] Unfortunately, the fluorescence intensity of TBMCA immediately showed strong enhancement upon the exposure to phosphate buffered saline (PBS) (Figure S4 in the Supporting Information). In addition, the fluorescence intensity of TBMCA was increased only 1.2-fold after treatment of 1 mM NaF for 3 h in PBS (Figure S1 and S4 in the Supporting Information), which is consistent with a previous report.[9d] We initially conjectured that the strong enhancement of fluorescence intensity in PBS was due to the instability of the TBDMS moiety in TBMCA. However, the fluorescence intensity of TBMCA was barely changed in PBS over a 24 h period (Figure S2 in the Supporting Information). Then, we examined fluorescence emission changes of TBMCA as a function of solvent polarity and observed increased fluorescence intensity of TBMCA in accordance with increased polarity of solvent (Figure S3 and S4 in the Supporting Information). Based on this observation, we postulated that the covalent bond character of the Si–O bond of TBMCA is much weaker in water, due to its interaction with water molecules, which renders mimicking the intramolecular charge transfer (ICT) events *via* stronger Si–O bond polarization and leads to turn-on of fluorescence in water without actual desilylation. Consequently, there was only a marginal enhancement of fluorescence when TBMCA was treated with fluoride anion in water (Figure S1 in the Supporting Information). Therefore, we decided to replace TBDMS (dimethyl) moiety with a bulkier TBDPS (diphenyl) moiety to reduce the accessibility of water molecules to the silicon atom.

TBPCA (2, *tert*-butyl diphenyl silyl 7-hydroxy courmarin-4-acetic acid methyl ester) was prepared using TBDPSCl by the same procedure as that

for TBMCA. TBPCA was prepared for the selective turn-on of quenched fluorescence by an ICT mechanism when 7-hydroxycoumarin 3 was released upon the attack of fluoride ion on the silyl ether moiety (Scheme 1). The fluorescence intensity of TBPCA is also affected by the solvent polarity, but significantly less than that of TBMCA (Figure S3 and S4 in the Supporting Information). In terms of sensitivity toward fluoride ion, we observed more than 4-fold enhancement of fluorescence intensity of TBPCA after treatment of 1 mM NaF for 3 h in PBS (Figure S1 in the Supporting Information). Therefore, we selected TBPCA as a fluoride sensor with excellent properties for the application in physiological conditions.

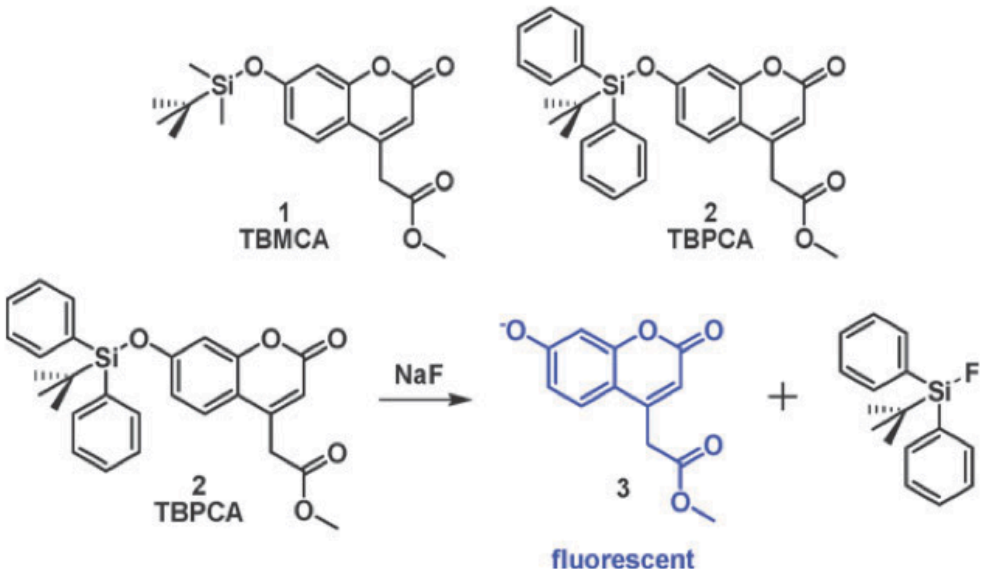

Scheme 1 Molecular structures of **TBMCA** and **TBPCA**, and the sensing mechanism of probe **TBPCA** for the detection of NaF.

The enhanced fluorescence intensity of TBMCA in water, but not in the case of TBPCA, is consistent with the computer-assisted rationalization with *ab initio* calculation and molecular modelling (see Supporting Information).[13] In fact, *ab initio* calculation intimates the importance of the electronic effect by the TBDPS and TBDMS group in polar solvents ; the Si–O polarity difference ($|\Delta Q|$ =

0.021 C) and the Si–O bond length difference (0.007 Å) of TBPCA between hexane and water were significantly smaller than those ($|\Delta Q|$ = 0.103 C, 0.009 Å) of TBMCA. In addition, the water -accessible area on silicon atom of TBPCA was 0.23 $Å^2$, which is significantly smaller than that (1.67 $Å^2$) of TBMCA, as calculated by molecular modelling software, Naccess, which means that the Si–O bond of TBMCA is quite accessible to water. These results also support our initial rationale above.

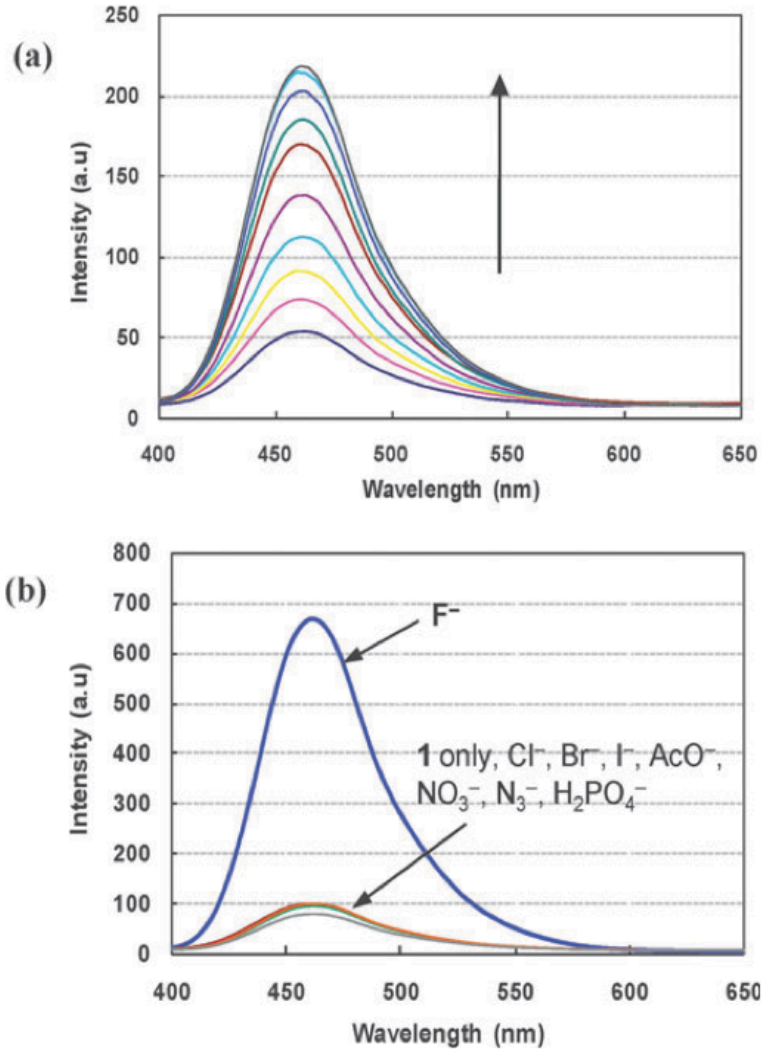

Figure 1. (a) Fluorescence emission change of **TBPCA** (2 μM) recorded 4 h after reaction with various concentrations of NaF (0–1.3 mM) in 10 mM HEPES buffer (pH 7.4) at 25 °C. (b) Comparison of fluorescence emission intensity of **TBPCA** (2 μM) after 4 h for various sodium salts (1 mM) in 10 mM HEPES buffer (pH 7.4) at 25 °C (blue line represents NaF).

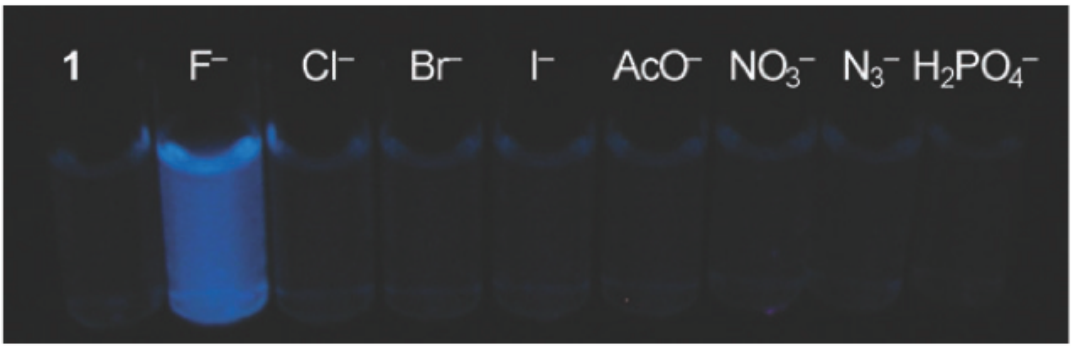

Figure 2. Optical changes in fluorescence emission of **TBPCA** (2 μM) when **TBPCA** is excited by UV irradiation (λ_{ex}: 365 nm) after 4 h for various sodium salts (1 mM) in 10 mM HEPES buffer (pH 7.4) at 25 °C. Left to right: **TBPCA**, F^-, Cl^-, Br^-, I^-, AcO^-, NO_3^-, N_3^-, $H_2PO_4^-$ (sodium salts).

We confirmed the linearity of the fluorescence emission intensity (λ_{em}: 461 nm) of TBPCA (2 μM) relative to fluoride concentrations in HEPES buffer at 25 °C (Figure 1A). On the basis of this calibration curve at 461 nm, the concentration of NaF can be confidently predicted by measuring the fluorescence emission of TBPCA. Even though fluoride anions have high selectivity and affinity towards the silicon atoms of TBDPS, it is difficult to overcome the strong hydration effect of fluoride in aqueous environments; therefore, an extended incubation time is required for the consistent determination of fluoride concentration through sufficient reaction of fluoride ions with TBPCA.[9b] For instance, the fluorescence emission intensity of TBPCA was maximized only 4 h after exposure to 1 mM NaF in the HEPES buffer at 25 °C (Figure S6 in the Supporting Information). The selectivity of TBPCA for F^- was confirmed by treatment of various anions (1 mM) as sodium salts such as Cl^-, Br^-, I^-, AcO^-, NO_3^-, N_3^-, $H_2PO_4^-$. As shown in Figure 1B, only NaF can efficiently exhibit fluorescence emission (λ_{ex}: 375 nm) and the fluorescence intensity in the case of NaF is more than seven times that produced in the case of the other anions. Figure 2 clearly shows the difference between the optical image

of TBPCA in the presence of NaF and UV light (λ_{ex}: 365 nm) and the optical image in the presence of other anions. Finally, we examined whether TBPCA can influence the cell viability in mammalian cells. After the treatment of the A549 human epithelial lung carcinoma cell line with TBPCA (20 μM) for 24 h, there was no reduction in the cell viability: the cell viability was measured by considering the mitochondrial function using Cell Counting Kit-8 (CCK8),[14] and this result indicates the possibility of using TBPCA for bioimaging live cells in aqueous media.[15]

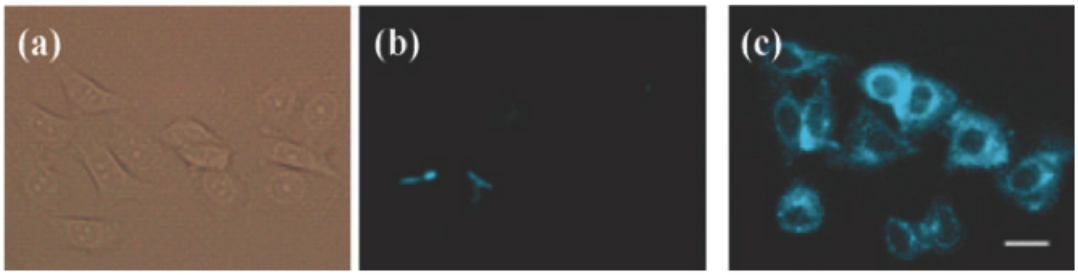

Figure 3 Brightfield image and fluorescence cell images of A549, human epithelial lung carcinoma. (a) Bright-field image of A549 cells incubated with **TBPCA** (20 μM) for 30 min and subsequently incubated for 3 h at 37 °C. (b) Fluorescence image of A549 incubated with **TBPCA** (20 μM) for 30 min and subsequently incubated without NaF for 3 h at 37 °C. (c)Fluorescence image of A549 cells incubated with **TBPCA** (20 μM) for 30 min and subsequently treated with 50 mM NaF for 3 h at 37 °C. The scale bar represents 20 μm.

TBPCA fulfills the requirements for displaying fluorescence in *in vitro* cell imaging: it can be retained in a cell, it is non-cytotoxic, and it can exhibit fluorescence upon sensing the appropriate physiological conditions. On the basis of these properties of **TBPCA**, which indicate that this probe is a selective chemodosimeter for fluoride anions, we explored the possibility of its use in biological systems by its application to A549 human lung carcinoma cell lines. The addition of 50 mM NaF to A549 cells loaded with **TBPCA** (20 μM) leads to a significant increase in the fluorescence intensity as compared to control experiments (Figure 3B and 3C). Due to the slow rate of this reaction, the **TBPCA**-loaded A549 cells with NaF have to be incubated for 3 h at 37 °C to obtain the maximum

fluorescence intensity; incubation for more than 3 h causes the deterioration of the fluorescence signal.

To take advantage of the chemodosimeter, **TBPCA** was also used for the quantification of fluoride ions in the cells. After 3 h incubation of the A549 cells with NaF (50 mM) under the physiological conditions, the cells were harvested and thoroughly washed. The harvested cells were sonicated and centrifuged for the preparation of cell lysate in PBS buffer. The resulting lysate was treated with **TBPCA** (2 μM) for 4 h at 25 °C to quantify the fluoride ions in the cell lysates; the quantification was performed on the basis of the fluorescence intensity and a standard curve prepared with NaF-doped cell lysates. This new quantification method reveals that 1.86×10^{-2} pmol fluoride anion is present in the cytoplasm per cellunder physiological conditions (Figure S12 in the Supporting Information).

Conclusion

In conclusion, we have successfully developed **TBPCA** as a fluoride ion probe for fluorescence cell bioimaging with desired properties, such as the detaining of the fluorophore inside a cell , non-cytotoxicity to mammalian cells , fluorescence upon sensing, appreciable solubility in water, and stoichiometric reaction with analytes . We also demonstrated fluorescence cell bioimaging using **TBPCA** for the detection of NaF in A549 human epithelial lung cancer cells under physiological conditions. Moreover, **TBPCA** can be utilized for the quantification of fluoride ions in living systems.

Supporting Information

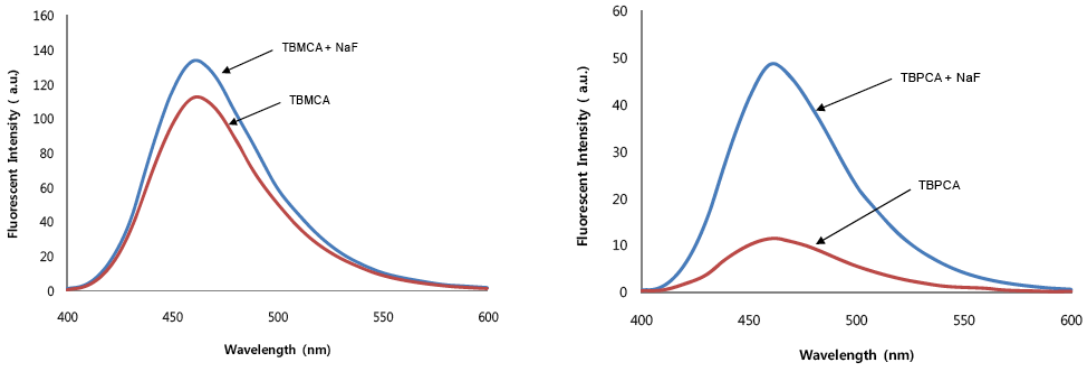

Figure S1. The fluorescence emission changes (ex: 375 nm) of left: **TBMCA** (2 μM) and right: **TBPCA** (2 μM) after the treatment of 1 mM NaF for 3 h in 10 mM PBS buffer (pH = 7.4) at 25 °C.

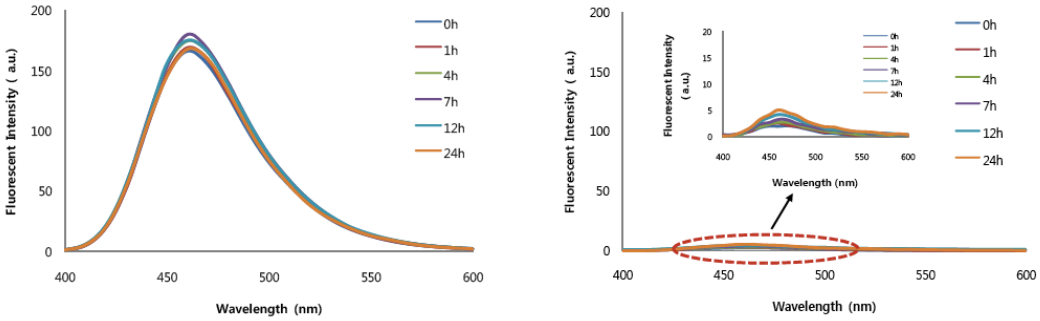

Figure S2. Fluorescence emission change (ex: 375 nm) in the case of **TBMCA** (2 μM, left panel) and **TBPCA** (2 μM, right panel) over 24-h period in 10 mM PBS buffer (pH = 7.4) at 25 °C. This data confirm that the Si-O bond itself was not influenced by the extended exposure to PBS.

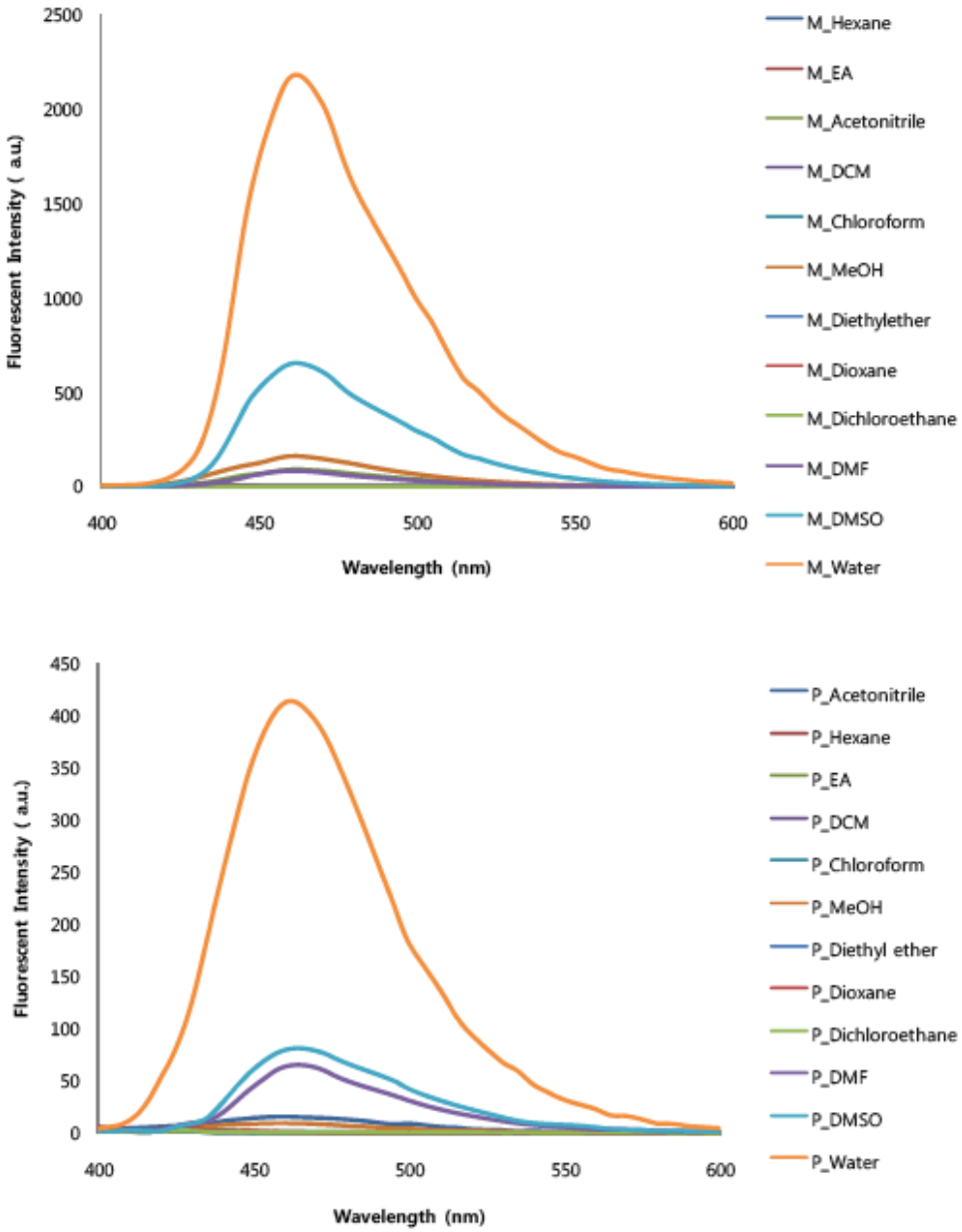

Figure S3. The fluorescence emission change (ex: 375 nm) in the case of **TBMCA** (2 μM, top panel) and **TBPCA** (2 μM, bottom panel) in accordance with solvent polarity.

Figure S4. Optical change in fluorescence emission of **TBMCA** (2 μM) and **TBPCA** (2 μM) excited by UV irradiation (ex: 365 nm) according to the solvent polarity.(left panel) Comparison of optical change in fluorescence emission of **TBMCA** and **TBPCA** excited by UV irradiation in the absence or presence of NaF (1 mM) after 3 h in PBS (right panel); 1: **TBMCA** in DMSO, 2: **TBMCA** in PBS, 3: **TBPCA** in DMSO, 4: **TBPCA** in PBS, 5: **TBMCA** in PBS, 6: **TBMCA** + NaF in PBS, 7: **TBPCA** in PBS, 8: **TBPCA** + NaF in PBS.

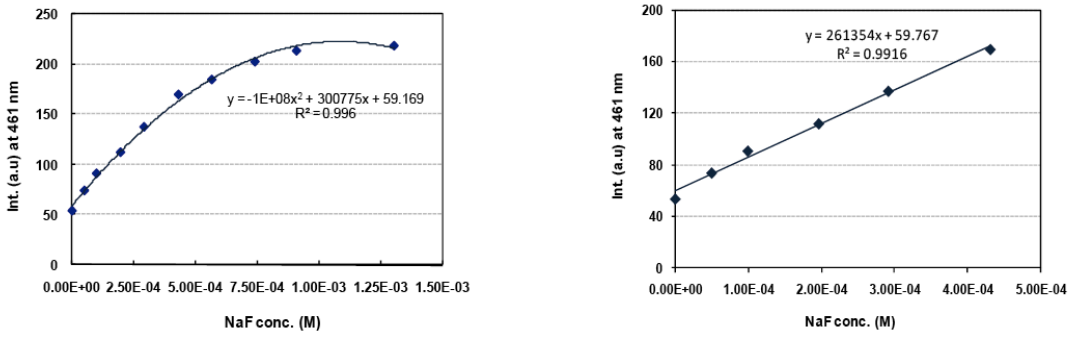

Figure S5. (Left) Fluorescence standard curve (λ_{em}: 461 nm) of **TBPCA** (2 μM) monitored after 4 h incubation according to NaF concentration in 10 mM HEPES buffer (pH = 7.4) at 25 °C. [NaF (equiv) = 0, 25, 50, 100, 150, 225, 300, 400, 500, 750]; (Right) Linear responses of **TBPCA** (2 μM) as a function of NaF concentration was observed ranging between 0 and 4.3×10^{-4} M. According to regression equation for fluorescence standard curve, detection limit was estimated to be 3.88×10^{-4} M.

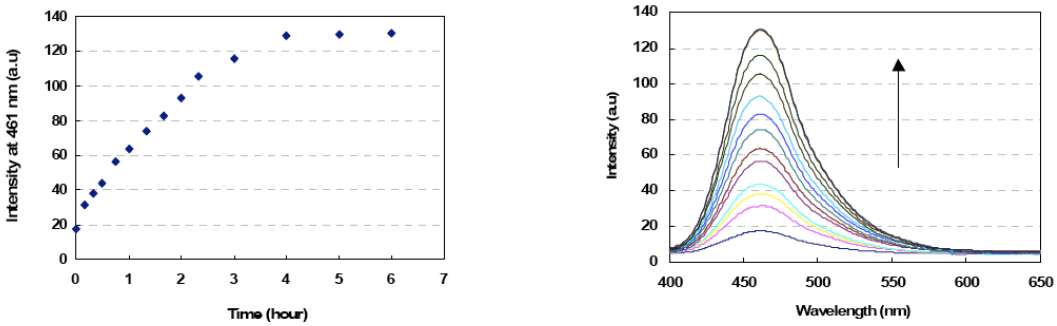

Figure S6. At 1 mM NaF, the fluorescence emission change (ex: 375 nm) of **TBPCA** (2 μM) with time in 10 mM HEPES buffer (pH = 7.4) at 25 °C. The fluorescence emission intensity of **TBPCA** (2 μM) was maximized at 4 h. [Time = 0, 10 min, 20 min, 30 min, 45 min, 1 h, 1 h 20 min, 1 h 40 min, 2 h, 2 h 30 min, 3 h, 4 h, 5 h, 6 h.]

Figure S7. Fluorescence optical change of **TBPCA** (2 μM) excited by UV lamp (ex: 365 nm) 4 h after the treatment with 1 mM NaF in 10 mM HEPES buffer (pH = 7.4) at 25 °C. Left: Only **TBPCA** (Fluorescence-OFF), Right: **TBPCA** + NaF (Fluorescence-ON).

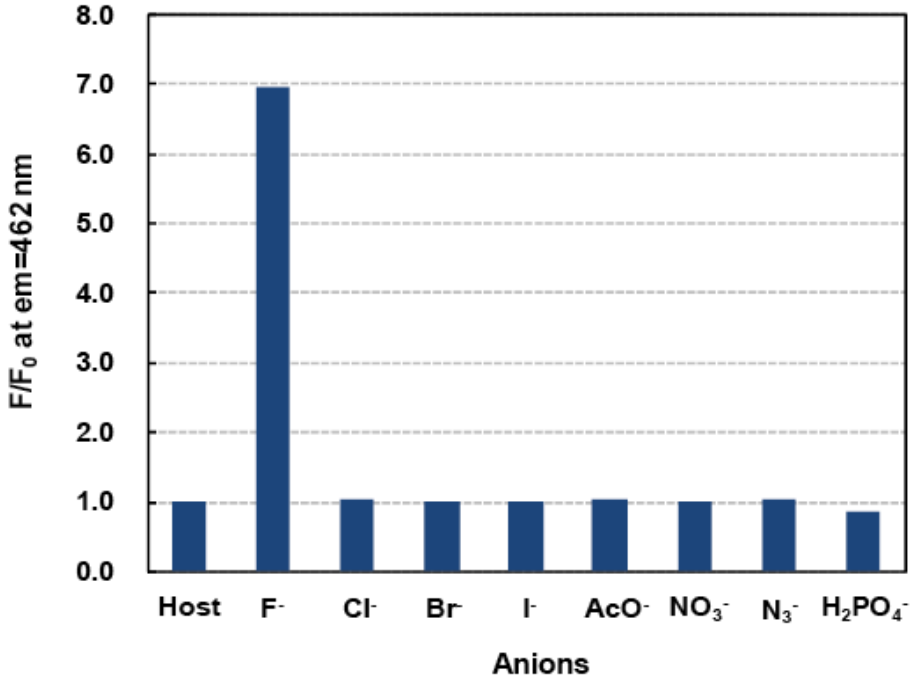

Figure S8. Comparison (F/F0 value) of the fluorescence emission changes (ex: 375 nm) of **TBPCA** (2 μM) 4 h after the treatment with various sodium salts (1 mM) in 10 mM HEPES buffer (pH = 7.4) at 25 °C. F_0: fluorescence emission intensity (em: 461 nm) of **TBPCA**, F: fluorescence emission intensity (em: 461 nm) of **TBPCA** for each sodium salts.

Cell culture: A549 human lung carcinoma cells were obtained from American Type Culture Collection [ATCC, Manassas, VA, USA]. A549 cells were cultured in RPMI 1640 [GIBCO, Invitrogen] supplemented with 10% (v/v) fetal bovine serum [GIBCO, Invitrogen] and 1 % (v/v) Antibiotic-Antimycotic solution [GIBCO, Invitrogen]. The cells were maintained in a humidified atmosphere of 5% CO2 and 95% air at 37°C, and cultured in T75 Flask [Nalgene Nunc International, Naperville, IN, USA] according to manufacturers' instruction. The growth medium was changed every two to three days. Cells were grown to confluence prior to the experiment.

Inverted Fluorescent Microscope for Fluorescent Imaging Protocol : Human lung carcinoma (A549) cells (1×10^4 cells/mL) were seeded on a Lab-Tek glass chamber

slide [Nalge Nunc International, Naperville, IN, USA] in 35 mm cell culture dish. After 24 h, cells were treated with **TBPCA** (20 μM) in RPMI 1640 for 1 h and washed two times with PBS (phosphate buffered saline) [Welgene, Korea]. Then, RPMI 1640 containing various concentrations of NaF was treated to cells for 3 h. Finally, the glass chamber slide was taken from culture dish and loaded on the fluorescent microscope [IX71, Olympus, Japan]. The fluorescent images were taken with blue filter (excitation: 380 nm, emission: >450 nm). Image analysis was performed in Image-pro plus 6.2 [Media Cybernetics, USA].

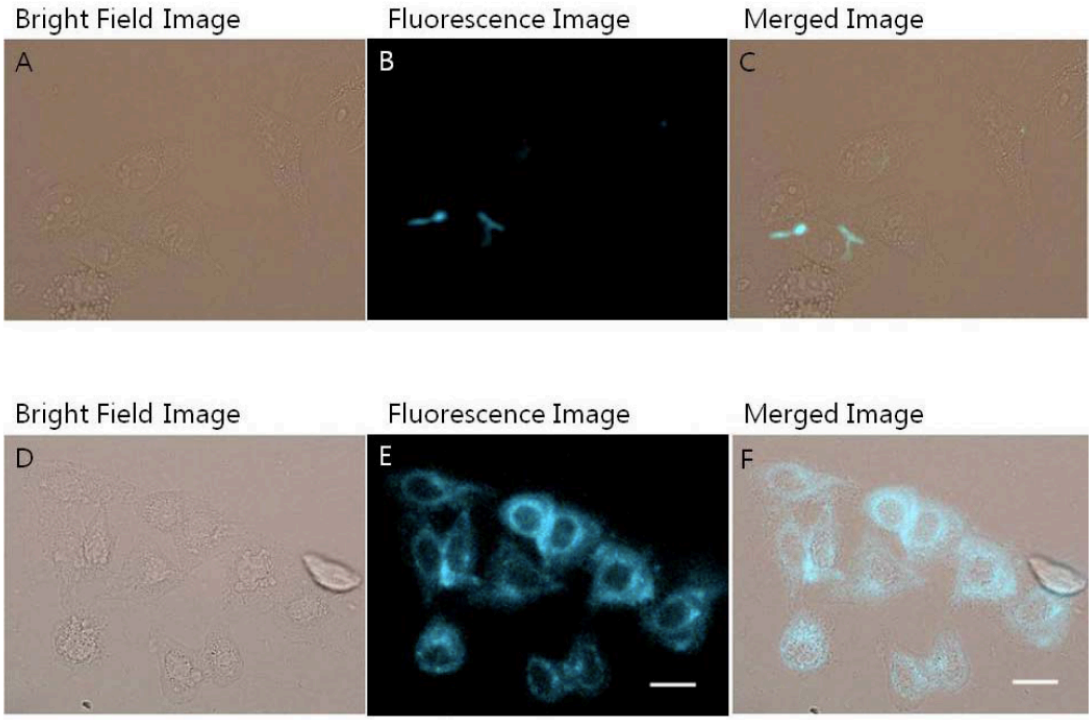

Figure S9. Bright-field image, fluorescence images, and merged images of A549, human epithelial lung carcinoma. Bright-field image (A), fluorescence image (B), and merged image (C) of A549 cells incubated with **TBPCA** (20 μM) for 30 min and subsequently incubated for 3 h at 37 °C. Bright-field image (D), fluorescence image (E), and merged image (F) of A549 incubated with **TBPCA** (20 μM) for 30 min and subsequently incubated with 50 mM NaF for 3 h at 37 °C. The scale bar represents 20 μm.

Cell viability test: Cell viability was measured to determine the cytotoxicity of our probe using the Cell Counting Kit (CCK)-8 assay [Dojindo, Tokyo, Japan], and the experimental procedure is based on the manufacturer's manual. Cells were cultured into 96-well plates at a density of 2 x 10^3 cells/well for 24 h, followed by the treatment of **TBPCA** (20 μM). After 24 h incubation with 20 μM of **TBPCA**, 10 μL of WST-8 solution (2-(2-methoxy-4-nitrophenyl)-3-(4-nitrophenyl)-5-(2,4-disulfophenyl)-2*H*-tetrazolium, monosodium salt) was added to each well, and plates were incubated for additional 2 h at 37 °C. The absorbance of each well at 450 nm was measured with a reference at 630 nm using a Bio-Tek model ELx800TM microplate reader [Bio-Tek Instruments, Inc., Winooski, VT, USA]. The percentage of cell viability was calculated by following formula: % cell viability = (mean absorbance in test wells) / (mean absorbance in control well) x 100. Each experiment was performed in triplicate experiments. Following data are the original cell viability assay.

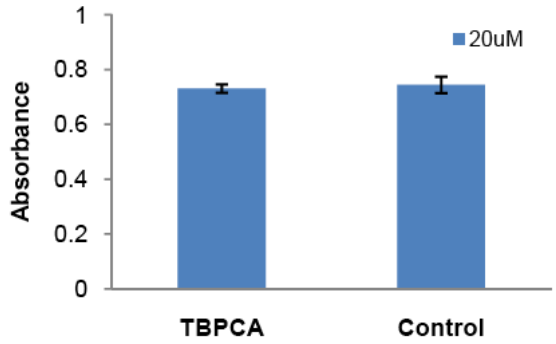

Figure S10. Comparison of the cell viability of **TBPCA** (20 μM) and control by CCK assay in human epithelial lung (A549) cell after 24 h at 37 °C.

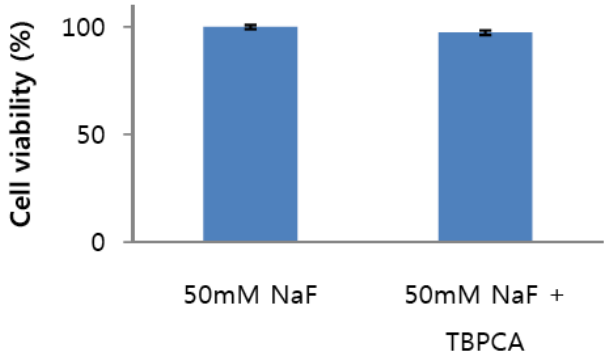

Figure S11. Comparison of the cell viability of **TBPCA** (20 μM) and control in the presence of 50mM NaF by CCK assay in human epithelial lung (A549) cell after 5 h at 37 °C.

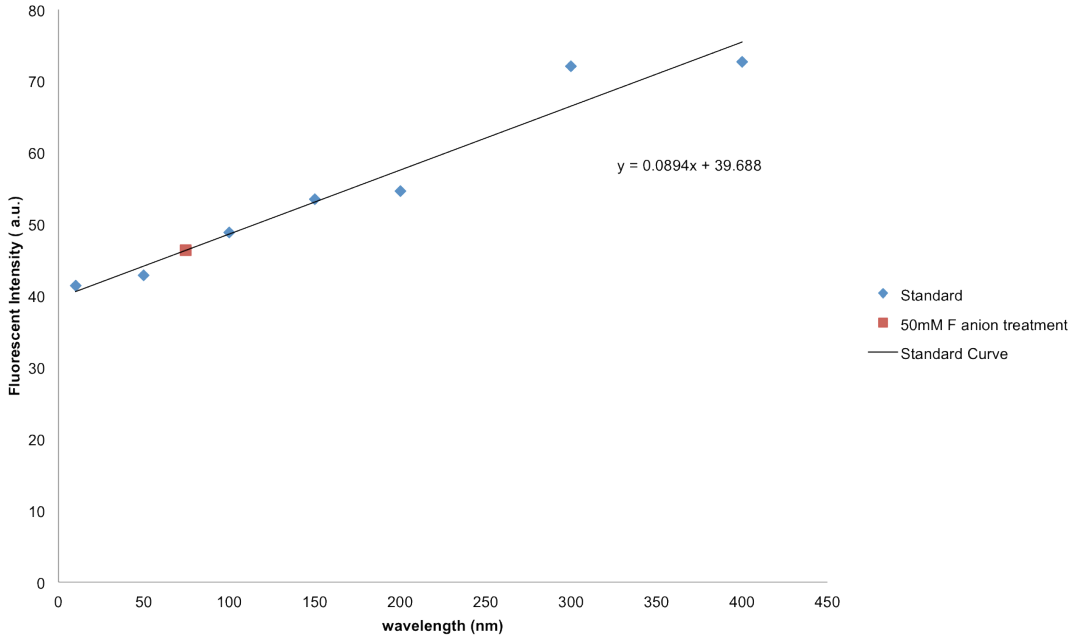

Figure S12. The standard curve (blue diamond) for the identification of fluoride anions in cytoplasm per cell (red square) under the physiological condition after the treatment of 50 mM NaF for 3 h.

Quantification of Fluoride Ions in Cells : A549 cells were cultured into 6-well plates at a density of 1 x 10^6 cells/well for 24 h. After 3 h incubation of the cells with NaF (50 mM) under the physiological conditions, the cells were harvested and thoroughly washed. At this stage, cell number was counted (2 x 10^6 cells). The harvested cells

were sonicated and centrifuged for the preparation of cell lysates in PBS buffer. The resulting supernatant in 500 μl PBS was treated with **TBPCA** (2 μM) for 4 h at 25 °C to quantify the fluoride ions in the cell lysates; the quantification was performed on the basis of the fluorescence intensity and a standard curve prepared with NaF-doped cell lysates. Fluorescent intensity was measured by Cary Eclipse Fluorescence spectrophotometer (Varian Assoc., Palo Alto, USA). A standard curve is obtained from raw data. Quantification of F^- ions in cellular cytoplasm per single cell was determinded from stardard curve and fluorescent intensity of 50 mM NaF treated cell lysates (46.34).

Ab initio Calculation: Theoretical calculation was carried out to compare covalent bond character of siliconoxygen bond in **TBMCA** and **TBPCA**. The geometry of each product is optimized by the Materials Studio 4.2® program. Electrostatic potential (ESP) charge was calculated for each atom by population analysis. Conductor-like screening model (COSMO) solvation procedure was adopted to generate two different solvent systems (water and n-hexane). The distance between oxygen 13 and silicon 14 was measured from resulted 3D coordinate of the optimized structures. All calculation was performed by the density functional theory at DND level. A generalized gradient approximation (GAA) for the exchange correlation function of Perdew, Burke, and Ernzerhof (PBE) was used with the double-numerical plus d-functions (DND) as implemented in DMol3. The resulting outcomes are summarized in Table S1. The variation of charge difference and bond length is larger in **TBMCA** than in the case of **TBPCA**. The silicon-oxygen bond on **TBMCA** is more flexible in different solvent system. We finally conclude that the covalent bond character of silicon-oxygen bond is stronger in **TBPCA** than in **TBMCA**.

	Absolute variation value of Si-O charge difference	Variation of Si-O bond length
TBPCA	0.021 C	0.007 Å
TBMCA	0.103 C	0.009 Å

Table S1. Comparison of variation of Si-O charge difference and bond length of **TBPCA** and **TBMCA** in two different solvation models (water and n-hexanes). (C: coulomb).

Calculation Input : All the *ab initio* calculations are performed under following condition, except the COSMO_Dielectric parameter, which depends on solvent system (water = 78.5400, n-hexane=1.8900).

```
# Task parameters
Calculate                     optimize
Opt_energy_convergence        2.0000e-005
Opt_gradient_convergence      4.0000e-003 A
Opt_displacement_convergence  5.0000e-003 A
Opt_iterations                50
Opt_max_displacement          0.3000 A
Symmetry                      on

# Electronic parameters


Spin_polarization             restricted
Charge                        0
Basis                         dnd
Pseudopotential               none
Functional                    pbe
Aux_density                   octupole
Integration_grid              medium
Occupation                    fermi
Cutoff_Global                 4.0000 angstrom
Scf_density_convergence       1.0000e-005
Scf_charge_mixing             0.2000
Scf_iterations                50
Scf_diis                      6 pulay
Cosmo                         ibs
COSMO_Dielectric              78.5400 or 1.8900
```

```
# Print options
Print                          eigval_last_it

# Calculated properties
Mulliken_analysis              charge
Hirshfeld_analysis             dipole
Esp_fit                        on
Frequency_analysis             on
```

Calculation Output :

TBPCA in water

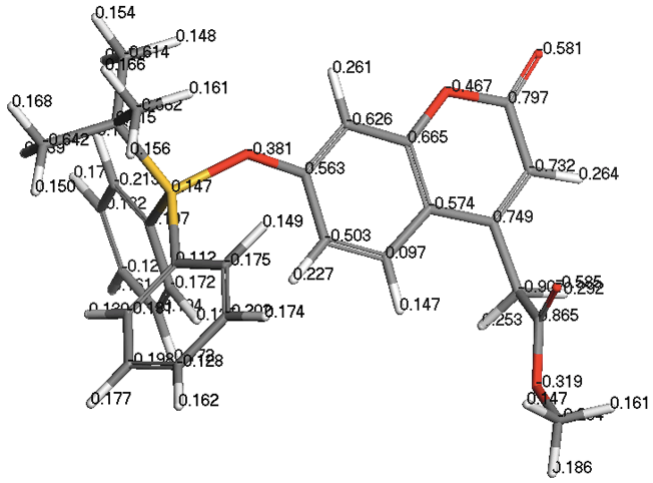

df		ATOMIC COORDINATES (au)			DERIVATIVES (au)		
df		x	y	z	x	y	z
df	C	0.637271	1.150411	2.090473	0.000419	-0.000513	-0.000207
df	C	2.064971	0.052627	0.121739	-0.000277	0.000594	0.000183
df	C	4.589865	0.689069	-0.187678	0.000020	-0.000064	0.000388
df	C	5.800001	2.438718	1.421651	0.000232	-0.000017	-0.000589
df	C	4.321972	3.509936	3.375045	-0.000432	0.000122	0.000088
df	C	1.787454	2.890407	3.722824	0.000334	0.000038	0.000217
df	O	5.325754	5.235643	5.037533	0.000278	0.000068	-0.000040
df	C	7.851465	6.018519	4.875819	0.000006	-0.000307	0.000117
df	C	9.357960	4.908462	2.899671	-0.000285	0.000416	-0.000532
df	C	8.416279	3.172487	1.234600	0.000165	0.000057	0.000608
df	O	8.544548	7.580069	6.445406	-0.000158	0.000097	-0.000070
df	C	10.087215	2.039269	-0.765245	-0.000457	-0.000426	-0.000453
df	C	10.760941	-0.711177	-0.265114	0.000393	0.000211	0.000239
df	O	11.375505	-1.888410	-2.444192	-0.000070	0.000026	0.000037
df	C	12.174741	-4.509554	-2.183826	0.000009	-0.000082	-0.000081
df	O	10.802664	-1.719133	1.811707	-0.000103	-0.000247	-0.000112
df	O	-1.823622	0.571304	2.534594	0.000006	0.000081	0.000319
df	Si	-4.215418	-0.232077	0.499394	0.000190	-0.000102	-0.000438
df	C	-7.111439	-0.140282	2.666046	-0.000258	0.000120	-0.000234
df	C	-7.278029	2.339314	4.189497	0.000318	0.000228	0.000137
df	C	-6.886686	-2.345244	4.565917	-0.000066	-0.000034	0.000096
df	C	-9.531273	-0.507642	1.085787	0.000001	-0.000150	0.000111
df	C	-4.226052	2.053704	-2.249828	-0.000332	-0.000288	0.000121
df	C	-3.641369	-3.545754	-0.690350	-0.000430	-0.000190	0.000098
df	C	-2.687737	1.592698	-4.381909	-0.000241	0.000194	-0.000068
df	C	-2.562544	3.312144	-6.388765	0.000077	0.000118	0.000050
df	C	-3.990494	5.535608	-6.322688	0.000439	-0.000114	0.000260

df	C	-5.544048	6.027423	-4.239215	-0.000215	-0.000076	-0.000402
df	C	-5.643301	4.312713	-2.226421	-0.000016	0.000129	0.000242
df	C	-2.111213	-5.253384	0.670546	0.000129	0.000003	-0.000215
df	C	-1.793441	-7.752714	-0.136704	-0.000140	-0.000046	0.000320
df	C	-3.015015	-8.607227	-2.324962	0.000129	0.000138	-0.000478
df	C	-4.547498	-6.946171	-3.698286	-0.000066	-0.000108	0.000530
df	C	-4.854384	-4.444998	-2.886806	0.000316	0.000046	0.000032
df	H	1.198567	-1.330734	-1.140648	-0.000043	0.000061	-0.000193
df	H	5.646958	-0.195509	-1.725214	0.000012	-0.000087	0.000012
df	H	0.701596	3.765195	5.246145	-0.000147	0.000023	0.000009
df	H	11.329729	5.514160	2.825664	-0.000009	-0.000140	0.000100
df	H	11.892772	3.081297	-0.843287	0.000040	-0.000074	0.000091
df	H	9.230479	2.208216	-2.655651	-0.000029	0.000069	0.000032
df	H	13.891581	-4.619855	-1.019081	0.000099	-0.000024	0.000080
df	H	12.558816	-5.149845	-4.116305	0.000022	-0.000046	-0.000153
df	H	10.654872	-5.633604	-1.322505	-0.000203	0.000009	0.000074
df	H	-8.833601	2.182310	5.578996	0.000112	-0.000100	0.000059
df	H	-7.686152	3.994845	2.997264	-0.000404	-0.000025	-0.000059
df	H	-5.519807	2.712668	5.240851	0.000039	0.000017	-0.000198
df	H	-6.835780	-4.198880	3.614347	-0.000033	-0.000010	-0.000056
df	H	-8.551009	-2.325727	5.832946	-0.000004	-0.000009	-0.000093
df	H	-5.184648	-2.174783	5.758880	-0.000039	0.000151	0.000091
df	H	-9.490021	-2.289150	-0.000147	0.000113	0.000047	-0.000084
df	H	-9.845434	1.058707	-0.254626	-0.000059	0.000058	0.000018
df	H	-11.188075	-0.590347	2.360236	0.000069	0.000029	-0.000003
df	H	-1.566702	-0.142006	-4.497708	0.000309	0.000041	0.000090
df	H	-1.349487	2.906676	-8.015423	0.000111	-0.000052	-0.000123
df	H	-3.906366	6.874549	-7.897764	-0.000051	-0.000017	-0.000196
df	H	-6.674324	7.759376	-4.167171	0.000041	0.000076	0.000071
df	H	-6.856095	4.764972	-0.617851	-0.000067	0.000058	0.000164
df	H	-1.145949	-4.629234	2.393950	0.000081	0.000068	0.000062
df	H	-0.591828	-9.037938	0.950503	-0.000035	0.000059	-0.000028
df	H	-2.765920	-10.561205	-2.959936	0.000052	-0.000063	0.000009
df	H	-5.498914	-7.593361	-5.419178	0.000099	-0.000047	-0.000126
df	H	-6.050304	-3.177553	-4.003548	0.000008	0.000006	0.000076

TBPCA in n-Hexane

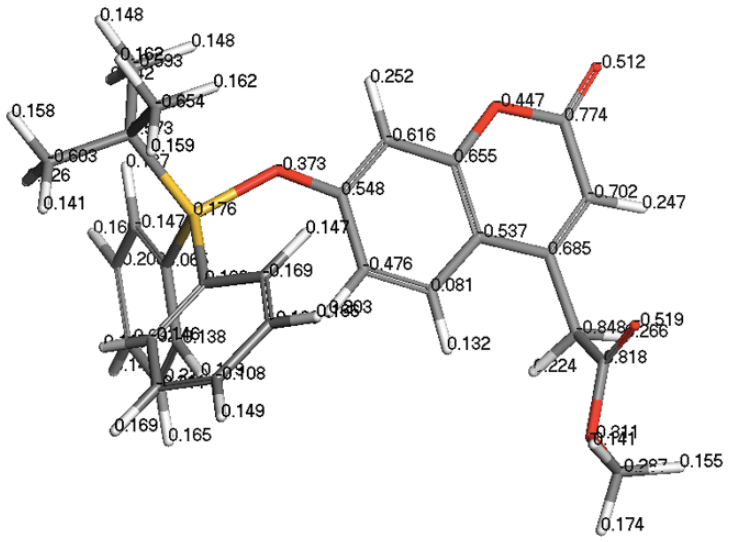

df		ATOMIC COORDINATES (au)			DERIVATIVES (au)		
df		x	y	z	x	y	z
df	C	0.636577	1.119613	2.176827	-0.000223	-0.000284	0.000106
df	C	2.072203	0.161399	0.142631	0.000079	0.000050	0.000049
df	C	4.600982	0.818780	-0.095289	-0.000087	0.000069	-0.000033
df	C	5.807756	2.420314	1.662432	0.000083	-0.000101	0.000090
df	C	4.323570	3.353712	3.680370	-0.000144	0.000306	-0.000194
df	C	1.781631	2.715994	3.947897	0.000030	0.000141	-0.000043
df	O	5.308377	4.937466	5.473954	0.000196	-0.000515	0.000379
df	C	7.840100	5.769957	5.375463	-0.000087	0.000157	-0.000246
df	C	9.351914	4.797407	3.319033	0.000064	0.000114	0.000052
df	C	8.420947	3.191476	1.527611	0.000032	-0.000071	-0.000161
df	O	8.521196	7.224594	7.027415	-0.000057	0.000101	-0.000085
df	C	10.082505	2.271979	-0.588593	-0.000134	0.000066	0.000180
df	C	10.785325	-0.512240	-0.379847	0.000097	0.000095	0.000234
df	O	11.039629	-1.547446	-2.719858	-0.000032	-0.000073	-0.000166
df	C	11.845820	-4.168615	-2.732643	0.000030	0.000012	-0.000095
df	O	11.136123	-1.655091	1.584350	-0.000048	-0.000011	-0.000135
df	O	-1.835103	0.526707	2.559096	0.000187	0.000105	-0.000341
df	Si	-4.159627	-0.261296	0.467033	-0.000220	0.000035	0.000099
df	C	-7.131078	-0.120754	2.531519	-0.000157	0.000079	-0.000103
df	C	-7.329345	2.367372	4.032739	0.000023	-0.000008	0.000110
df	C	-7.004409	-2.318590	4.447381	0.000055	-0.000130	0.000143
df	C	-9.491000	-0.454156	0.860385	0.000126	-0.000030	0.000183
df	C	-4.061827	1.992314	-2.309104	0.000096	-0.000010	-0.000051
df	C	-3.620599	-3.607757	-0.652685	0.000049	-0.000013	-0.000196
df	C	-2.908345	1.288346	-4.608735	0.000154	0.000227	0.000193
df	C	-2.767059	2.961630	-6.652650	0.000024	-0.000069	-0.000178
df	C	-3.774967	5.395002	-6.443312	-0.000109	0.000055	0.000080

df	C	-4.916199	6.143212	-4.178674	0.000159	-0.000074	-0.000136
df	C	-5.049749	4.463869	-2.143116	-0.000139	-0.000074	0.000133
df	C	-2.093093	-5.278227	0.753652	-0.000059	0.000011	0.000125
df	C	-1.817876	-7.809967	0.045094	0.000121	-0.000007	0.000044
df	C	-3.075410	-8.731004	-2.092820	-0.000135	0.000047	0.000048
df	C	-4.601761	-7.109083	-3.514053	0.000085	-0.000149	0.000048
df	C	-4.872075	-4.576992	-2.797832	0.000078	0.000067	0.000023
df	H	1.200558	-1.103861	-1.235877	-0.000033	0.000046	-0.000017
df	H	5.675807	0.057237	-1.687355	0.000026	-0.000050	0.000083
df	H	0.688454	3.470446	5.528913	0.000023	0.000020	-0.000011
df	H	11.316389	5.428855	3.288290	-0.000081	-0.000114	-0.000007
df	H	11.877530	3.334586	-0.570748	-0.000035	-0.000002	0.000001
df	H	9.203762	2.620083	-2.444706	-0.000003	-0.000061	-0.000056
df	H	13.741880	-4.343788	-1.899742	-0.000036	-0.000021	-0.000025
df	H	11.869210	-4.720911	-4.729851	-0.000040	-0.000015	0.000054
df	H	10.505597	-5.341616	-1.662339	-0.000037	-0.000034	-0.000024
df	H	-8.980882	2.267480	5.313676	-0.000059	0.000029	-0.000059
df	H	-7.615560	4.024624	2.808033	0.000072	0.000008	-0.000043
df	H	-5.638002	2.703849	5.199187	-0.000071	-0.000044	0.000037
df	H	-6.971423	-4.178233	3.508348	-0.000011	0.000005	0.000015
df	H	-8.694819	-2.256781	5.678267	0.000042	0.000029	-0.000077
df	H	-5.326632	-2.181735	5.678793	0.000014	0.000017	0.000007
df	H	-9.460646	-2.264074	-0.177757	0.000006	0.000011	0.000038
df	H	-9.698248	1.087999	-0.528486	0.000012	-0.000033	-0.000036
df	H	-11.204489	-0.458423	2.060955	-0.000004	0.000032	-0.000054
df	H	-2.109570	-0.609158	-4.820240	0.000017	-0.000098	0.000049
df	H	-1.864957	2.358882	-8.415526	-0.000047	0.000033	0.000026
df	H	-3.671125	6.707190	-8.039336	0.000048	0.000014	-0.000034
df	H	-5.702185	8.048202	-3.992201	-0.000071	0.000057	-0.000022
df	H	-5.935345	5.111656	-0.393090	0.000002	-0.000026	-0.000015
df	H	-1.098628	-4.592189	2.434982	0.000035	0.000007	-0.000046
df	H	-0.621716	-9.068106	1.168365	-0.000040	0.000013	-0.000022
df	H	-2.859766	-10.712445	-2.649653	0.000063	-0.000003	0.000022
df	H	-5.591988	-7.817369	-5.187039	0.000019	-0.000001	0.000053
df	H	-6.078337	-3.342329	-3.939536	0.000054	0.000064	0.000010

TBMCA in water

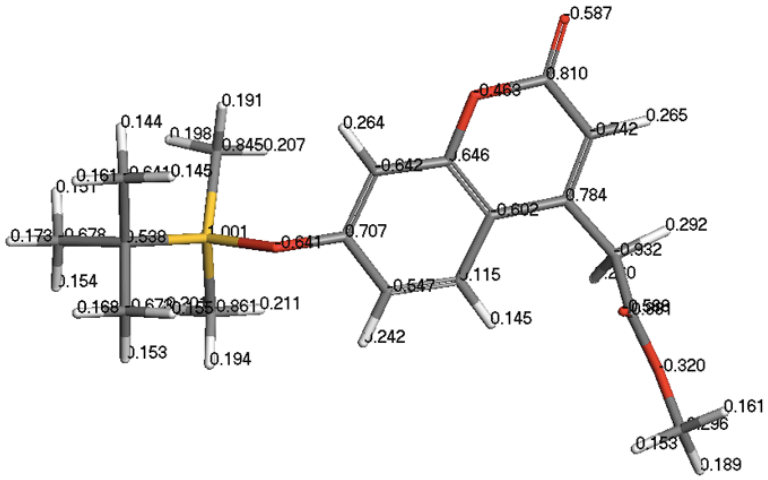

df		ATOMIC COORDINATES (au)			DERIVATIVES (au)		
df		x	y	z	x	y	z
df	C	-0.399952	0.409512	0.582780	0.000119	0.000129	-0.000045
df	C	1.266987	-1.536366	-0.165896	-0.000106	0.000097	0.000059
df	C	3.715341	-0.953661	-0.899117	0.000017	-0.000050	0.000185
df	C	4.609318	1.562458	-0.904917	-0.000159	-0.000006	0.000092
df	C	2.896393	3.470158	-0.153593	0.000086	-0.000245	0.000066
df	C	0.427824	2.922209	0.584397	-0.000085	0.000007	-0.000193
df	O	3.586495	5.974839	-0.108117	-0.000145	0.000123	-0.000101
df	C	6.022240	6.760484	-0.796760	0.000156	-0.000126	-0.000228
df	C	7.764564	4.816540	-1.559841	-0.000295	0.000323	-0.000130
df	C	7.132740	2.311497	-1.616136	0.000498	-0.000084	0.000066
df	O	6.439780	9.039502	-0.681479	0.000072	-0.000018	0.000208
df	C	9.042258	0.377667	-2.440260	-0.000396	-0.000452	0.000277
df	C	10.051317	-1.243350	-0.291937	-0.000308	0.000459	-0.000179
df	O	11.164940	-3.343824	-1.220033	0.000100	-0.000203	0.000034
df	C	12.359729	-4.971708	0.649077	-0.000116	-0.000131	-0.000045
df	O	9.944673	-0.714697	1.953582	0.000169	-0.000044	-0.000100
df	O	-2.768139	-0.152196	1.415306	-0.000001	-0.000383	0.000139
df	Si	-5.419718	-0.487471	-0.432734	-0.000125	0.000239	0.000269
df	C	-8.101239	-0.551163	1.967749	0.000329	0.000136	-0.000075
df	C	-8.293282	2.024034	3.311191	-0.000066	-0.000190	-0.000143
df	C	-7.637158	-2.635028	3.944538	-0.000034	0.000057	-0.000087
df	C	-10.603167	-1.090764	0.570114	-0.000109	-0.000025	0.000077
df	C	-5.620635	2.280851	-2.642946	0.000203	0.000135	-0.000065
df	C	-5.138545	-3.514749	-2.264251	-0.000254	-0.000246	-0.000187
df	H	0.611976	-3.494549	-0.149442	0.000080	-0.000009	0.000019
df	H	4.971224	-2.483544	-1.488362	-0.000031	0.000039	-0.000092
df	H	-0.840493	4.440754	1.174955	0.000025	-0.000002	0.000019

df	H	9.652445	5.454941	-2.094907	0.000006	-0.000103	-0.000037
df	H	10.691435	1.333833	-3.282725	0.000062	0.000053	0.000194
df	H	8.271122	-0.862268	-3.924813	0.000234	0.000197	-0.000058
df	H	13.902737	-3.952186	1.593655	0.000015	0.000006	-0.000085
df	H	13.098551	-6.577784	-0.430498	0.000024	0.000045	0.000075
df	H	10.961397	-5.605617	2.045902	0.000026	0.000064	0.000034
df	H	-9.837870	1.975871	4.721575	-0.000096	0.000091	-0.000038
df	H	-8.715326	3.569735	1.975353	-0.000023	-0.000032	0.000084
df	H	-6.530752	2.506450	4.316522	0.000067	0.000059	-0.000028
df	H	-5.879704	-2.304731	5.015978	-0.000014	0.000035	0.000078
df	H	-7.516724	-4.525314	3.070636	0.000103	0.000039	-0.000022
df	H	-9.219113	-2.675922	5.313698	-0.000072	-0.000023	0.000059
df	H	-10.594882	-2.961452	-0.352736	-0.000032	-0.000022	-0.000014
df	H	-11.014633	0.345967	-0.885587	0.000039	-0.000072	-0.000048
df	H	-12.188015	-1.070538	1.934559	0.000003	0.000060	-0.000012
df	H	-4.102499	2.225983	-4.071598	-0.000110	0.000027	-0.000034
df	H	-5.486985	4.097915	-1.631074	0.000096	-0.000098	0.000012
df	H	-7.441745	2.254967	-3.663981	-0.000141	0.000104	0.000012
df	H	-6.850035	-3.852927	-3.406910	0.000032	-0.000075	0.000048
df	H	-4.868214	-5.154311	-1.006029	0.000145	0.000085	-0.000062
df	H	-3.516657	-3.440047	-3.574884	0.000011	0.000030	0.000001

TBMCA in n-Hexane

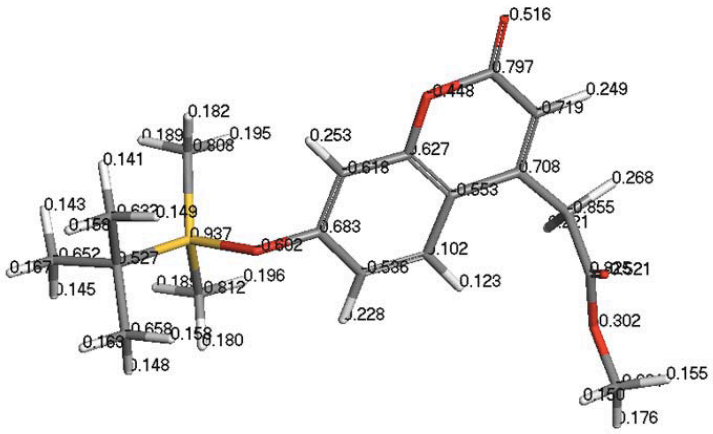

df		ATOMIC COORDINATES (au)			DERIVATIVES (au)		
df		x	y	z	x	y	z
df	C	-0.294569	0.494789	0.554641	-0.000041	0.000048	0.000008
df	C	1.376202	-1.437629	-0.213461	0.000147	-0.000074	-0.000019
df	C	3.815603	-0.834577	-0.966877	-0.000031	0.000007	0.000121
df	C	4.690853	1.686522	-0.980312	0.000074	-0.000044	0.000151
df	C	2.977810	3.586133	-0.203436	0.000092	0.000104	0.000226
df	C	0.519859	3.008449	0.559410	-0.000116	-0.000151	-0.000058
df	O	3.637828	6.086961	-0.160339	-0.000143	-0.000063	-0.000242
df	C	6.072361	6.910898	-0.879993	0.000109	0.000118	0.000177
df	C	7.812961	4.963357	-1.681805	0.000014	-0.000033	-0.000157
df	C	7.198544	2.459944	-1.733722	-0.000255	0.000000	-0.000146
df	O	6.482105	9.173884	-0.768275	0.000011	-0.000096	0.000131
df	C	9.113659	0.522991	-2.562674	0.000345	0.000170	-0.000203
df	C	10.120649	-1.060245	-0.373314	-0.000082	-0.000124	0.000066
df	O	10.288315	-3.533646	-1.045614	-0.000076	-0.000089	0.000048
df	C	11.314944	-5.181151	0.893519	0.000109	0.000033	-0.000171
df	O	10.746389	-0.232457	1.678186	0.000102	0.000051	0.000039
df	O	-2.658684	-0.080333	1.400756	0.000214	-0.000063	0.000332
df	Si	-5.296075	-0.505877	-0.421149	-0.000122	-0.000209	-0.000413
df	C	-7.959839	-0.659556	1.997079	-0.000110	-0.000497	0.000044
df	C	-8.178080	1.895348	3.378185	0.000285	0.000223	-0.000092
df	C	-7.427378	-2.757003	3.941148	0.000030	0.000163	-0.000106
df	C	-10.468401	-1.225734	0.627352	0.000135	-0.000047	-0.000099
df	C	-5.609868	2.243149	-2.647617	-0.000114	-0.000308	-0.000384
df	C	-4.958244	-3.519586	-2.268483	-0.000019	0.000261	0.000337
df	H	0.728279	-3.398003	-0.192797	-0.000104	0.000073	-0.000181
df	H	5.085022	-2.353945	-1.556966	0.000021	0.000014	-0.000019
df	H	-0.748218	4.518450	1.170507	0.000034	0.000064	-0.000019

df	H	9.686299	5.625279	-2.237354	-0.000070	0.000038	-0.000156
df	H	10.757527	1.490344	-3.399635	-0.000027	0.000026	0.000159
df	H	8.328392	-0.735296	-4.022185	-0.000046	-0.000018	0.000086
df	H	13.237337	-4.584707	1.405642	-0.000060	0.000028	0.000055
df	H	11.333011	-7.070514	0.043234	-0.000013	0.000001	0.000015
df	H	10.100719	-5.144782	2.580621	-0.000055	-0.000039	0.000029
df	H	-9.704438	1.803459	4.805851	-0.000067	0.000002	-0.000037
df	H	-8.645870	3.450614	2.069067	-0.000190	-0.000050	0.000066
df	H	-6.412741	2.391589	4.369734	0.000005	-0.000051	0.000051
df	H	-5.650940	-2.418162	4.975699	-0.000074	0.000034	0.000053
df	H	-7.306773	-4.638226	3.047465	0.000104	0.000013	0.000026
df	H	-8.977297	-2.833116	5.344420	-0.000010	-0.000053	-0.000036
df	H	-10.442429	-3.083285	-0.321872	-0.000059	0.000025	0.000176
df	H	-10.932777	0.225609	-0.797144	0.000006	0.000033	-0.000003
df	H	-12.035875	-1.257853	2.011441	-0.000025	0.000024	-0.000029
df	H	-4.078656	2.248511	-4.063282	0.000162	0.000009	0.000065
df	H	-5.550563	4.071930	-1.647907	0.000042	0.000150	0.000029
df	H	-7.419446	2.152264	-3.683112	-0.000142	0.000228	0.000199
df	H	-6.649768	-3.865425	-3.438741	0.000016	0.000092	-0.000019
df	H	-4.694651	-5.170907	-1.024390	0.000010	-0.000021	-0.000019
df	H	-3.323089	-3.428459	-3.561499	-0.000018	-0.000002	-0.000077

Molecular Modeling: Atomic solvent accessible area was calculated to compare the steric hindrance of the phenyl and methyl group. The various conformers of each molecule were generated by diverse conformation generation protocol implemented in Discovery Studio 1.7® program. Truncated structure was used for simplification (Figure S13). Energetically most-stable top 10 conformers of **TBPCA** and **TBMCA** were selected for further calculation. Finally, the accessible area of oxygen 13 and silicon 14 was calculated by Naccess 2.1.1. program. Probe size (radius of the water molecule) and z-slice value were set as 1.40 Å and 0.05, respectively. Calculated result is illustrated in figure S14.

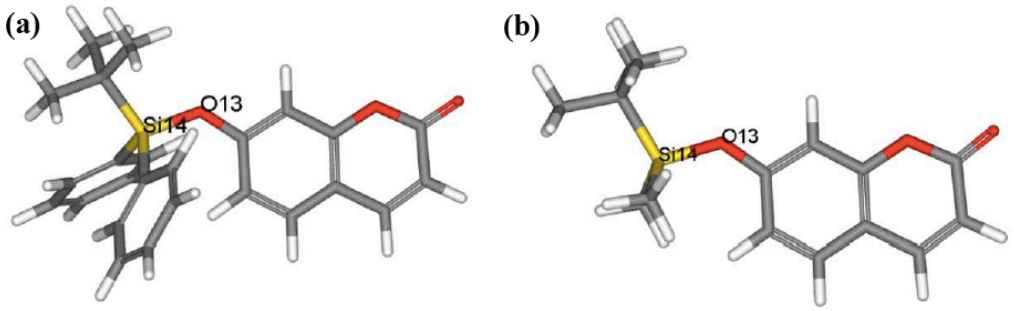

Figure S13. (a) Truncated structure of **TBPCA**, (b) Truncated structure of **TBMCA**

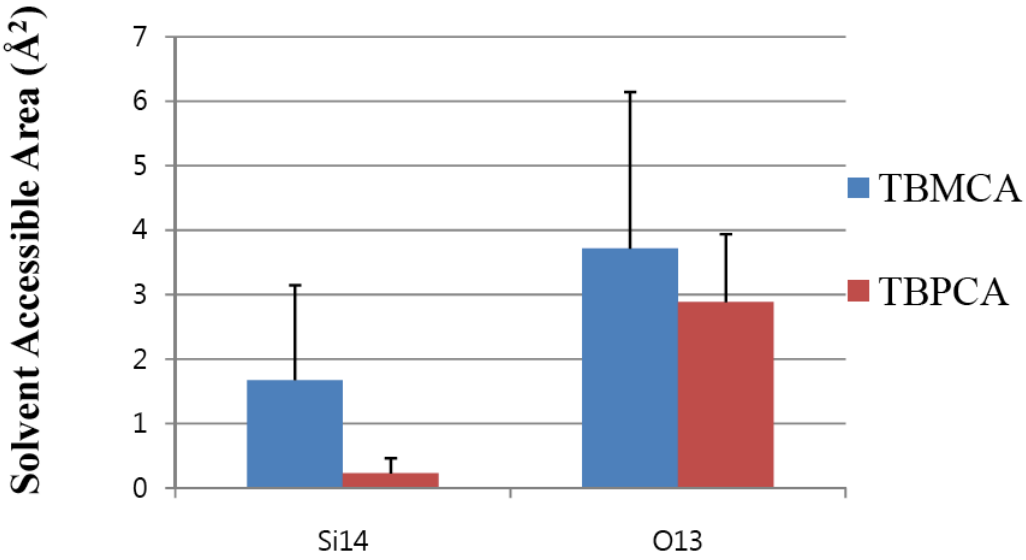

Figure S14. Average values of accessible area of oxygen 13 and silicon 14 on the truncated TBMCA and TBPCA.

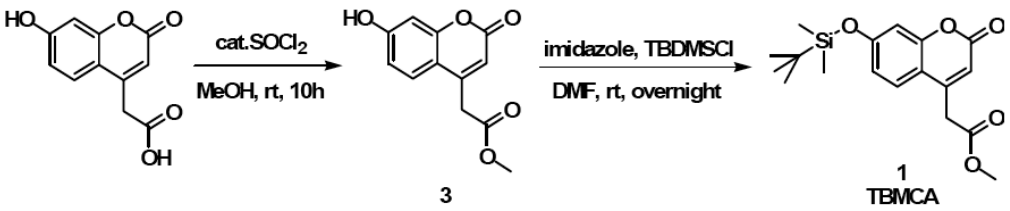

Scheme S1. Synthesis of **TBMCA**

***tert*-butyldimethylsilyl 7-hydroxycourmarin-4-acetic acid methyl ester, TBMCA (1)** 7-Hydroxycoumarin-4-acetic acid methyl ester (**3**) was synthesized in accordance with a known procedure.[16] To a solution of compound **3** (153 mg, 0.65 mmol) in DMF were added 2 equiv. of imidazole (88.5 mg, 1.30 mmol) and TBDMSCl (195 mg, 1.30 mmol). The reaction mixture was stirred at room temperature overnight, and condensed under reduced pressure. The resulting residue was diluted with ethyl acetate, and washed with deionized water (x 3) and brine. The combined organic phase was dried in anhydrous Na2SO4. Silica-gel flash column chromatography (Hex/E.A. = 20:1 to 5:1) afforded **TBMCA** (202 mg, 66 % yield). ^{1}H NMR (300 MHz, $CDCl_3$): δ 0.26 (s, 6H), 1.00 (s, 9H), 3.75 (s, 5H), 6.25 (s, 1H), 6.78–6.81 (m, 2H), 7.45 (d, J = 9.39 Hz, 1H); ^{13}C NMR (75 MHz, $CDCl_3$): δ -4.39, 18.26, 25.55, 38.02, 52.71, 107.98, 113.06, 114.19, 117.43, 125.43, 147.89, 155.29, 159.49, 160.83, 169.22; HRMS (FAB): *m/z* calcd for $C_{18}H_{24}O_5Si$ $[M+H]^+$: 349.1471, found: 349.1472.

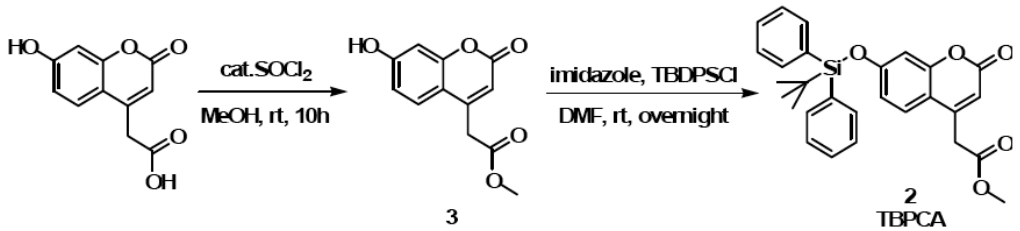

Scheme S2. Synthesis of **TBPCA**

TBPCA was synthesized using a synthetic procedure for **TBMCA** in 57 % yield. ^{1}H NMR (300 MHz, $CDCl_3$): δ 1.13 (s, 9H), 3.68 (s, 2H), 3.71 (s, 3H), 6.19 (s, 1H), 6.71 (s, 1H), 6.75 (d, J = 8.70 Hz, 1H), 7.31–7.46 (m, 7H), 7.72 (dd, J = 6.10 Hz, 1.45 Hz,

4H); ^{13}C NMR (75 MHz, $CDCl_3$): δ 19.46, 26.43, 37.86, 52.64, 107.93, 113.01, 114.06, 117.17, 125.30, 128.08, 130.38, 131.70, 135.41, 147.92, 155.03, 159.21, 160.77, 169.20; HRMS (FAB): *m/z* calcd for $C_{28}H_{28}O_5Si$ $[M+H]^+$: 473.1784, found: 473.1790.

Reference

[1] a) K. L. Kirk, *Biochemistry of the Halogens and Inorganic Halides, Plenum Press, New York*, **1991**, p. 58; b) H. S. Horowitz, *J. Public Health Dent.*, **2003**, *63*, 3.

[2] a) B. L. Riggs, *Bone and Mineral Research, Annual 2, Elsevier, Amsterdam,* **1984**, pp. 366; b) J. R. Farley, J. E. Wergedal, D. J. Baylink, *Science*, **1983**, *222*, 330; c) M. Kleerekoper, *Endocrinol. Metab. Clin. North Am*., **1998**, *27*, 441.

[3] a) A. Wiseman, *Handbook of Experimental Pharmacology XX/2, Springer-Verlag, Berlin*, **1970**, Part 2, pp. 48; b) J. A. Weatherall, *Pharmacology of Fluorides. in Handbook of Experimental Pharmacology XX/1, Springer-Verlag, Berlin,* **1969**, Part 1, pp. 141; c) R. H. Dreisbuch, *Handbook of Poisoning, Lange Medical Publishers, Los Altos, CA,* **1980**.

[4] M. L. Cittanova, B. Lelongt, M. C. Verpont, *Anesthesiology*, **1996**, *84*, 428.

[5] P. P. Singh, M. K. Barjatiya, S. Dhing, R. Bhatnagar, S. Kothari, V. Dhar, *Urol. Res.*, **2001**, *29*, 238.

[6] a) T.-J. Chen, T.-M. Chen, C.-H. Chen, Y.-K. Lai, *J. Cell. Biochem.*, **1998**, *69*, 221; b) M. H. Arhima, O. P. Gulati, S. C. Sharma, *Phytother. Res.,* **2004**, *18*, 244.

[7] a) C. D. Anuradha, S. Kanno, S. Hirano, *Arch. Toxicol.*, **2000**, *74*, 226; b) M. Refsnes, P. E. Schwarze, J. A. Holme, M. Lag, Hum. *Exp. Toxicol.,* **2003**, *22*, 111; c) M. Matsui, M. Morimoto, K. Horimoto, Y. Nishimura, *Toxicol. In vitro*, **2007**, *21*, 1113.

[8] a) C. B. Black, B. Andrioletti, A. C. Try, C. Ruiperez, J. L. Sessler*, J. Am. Chem. Soc*., **1999**, *121*, 10438; b) S. Yamaguchi, S. Akiyama, K. Tamao, *J.*

Am. Chem. Soc., **2000**, *122*, 6793; c) E. J. Cho, J. W. Moon, S. W. Ko, J. Y. Lee, S. K. Kim, J. Yoon, K. C. Nam, *J. Am. Chem. Soc.*, **2003**, *125*, 12376; d) M. Va´zquez,L. Fabbrizzi, A. Taglietti, R. M. Pedrido, A. M. Gonza´lez-Noya, M. R. Bermejo, *Angew. Chem., Int. Ed.*, **2004**, *43*, 1962; e) T.-H. Kim, T. M. Swager, *Angew. Chem. Int. Ed.,* **2003**, *42*, 4803; f) X. Jiang, M. C. Vieweger, J. C. Bollinger, B. Dragnea, D. Lee, *Org. Lett.*, **2007**, *9*, 3579; g) X. Y. Liu, D. R. Bai, S. Wang, *Angew. Chem. Int. Ed*., **2006**, *45*, 5475; h) T. W. Hudnall, F. P. Gabbaï, *Chem. Commun.*, **2008**, 4596.

[9] a) T. W. Hudnall, F. P. Gabbaï, *J. Am. Chem. Soc.,* **2007**, *129*, 11978; b) S. Y. Kim, J. -I. Hong, *Org. Lett*., **2007**, *9*, 3109; c) C. -W. Chiu, F. P. Gabbaï, *J. Am. Chem. Soc.*, **2006**, *128*, 14248; d) X.-F. Yang, *Spectrochim. Acta, Part A*, **2007**, *67*, 321; e) A. B. Descalzo, D. Jime´nez, J. E. Haskouri, D. Beltra´n, P. Amoro´s, M. D. Marcos, R. Martı´nez-Ma´n˜ez, J. Soto, *Chem. Commun.*, **2002**, 562; f) M. Cametti, K. Rissanen, *Chem. Commun*., **2009**, 2809.

[10] C. C. Woodroofe, S. J. Lippard, *J. Am. Chem. Soc*., **2003**, *125*, 11458.

[11] *Protective Groups in Organic Synthesis, ed*. T. W. Greene, P. G. M. Wuts, Wiley, New York, 3rd edn, **1999**, pp. 113.

[12] Q. Zhu, M. Uttamchandani, D. Li, M. L. Lesaicherre, S. Q. Yao, *Org. Lett*., **2003**, *5*, 1257.

[13] The ab initio calculation of the Si–O bond in two different solvent systems (water and n-hexane) was done using the Material Studio 4.2s program and the water-accessible area of the Si–O bond was calculated using Naccess (V2.1.1) with stable conformers of TBMCA and TBPCA. See ESIw for detailed procedures.

[14] T. Mosmann, *J. Immunol. Methods*, **1983**, *65*, 55.

[15] J. Park, H. Y. Lee, M.-H. Cho, S. B. Park, *Angew. Chem. Int. Ed.*, **2007**, *46*, 2018.

[16] Q. Zhu, M. Uttamchandani, D. Li, M. L. Lesaicherre, S. Q. Yao, *Org. Lett*. **2003**, *5*, 1257.

Chapter 6. Ratiometric Analysis of Zidovudine (ZDV) Incorporation by Reverse Transcriptases or Polymerases via Bio-orthogonal Click Chemistry

- *Chem. Commun.* **2011**. 7614.

Introduction

Zidovudine (ZDV), also known as azidothymidine (AZT), is approved by the FDA in 1987 for the treatment of acquired immunodeficiency syndrome (AIDS). It belongs to the class of nucleoside analog reverse transcriptase inhibitor (NRTI).[1] This anti-retroviral drug provided a major breakthrough in AIDS therapy and significantly slowed the spread of HIV.[2,3] Owing to the structural features of ZDV, the incorporation of ZDV into DNA leads to the premature termination of DNA replication.[4] Although ZDV is known as a highly selective inhibitor for viral reverse transcriptases over eukaryotic DNA polymerases,[5] its incorporation into a patient's DNA by DNA polymerases has been reported in several clinical studies. Incorporation of ZDV into a patient's DNA is associated with significant side effects, including anemia, neutropenia, hepatotoxicity, and cardiomyopathy, upon chronic, high-dose ZDV therapy for AIDS treatment.[6-8]

The specific tracing of ZDV has been pursued using radioisotopes and ZDV-specific antibodies and successfully applied with good sensitivity in molecular biology.[9] However, these analytical methods have their own limitations. For example, the radioisotope-based detection system requires extreme safety caution and special equipment. The immunostaining method requires expensive ZDV-specific antibody and multiple washing steps. Herein, we report the chemotype-based

specificdetection of ZDV using a bio-orthogonal fluorescent small molecule probe as a ratiometric analysis tool for ZDV-incorporation level by various DNA synthesizing enzymes as well as a visualization tool of cellular ZDV-incorporated DNA .

Results and Discussion

In order to detect the ZDV-incorporation levels in DNA under various biological environments, we envisioned the utilization of the inherent azide moiety at the 3′ position on the sugar frame of ZDV for a fluorescence-based monitoring system (Figure 1). The Cu(I)-catalyzed alkyne –azide cycloaddition , namely Click reaction, is one of the practical tools used to decipher complex biological phenomena without any cross-interactions.[10,11] Therefore, we prepared an alkyne -containing fluorescent molecule as a zidovudine probe (**ZP**) for bio-orthogonal specific formation of triazole with the azide moiety at the 3′ position of ZDV.

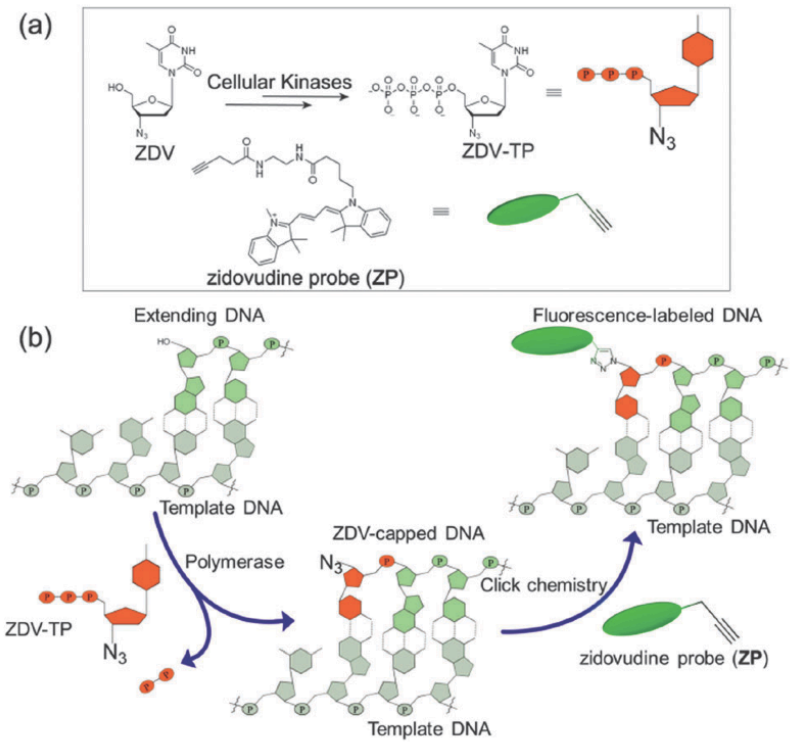

Figure 1. (a) Structure of ZDV-TP generated by *in vivo* phosphorylation of ZDV and zidovudine probe (**ZP**). (b) Schematic illustration of specific detection of ZDV-

incorporated DNA using **ZP**. DNA extension is terminated by ZDV incorporation and the resulting ZDV-capped DNA can be selectively visualized by covalent labeling of an alkyne -containing fluorophore (**ZP**) *via* bio-orthogonal click chemistry.

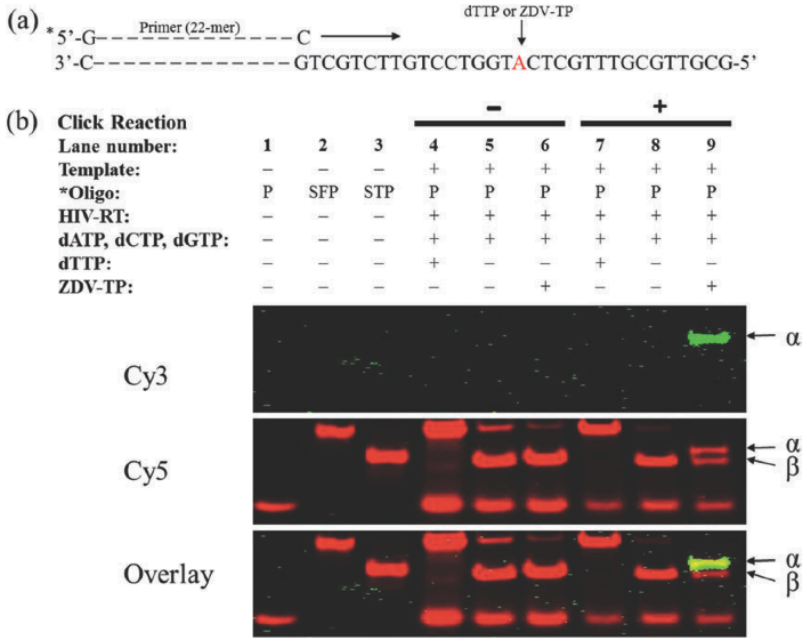

Figure 2. Primer extension assay with *in-gel* fluorescence imaging of ZDV-incorporated oligonucleotides. (a) DNA template and primer used in this assay. (b) d-PAGE analysis of resulting DNA products under abovementioned conditions. 1 equiv. of ZDV-TP (50 nM) was used in a primer extension assay. Click reaction: (+) means click reaction is performed, (−) means click reaction is not performed. α: Cy3-labeled ZDV-incorporated DNA product; β: terminated product due to the absence of dTTP. * denotes Cy5-labeled oligonucleotides . P: primer, 22-mer; SFP: synthetic full-length product, 53-mer; STP: synthetic terminated product, 38-mer. See the Supporting Infomation for a detailed experimental procedure.

With this designed **ZP** probe in hand, the reaction condition was optimized for the click reaction of **ZP** with ZDV under physiological conditions by varying the concentrations of $CuSO_4$, ligand, and **ZP** in the presence of ascorbic acid. On the basis of reported procedures in several bioconjugation studies, we successfully applied tris-(benzyltriazolylmethyl) amine (TBTA) as a ligand for the stabilization of reactive Cu(I) species in biological systems.[12] Although complete consumption of ZDV was achieved with high concentrations of the $CuSO_4$/TBTA complex (1/1 ratio, 870 μM, 20 equiv.), this condition was associated with the formation of many

unidentifiable by-products in the HPLC analysis. Hence, the complete conversion of ZDV was achieved using a large excess amount of **ZP** (more than 400 equiv.) rather than the relatively high $CuSO_4$/TBTA concentration (Figure S1 in the Supporting Information).

For a proof-of-concept study, the bio-orthogonal detection system for ZDV was tested using a primer extension assay.[13] As shown in Figure 2, the 22-mer DNA primer was labeled with Cy5 at the 5′ end and subjected to *in vitro* primer extension using reverse transcriptase in order to monitor the ZDV incorporation into the extended DNA using a click-chemistry-based detection system in the denaturing urea polyacrylamide gel electrophoresis (d-PAGE). The DNA template was designed to have a single adenine site (red in Figure 2a), where its complementary partner, either dTTP or ZDV-TP (5′-triphosphate form of ZDV), could be incorporated into the growing DNA. All of the extended DNA could then be visualized in red using *in-gel* fluorescence imaging of Cy5 at the 5′ end of the primer (red in Fig. 2b). In the absence of its ordinary building block, dTTP, the primer was terminated at the complementary region of the template where the adenine residue is located (lane 5), whereas in the presence of dTTP, a fully extended DNA was obtained (lane 4). The band on the top is assumed due to the bypass tendency of reverse transcriptase in the dTTP-deficient condition (lanes 5 and 6).[14] When the primer extension assay was performed with the replacement of dTTP by ZDV-TP, an early-terminated DNA was also observed (lane 6) due to the ZDV incorporation. Even though these data show the early termination of DNA extension in the presence of ZDV-TP, it is, nonetheless, impossible to tell whether this truncated DNA is caused by the absence of dTTP (as in lane 5) or by the incorporation of ZDV, given that the ZDV-

incorporated DNA product (38-mer) is only one nucleotide longer than the simple termination product (37-mer).

These two types of terminated DNA products, however, can be clearly differentiated through the visualization of the ZDV-incorporated DNA using our bio-orthogonal detection system with Cy3-labeled **ZP** (green in Figure 2b). The positive charge of Cy3 dye is an advantageous characteristic of **ZP** for analyzing the outcomes of the *in-gel* imaging experiments as it induces a band-shift of the ZDV-incorporated DNA, which enables us to quantify the efficiency of ZDV incorporation.

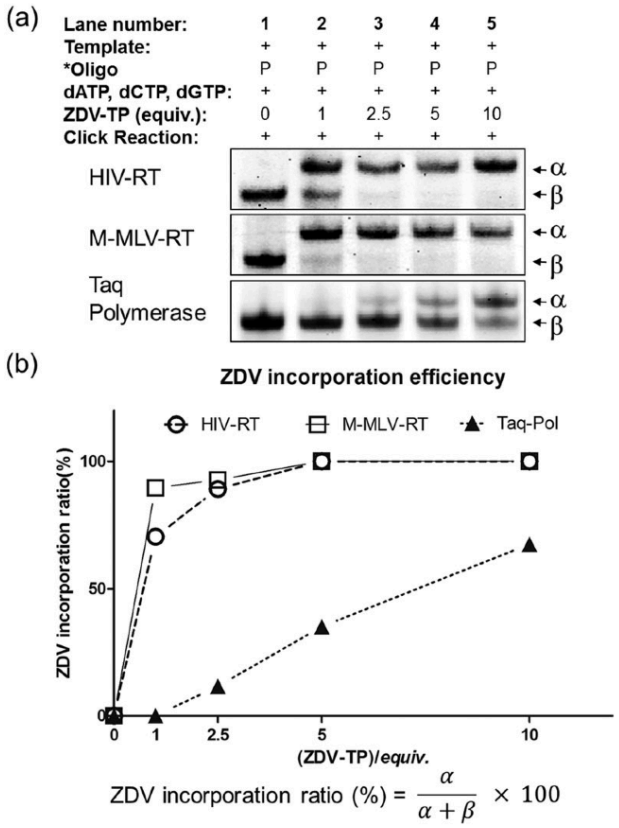

Figure 3. Quantitative measurement of ZDV-incorporation efficiency for direct comparison of DNA-synthesizing enzymes. (a) d-PAGE analysis of primer extension products using two different reverse transcriptases (HIV-RT, M-MLV-RT) or aDNA polymerase (Taq polymerase) and the subsequent click reaction with **ZP**. (b) The quantification data of *in-gel* fluorescence imaging for ZDV incorporation. Open circle: HIV-RT; open rectangle: M-MLV-RT; closed triangle: Taq polymerase. The template and primer used in this reaction are identical to those in Figure 2a. α: Cy3-labeled terminated product; β: Terminated product due to the absence of dTTP. * denotes Cy5-labeled oligonucleotides . P: primer.

When the click-based labeling of **ZP** was executed on the identical reaction products of the primer extension assay, the ZDV-containing DNA was visualized in green (lane 9) with excellent specificity. In addition, we observed a shifted band (α) of the ZDV-incorporated DNA product *via* a covalent installment of the cationic Cy3 dye, which was not observed in the simple termination product (lane 8). The shifted band (α) observed in the Cy5 channel is clearly merged with the Cy3 signal (lane 9). In contrast, the termination product we observed in the presence of dTTP was only the ZDV-incorporated product which was clearly visualized as an α band without a β band (Figure S2 in the Supporting Information). Based on this interesting observation, we were able to measure the incorporation efficiency of ZDV into the DNA sequence by comparing the fluorescence intensity of the shifted band (α) to that of the unshifted band (β).

The *in-gel* fluorescence imaging method presented herein allows the ratiometric analysis of ZDV incorporation levels in different kinds of DNA-synthesizing enzymes. In order to directly compare the ZDV incorporation efficiency, the primer extension assay was performed with two viral reverse transcriptases (HIV-RT, human immunodeficiency virus reverse transcriptase ; M-MLV-RT, moloney murine leukemia virus reverse transcriptase) and Taq polymerase using various concentrations of ZDV-TP under dTTP-deficient conditions and the subsequent Click reaction with **ZP**. Based on the *in-gel* fluorescence analysis of the resulting DNA products, it was found that the incorporation level of ZDV was increased in a dose-dependent manner by two different reverse transcriptases and Taq polymerase. Both reverse transcriptases exhibit a significantly higher ZDV incorporation than Taq polymerase (Figure 3a). Particularly, M-MLV-RT was the most susceptible to ZDV-based early termination of the elongating DNA strand *via* a

ZDV incorporation of up to 100% at a ratio of five equivalents of ZDV-TP to the template strand. The results indicate that in the presence of one equivalent of ZDV-TP (Figure 3b), the pseudo building block, ZDV, was inserted into the elongating strand with 70% and 90% efficiency by HIV-RT and M-MLV-RT, respectively, whereas no incorporation was observed with Taq polymerase.

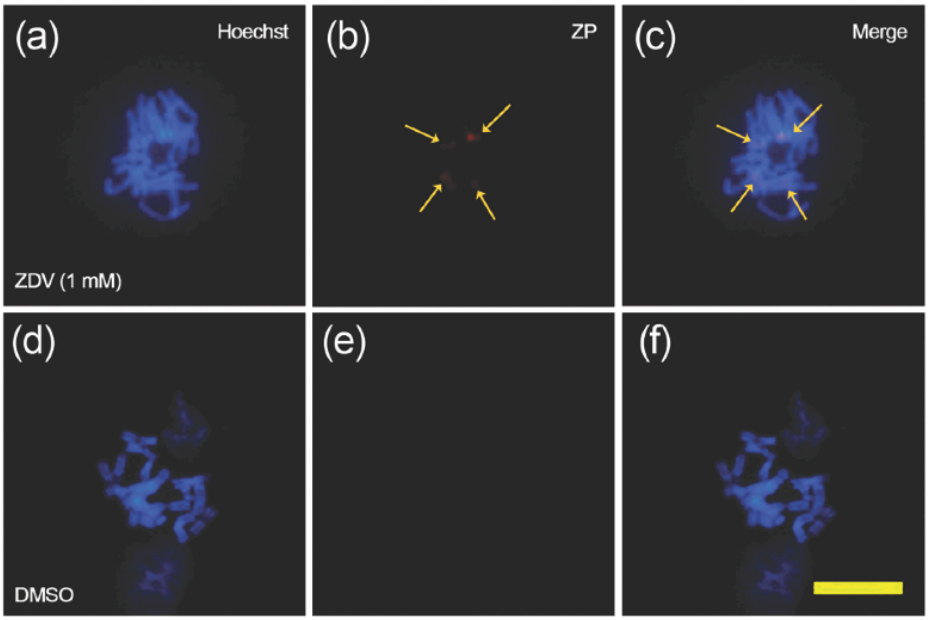

Figure 4. Metaphase chromosomes extracted from CHO-K1 cells treated either with 1 mM of ZDV (a, b, c) or with DMSO(d, e, f). The chromosomes were stained with Hoechst (a, d) or **ZP** (b, e) *via* click reaction. The yellow arrows indicate Cy3-labeled ZDVs that are incorporated in DNA at the end of chromosomes. Scale bar: 5 μm.

Following the *in-gel*-based *in vitro* confirmation of the specific detection of ZDV in DNA strands, *ex vivo* imaging experiments were carried out in order to detect the ZDV incorporation in mammalian cells. To facilitate the clear observation of the incorporated ZDV in DNA, metaphase chromosomes were extracted from CHO-K1 Chinese hamster ovary cells after 4 h treatment with ZDV (1 mM) and the subsequent Click-based labeling of ZDV incorporated in DNA with **ZP**. As shown in Figure 4, DNA-incorporated ZDVs are particularly localized at the end of chromosomes (yellow arrows), which is suspected to be a telomere region in CHO-

K1 cell lines.[8,15] This observation is consistent with a previous report using the ZDV-specific antibody.

Conclusion

In summary, DNA-synthesizing enzymes may erroneously recognize ZDV-TP as an authentic building block and thus insert this synthetic analogue at the end of the elongating DNA strand and this undesired incorporation of ZDV into mammalian cells leads to the early termination of DNA replication , which is the major cause of side effects in NRTI-based AIDS treatment.[16] In order to provide the quantitative measurement tool for the side effect studies of ZDV therapy, we accomplished the bio-orthogonal tracing of ZDV-incorporated DNA in the *in-gel* fluorescence imaging system as well as cellular imaging of ZDV-incorporated mammalian chromosomes. Our method clearly visualizes ZDV-incorporated oligonucleotides using Click-chemistry-based covalent incorporation of the alkyne-containing fluorescent small-molecule probe (**ZP**). Most importantly, unlike other existing methods such as autoradiography or immunostaining, we were able to quantify the incorporation efficiency of ZDV by different kinds of DNA-synthesizing enzymes on the basis of our unique observation of band shifts induced by specific labeling of cationic Cy3-labeled **ZP**.

Supporting Information

General Information: All reactions were performed using oven-dried glassware under dry argon atmosphere. Dichloromethane (DCM) was dried by distillation from CaH2. Other solvents and organic reagents were purchased from commercial venders and used without further purification unless otherwise mentioned. *N*-Bocethylenediamine, *N,N′*-dicyclohexylcarbodiimide (DCC),*N,N*-dimethylformamide (DMF), 1-ethyl-3-(3-dimethylaminopropyl)carbodiimide hydrochloride (EDC hydrochloride), *N,N*-diisopropylethylamine (DIPEA), and 4-pentanoic acid were purchased from Sigma-Aldrich, USA. Trifluoroacetic acid (TFA) was purchased from TCI [Tokyo chemical industry Co., Ltd., Japan]. The ^{1}H and ^{13}C NMR spectra were recorded on a Varian Inova-500 [Varian Assoc., USA], and chemical shifts were measured in ppm downfield from internal tetramethylsilane (TMS) standard. Multiplicity was indicated as follows: s (singlet), d (doublet), t (triplet), q (quartet), m (multiplet), dd (doublet of doublet), td (triplet of doublet), etc. Coupling constants were reported in Hz. Low resolution mass spectrometry (LRMS) analysis was performed with Finnigan MSQ Plus Surveyer HPLC/MS system [Thermo Electron Corp., USA] using electron spray ionization (ESI). Reverse phase HPLC analysis was performed on a VPODS C-18 column (150 x 4.6 mm) at a flow rate of 1.0 mL/min for analytical analysis, and PRC-ODS C-18 column (250 x 20 mm) at a flow rate of 10.0 mL/min for preparation by LC-6AD pump with SPD-10A detector equipped with photodiode array (PDI) [Shimadzu, Japan]. HPLC solvents consist of water [HPLC grade, B&J, USA] containing 0.1% TFA as eluent A and acetonitrile [HPLC grade, B&J, USA] containing 0.1% TFA as eluent B.

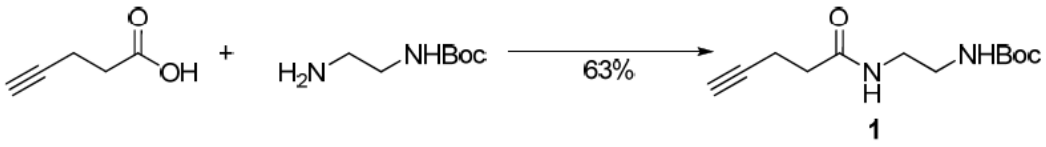

Scheme S1. Synthesis of compound **1**

To a solution of DCC (505 mg, 2.447 mmol) in anhydrous DCM (12 mL), was added 4-pentynoic acid (200 mg, 2.039 mmol) at 0oC and stirred for 30 min. *N*-Boc-ethylenediamine (359 mg, 2.243 mmol) was added in dropwise to the reaction mixture. The resulting mixture was allowed to warm up to room temperature and stirred for 1 h. The precipitated white solid was removed by filtration and washed with DCM. The filtrate was concentrated *in vacuo* and purified with silica-gel flash column chromatography (1:20 = MeOH:DCM, v/v) to provide **1** (309 mg, 63% w/w). ^{1}H NMR (500 MHz, CD_3OD) δ 3.25 (t, *J* = 6.0, 2H), 3.15 (t, *J* = 6.0, 2H), 2.46 (td, *J* = 6.8, 2.3 Hz, 2H), 2.38 (t, *J* = 7.0 Hz, 2H), 2.26 (t, *J* = 2.2 Hz, 1H), 1.43 (s, 9H); LRMS (ESI+) *m/z* calcd for $C_{12}H_{20}N_2O_3$ $[M+H]^+$ 241.15, found *m/z* 241.08

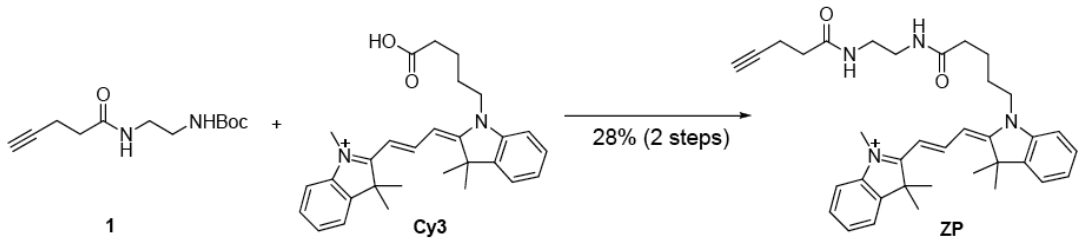

Scheme S2. Synthesis of the **ZP**

To a solution of compound **1** (20 mg, 0.0832 mmol) in DCM (500 μL), was added TFA (500 μL) at room temperature and the resulting mixture was stirred for 1.5 h. DCM and TFA were removed under the reduced pressure by azeotrope with acetonitrile for several times. The crude mixture was diluted with DMF (600 μL) and added with DIPEA (21.7 μL, 0.125 mmol) followed by stirring for 10 min. Cy3 (47.5 mg, 0.0832 mmol) and EDC hydrochloride (31.9 mg, 0.167 mmol) were added to the

reaction mixture and stirred at room temperature for overnight. The crude reaction mixture was purified with reverse phase HPLC charged with C18 column to provide **ZP** (13 mg, 28% w/w). The elution protocol for analytical HPLC is following: (1) 95% eluent A for 5 min, (2) a linear gradient to 5% eluent over 75 min, (3) a linear gradient to 0% eluent A over 5 min, (4) a constant flow with 0% eluent for 5 min. ^{1}H NMR (500 MHz, CD_3OD) δ 8.54 (t, *J* = 13.5 Hz, 1H), 7.54 (d, *J* = 7.5 Hz, 2H), 7.44 (td, *J* = 7.7, 3.8 Hz, 2H), 7.36 (dd, *J* = 7.7, 2.2 Hz, 2H), 7.31 (td, *J* = 7.5, 4.3 Hz, 2H), 6.44 (dd, *J* = 13.5, 5.5 Hz, 2H), 4.16 (t, *J* = 7.2 Hz, 2H), 3.68 (s, 3H), 3.26 (s, 4H), 2.41 (td, *J* = 6.6, 2.2 Hz, 2H), 2.33 (t, *J* = 7.0 Hz, 2H), 2.28 (t, *J* = 7.0 Hz, 2H), 2.25 (q, *J* = 2.3 Hz, 1H), 1.87–1.79 (m, 4H), 1.77 (s, 6H), 1.76 (s, 6H); ^{13}C NMR (125 MHz, CD_3OD) δ 176.7, 176.0, 175.6, 174.3, 152.1, 144.1, 143.4, 142.2, 142.1, 130.0, 129.9, 126.8, 126.7, 123.5, 123.4, 112.4, 112.3, 103.8, 103.7, 83.5, 70.4, 50.6, 50.6, 44.9, 40.1, 39.9, 36.3, 36.0, 28.3, 28.1, 27.9, 23.9, 15.6; MS (ESI+) *m/z* calcd for $C_{36}H_{45}N_4O_2$ $[M]^+$ 565.35, found *m/z* 565.48.

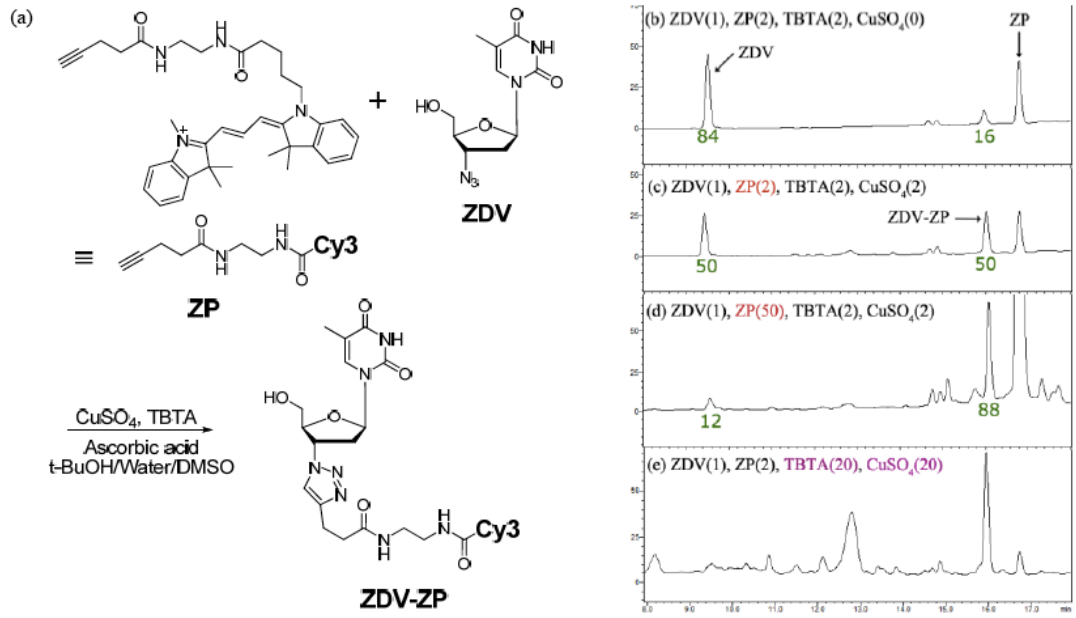

Figure S1. Reaction profile of **ZP** with ZDV via various conditions of click reaction. (a) Chemical equation of the click reaction between **ZP** and ZDV. The reaction is monitored by HPLC at 254 nm under each condition; (b) TBTA (87 μM), ascorbic acid (43 mM), ZDV (43 μM) and **ZP** (87 μM); (c) CuSO4 (87 μM), TBTA (87 μM), ascorbic acid (43 mM), ZDV (43 μM) and **ZP** (87 μM); (d) CuSO4 (87 μM), TBTA (87 μM), ascorbic acid (43 mM), ZDV (43 μM) and **ZP** (2.2 mM); (e) CuSO4 (870 μM), TBTA (870 μM), ascorbic acid (43 mM), ZDV (43 μM) and **ZP** (87 μM). The numbers inside parentheses stand for the equivalent quantities of reagents to the ZDV. All reactions were performed for 2 h at 37°C in aqueous solution containing *t*-BuOH (2%) and DMSO (4%). Tris-(benzyltriazolylmethyl)amine (TBTA), *tert*-butanol (*t*-BuOH) and dimethyl sulfoxide (DMSO) were purchased from Sigma-Aldrich, USA.

The reaction condition was optimized by screening various concentrations of reagents such as $CuSO_4$/TBTA and **ZP**. The formation of the desired product, **ZDV-ZP**, was confirmed by LC/MS of the indicated peak [MS (ESI+) *m/z* calcd for $C_{48}H_{58}N_9O_6$ $[M]^+$ 832.45, found *m/z* 832.40]. Although the high concentration of $CuSO_4$ and TBTA (870 μM each) provides the complete conversion of ZDV, the resulting mixture contains many unidentifiable by-products caused by high concentration of reactive Cu(I) species [Figure S1(e)], which is not desirable for bio-orthogonal detection of ZDV. In contrast, most of ZDV (~90%) was converted to the desired

adduct, ZDV-ZP, using 50 equivalent of **ZP** in the presence of relatively low concentrations of CuSO4/TBTA within 2 h [Figure S1(d)]. Therefore, we concluded that the bio-orthogonal detection of ZDV-incorporated DNA can be robustly achieved without damages on DNA and biopolymers in the presence of high excess of **ZP** (at least 400 equiv. to ZDV) with $CuSO_4$ (87 μM), TBTA (87 μM), and ascorbic acid (43 mM).

Primer extension assay : For the primer extension reaction of HIV reverse transcriptase (RT) [Ambion, Inc.,USA] or M-MLV RT [Ambion, Inc.,USA], the reaction was performed in Tris buffer [Tris HCl (pH 8.3, 50 mM), KCl (75 mM), $MgCl_2$ (3 mM), DTT (5 mM)] which contains the following in a volume of 20 μL:

Template (50 nM) [Bioneer Corp., S. Korea]

Primer (100 nM) [Bioneer Corp., S. Korea]

HIV or M-MLV RT (20 U, unit defined by the manufacturer)

dATP/dGTP/dCTP (1 μM each)

ZDV-TP (described concentration) [eEnzyme®,USA].

Template

3'-CAGATAGTCTTCACGAGGCAGGTCGTCTTGTCCTGGTACTCGTTTGCGTTGCG-5'

Primer

Cy5-5'-GTCTATCAGAAGTGCTCCGTCC-3'

SFP

Cy5-5'-GTCTATCAGAAGTGCTCCGTCCAGCAGAACAGGACCATGAGCAAACGCAACGC-3'

STP

Cy5-5'-GTCTATCAGAAGTGCTCCGTCCAGCAGAACAGGACCAT-3'

In the case of Taq polymerase [Genenmed Inc., S. Korea, 20 U], slightly modified Tris buffer [Tris HCl (pH 9.1, 50 mM), $(NH_4)_2SO_4$ (16 mM), $MgCl_2$ (2.5 mM) and

BSA (15 μg/ml)] were used instead of abovementioned Tris buffer. The template-primer annealing was proceeded in advance of the primer extension reaction by mixing the abovementioned components without reverse transcriptases or polymerase, followed by denaturing at 85 °C for 5 min and cooling to 55 °C for 8 min and 37 °C for 10 min. After the annealing step, the corresponding DNA synthesizing enzymes were added and the reaction vessel was incubated for 60 min at 42 °C (for HIV or M-MLV RT) or 72 °C (for Taq polymerase).

Click chemistry : To the product mixture of the primer extension reaction, $CuSO_4$ (87 μM), TBTA (87 μM), ascorbic acid (43 mM) and **ZP** (17 μM) were added in final volume of 23 μL solution and incubated for 2 h at 37 °C for the proof-of-concept experiment (Figure 2). The direct comparison experiments of ZDV incorporation were performed with up to 2174 μM of **ZP** in the presence of three different DNA synthesizing enzymes.

Denaturing urea polyacrylamide gel electrophoresis (d-PAGE) : The resulting reaction mixture (2 μL) was mixed with gel-loading buffer (8 μL, containing 1x TBE buffer, 7 M urea, 12% v/v glycerol) and heated at 95 °C for 5 min. The samples were directly incubated at ice for 5 min and three microliters of samples were run by d-PAGE (10% v/v) under 120 V and 10 A for 120 min.

Fluorescence detection and quantification : The *in-gel* fluorescence signal was visualized at the Cy3 (532 nm excitation) or Cy5 (633 nm excitation) channel by Typhoon Trio [Amersham Bioscience, USA] and quantified by ImageQuant TL program [Amersham Bioscience, USA].

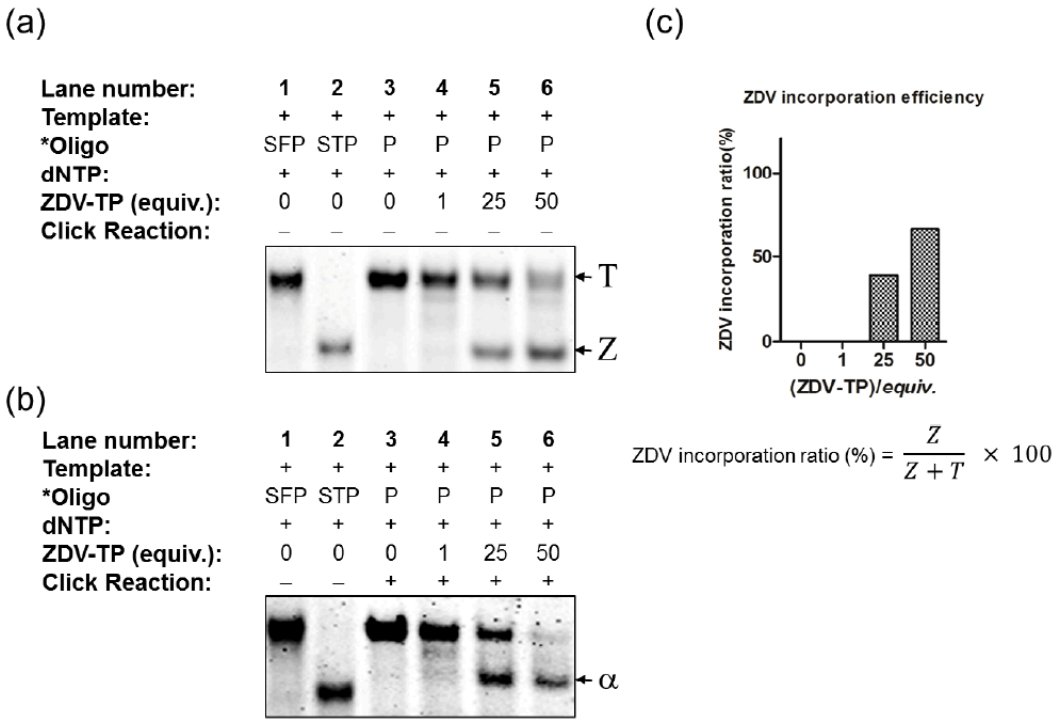

Figure S2. ZDV incorporation efficiency of M-MLV-RT in the presence of dTTP. (a) d-PAGE analysis of primer extension products by increasing concentrations of ZDV-TP without Click reaction or (b) with Click reaction. (c) The quantification data of *in-gel* fluorescence click reaction with **ZP**. * denotes Cy5-labeled oligonucleotides. P: primer, 22-mer; SFP: synthetic full-length product, 53-mer; STP: synthetic terminated product, 38-mer.

Cell incubation and chromosome spread preparation : CHO-K1 cells were cultured in HAM's F12 medium [WelGENE Inc., S. Korea] supplemented with 10% v/v fetal bovine serum (FBS) [Gibco, USA]. CHO-K1 cells were incubated in thymidine deficient HAM's F12 medium containing 10% v/v dialyzed FBS [WelGENE Inc., S. Korea] for 24 h prior to the treatment of ZDV. The cells were incubated for 4 h at 37 °C in the presence of 1 mM 3′-azido-3′-deoxythymidine (ZDV) [Sigma-Aldrich, USA] or DMSO and washed with Ca^{2+}- and Mg^{2+}-free phosphate buffered saline (PBS) [WelGENE Inc., S. Korea]. After washing, the cells were incubated under fresh medium containing 3.0 μM thymidine and 10% v/v FBS for 24 h. The chromosome spread was prepared by the 1 h treatment of demecolcine (1 μg/mL) [Aldrich, USA]

followed by the trypsinization and hypotonic treatment with 75 mM KCl solution, and subsequent fixation with methanol and acetic acid.[17]

Chromosome staining : **ZP** (10 μM), $CuSO_4$/TBTA (1 mM), and ascorbic acid (100 mM) were added to the chromosome mixture after fixation for 1 h at room temperature in the dark. To remove the residual **ZP**, 1 mM of 2-azido-2-deoxy-D-glucose [Aldrich, USA] was added to the chromosome mixture for additional 1 h at room temperature. This treatment provides the click reaction of remaining **ZP** with 2-azido-2-deoxy-D-glucose and enhances the hydrophilicity of **ZP**, which allows the effective removal of **ZP** in resulting samples via washing twice with PBS. Then, 20 μM of Hoechst solution [Molecular Probe, USA] was treated to the slide glass spreaded with chromosome samples for 5 min.

Fluorescence Imaging : We carried out fluorescence microscopy studies with Olympus Inverted Microscope Model IX71 [Model: IX71-F22FL/PH], equipped for epi-illumination using a halogen bulb [Philips No. 7724]. Emission signal of each experiments were observed at two spectral settings: blue channel using a 330-385 band pass exciter filter, a 400 nm center wavelength chromatic beam splitter, and a 420 nm-long pass barrier filter [Olympus filter set UMWU2]; red channel using a 510-550 band pass exciter filter, 570 nm center wavelength chromatic beam splitter, and a 590 nm long pass barrier filter [Olympus filter set, U-MWG2]. Emission signals of each experiment were detected with 12.5 M pixel recording digital color camera [Olympus, DP71].

Chromosome imaging: blue channel, exposal time (1/2000 s)

ZP imaging: red channel, exposal time (1/5 s)

Reference

[1] R. Yarchoan, H. Mitsuya, C. E. Myers, S. Broder, *N. Engl. J. Med*. **1989**, *321*, 726.

[2] M. A. Fischl, D. D. Richman, M. H. Grieco, M. S. Gottlieb, P. A. Volberding, O. L. Laskin, J. M. Leedom, J. E. Groopman, D. Mildvan, R. T. Schooley, G. G. Jackson, D. T. Durack, D. King, *N. Engl. J. Med*. **1987**, *317*, 185 and the AZT collaborative working group.

[3] E. M. Connor, et al., *N. Engl. J. Med*. **1994**, *331*, 1173.

[4] E. D. Clercq, *Nat. Rev. Drug Discovery* **2002**, *1*, 13.

[5] W. Nickel, S. Austermann, G. Bialek, F. Grosse, *J. Biol. Chem*. **1992**, *267*, 848.

[6] M. A. Fischl, et al., *J. Am. Med. Assoc*. **1989**, *262*, 2405.

[7] R. P. Agarwal, O. A. Olivero, *Mutat. Res., Genet. Toxicol. Environ. Mutagen.* **1997**, *390*, 223.

[8] O. A. Olivero, M. C. Poirier, *Mol. Carcinog*. **1993**, *8*, 81.

[9] O. A. Olivero, J. J. Fernandez, B. B. Antiochos, J. L. Wagner, M. E. S. Claire, M. C. Poirier, *J. Acquired Immune Defic. Syndr*. **2002**, *29*, 323.

[10] W. P. Heal, B. Jovanovic, S. Bessin, M. H. Wright, A. I. Magee, E. W. Tate, *Chem. Commun*. **2011**, *47*, 4081.

[11] R. K. V. Lim, Q. Lin, *Chem. Commun.* **2010**, *46*, 1589.

[12] A. E. Speers, G. C. Adam, B. F. Cravatt, *J. Am. Chem. Soc*. **2003**, *125*, 4686.

[13] X. Liu, W. Xie, R. H. Huang, *Bioorg. Med. Chem. Lett.* **2005**, *15*, 3775.

[14] J. Abbotts, S. H. Wilson, *J. Enzyme Inhib. Med. Chem.* **1992**, *6*, 35.

[15] O. A. Olivero, F. A. Beland, M. C. Poirier, *Int. J. Oncol*. **1994**, *4*, 49.

[16] A. Carr, D. A. Cooper, *Lancet* **2000**, *356*, 1423.

[17] H. Ris, *Methods in Cell Biology* (Turner, J. N., Ed.), **1981**, *22*, 80, Academic press, New York.

Part II

Screening and Target Identification of Bioactive Small molecules

Chapter 1. Screening of a Benzopyran-Containing Androgen Receptor Antagonist to Treat Antiandrogen-Resistant Prostate Cancer

Introduction

Prostate cancer is a major cause of death in men worldwide, especially in the USA.[1] Key molecular targets in prostate cancer therapy are the androgen receptor (AR) and its endogenous ligands, such as dihydrotestosterone (DHT). The AR is a member of the nuclear receptor superfamily of ligand-dependent transcription factors, and the identification of AR antagonists is an important step in the development of therapeutic agents for the treatment of prostate cancer.[2-4] Currently, AR antagonists such as flutamide and bicalutamide are used as small-molecule antiandrogens in clinical settings. Although these nonsteroidal antiandrogens possess minimal side effects and relatively good oral bioavailability,[5,6] resistance to antiandrogen therapy has been reported, particularly after long-term drug treatment of prostate cancer.

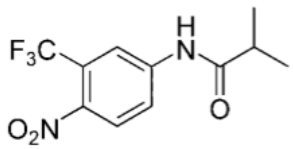

Flutamide

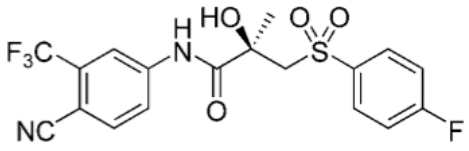

Bicalutamide

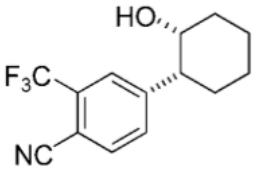

PF-0998425

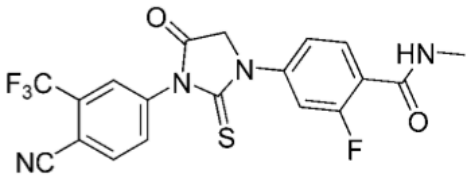

MDV3100

One proposed way by which antiandrogen resistance occurs is through AR mutation, causing the antiandrogens to function as agonists instead of antagonists.[7,8] The T877A AR mutation was identified in androgen-sensitive human

prostate adenocarcinoma (LNCaP) cells in which flutamide acts as an agonist.[9] In addition, the W741C and W741L AR mutations have been identified in a cell line and prostate cancer patients, respectively, with drug resistance to bicalutamide (Bic).[10,11] Once the patient develops hormone-refractory prostate cancer, it is very difficult to treat them with currently available drugs. Therefore, there is widespread demand for new therapeutic agents that overcome the problems associated with advanced prostate cancer. To date, studies have been carried out by various research groups: Koh's group[12] used molecular-design-based research to discover new antiandrogen compounds and Sawyer's group[13] recently reported the development of MVD3100 against hormone-refractory prostate cancer. It is worth mentioning that these nonsteroidal antiandrogen agents, and also PF-0998425 developed by Pfizer,[14] share a common substructure derived from the well-known structure of bicalutamide; therefore, the identification of new molecular frameworks for antiandrogens has long been awaited by the scientific community.

Results and Discussion

Herein, we present a novel, nonsteroidal, small-molecule AR antagonist as a potential agent against prostate cancer. We previously reported a method for the concise and diversity-oriented synthesis (DOS) of novel scaffolds embedded with well-known privileged substructures via various chemical transformations.[15,16] Using the DOS approach, we have constructed a novel collection of natural product-like small molecules.[17] We then generated LNCaP prostate cancer cell line stably expressing a luciferase reporter containing triple copies of androgen receptor-binding element (ARE) and used this cell line for the cell-based luciferase reporter assay. By carrying out a medium-throughput screening exercise with our collection of 2000

druglike small molecules, we identified a novel molecular framework **6** with antagonistic potential in competition with the endogenous agonist DHT.

Compd	R^1	R^2	R^3	R^4	Activity[a] [%]
6a	H	H	Ph	Bn	87.0
6b	F	H	Ph	Bn	54.3
6c	OMe	H	Ph	Bn	49.7
6d	H	OMe	Ph	Bn	39.7
6e	OMe	OMe	Ph	Bn	75.7
6f	OH	H	Ph	Bn	15.1
6g	H	OH	Ph	Bn	103.5
6h	OH	OH	Ph	Bn	–[b]
6i	OH	H	Ph	H	123.5
6j	OH	H	Ph	Me	106.5
6k	OH	H	Ph	Ph	56.2
6l	OH	H	Ph	Methoxycarbonyl	118.5
6m	OH	H	Ph	*p*-Acetylphenyl	44.8
6n	OH	H	Ph	3-Chloro-4-methylphenyl	–[c]
6o	OH	H	Ph	*o*-Ethoxyphenyl	50.1
6p	OH	H	Ph	3,5-Dimethylbenzyl	35.4
6q	OH	H	Ph	*p*-Fluorobenzyl	61.1
6r	OH	H	Ph	Thiophen-2-ylmethyl	46.1
6s	OH	H	H	Bn	78.6
Bic[d]	–	–	–	–	28.2

Table 1. Compounds in the focused library and their antagonistic activities.

[a] Relative luciferase activity induced by the treatment of individual compounds at 10 μM in the presence of 10 nM DHT; 100 % refers the luciferase activity under the treatment of 10 nM DHT. [b] Not determined due to compound instability. [c] Not determined due to compound cytotoxicity. [d] Bicalutamide.

Using the initial screening results, we designed a focused library containing 19 analogues to enhance the efficacy of **6**, as well as to understand the structure–activity relationships (see Table 1). The synthesis of the desired analogues was accomplished through a series of reactions: cyclization of hydroxyacetophenones **1** with cyclopentanone, triflation, palladium-mediated vinylation, and subsequent Diels–Alder reaction with various maleimides provided a diastereochemically enriched

tetracyclic framework **5** via *endo*-favored cycloaddition (see Scheme 1). Interestingly, we obtained the desired molecular framework **6** in the form of an allylic alcohol, rather than an epoxide, as a single diastereomer after *m*CPBA treatment, probably because of ring distortion in the sterically crowded structure. The allylic alcohol moiety in scaffold **6** was shown to be essential for antagonistic activity, as other benzopyran-fused tetracycles, such as monoene, hydrogenated tetracycle, aromatized tetracycle were shown to be inactive.[15] The exact structure of this molecular framework was determined by NMR as well as X-ray crystallography (see Figure 1).

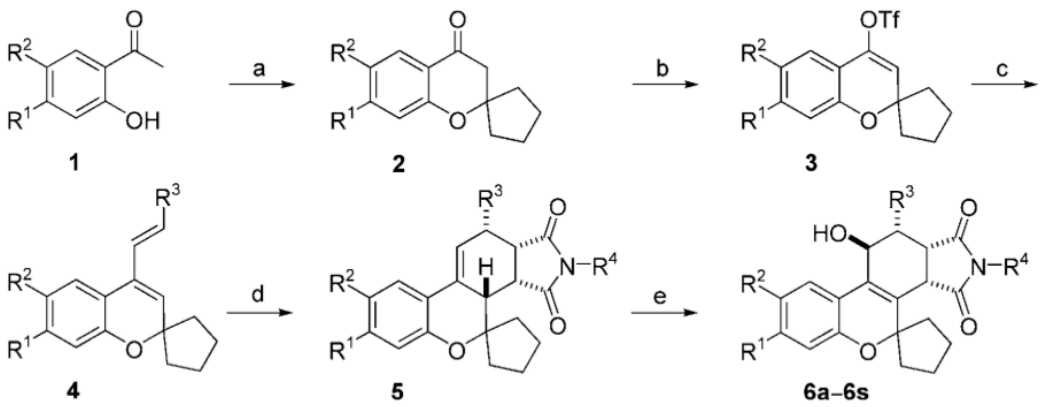

Scheme 1. Synthetic Scheme of the novel benzopyran-embedded molecular framework **6**. *Reagents and conditions*: a) cyclopentanone, pyrrolidine, EtOH, reflux; b) Tf_2O, DTBMP, CH_2Cl_2, 0 °C; c) boronic acids, Na_2CO_3, $Pd(PPh_3)_4$, EtOH/toluene/H_2O, 70 °C; d) maleimide derivatives, toluene, reflux; e) *m*CPBA, DTBMP, CH_2Cl_2, 0 °C.

After the construction of the 19-membered focused library with the novel molecular framework **6**, we evaluated their antagonistic activities against DHT by using an ARE-luciferase reporter assay in LNCaP stable cell line, established by the transfection of ARE-luciferase/pcDNA3 (9:1) plasmid mixture using lipofectamine 2000. ARE-luciferase-containing LNCaP cells were treated with 20 nm of DHT, as well as either 10 μm of test compound or bicalutamide. As shown in Table 1, treatment with compound **6 f** can antagonize AR-dependent transcriptional activation by up to 15 % compared with that of fully agonized AR activity. In comparison,

various substituents at the R^1 and R^2 positions (**6 a–e**) did not affect the antagonistic efficacy of molecular framework **6**. In particular, the significant reduction in efficacy seen for compound **6 g**—a regioisomer of **6 f** with the hydroxy group in the R^1 position—demonstrates the site-specific hydrogen bonding interaction. The introduction of various appendages at the R^3 and R^4 positions (**6 i–s**) did not improve the antagonistic efficacy over that of compound **6 f** in the cell-based reporter gene assay, and some of these modification lead to cytotoxicity in LNCaP cell lines. Therefore, we successfully demonstrated the structure–activity relationship of a nonsteroidal, small-molecule AR antagonist **6 f**.

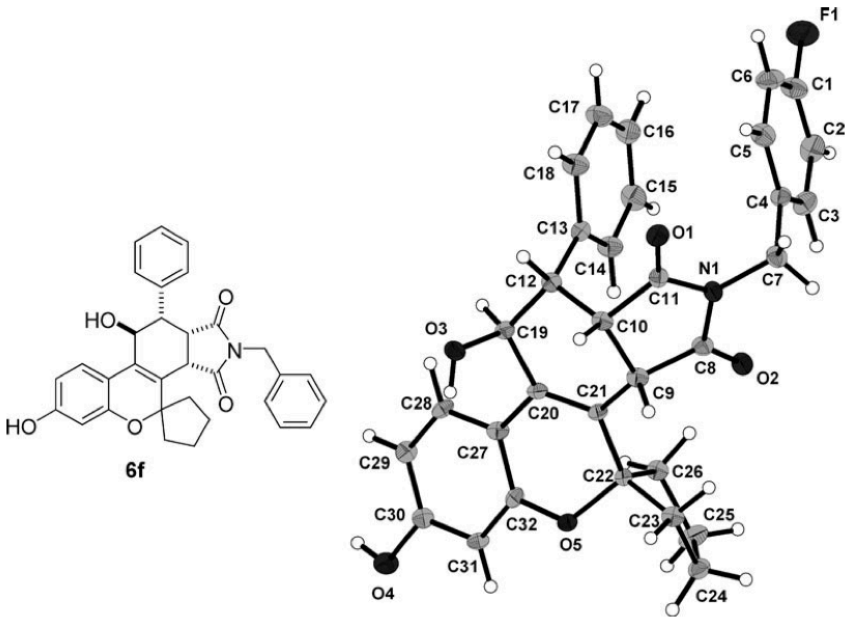

Figure 1. Novel antagonist **6 f** (left), and the X-ray crystal structure of its representative core skeleton (**6 q**) (right).

The antagonistic activity of **6 f** in competition with DHT was further verified by luciferase reporter gene assay after transfection of wild-type (WT) AR in 293T (human embryonic kidney) cells; these cells have no endogenous AR, and therefore no basal levels of AR activity can be expected in this system. As shown in Figure 2, the full agonistic activity of WT AR was achieved by the transient co-transfection of

plasmids containing ARE-luciferase and WT AR in the presence of DHT. The antagonistic activity of compound **6 f** was comparable to that of bicalutamide in 293T cells.

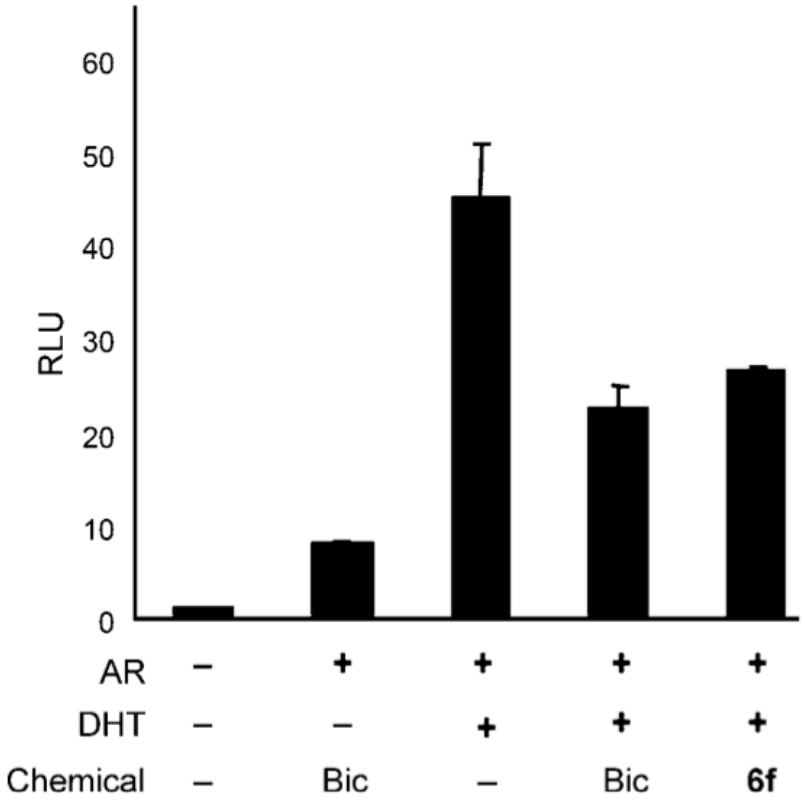

Figure 2. Antagonistic activities of compound **6 f** in cell-based luciferase reporter assay in 293T cells co-transfected with ARE-luciferase and WT AR. RLU=relative light units ±SEM. 20 nM of DHT, 10 μM of bicalutamide (Bic) or compound **6 f**.

We then subjected the new AR antagonist, compound **6 f**, to immunoblot analysis to monitor the androgen-dependent AR target-gene expressions in LNCaP cells. The expression level of prostate specific antigen (*PSA*), a biomarker for prostate cancer, was significantly retarded after treatment with both compound **6 f** and bicalutamide (see Figure 3 a). The transcription levels of AR target genes exemplified by*PSA*, kallikrein-related peptidase 2 (*KLK2*), and NK3 transcription factor related locus 1 (*NKX3.1*) were diminished by the antagonist effects of compound **6 f**, which had potency similar to that of bicalutamide (see Figure 3 b). We also demonstrated

diminished proliferation of prostate cancer cells using a BrdU incorporation assay and a cellular proliferation assay (see Figure 3 c and 3 d). Compound **6 f** suppressed DHT-induced cellular growth more effectively than bicalutamide. However, this growth inhibition was not associated with the cytotoxicity of compound **6 f**; this was confirmed by measuring the enzymatic activities of caspases 3/7 and CCK in a cell viability assay using various cell lines (see Supporting Information). Compound **6 f** preserves >95 % cell viability after 24 h treatment at 20 μm concentration in HeLa human cervical cancer cell, LNCaP human prostate cancer cell, and NIH-3T3 mouse fibroblast normal cell.

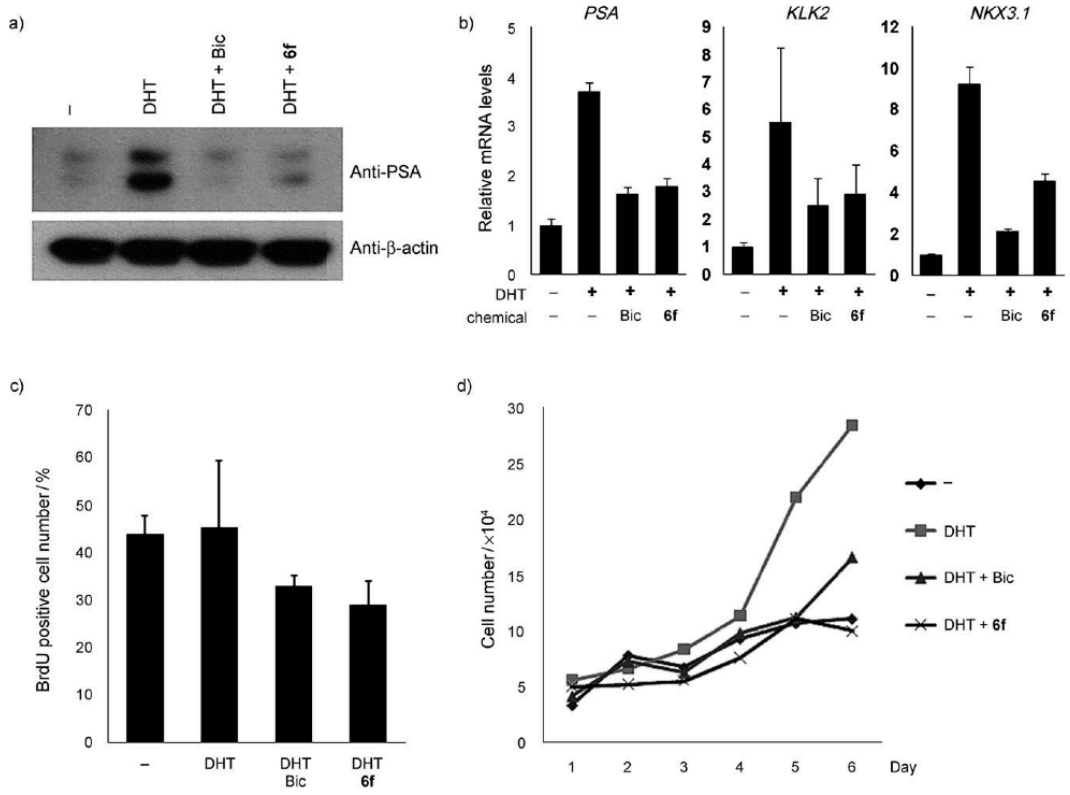

Figure 3. Confirmation of antagonistic activity of compound **6 f** by in vitro evaluation. a) Western blot analysis of AR-dependent gene expression in LNCaP cells (normalized to β-actin); b) Quantitative RT-PCR analysis of mRNA on AR-dependent genes, such as *PSA*, *KLK2*, and *NKX3.1* in LNCaP cells; c) BrdU assay after 24 h ligand treatment; d) Cellular proliferation assay; 20 nM of DHT, 10 μM of bicalutamide (Bic) or compound **6 f**.

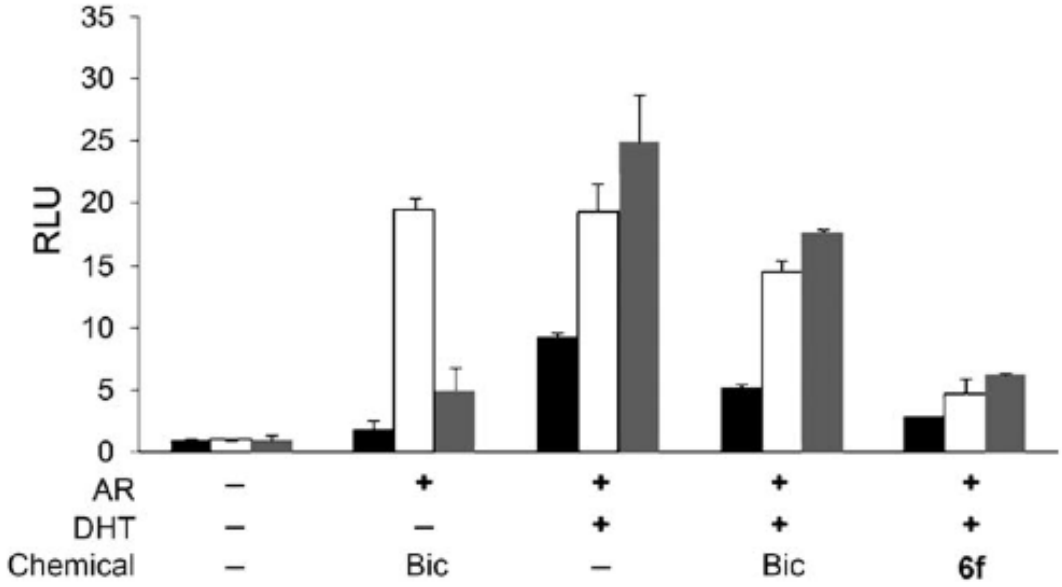

Figure 4. Antagonistic activities of bicalutamide and compound **6 f** in cell-based reporter-gene assay in 293T cells co-transfected with ARE-luciferase and WT AR (■) or AR mutant plasmids (W741L,□; T877A,▒). RLU=relative light units ±SEM.

Although we demonstrated the excellent potency of compound **6 f**, comparable to that of bicalutamide (a leading therapeutic agent), it remained to be seen whether compound **6 f** is effective against hormone-refractory prostate cancer. To verify this, 293T cells were transiently transfected with either WT AR or AR mutant plasmids (W741L or T877A), for inducing antiandrogen resistance, along with the ARE-luciferase reporter. As shown in Figure 4, both compound **6 f** and bicalutamide showed antagonistic activities against WT AR. However, bicalutamide acted as an agonist, not an antagonist, on the bicalutamide-resistant AR mutant (W741L) even without DHT treatment, whereas compound **6 f** retained its antagonistic activity toward this AR mutant. In the case of T877A AR mutant, compound **6 f** effectively antagonized the AR activity. Surprisingly, bicalutamide had little or no antagonistic effects on either of the clinically relevant AR mutant cell lines. Therefore, compound **6 f** might be suitable for use as a potential therapeutic agent in the treatment of hormone-refractory prostate cancer through antagonizing antiandrogen-

resistant mutant ARs. Unfortunately, we failed to demonstrate the in vivo efficacy of compound **6 f**, due to its poor solubility and oral bioavailability (data not shown).

Conclusion

We discovered a novel nonsteroidal AR antagonist using a cell-based reporter gene assay, along with our small-molecule library constructed using a diversity-oriented synthetic pathway. From 19 synthetic analogues containing a novel benzopyran-fused tetracyclic core skeleton, compound **6 f** was identified as having an excellent antagonistic activity confirmed by western blot analysis, RT-PCR, and in vitro cellular proliferation assay. We also demonstrated that compound **6 f** is active against not only WT AR but also mutant AR, such as T877A or W741L (bicalutamide-resistant AR mutant). The poor bioavailability/water solubility of compound **6 f** may limit its potential as a therapeutic agent; however, this new molecular framework might provide valuable insight for the development of therapeutics able to treat advanced prostate cancer. Studies into the mode-of-action are currently underway.

Supporting Information

Cell Culture : LNCaP cells [ATCC, VA, USA] were cultured in Iscove's modified Dulbecco's media (IMDM) [Welgene, Daegu, South Korea] supplemented with 10% (v/v) FBS [GIBCO, Invitrogen, CA, USA] and 1 % (v/v) antibiotic-antimycotic solution [GIBCO, Invitrogen, CA, USA]. 293T cells [ATCC, VA, USA] were cultured in Dulbecco's modified Eagle's medium (DMEM) [GIBCO, Invitrogen, CA, USA] supplemented with 10% (v/v) FBS and 1 % (v/v) antibiotic-antimycotic solution. The cells were maintained in a humidified atmosphere of 5% CO_2 and 95% air at 37 °C, and cultured in T75 flask [Nalgene Nunc International, IN, USA]. The surface of T75 was coated with poly-D-lysine [Sigma, MO, USA] before cell culture.

Establishment of stable cell lines : LNCaP cells were seed in 100 mm culture dish [Corning, MA, USA]. ARE-luciferase: pcDNA3 (9:1) plasmid mixture was transfected to LNCaP cells using lipofectamine 2000 [Invitrogen, CA, USA]. After 24 h, G418 [Sigma, MO, USA] was added to the media for the selection. In the next, one cell originated colony selection was performed. After colony selection, ARE-luciferase containing colony was founded by luciferase assay.

High throughput screening for androgen receptor antagonist : 1×10^4 of LNCaP stable cells were seeded on 96-well white plate [BD falcon, MD, USA] coated with poly-D-lysine hydrobromide [Sigma, MO, USA] and cultured with phenol red-free IMDM medium supplemented with 10% charcoal:dextran stripped FBS [Gemini Bio-Products, CA, USA] and 1% (v/v) antibiotic-antimycotic solution. After 24 h, 20 nM of dihydrotestosterone (DHT) [TCI, Tokyo, Japan], 10 μM of each compound (about 2,000 compounds) and 20 μM of bicalutamide [LKT laboratories, MN, USA] were

treated to cells and incubate for another 24 h. The cells were washed with PBS and drained out the PBS using Hydroflex^{TM} [Tecan, Switzerland]. After the injection of 50 μL of passive cell lysis buffer [Promega, WI, USA] to individual wells of 96-well plate, the plate was incubated for 30 min at room temperature. Finally, 50 μL of luciferase assay reagent solution [Promega, WI, USA] was added to each well. The resulting luminescence was detected by Synergy HT [BioTek, VT, USA].

Caspase 3/7 luciferase assay : Caspase 3/7 activity was measured by using Caspase-Glo 3/7 assay kit [Promega, WI, USA]. 1×10^4 of LNCaP cells were seeded on poly-D-lysine-treated 96-well white plate. After 24 h, 20 nM of DHT and 10 μM of each compounds were introduced to cells in plate and incubated for additional 24 h. 100 μL of caspase assay solution was added to individual wells of 96-well plate. The solution in the well was gently mixed for 30 seconds and incubated for additional 1 h at room temperature. The resulting luminescence was detected by Synergy HT.

Luciferase assays : 293T cells were grown and transiently transfected using calcium phosphate method. For luciferase assays, 1×10^5 cells were seeded in phenol red-free DMEM medium [Welgene, Daegu, South Korea] supplemented with 10% charcoal:dextran-stripped FBS for 24 h. Cells were transfected with 500 ng of an ARE-luciferase reporter along with 25 ng of several AR constructs and 100 ng of a β-galactosidase expression construct. After 24 h of transfection, cells were treated with 20 nM DHT and 20 μM chemicals for 18 h and then luciferease activity was measured. Transfection efficiency was normalized using a β-galactosidase activity and the results were obtained from at least three independent experiments.

Western Blot Analysis : The samples of protein extracts were loaded and separated using 12% SDS-PAGE and then transferred to a PVDF membrane. The membrane was blocked for 30 min at room temperature using 5% skim milk / 0.1% PBST. After blocking, the membrane was incubated with a primary antibody by diluting in blocking buffer (1:1000) for 1 h. The membrane was washed in 0.1% PBST four times at 10-min interval. Then, the membrane was incubated with a secondary HRP antibody for additional 1 h. The membrane was washed in 0.1% PBST four times at 10-min interval. After final wash, the membrane was added ECL solution for 3 min at RT, and captured western blot image using X-ray film. PSA antibody (SC-7638) was purchased from Santa Cruz Biotechnology [CA, USA].

in vitro Cytotoxicity assay : Cell viability was measured by the Cell Counting Kit (CCK)-8 assay [Dojindo, Japan], and the experimental procedure is based on the manufacturer's manual. Cells were cultured into 96-well plates at a density of 2×10^4 cells/well for 24 h, followed by the treatment of compound 6f in various concentrations. After 24 h incubation with compound 6f, 10 μL of WST-8 solution (2-(2-methoxy-4-nitrophenyl)-3-(4-nitrophenyl)-5-(2,4-disulfophenyl)-2*H*-tetrazolium, monosodium salt, [Sigma-Aldrich, MO, USA]) was added to each well, and plates were incubated for additional 2 h at 37 °C. The absorbance of each well at 450 nm was measured with a reference at 630 nm using ELx800^{TM} microplate reader [BioTek, VT, USA]. The number of cell viability was calculated by following formula: (mean absorbance in test wells) / (mean absorbance in control wells) × 10.

BrdU incorporation assay : LNCaP cells were seeded on coverslips in phenol red-free DMEM medium supplemented with 5% charcoal:dextran-stripped FBS for 24 h. Cells

were incubated in bromodeoxyuridine (BrdU) [Sigma, MO, USA], DHT, and chemical-containing culture media for 24 h. After fixation of cells, BrdU labeling was processed used by BrdU antibody, ab6326 [Abcam, UK]. The positively stained cell population was quantified and then expressed as percentage compared to the total cells.

Proliferation assay : 7×10^4 LNCaP cells were seeded in 6-well plate [Corning, MA, USA]. After 24 h, compounds were treated to cells with DHT. Cells were detached after 1, 2, 3, 4, 5, and 6 days and then the cell number was counted with hematocytometer.

Quantitative RT-PCR : Total RNA were isolated by Trizol method and then used for reverse transcription. Quantitative RT-PCR was performed in Applied Biosystems 7300 [Applied Biosystems Inc., CA, USA]. Product formation was detected by incorporation of SYBR green [Molecular Probes, OR, USA].

The following primers were used:

PSA sense 5'-CTCTCGTGGCAGGGCAGTCTG-3'

PSA antisense 5'-GGTCGTGGCTGGAGTCATCAC-3'

KLK2 sense 5'-AGCCTTCATTCTCCAGGACC-3'

KLK2 antisense 5'-CGTGAGAATGCCTCCAGACT-3'

NKX3.1 sense 5'-TGAAGGCGCAGGCTTACTG-3'

NKX3.1 antisense 5'-TAGGCTGCCTTCTTTTCCATGT-3'

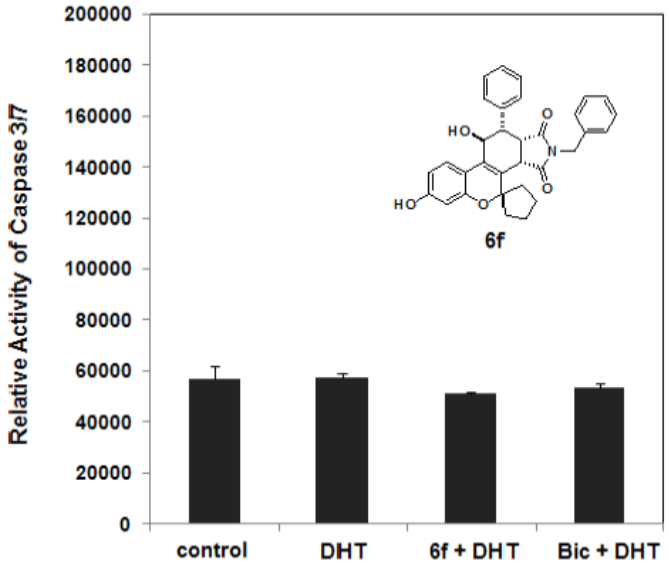

Figure S1. Caspase 3/7 activity measurement; 20 nM of DHT, 10 μM of compound 6f or bicalutamide.

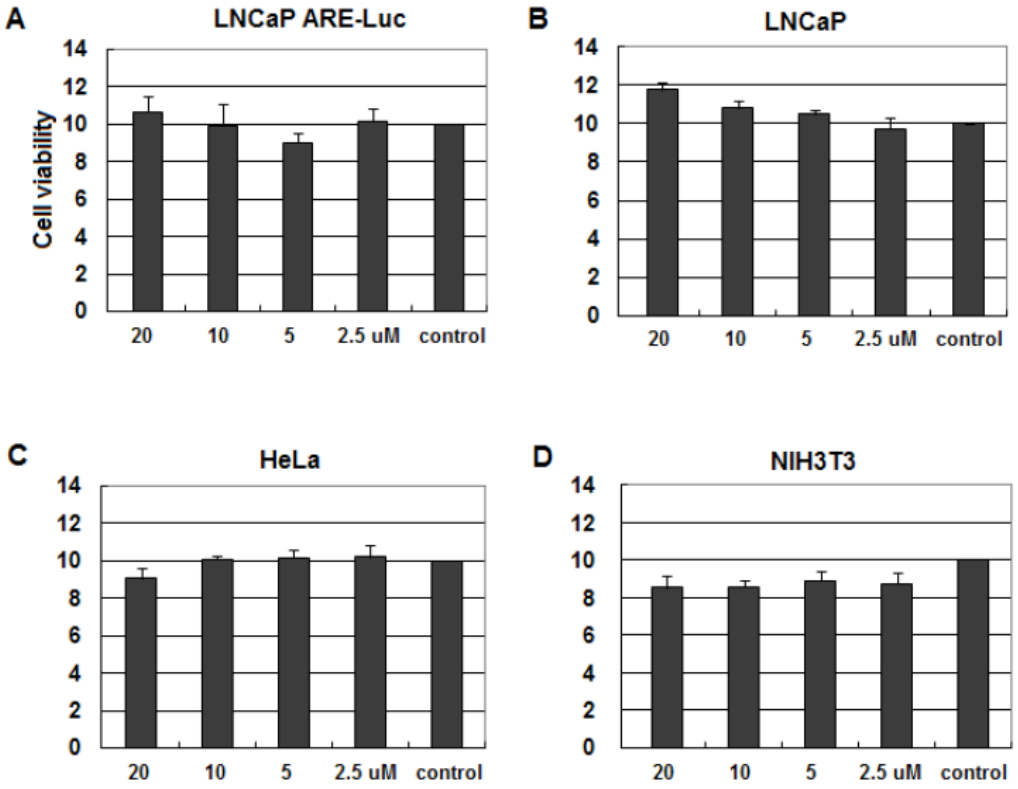

Figure S2. Cell viability of compound 6f measured by the Cell Counting Kit (CCK)-8 assay in various cell lines: (A) LNCaP cell line stably expressing luciferase reporter containing 3X androgen receptor binding element (ARE); (B) LNCaP cell line; (C) cervical cancer cell line (HeLa); (D) mouse embryonic fibroblast cell line (NIH3T3).

General Information about Synthesis : ^{1}H and ^{13}C NMR spectra were recorded on a Varian Inova-500 [Varian Assoc., Palo Alto, USA], and chemical shifts were measured in ppm relative to internal tetramethylsilane (TMS) standard or specific solvent signal. Multiplicity was indicated as follows: s (singlet); d (doublet); t (triplet); q (quartet); m (multiplet); dd (doublet of doublet); dt (doublet of triplet); td (triplet of doublet); bs (broad singlet), etc. Coupling constants were reported in Hz. Routine mass analyses were performed on LC/MS system equipped with a reverse phase column (C-18, 50 × 2.1 mm, 5 μm) and photodiode array detector using atmospheric pressure chemical ionization (APCI). The HRMS analyses were conducted at the Mass Spectrometry Laboratory of Seoul National University by direct injection on JEOL JMS AX505WA spectrometer using fast atom bombardment (FAB) method.

All reagents in this synthetic procedure were purchase from Sigma-Aldrich [MO, USA] and TCI [Japan]. The progress of reaction was monitored using thin-layer chromatography (TLC) (silica gel 60 F_{254} 0.25 mm), and components were visualized by observation under UV light (254 and 365 nm) or by treating the TLC plates with anisaldehyde staining solution followed by heating. Silica gel 60 (0.040–0.063 mm) used in flash column chromatography was purchased from Merck [Germany]. All reactions were conducted in oven-dried glassware under dry argon atmosphere, unless otherwise specified. CH_2Cl_2 was distilled from CaH_2 immediately prior to use. Other solvents and organic reagents were purchased from commercial venders and used without further purification unless otherwise mentioned.

General procedure for the cyclization of hydroxyacetophenone : Hydroxyacetophenone **1** (1.0 equiv.) was dissolved in EtOH. Pyrrolidine (3.0 equiv.) and cyclopentanone (3.0 equiv.) were added in this mixture sequentially and then

heated to reflux for about 24 h. After the completion of reaction monitored by TLC, the reaction mixture was concentrated *in vacuo*. Evaporated residue was re-dissolved in ethyl acetate and washed several times with 1N HCl solution. After washing with brine, the combined organic layer was dried over anhydrous $MgSO_4$, filtrated, and evaporated under reduced pressure. The resulting mixture was purified with silica gel flash column chromatography to provide desired product **2**. If there was more than one free hydroxyl groups in benzopyran ring generated by demethylation, silyl protection was needed before the next reaction.[15]

Compound 2a (R^1 = hydro, R^2 = hydro)

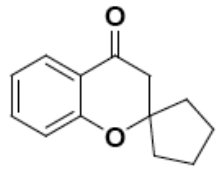

Colorless oil (76% from hydroxyacetophenone); this compound was previously reported.[18]

Compound 2b (R^1 = fluoro, R^2 = hydro)

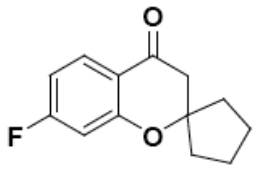

Colorless oil (37% from 4'-fluoro-2'-hydroxyacetophenone); ^{1}H-NMR (500 MHz, $CDCl_3$): δ 7.87 (dd, *J* = 8.5 and 6.5 Hz, 1H), 6.69 (td, *J* = 8.5 and 2.0 Hz, 1H), 6.61 (dd, *J* = 10.0 and 2.0 Hz, 1H), 2.81 (s, 2H), 2.09–2.05 (m, 2H), 1.88–1.85 (m, 2H), 1.74–1.63 (m, 4H).

Compound 2c (R^1 = methoxy, R^2 = hydro)

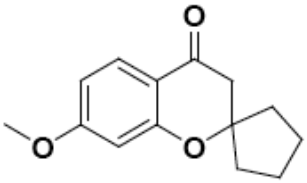

Colorless crystal (58% from 2'-hydroxy-4'-methoxyacetophenone); this compound was previously reported.[15]

Compound 2d (R^1 = hydro, R^2 = methoxy)

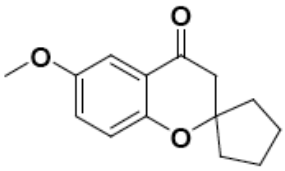

Colorless crystal (72% from 2'-hydroxy-5'-methoxyacetophenone); ^{1}H-NMR (500 MHz, $CDCl_3$): δ 7.30 (d, *J* = 3.0 Hz, 1H), 7.07 (d, *J* = 9.0 and 3.0 Hz, 1H), 6.85 (d, *J* = 9.0 Hz, 1H), 3.79 (s, 3H), 2.81 (s, 2H), 2.09–2.04 (m, 2H), 1.89–1.85 (m, 2H), 1.73–1.61 (m, 4H).

Compound 2e (R^1 = methoxy, R^2 = methoxy)

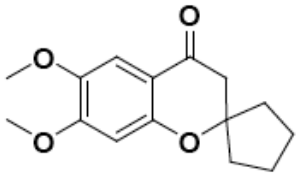

Colorless crystal (81% from 2'-hydroxy-4',5'-methoxyacetophenone); ^{1}H-NMR (500 MHz, $CDCl_3$): δ 7.27 (s, 1H), 6.40 (s, 1H), 3.91 (s, 3H), 3.87 (s, 3H), 2.77 (s, 2H), 2.10–2.04 (m, 2H), 1.88–1.84 (m, 2H), 1.77–1.60 (m, 4H).

Compound 2f (R^1 = hydroxy, R^2 = hydro)

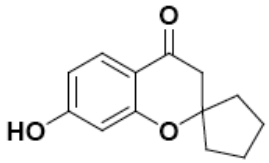

Colorless crystal (91% from compound 2c); this compound was previously reported.[18]

Compound 2g (R^1 = hydro, R^2 = hydroxy)

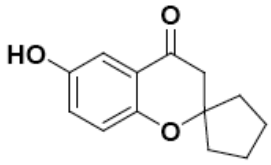

Colorless crystal (93% from compound 2d); ^{1}H-NMR (500 MHz, CD_3OD): δ 7.15 (d, *J* = 3.5 Hz, 1H), 6.99 (d, *J* = 9.0 and 3.5 Hz, 1H), 6.80 (d, *J* = 9.0 Hz, 1H), 4.92 (bs, 1H), 2.79 (s, 2H), 2.05–2.00 (m, 2H), 1.86–1.82 (m, 2H), 1.75–1.61 (m, 4H).

Compound 2h (R^1 = hydroxy, R^2 = hydroxy)

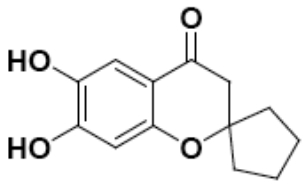

Colorless crystal (86% from compound 2e); ^{1}H-NMR (500 MHz, CD_3OD): δ 7.12 (s, 1H), 6.28 (s, 1H), 4.96 (bs, 2H), 2.69 (s, 2H), 2.02–1.97 (m, 2H), 1.82–1.77 (m, 2H), 1.72–1.57 (m, 4H).

General procedure for the formation of enol-O-triflate : The compound **2** (1.0 equiv.) and 2,6-di-*tert*-butyl-4-methylpyridine (DTBMP, 1.3 equiv.) were dissolved in anhydrous CH_2Cl_2. Triflic anhydride (Tf_2O, 1.2 equiv.) was added in this mixture at 0 °C with ice-bath under N_2 atmosphere. After the reaction mixture was stirred for 10 min at the same temperature, the resulting solid was filtered off and the filtrate was concentrated *in vacuo*. Evaporated residue was re-dissolved in ethyl acetate and washed with sat. $NaHCO_3$ solution and brine. The combined organic layer was dried over anhydrous $MgSO_4$, filtrated, and evaporated under reduced pressure. The resulting mixture was purified with silica gel flash column chromatography to provide desired product **3**.

*General procedure of Suzuki coupling for compound **4** :* Compound **3** (1.0 equiv.), boronic acid derivative (1.1 equiv.), $Pd(PPh_3)_4$ (5 mol%) and Na_2CO_3 (3.0 equiv.) were suspended in solvent mixture of EtOH : toluene : H_2O (1 : 1 : 0.5). The reaction mixture was stirred 70 °C for about 10 h. After reaction completion monitored by TLC, the resulting mixture was diluted with ethyl acetate and then washed with brine. The organic layer was dried over anhydrous $MgSO_4$, filtrated, and evaporated under reduced pressure. The resulting crude product **4** was used in the next reaction without further purification.

*General procedure of Diels-Alder reaction for compound **5** :* The crude diene compound **4** and maleimide derivative (1.1 equiv.) were dissolved in toluene. This reaction mixture was heated to reflux for 24 h. After reaction completion monitored by TLC, the reaction mixture was concentrated *in vacuo*. The resulting mixture was purified with silica gel flash column chromatography to provide desired product **5**.

Compound 5a

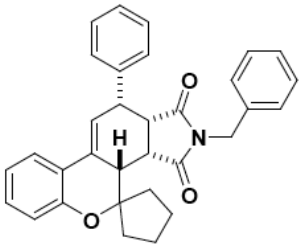

Yellowish solid (70% from enol-*O*-triflate); ^{1}H-NMR (500 MHz, $CDCl_3$): δ 7.52 (dd, J = 8.0 and 1.5 Hz, 1H), 7.40 (t, J = 7.5 Hz, 2H), 7.35–7.29 (m, 3H), 7.24–7.20 (m, 2H), 7.18–7.15 (m, 1H), 7.13–7.10 (m, 1H), 7.03–6.96 (m, 4H), 6.20 (q, J = 2.5 Hz, 1H), 4.55–4.35 (AB q, J_{AB} = 14.3 Hz, 2H), 3.77 (t, J = 5.5 Hz, 1H), 3.52 (dd, J = 8.0 and 5.5 Hz, 1H), 3.44 (dd, J = 8.0 and 6.5 Hz, 1H), 2.90–2.86 (m, 1H), 2.81 (dd, J = 5.0 and 1.5 Hz, 1H), 2.17–2.15 (m, 1H), 2.04–1.96 (m, 2H), 1.92–1.83 (m, 2H), 1.73–1.69 (m, 1H), 1.49–1.42 (m, 1H); ^{13}C-NMR (125 MHz, $CDCl_3$): δ 175.4, 175.2, 152.9, 138.8, 135.8, 133.4, 129.4, 128.9, 128.4, 128.3, 128.2, 128.1, 127.4, 127.2, 122.8, 122.0, 121.5, 119.3, 86.9, 48.1, 45.4, 43.2, 42.8, 42.1, 39.8, 36.1, 23.6, 23.3.

Compound 5b

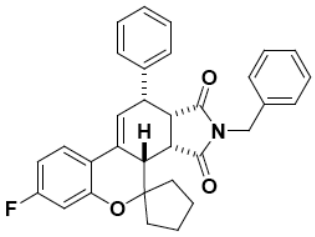

Yellowish solid (62% from enol-*O*-triflate); ^{1}H-NMR (500 MHz, $CDCl_3$): δ 7.35–7.29 (m, 3H), 7.26–7.23 (m, 1H), 7.20–7.19 (m, 2H), 7.06–7.02 (m, 1H), 6.96–6.91 (m, 4H), 6.59–6.54 (m, 2H), 6.41 (q, J = 2.5 Hz, 1H), 4.44–4.28 (AB q, J_{AB} = 14.3 Hz, 2H), 3.67 (t, J = 5.5 Hz, 1H), 3.44 (dd, J = 8.0 and 5.5 Hz, 1H), 3.37 (dd, J = 8.0 and 6.5 Hz, 1H), 2.77–2.73 (m, 1H), 2.71–2.69 (m, 1H), 2.05–1.98 (m, 1H), 1.92–1.86 (m, 2H), 1.81–1.72 (m, 2H), 1.64–1.60 (m, 1H), 1.39–1.33 (m, 1H); 13C-NMR (125 MHz, CDCl3): δ 175.4, 175.3, 164.6, 162.6, 154.3, 154.2, 138.7, 135.9, 132.7, 129.0, 128.5, 128.4, 127.7, 127.5, 124.2, 124.1, 121.1, 121.0, 118.4, 109.3, 109.2, 106.5, 106.3, 87.8, 48.3, 45.3, 43.4, 43.0, 42.3, 40.1, 36.3, 23.8, 23.4.

Compound 5c

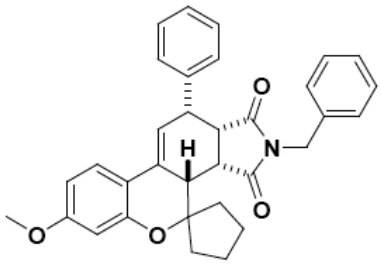

Yellowish solid (75% from enol-*O*-triflate); ^{1}H-NMR (500 MHz, $CDCl_3$): δ 7.38–7.33 (m, 3H), 7.29–7.25 (m, 1H), 7.24–7.21 (m,2H), 7.10–7.07 (m, 1H), 7.01–6.95 (m, 4H), 6.51 (dd, J = 8.5 and 2.5 Hz, 1H), 6.45 (d, J = 2.5 Hz, 1H), 6.39 (dd, J = 4.5 and 2.5 Hz, 1H), 4.50–4.31 (AB q, J_{AB} = 14.5 Hz, 2H), 3.77 (s, 3H), 3.73 (t, J = 5.5 Hz, 1H), 3.47 (dd, J = 8.0 and 5.5 Hz, 1H), 3.39 (dd, J = 8.0 and 6.0 Hz, 1H), 2.82–2.78 (m, 1H), 2.74–2.73 (m, 1H), 2.11–2.08 (m, 1H), 2.01–1.91 (m, 2H), 1.87–1.80 (m, 2H), 1.69–1.65 (m, 1H), 1.46–1.41 (m, 1H).

Compound 5d

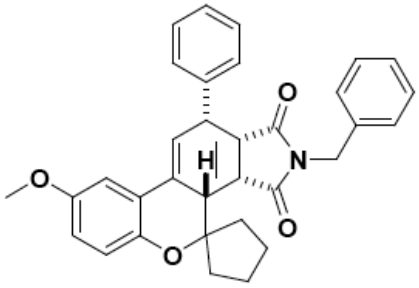

Yellowish solid (71% from enol-*O*-triflate); ^{1}H-NMR (500 MHz, $CDCl_3$): δ 7.38–7.35 (m, 2H), 7.32–7.30 (m, 1H), 7.27–7.25 (m, 2H), 7.11–7.09 (m, 1H), 7.05–7.00 (m, 4H), 6.94 (d, J = 3.0 Hz, 1H), 6.78 (d, J = 8.5 Hz, 1H), 6.72 (dd, J = 8.5 and 2.5 Hz, 1H), 6.49 (dd, J = 5.0 and 2.5 Hz, 1H), 4.52–4.33 (AB q, J_{AB} = 14.5 Hz, 2H), 3.73 (t, J = 5.5 Hz, 1H), 3.50 (dd, J = 8.5 and 5.5 Hz, 1H), 3.42 (dd, J = 8.5 and 6.5 Hz, 1H), 2.82–2.78 (m, 1H), 2.74–2.72 (m, 1H), 2.11–2.07 (m, 1H), 1.99–1.91 (m, 2H), 1.86–1.77 (m, 2H), 1.68–1.64 (m, 1H), 1.42–1.35 (m, 1H).

Compound 5e

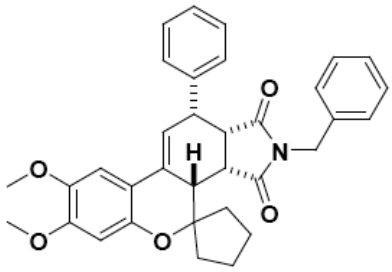

Yellowish solid (62% from enol-*O*-triflate); ^{1}H-NMR (500 MHz, $CDCl_3$): δ 7.38–7.35 (m, 2H), 7.32–7.28 (m, 3H), 7.11–7.08 (m, 1H), 7.01–6.96 (m, 4H), 6.83 (s, 1H), 6.46 (s, 1H), 6.30 (dd, J = 4.5 and 2.0 Hz, 1H), 4.51–4.33 (AB q, J_{AB} = 14.3 Hz, 2H), 3.85 (s, 6H), 3.74 (t, J = 5.5 Hz, 1H), 3.47 (dd, J = 8.5 and 5.5 Hz, 1H), 3.43 (dd, J = 8.0 and 6.5 Hz, 1H), 2.81–2.77 (m, 1H), 2.74–2.73 (m, 1H), 2.13–2.08 (m, 1H), 2.03–1.91 (m, 2H), 1.88–1.80 (m, 2H), 1.70–1.64 (m, 1H), 1.46–1.40 (m, 1H).

Compound 5f

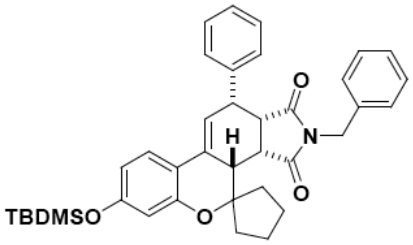

Yellowish solid (74% from enol-*O*-triflate); ^{1}H-NMR (500 MHz, $CDCl_3$): δ 7.36–7.33 (m, 3H), 7.30–7.26 (m, 1H), 7.25–7.23 (m, 2H), 7.11–7.07 (m, 1H), 7.03–6.97 (m, 4H), 6.46 (dd, J = 8.5 and 2.5 Hz, 1H), 6.43 (d, J = 2.5 Hz, 1H), 6.39 (dd, J = 4.5 and 2.5 Hz, 1H), 4.53–4.32 (AB q, J_{AB} = 14.5 Hz, 2H), 3.71 (t, J = 5.5 Hz, 1H), 3.48 (dd, J = 8.0 and 5.5 Hz, 1H), 3.39 (dd, J = 8.0 and 6.5 Hz, 1H), 2.82–2.78 (m, 1H), 2.74–2.73 (m, 1H), 2.11–2.08 (m, 1H), 2.01–1.91 (m, 2H), 1.87–1.79 (m, 2H), 1.69–1.65 (m, 1H), 1.43–1.37 (m, 1H), 0.99 (s, 9H), 0.22 (s, 6H); ^{13}C-NMR (125 MHz, $CDCl_3$): δ 175.6, 175.4, 157.2, 154.1, 139.1, 136.0, 134.4, 133.4, 129.1, 128.9, 128.6, 128.5, 128.3, 127.5, 127.3, 123.8, 119.1, 116.0, 114.4, 110.4, 87.4, 48.3, 45.4, 43.4, 42.9, 42.3, 40.1, 36.3, 25.9, 23.8, 23.4, 18.4, -4.09, -4.12.

Compound 5g

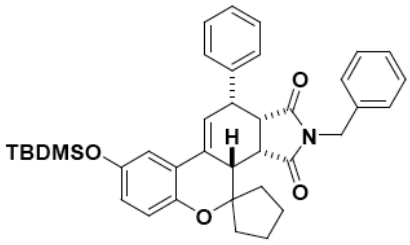

Yellowish solid (69% from enol-*O*-triflate); ^{1}H-NMR (500 MHz, $CDCl_3$): δ 7.39–7.36 (m, 2H), 7.33–7.30 (m, 1H), 7.28–7.26 (m, 2H), 7.12–7.09 (m, 1H), 7.06–7.01 (m, 4H), 6.95 (d, J = 3.0 Hz, 1H), 6.78 (d, J = 8.5 Hz, 1H), 6.72 (dd, J = 8.5 and 2.5 Hz, 1H), 6.49 (dd, J = 5.0 and 2.5 Hz, 1H), 4.52–4.33 (AB q, J_{AB} = 14.5 Hz, 2H), 3.73 (t, J = 5.5 Hz, 1H), 3.50 (dd, J = 8.5 and 5.5 Hz, 1H), 3.42 (dd, J = 8.5 and 6.5 Hz, 1H), 2.82–2.78 (m, 1H), 2.74–2.72 (m, 1H), 2.11–2.07 (m, 1H), 1.99–1.91 (m, 2H), 1.86–1.77 (m, 2H), 1.68–1.64 (m, 1H), 1.42–1.35 (m, 1H), 1.00 (s, 9H), 0.20 (s, 6H); ^{13}C-NMR (125 MHz, $CDCl_3$): δ 175.5, 175.3, 150.1, 147.6, 138.9, 136.0, 133.8, 129.0, 128.4, 127.6, 127.4, 122.6, 121.7, 121.3, 119.9, 113.4, 86.8, 48.3, 45.5, 43.4, 43.0, 42.3, 39.8, 36.3, 26.0, 23.8, 23.5, 18.4, -4.12, -4.15.

Compound 5h

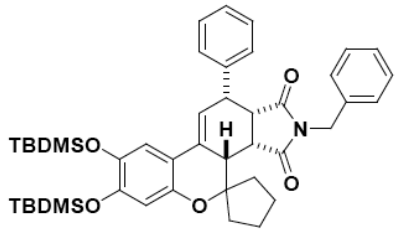

Yellowish solid (71% from enol-*O*-triflate); ^{1}H-NMR (500 MHz, $CDCl_3$): δ 7.36–7.33 (m, 2H), 7.28 (t, J = 7.5 Hz, 1H), 7.25–7.23 (m, 2H), 7.10–7.08 (m, 1H), 7.04–6.99 (m, 4H), 6.86 (d, J = 1.0 Hz, 1H), 6.42 (d, J = 1.0 Hz, 1H), 6.25 (dd, J = 4.5 and 2.0 Hz, 1H), 4.53–4.31 (AB q, J_{AB} = 14.2 Hz, 2H), 3.69 (t, J = 5.5 Hz, 1H), 3.45 (dd, J = 8.5 and 5.5 Hz, 1H), 3.36 (dd, J = 8.0 and 6.5 Hz, 1H), 2.79–2.75 (m, 1H), 2.69–2.68 (m, 1H), 2.09–2.07 (m, 1H), 1.99–1.88 (m, 2H), 1.84–1.76 (m, 2H), 1.67–1.63 (m, 1H), 1.39–1.32 (m, 1H), 0.98 (s, 9H), 0.97 (s, 9H), 0.22 (s, 3H), 0.20 (s, 3H), 0.18 (s, 3H), 0.16 (s, 3H)

Compound 5i

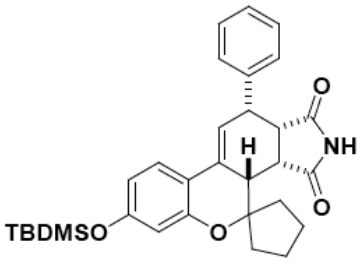

Yellowish solid (62% from enol-*O*-triflate); ^{1}H-NMR (500 MHz, $CDCl_3$): δ 7.67 (bs, 1H), 7.40–7.35 (m, 5H), 7.32–7.29 (m, 1H), 6.54 (dd, *J* = 4.5 and 2.5 Hz, 1H), 6.44 (dd, *J* = 6.5 and 2.0 Hz, 1H), 6.43 (s, 1H), 3.73 (t, *J* = 5.5 Hz, 1H), 3.54 (dd, *J* = 8.5 and 5.5 Hz, 1H), 3.44 (dd, *J* = 8.5 and 7.0 Hz, 1H), 2.73–2.69 (m, 2H), 2.11–2.07 (m, 1H), 2.00–1.90 (m, 2H), 1.87–1.79 (m, 2H), 1.69–1.66 (m, 1H), 1.43–1.37 (m, 1H), 0.97 (s, 9H), 0.20 (s, 3H), 0.19 (s, 3H).

Compound 5j

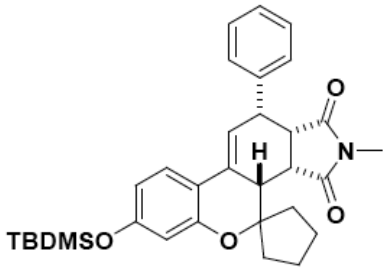

Yellowish solid (69% from enol-*O*-triflate); ^{1}H-NMR (500 MHz, $CDCl_3$): δ 7.43–7.32 (m, 6H), 6.51 (dd, *J* = 4.5 and 2.5 Hz, 1H), 6.45–6.43 (m, 2H), 3.75 (t, *J* = 5.5 Hz, 1H), 3.50 (dd, *J* = 8.0 and 5.5 Hz, 1H), 3.43 (dd, *J* = 8.0 and 7.0 Hz, 1H), 2.82–2.76 (m, 2H), 2.75 (s, 3H), 2.14–2.09 (m, 1H), 2.00–1.94 (m, 2H), 1.86–1.79 (m, 2H), 1.78–1.67 (m, 1H), 1.45–1.39 (m, 1H), 0.97 (s, 9H), 0.21 (s, 3H), 0.20 (s, 3H).

Compound 5k

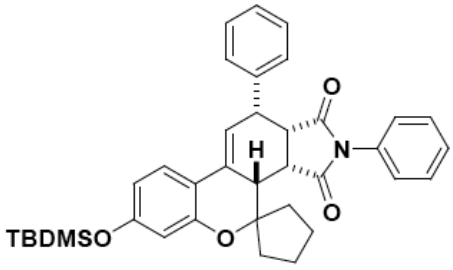

Yellowish solid (83% from enol-*O*-triflate); ^{1}H-NMR (500 MHz, $CDCl_3$): δ 7.47 (d, *J* = 8.0 Hz, 2H), 7.43–7.41 (m, 1H), 7.38 (d, *J* = 8.0 Hz, 2H), 7.36–7.30 (m, 2H), 7.23–7.20 (m, 2H), 6.86 (s, 1H), 6.85–6.83 (m, 1H), 6.66 (dd,

J = 5.0 and 2.5 Hz, 1H), 6.46 (s, 1H), 6.46–6.44 (m, 1H), 3.85 (t, *J* = 4.5 Hz, 1H), 3.64 (t, *J* = 2.5 Hz, 1H), 2.89–2.86 (m, 2H), 2.08–1.99 (m, 3H), 1.87–1.80 (m, 2H), 1.70–1.69 (m, 1H), 1.55–1.48 (m, 1H), 0.98 (s, 9H), 0.21 (s, 3H), 0.20 (s, 3H).

Compound 5l

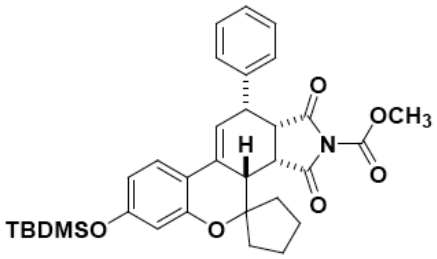

Yellowish solid (56% from enol-*O*-triflate); ^{1}H-NMR (500 MHz, $CDCl_3$): δ 7.42–7.37 (m, 5H), 7.35–7.32 (m, 1H), 6.52 (dd, *J* = 4.5 and 2.5 Hz, 1H), 6.46 (dd, *J* = 8.0 and 2.5 Hz, 1H), 6.44 (d, *J* = 2.5 Hz, 1H), 3.80–3.79 (m, 1H), 3.79 (s, 3H), 3.59 (dd, *J* = 8.5 and 5.0 Hz, 1H), 3.50 (dd, *J* = 8.5 and 7.0 Hz, 1H), 2.79–2.78 (m, 1H), 2.71–2.67 (m, 1H), 2.11–2.09 (m, 1H), 2.02–1.91 (m, 2H), 1.89–1.81 (m, 2H), 1.72–1.68 (m, 1H), 1.48–1.41 (m, 1H), 0.99 (s, 9H), 0.21 (s, 3H), 0.20 (s, 3H).

Compound 5m

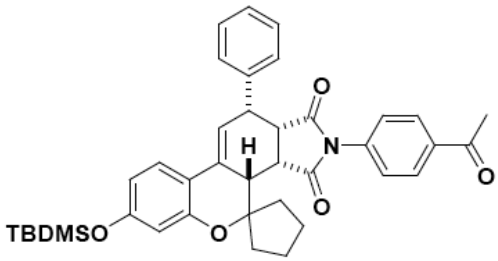

Yellowish solid (78% from enol-*O*-triflate); ^{1}H-NMR (500 MHz, $CDCl_3$): δ 7.82 (dd, *J* = 8.5 and 1.0 Hz, 2H), 7.46–7.39 (m, 5H), 7.34–7.31 (m, 1H), 7.02 (dd, *J* = 8.5 and 1.0 Hz, 2H), 6.65–6.64 (m, 1H), 6.47–6.45 (m, 2H), 3.86–3.85 (m, 1H), 3.69–3.65 (m, 2H), 2.89–2.82 (m, 2H), 2.52 (d, *J* = 1.0 Hz, 3H), 2.11–2.08 (m, 1H), 2.05–1.99 (m, 2H), 1.90–1.80 (m, 2H), 1.72–1.68 (m, 1H), 1.52–1.48 (m, 1H), 0.99 (s, 9H), 0.22 (s, 3H), 0.21 (s, 3H); ^{13}C-NMR (125 MHz, $CDCl_3$): δ 197.2, 174.8, 174.7, 157.3, 154.0, 138.9, 136.5, 136.0, 134.7, 133.1, 129.4, 129.0, 128.6, 127.5, 126.4, 125.6, 123.9, 119.5, 115.8, 114.7, 110.3, 87.5, 49.1, 45.8,

43.4, 42.8, 39.9, 36.1, 26.8, 25.9, 23.8, 23.6, 18.5, -4.16, -4.18.

Compound 5n

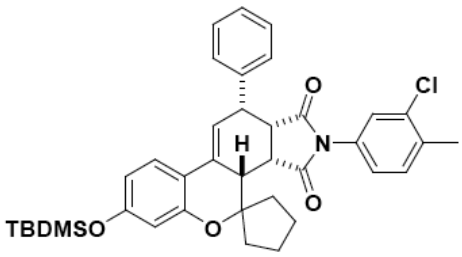

Yellowish solid (75% from enol-*O*-triflate); ^{1}H-NMR (500 MHz, $CDCl_3$): δ 7.44–7.37 (m, 5H), 7.32–7.29 (m, 1H), 7.06 (d, *J* = 8.0 Hz, 1H), 6.90 (s, 1H), 6.66–6.64 (m, 1H), 6.63 (dd, *J* = 5.0 and 2.5 Hz, 1H), 6.46–6.44 (m, 2H), 3.83–3.82 (m, 1H), 3.62–3.58 (m, 2H), 2.86–2.81 (m, 2H), 2.26 (s, 3H), 2.09–1.96 (m, 3H), 1.87–1.79 (m, 2H), 1.69–1.67 (m, 1H), 1.51–1.44 (m, 1H), 0.98 (s, 9H), 0.21 (s, 3H), 0.20 (s, 3H); ^{13}C-NMR (125 MHz, $CDCl_3$): δ 175.0, 174.8, 157.3, 154.0, 139.0, 136.4, 134.5, 134.4, 133.0, 131.4, 131.0, 130.5, 129.0, 128.6, 127.4, 127.0, 126.8, 126.7, 124.6, 123.8, 119.4, 115.8, 114.6, 110.4, 87.5, 48.9, 45.7, 43.2, 42.8, 42.7, 39.9, 36.0, 25.9, 23.8, 23.6, 20.0, 18.5, -4.15.

Compound 5o (2 *Rotamer*s)

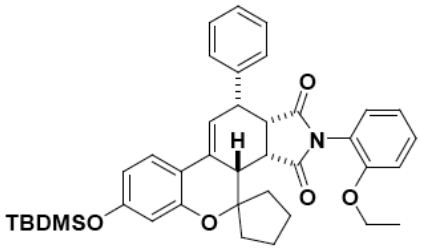

Yellowish solid (44% from enol-*O*-triflate); ^{1}H-NMR (500 MHz, $CDCl_3$): δ 7.48–7.45 (m, 3H), 7.42–7.35 (m, 7H), 7.31–7.27 (m, 2H), 7.23–7.17 (m, 2H), 6.92 (dd, *J* = 8.0 and 1.5 Hz, 1H), 6.86 (dd, *J* = 7.5 and 1.0 Hz, 1H), 6.83–6.80 (m, 2H), 6.72 (td, *J* = 7.5 and 1.0 Hz, 1H), 6.67 (dd, *J* = 5.0 and 2.5 Hz, 1H), 6.58 (dd, *J* = 4.5 and 2.5 Hz, 1H), 6.47 (dd, *J* = 8.5 and 2.5 Hz, 1H), 6.44–6.42 (m, 3H), 6.25 (dd, *J* = 7.5 and 1.5 Hz, 1H), 3.93–3.90 (m, 2H), 3.85–3.80 (m, 2H), 3.74–3.63 (m, 4H), 3.59–

3.54 (m, 2H), 2.91–2.90 (m, 1H), 2.83–2.79 (m, 3H), 2.05–1.97 (m, 6H), 1.85–1.79 (m, 4H), 1.71–1.67 (m, 2H), 1.56–1.52 (m, 1H), 1.43–1.40 (m, 1H), 1.23 (t, J = 7.0 Hz, 3H), 0.98 (s, 9H), 0.97 (s, 9H), 0.90 (t, J = 7.0 Hz, 3H), 1.21 (s, 6H), 1.19 (s, 3H), 1.18 (s, 3H).

Compound 5p

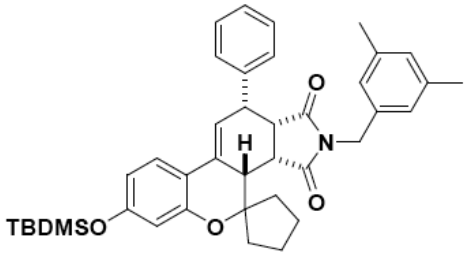

Yellowish solid (59% from enol-*O*-triflate); ^{1}H-NMR (500 MHz, $CDCl_3$): δ 7.38–7.35 (m, 2H), 7.33–7.30 (m, 2H), 7.26–7.24 (m, 3H), 6.79 (s, 3H), 6.44–6.39 (m, 3H), 4.46–4.25 (AB q, J_{AB} = 13.5 Hz, 2H), 3.73–3.72 (m, 1H), 3.49–3.47 (m, 1H), 3.40–3.37 (m, 1H), 2.77–2.73 (m, 2H), 2.15 (s, 3H), 2.15–2.11 (m, 1H), 1.98–1.92 (m, 2H), 1.85–1.80 (m, 2H), 1.69–1.67 (m, 1H), 1.42–1.36 (m, 1H), 0.98 (s, 9H), 0.22 (s, 3H), 0.21 (s, 3H); ^{13}C-NMR (125 MHz, $CDCl_3$): δ 175.5, 175.2, 157.1, 154.2, 139.2, 138.0, 136.1, 133.8, 129.4, 129.1, 128.5, 127.3, 126.7, 123.8, 118.8, 116.0, 114.3, 110.4, 87.3, 48.4, 45.1, 43.7, 43.1, 42.4, 40.1, 36.4, 25.9, 23.7, 23.3, 21.4, 18.4, -4.17.

Compound 5q

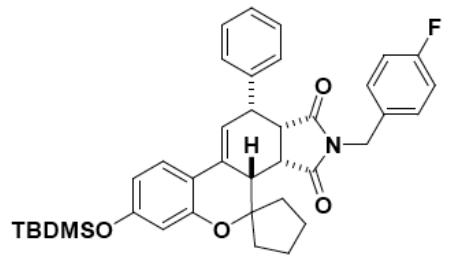

Yellowish solid (73% from enol-*O*-triflate); ^{1}H-NMR (500 MHz, $CDCl_3$): δ 7.37 (t, J = 7.5 Hz, 2H), 7.33–7.30 (m, 2H), 7.28–7.26 (m, 2H), 6.97–6.95 (m, 2H), 6.71–6.67 (m, 2H), 6.47 (dd, J = 8.5 and 2.5 Hz, 1H), 6.43 (d, J = 2.5 Hz, 1H), 6.39 (dd, J = 4.5 and 2.5 Hz, 1H), 4.50–4.30 (AB q, J_{AB} = 14.3 Hz, 2H), 3.74 (t, J =

5.5 Hz, 1H), 3.51 (dd, *J* = 8.0 and 5.5 Hz, 1H), 3.43 (dd, *J* = 8.0 and 6.5 Hz, 1H), 2.83–2.79 (m, 1H), 2.75–2.74 (m, 1H), 2.12–2.10 (m, 1H), 2.01–1.93 (m, 2H), 1.88–1.80 (m, 2H), 1.70–1.66 (m, 1H), 1.44–1.40 (m, 1H), 0.99 (s, 9H), 0.23 (s, 6H); ^{13}C-NMR (125 MHz, $CDCl_3$): δ 175.5, 175.4, 163.2, 161.2, 157.3, 154.1, 139.0, 133.3, 131.8, 130.1, 130.0, 129.0, 128.5, 127.4, 123.8, 119.0, 118.9, 115.8, 115.3, 115.2, 114.4, 110.3, 87.3, 48.3, 45.4, 43.3, 42.9, 41.5, 40.0, 36.3, 25.8, 23.7, 23.4, 18.4, -4.16, -4.19.

Compound 5r

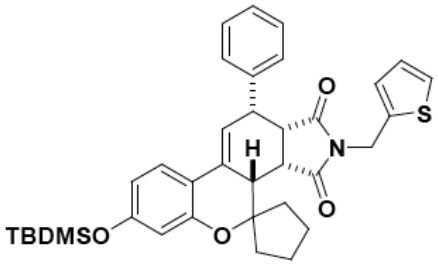

Yellowish solid (69% from enol-*O*-triflate); ^{1}H-NMR (500 MHz, $CDCl_3$): δ 7.41–7.38 (m, 2H), 7.33–7.28 (m, 4H), 7.00 (dd, *J* = 5.0 and 1.0 Hz, 1H), 6.79–6.78 (m, 1H), 6.70 (dd, *J* = 4.5 and 3.5 Hz, 1H), 6.43 (s, 1H), 6.43–6.39 (m, 2H), 4.63–4.54 (AB q, J_{AB} = 14.5 Hz, 2H), 3.73 (t, *J* = 5.5 Hz, 1H), 3.48 (dd, *J* = 8.0 and 5.0 Hz, 1H), 3.40 (dd, *J* = 8.0 and 6.5 Hz, 1H), 2.82–2.78 (m, 1H), 2.74–2.73 (m, 1H), 2.13–2.11 (m, 1H), 2.00–1.91 (m, 2H), 1.88–1.80 (m, 2H), 1.70–1.66 (m, 1H), 1.43–1.39 (m, 1H), 0.99 (s, 9H), 0.23 (s, 3H), 0.22 (s, 3H); ^{13}C-NMR (125 MHz, $CDCl_3$): δ 175.1, 174.9, 157.1, 154.1, 139.1, 137.6, 133.4, 129.1, 128.5, 127.6, 127.4, 126.6, 125.6, 123.9, 123.8, 118.9, 115.9, 114.3, 110.3, 87.3, 48.3, 45.3, 43.4, 42.9, 40.0, 36.5, 36.3, 25.9, 23.7, 23.4, 18.4, -4.13, -4.16.

Compound 5s

Yellowish solid (59% from enol-*O*-triflate); ^{1}H-NMR (500 MHz, $CDCl_3$): δ 7.24 (d, *J* = 8.5 Hz, 1H), 7.05 (t, *J* = 7.5 Hz, 1H), 6.96 (t, *J* = 7.5 Hz, 2H), 6.93–6.92 (m, 2H),

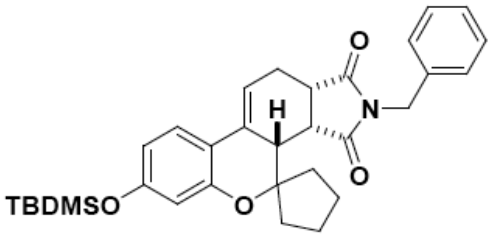

6.43 (dd, J = 8.5 and 2.5 Hz, 1H), 6.38 (d, J = 2.5 Hz, 1H), 6.07–6.04 (m, 1H), 4.60–4.40 (AB q, J_{AB} = 14.3 Hz, 2H), 3.41 (dd, J = 8.5 and 5.5 Hz, 1H), 3.19 (t, J = 7.0 Hz, 1H), 2.96–2.91 (m, 1H), 2.81–2.77 (m, 1H), 2.53 (d, J = 4.5 Hz, 1H), 2.22–2.18 (m, 1H), 2.09–2.04 (m, 1H), 1.95–1.87 (m, 2H), 1.84–1.75 (m, 2H), 1.66–1.62 (m, 1H), 1.36–1.304 (m, 1H), 0.97 (s, 9H), 0.20 (s, 6H); ^{13}C-NMR (125 MHz, $CDCl_3$): δ 179.2, 176.4, 156.9, 153.9, 135.7, 133.6, 128.9, 128.5, 127.8, 127.4, 123.6, 116.5, 116.2, 114.3, 110.3, 87.5, 44.8, 42.7, 42.5, 42.1, 39.7, 36.2, 25.9, 25.3, 23.7, 23.3, 18.4, -4.13, -4.18.

*General procedure of allylic alcohol formation for compound **6** :* The compound **5** (1.0 equiv.) and DTBMP (2.0 equiv.) were dissolved in CH_2Cl_2. m-Chloroperoxybenzoic acid (mCPBA, 1.5 equiv.) was added in this mixture at 0 °C with icebath and the reaction mixture was stirred for 1 h at the same temperature. After reaction completion monitored by TLC, the reaction mixture was diluted with ethyl acetate and washed with sat. NH_4Cl solution and brine. The combined organic layer was dried over anhydrous $MgSO_4$, filtrated, and evaporated under reduced pressure. The resulting mixture was purified with silica gel flash column chromatography to provide desired product **6**. Silyl deprotection was done in the case of need.

Compound 6a

Yellowish solid (61% from compound **5a**); ^{1}H-NMR (500 MHz, $CDCl_3$): δ 7.36 (d, J = 7.5 Hz, 1H), 7.24–7.20 (m, 4H), 7.14–7.09 (m, 7H), 6.98 (t, J = 7.5 Hz, 1H), 6.95 (d,

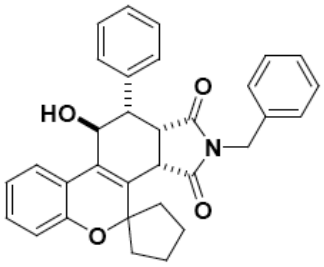

J = 8.0 Hz, 1H), 5.03 (bs, 1H), 3.99–3.86 (AB q, J_{AB} = 14.3 Hz, 2H), 3.78 (d, J = 4.0 Hz, 1H), 3.70–3.67 (m, 2H), 2.31–2.23 (m, 2H), 2.19–2.14 (m, 1H), 2.13–2.06 (m, 1H), 2.00–1.83 (m, 4H); ^{13}C-NMR (125 MHz, $CDCl_3$): δ 177.2, 174.2, 153.7, 136.3, 135.5, 131.3, 130.1, 129.0, 128.8, 128.3, 127.9, 127.8, 123.1, 121.8, 118.0, 88.9, 65.0, 46.1, 42.0, 41.8, 41.5, 36.1, 32.5, 29.9, 23.5, 22.7; LRMS (APCI) *m/z* calculated for $C_{32}H_{28}NO_4$ [M–H]$^-$: 490.21; Found: 490.25.

Compound 6b

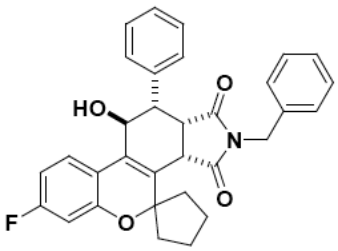

Yellowish solid (51% from compound **5b**); ^{1}H-NMR (500 MHz, DMSO-d_6): δ 7.46 (dd, J = 9.5 and 6.5 Hz, 1H), 7.19–7.14 (m, 6H), 7.00 (d, J = 7.0 Hz, 2H), 6.88 (t, J = 3.5 Hz, 2H), 6.79–6.76 (m, 1H), 6.77 (d, J = 9.5 Hz, 1H), 5.62 (d, J = 6.5 Hz, 1H), 4.78 (d, J = 6.0 Hz, 1H), 4.30 (d, J = 7.5 Hz, 1H), 3.93–3.83 (AB q, J_{AB} = 15.5 Hz, 2H), 3.65 (t, J = 7.0 Hz, 1H), 3.54 (d, J = 6.5 Hz, 1H), 2.29–2.25 (m, 1H), 2.10–2.06 (m, 2H), 1.96–1.90 (m, 2H), 1.82–1.70 (m, 3H); ^{13}C-NMR (125 MHz, Acetone-d_6): δ 178.3, 176.1, 165.5, 163.5, 156.2, 156.1, 138.8, 137.4, 132.2, 130.1, 129.7, 129.3, 129.1, 128.6, 128.0, 127.0, 126.9, 120.9, 109.2, 109.0, 105.8, 105.6, 90.9, 65.7, 48.7, 43.0, 42.6, 36.9, 33.9, 24.4, 23.8; LRMS (APCI) *m/z* calculated for $C_{32}H_{27}FNO_4$ [M–H]$^-$: 508.20; Found: 508.26.

Compound 6c

Yellowish solid (56% from compound **5c**); ^{1}H-NMR (500 MHz, DMSO-d_6): δ 7.32 (d,

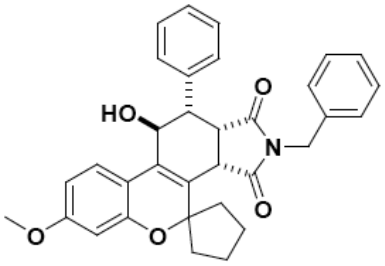

J = 9.0, 1H), 7.18–7.13 (m, 6H), 7.02 (d, J = 7.0 Hz, 2H), 6.87–6.86 (m, 2H), 6.52 (dd, J = 8.5 and 2.0 Hz, 1H), 6.47 (s, 1H), 5.55 (d, J = 6.0 Hz, 1H), 4.74 (d, J = 5.0 Hz, 1H), 4.24 (d, J = 7.5 Hz, 1H), 3.93–3.83 (AB q, J_{AB} = 15.0 Hz, 2H), 3.74 (s, 3H), 3.65 (t, J = 6.5 Hz, 1H), 3.52 (d, J = 5.5 Hz, 1H), 2.27–2.23 (m, 1H), 2.10–2.03 (m, 2H), 1.92–1.90 (m, 2H), 1.80–1.71 (m, 3H); ^{13}C-NMR (125 MHz, Acetone-d_6): δ 178.4, 176.3, 162.4, 156.0, 138.9, 137.5, 132.6, 130.1, 129.7, 129.3, 129.0, 128.6, 126.3, 125.9, 117.4, 108.4, 104.0, 90.4, 65.7, 56.2, 48.8, 43.0, 42.6, 42.5, 36.9, 33.7, 24.5, 23.8; LRMS (APCI) *m/z* calculated for $C_{33}H_{30}NO_5$ $[M–H]^-$: 520.22; Found: 520.46.

Compound 6d

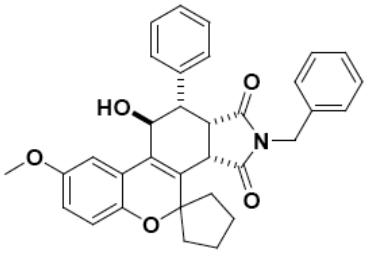

Yellowish solid (41% from compound **5d**); ^{1}H-NMR (500 MHz, DMSO-d_6): δ 7.22–7.16 (m, 6H), 7.03 (d, J = 7.5 Hz, 2H), 6.98 (d, J = 3.0 Hz, 1H), 6.92–6.90 (m, 2H), 6.85–6.79 (m, 3H), 5.65 (d, J = 4.5 Hz, 1H), 4.80 (bs, 1H), 4.54 (d, J = 6.5 Hz, 1H), 3.95–3.84 (AB q, J_{AB} = 15.5 Hz, 2H), 3.72 (s, 3H), 3.69–3.66 (m, 1H), 3.56 (d, J = 6.0 Hz, 1H), 2.27–2.25 (m, 1H), 2.13–2.00 (m, 2H), 1.97–1.92 (m, 2H), 1.82–1.72 (m, 3H); ^{13}C-NMR (125 MHz, Acetone-d_6): δ 178.4, 176.2, 155.9, 148.5, 138.9, 137.5, 132.9, 130.2, 129.9, 129.8, 129.4, 129.1, 128.7, 124.9, 118.9, 115.9, 110.8, 89.8, 65.6, 56.6, 48.9, 43.1, 42.9, 42.7, 37.0, 33.3, 24.5, 23.9; LRMS (APCI) *m/z* calculated for $C_{33}H_{30}NO_5$ $[M–H]^-$: 520.22; Found: 520.34.

Compound 6e

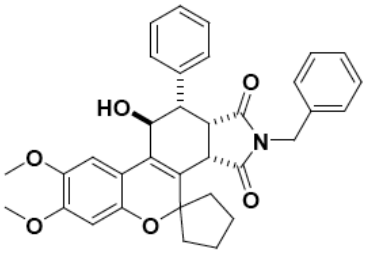

Yellowish solid (47% from compound **5e**); ^{1}H-NMR (500 MHz, DMSO-d_6): δ 7.21–7.14 (m, 6H), 7.03 (d, J = 7.5 Hz, 2H), 6.97 (s, 1H), 6.89–6.88 (m, 2H), 6.55 (s, 1H), 4.77 (s, 1H), 4.23 (d, J = 7.5 Hz, 1H), 3.91–3.81 (AB q, J_{AB} = 15.0 Hz, 2H), 3.75 (s, 3H), 3.68 (s, 3H), 3.64 (t, J = 6.5 Hz, 1H), 3.52 (d, J = 6.5 Hz, 1H), 2.26–2.20 (m, 1H), 2.17–2.13 (m, 1H), 2.04–1.87 (m, 3H), 1.78–1.68 (m, 3H); ^{13}C-NMR (125 MHz, DMSO-d_6): δ 178.0, 175.8, 150.5, 147.7, 143.8, 138.1, 136.2, 131.5, 129.0, 128.2, 127.9, 127.8, 124.5, 114.9, 109.1, 109.0, 102.2, 89.0, 64.3, 56.9, 56.8, 56.4, 56.3, 49.9, 47.8, 42.0, 41.5, 41.4, 41.3, 36.0, 32.6, 23.6, 23.0; LRMS (APCI) *m/z* calculated for $C_{34}H_{32}NO_6$ $[M–H]^-$: 550.23; Found: 550.09.

Compound 6f

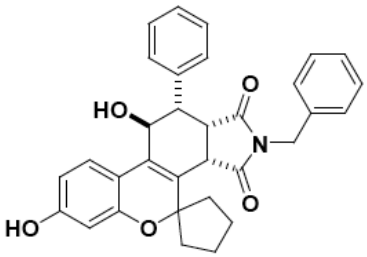

Yellowish solid (59% from compound **5f**); ^{1}H-NMR (500 MHz, DMSO-d_6): δ 9.58 (s, 1H), 7.21–7.12 (m, 7H), 7.02–7.01 (d, J = 6.5 Hz, 2H), 6.88–6.86 (m, 2H), 6.37 (dd, J = 8.5 and 2.0 Hz, 1H), 6.28 (d, J = 2.0 Hz, 1H), 5.50 (d, J = 6.0 Hz, 1H), 4.71 (dd, J = 6.0 and 1.5 Hz, 1H), 4.21 (d, J = 7.5 Hz, 1H), 3.93–3.83 (AB q, J_{AB} = 15.2 Hz, 2H), 3.67–3.64 (m, 1H), 3.52 (dd, J = 6.5 and 1.5 Hz, 1H), 2.28–2.22 (m, 1H), 2.13–2.09 (m, 1H), 2.06–1.99 (m, 1H), 1.96–1.87 (m, 2H), 1.81–1.68 (m, 3H); ^{13}C-NMR (125 MHz, DMSO-d_6): δ 178.0, 175.8, 159.1, 154.5, 138.1, 136.3, 131.5, 129.0, 128.2, 127.9, 127.8, 127.7, 125.7, 125.6, 123.8, 115.0, 109.1, 104.5, 104.4, 89.2, 64.4, 64.3, 47.8, 42.0, 41.5, 41.3, 41.2, 35.9, 32.8, 23.6, 22.9; LRMS (APCI) *m/z* calculated for $C_{32}H_{28}NO_5$ $[M–H]^-$: 506.20; Found: 506.22; HRMS (FAB) *m/z* calculated for $C_{32}H_{30}NO_5$

$[M+H]^+$: 508.2124; found: 508.2126.

Compound 6g

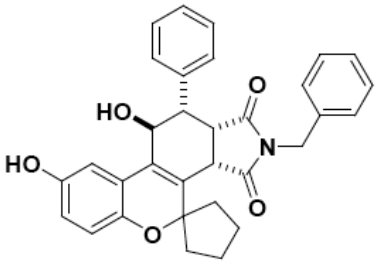

Reddish solid (42% from compound **5g**); ^{1}H-NMR (500 MHz, DMSO-d_6 / $CDCl_3$): δ 8.81 (s, 1H), 7.16–7.10 (m, 6H), 7.01 (d, J = 6.5 Hz, 2H), 6.89–6.88 (m, 2H), 6.78 (d, J = 2.5 Hz, 1H), 6.67 (d, J = 8.5 Hz, 1H), 6.59 (dd, J = 8.5 and 2.5 Hz, 1H), 5.51 (d, J = 6.5 Hz, 1H), 4.64 (d, J = 4.5 Hz, 1H), 4.17 (d, J = 7.5 Hz, 1H), 3.93–3.83 (AB q, J_{AB} = 14.7 Hz, 2H), 3.68–3.66 (m, 1H), 3.54 (d, J = 6.0 Hz, 1H), 2.25–2.22 (m, 1H), 2.11–2.10 (m, 1H), 2.01–1.88 (m, 3H), 1.79–1.69 (m, 3H); ^{13}C-NMR (125 MHz, DMSO-d_6 / $CDCl_3$): δ 177.8, 175.4, 152.1, 145.7, 137.9, 136.1, 131.5, 128.9, 128.8, 128.4, 128.1, 128.0, 127.7, 123.7, 117.8, 116.1, 110.9, 88.4, 64.4, 47.6, 41.8, 41.6, 36.0, 32.1, 23.6, 23.0; LRMS (APCI) *m/z* calculated for $C_{32}H_{28}NO_5$ $[M–H]^–$: 506.20; Found: 506.20.

Compound 6h

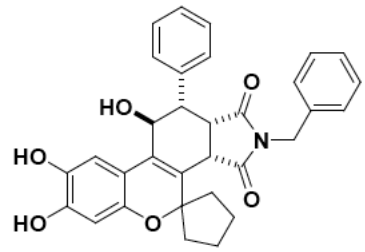

Reddish solid (32% from compound **5h**); ^{1}H-NMR (500 MHz, DMSO-d_6): δ 7.21–7.12 (m, 6H), 7.01 (d, J = 7.0 Hz, 2H), 6.87–6.85 (m, 2H), 6.74 (s, 1H), 6.29 (s, 1H), 5.50 (d, J = 6.0 Hz, 1H), 4.56 (d, J = 4.0 Hz, 1H), 4.19 (d, J = 7.5 Hz, 1H), 3.93–3.83 (AB q, J_{AB} = 15.3 Hz, 2H), 3.64 (t, J = 7.0 Hz, 1H), 3.50 (d, J = 7.0 Hz, 1H), 2.22–2.18 (m, 1H), 2.13–2.11 (m, 1H), 1.97–1.83 (m, 3H), 1.76–1.67 (m, 3H); ^{13}C-NMR (125 MHz, DMSO-d_6): δ 178.1, 175.8, 146.9, 146.4, 140.0, 138.1, 136.3, 131.3, 129.3, 129.0,

127.8, 124.3, 114.4, 111.6, 105.3, 105.2, 88.6, 64.6, 47.7, 41.9, 41.5, 41.3, 35.9, 32.1, 23.6, 23.0; LRMS (APCI) *m/z* calculated for $C_{32}H_{28}NO_6$ $[M–H]^-$: 522.19; Found: 522.21.

Compound 6i

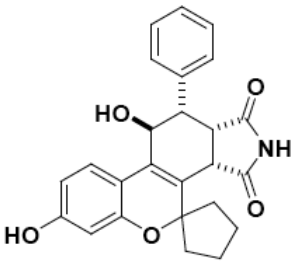

Yellowish solid (39% from compound **5i**); ^{1}H-NMR (500 MHz, DMSO-d_6): δ 10.60 (s, 1H), 9.55 (s, 1H), 7.20–7.17 (m, 4H), 7.08–7.06 (m, 2H), 6.35 (dd, *J* = 9.0 and 2.5 Hz, 1H), 6.26 (d, *J* = 2.5 Hz, 1H), 5.41 (d, *J* = 6.5 Hz, 1H), 4.68–4.67 (m, 1H), 4.05 (d, *J* = 7.0 Hz, 1H), 3.48–3.44 (m, 2H), 2.30–2.25 (m, 1H), 2.08–2.00 (m, 2H), 1.95–1.84 (m, 2H), 1.81–1.67 (m, 3H); ^{13}C-NMR (125 MHz, Acetone-d_6): δ 178.9, 177.1, 159.9, 156.0, 139.3, 132.4, 130.3, 129.6, 128.7, 126.2, 125.4, 116.5, 109.6, 105.3, 90.2, 65.7, 48.6, 44.1, 43.3, 36.8, 33.6, 24.5, 23.8; LRMS (APCI) *m/z* calculated for $C_{25}H_{22}NO_5$ $[M–H]^-$: 416.15; Found: 416.21.

Compound 6j

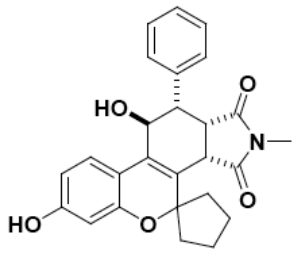

Yellowish solid (45% from compound **5j**); ^{1}H-NMR (500 MHz, CD_3OD): δ 7.23 (d, *J* = 8.5 Hz, 1H), 7.20–7.16 (m, 3H), 7.10–7.08 (m, 2H), 6.42 (dd, *J* = 8.5 and 2.5 Hz, 1H), 6.34 (d, *J* = 2.5 Hz, 1H), 4.88 (d, *J* = 1.5 Hz, 1H), 3.91 (d, *J* = 7.0 Hz, 1H), 3.65–3.32 (m, 2H), 2.33–2.15 (m, 3H), 2.26 (s, 3H), 2.00–1.97 (m, 2H), 1.88–1.80 (m, 3H); ^{13}C-NMR (125 MHz, CD_3OD): δ 179.7, 176.7, 160.0, 155.9, 138.5, 132.1, 129.8, 129.4, 128.8, 125.7, 125.3, 116.0, 109.6, 105.2, 90.2, 65.4, 48.8, 43.2, 42.1, 36.6, 33.4, 24.2, 23.9, 23.6; LRMS (APCI)

m/z calculated for $C_{26}H_{24}NO_5$ $[M–H]^-$: 430.17; Found: 430.22.

Compound 6k

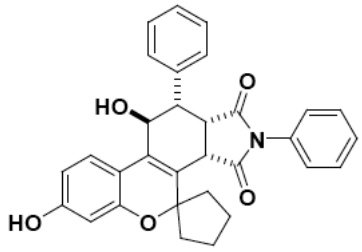

Yellowish solid (55% from compound **5k**); ^{1}H-NMR (500 MHz, DMSO-d_6): δ 9.61 (s, 1H), 7.29–7.22 (m, 7H), 7.12 (dd, J = 8.5 and 1.5 Hz, 2H), 6.37 (dd, J = 8.5 and 2.5 Hz, 1H), 6.35–6.33 (m, 2H), 6.29 (d, J = 2.5 Hz, 1H), 5.54 (d, J = 6.5 Hz, 1H), 4.74 (dd, J = 6.5 and 1.5 Hz, 1H), 4.34 (d, J = 6.5 Hz, 1H), 3.70 (dd, J = 7.5 and 6.5 Hz, 1H), 3.58 (d, J = 6.5 Hz, 1H), 2.34–2.27 (m, 1H), 2.16–2.04 (m, 2H), 1.97–1.90 (m, 2H), 1.79–1.66 (m, 3H); ^{13}C-NMR (125 MHz, DMSO-d_6): δ 177.0, 175.2, 159.2, 154.5, 138.5, 132.4, 131.7, 129.5, 129.3, 129.0, 128.3, 127.5, 127.4, 125.8, 125.7, 123.7, 115.1, 109.2, 104.5, 89.2, 64.5, 64.4, 48.1, 41.8, 41.4, 36.0, 32.9, 23.7, 23.1; LRMS (APCI) *m/z* calculated for $C_{31}H_{26}NO_5$ $[M–H]^-$: 492.19; Found: 492.21.

Compound 6l

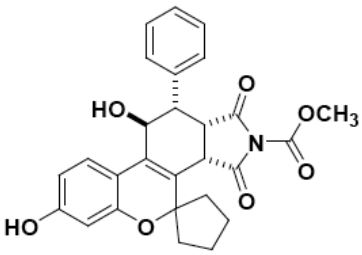

Yellowish solid (38% from compound **5l**); ^{1}H-NMR (500 MHz, CD_3OD): δ 7.26 (d, J = 8.5 Hz, 1H), 7.21–7.17 (m, 3H), 7.12 (d, J = 8.0 Hz, 2H), 6.43 (d, J = 8.5 Hz, 1H), 6.34 (s, 1H), 4.90 (s, 1H), 4.09 (d, J = 7.0 Hz, 1H), 3.67 (s, 3H), 3.67–3.63 (m, 2H), 2.24–2.10 (m, 3H), 2.03–1.99 (m, 2H), 1.86–1.80 (m, 3H); ^{13}C-NMR (125 MHz, CD_3OD): δ 175.2, 172.7, 160.2, 156.0, 149.5, 137.5, 132.8, 130.0, 129.7, 129.0, 128.5, 125.9, 124.1, 115.8, 109.7, 105.2, 90.0, 65.4, 54.6, 43.4, 42.4, 36.5, 33.6, 24.2, 23.6; LRMS (APCI) *m/z* calculated for $C_{27}H_{23}NO_7$ $[M–H]^-$: 474.16; Found: 474.16.

Compound 6m

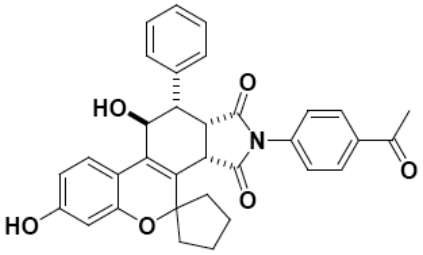

Yellowish solid (41% from compound **5m**); ^{1}H-NMR (500 MHz, DMSO-d_6): δ 9.59 (s, 1H), 7.83 (d, J = 8.5 Hz, 2H), 7.24–7.21 (m, 4H), 7.10 (d, J = 6.5 Hz, 2H), 6.53 (d, J = 8.5 Hz, 2H), 6.36 (dd, J = 8.0 and 2.0 Hz, 1H), 6.28 (d, J = 2.5 Hz, 1H), 5.53 (d, J = 6.5 Hz, 1H), 4.74 (d, J = 6.0 Hz, 1H), 4.34 (d, J = 7.5 Hz, 1H), 3.73–3.70 (m, 1H), 3.58 (d, J = 6.0 Hz, 1H), 2.51 (s, 3H), 2.31–2.67 (m, 1H), 2.13–2.03 (m, 2H), 1.96–1.91 (m, 2H), 1.76–1.67 (m, 3H); ^{13}C-NMR (125 MHz, DMSO-d_6): δ 197.9, 176.8, 174.8, 159.2, 154.5, 138.3, 136.9, 136.3, 131.8, 129.3, 129.1, 128.4, 127.3, 125.8, 123.4, 115.0, 109.2, 109.1, 104.5, 89.2, 64.5, 64.4, 48.1, 41.9, 41.5, 41.2, 41.1, 36.0, 33.0, 27.5, 27.4, 23.7, 23.1; LRMS (APCI) *m/z* calculated for $C_{33}H_{28}NO_6$ $[M–H]^-$: 534.20; Found: 534.25.

Compound 6n

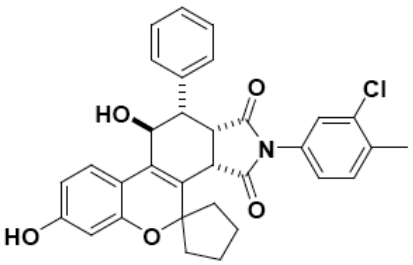

Yellowish solid (52% from compound **5n**); ^{1}H-NMR (500 MHz, DMSO-d_6): δ 9.60 (s, 1H), 7.28–7.22 (m, 5H), 7.11 (d, J = 8.0 Hz, 2H), 6.36 (dd, J = 6.0 and 2.5 Hz, 1H), 6.34 (dd, J = 8.0 and 2.0 Hz, 1H), 6.29 (d, J = 2.5 Hz, 1H), 6.21 (d, J = 2.0 Hz, 1H), 5.53 (d, J = 6.0 Hz, 1H), 4.74 (d, J = 4.5 Hz, 1H), 4.30 (d, J = 7.5 Hz, 1H), 3.72–3.69 (m, 1H), 3.57 (d, J = 6.5 Hz, 1H), 2.29–2.26 (m, 1H), 2.28 (s, 3H), 2.13–2.06 (m, 2H), 1.93–1.92 (m, 2H), 1.77–1.68 (m, 3H); ^{13}C-NMR (125 MHz, DMSO-d_6 / $CDCl_3$): δ 176.5, 174.5, 158.9, 154.3, 138.1, 136.0, 133.2, 131.5, 131.1,

130.8, 129.2, 128.9, 127.9, 127.3, 127.2, 125.6, 125.3, 123.1, 114.7, 108.8, 104.2, 88.8, 64.1, 47.9, 41.6, 41.1, 35.6, 32.6, 23.4, 22.7, 19.6; LRMS (APCI) *m/z* calculated for $C_{32}H_{27}ClNO_5$ $[M–H]^-$: 540.17; Found: 540.23.

Compound 6o

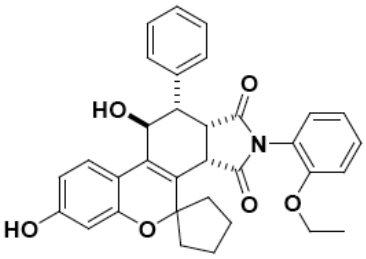

Yellowish solid (43% from compound **5o**); ^{1}H-NMR (500 MHz, DMSO-d_6 /$CDCl_3$): δ 9.48 (s, 1H), 7.29–7.19 (m, 5H), 7.15 (d, J = 6.5 Hz, 2H), 6.96 (d, J = 8.0 Hz, 1H), 6.68 (t, J = 7.5 Hz, 1H), 6.37 (dd, J = 8.0 and 2.5 Hz, 1H), 6.29 (d, J = 2.5 Hz, 1H), 5.52–5.48 (m, 2H), 4.77 (d, J = 6.0 Hz, 1H), 4.06 (d, J = 7.5 Hz, 1H), 4.00–3.91 (m, 2H), 3.80–3.78 (m, 1H), 3.62 (d, J = 6.0 Hz, 1H), 2.28–2.07 (m, 3H), 1.98–1.97 (m, 2H), 1.79–1.68 (m, 3H), 1.25–1.23 (m, 3H); ^{13}C-NMR (125 MHz, DMSO-d_6 / $CDCl_3$): δ 175.8, 173.6, 158.4, 153.8, 153.4, 137.6, 131.2, 129.8, 128.8, 128.3, 128.2, 127.4, 124.8, 122.4, 120.4, 119.7, 114.2, 112.8, 108.3, 103.8, 103.7, 88.3, 63.8, 63.7, 47.4, 41.1, 40.8, 40.7, 34.9, 32.1, 22.9, 22.2, 14.3; LRMS (APCI) *m/z* calculated for $C_{33}H_{30}NO_6$ $[M–H]^-$: 536.22; Found: 536.26.

Compound 6p

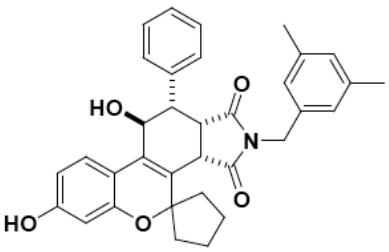

Yellowish solid (52% from compound **5p**); ^{1}H-NMR (500 MHz, $CDCl_3$): δ 7.12 (d, J = 9.0 Hz, 1H), 7.09–7.03 (m, 5H), 6.78 (s, 1H), 6.75 (s, 2H), 6.39 (d, J = 2.5 Hz, 1H), 6.36 (dd, J = 8.5 and 2.5 Hz, 1H), 4.88 (s, 1H), 3.84–3.73 (AB q, J_{AB} = 14.0 Hz, 2H), 3.66 (s, 1H), 3.52 (s, 1H), 3.51 (s, 1H), 2.84 (bs, 1H), 2.26–2.19 (m, 2H), 2.21 (s, 6H), 2.14–2.07 (m, 1H), 2.04–

1.99 (m, 1H), 1.87–1.81 (m, 4H); ^{13}C-NMR (125 MHz, $CDCl_3$): δ 178.0, 174.5, 157.8, 154.9, 138.3, 136.3, 135.3, 130.9, 129.7, 128.8, 128.6, 128.2, 126.9, 124.8, 124.7, 115.2, 109.3, 105.2, 89.5, 65.0, 46.4, 41.9, 41.6, 35.9, 32.6, 29.9, 23.4, 22.6, 21.4; LRMS (APCI) *m/z* calculated for $C_{34}H_{32}NO_5$ $[M–H]^-$: 534.24; Found: 534.22.

Compound 6q

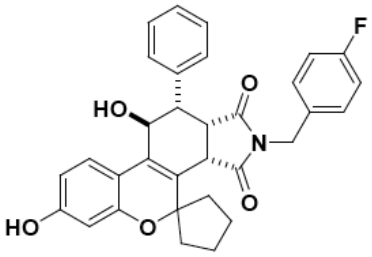

Yellowish solid (53% from compound **5q**); ^{1}H-NMR (500 MHz, DMSO-d_6): δ 9.58 (s, 1H), 7.18 (d, J = 8.5 Hz, 1H), 7.15–7.09 (m, 3H), 7.00–6.96 (m, 4H), 6.91–6.88 (m, 2H), 6.36 (dd, J = 8.5 and 2.5 Hz, 1H), 6.27 (d, J = 2.5 Hz, 1H), 5.49 (d, J = 6.5 Hz, 1H), 4.68 (d, J = 4.0 Hz, 1H), 4.20 (d, J = 7.5 Hz, 1H), 3.94–3.86 (AB q, J_{AB} = 15.3 Hz, 2H), 3.63 (dd, J = 7.5 and 6.5 Hz, 1H), 3.50 (dd, J = 6.0 and 1.5 Hz, 1H), 2.29–2.23 (m, 1H), 2.13–2.09 (m, 1H), 2.05–1.99 (m, 1H), 1.96–1.86 (m, 2H), 1.81–1.69 (m, 3H); ^{13}C-NMR (125 MHz, DMSO-d_6): δ 178.0, 175.9, 162.9, 161.0, 159.1, 154.5, 138.0, 132.4, 131.5, 130.2, 129.0, 128.2, 125.6, 123.7, 115.8, 115.6, 115.0, 109.1, 104.5, 104.4, 89.1, 64.4, 47.8, 41.8, 41.3, 41.2, 40.9, 36.0, 32.8, 23.7, 23.0; LRMS (APCI) *m/z* calculated for $C_{32}H_{27}FNO_5$ [M–H]–: 524.20; Found: 524.21.

Compound 6r

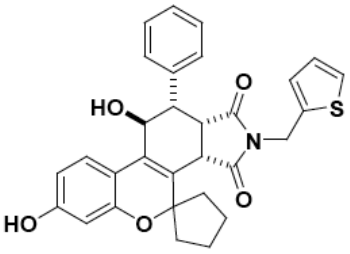

Yellowish solid (43% from compound **5r**); ^{1}H-NMR (500 MHz, DMSO-d_6): δ 9.58 (s, 1H), 7.19 (s, 1H), 7.32 (ds, J = 5.0 and 1.0 Hz, 1H), 7.20 (d, J = 9.0 Hz, 1H), 7.11–7.08 (m, 3H), 6.98–6.97 (m, 2H), 6.83 (dd, J = 5.0 and 3.5 Hz, 1H), 6.68 (d, J = 2.5 Hz, 1H), 6.36

(dd, J = 8.5 and 2.5 Hz, 1H), 6.27 (d, J = 2.5 Hz, 1H), 5.48 (d, J = 6.0 Hz, 1H), 4.70 (dd, J = 6.0 and 1.5 Hz, 1H), 4.13 (d, J = 7.5 Hz, 1H), 4.06–3.96 (AB q, J_{AB} = 15.0 Hz, 2H), 3.62–3.60 (m, 1H), 3.49 (dd, J = 6.0 and 1.5 Hz, 1H), 2.26–2.20 (m, 1H), 2.13–2.09 (m, 1H), 2.06–1.99 (m, 1H), 1.96–1.86 (m, 2H), 1.82–1.70 (m, 2H). ^{13}C-NMR (125 MHz, DMSO-d_6): δ 177.5, 175.3, 159.1, 154.5, 137.8, 137.7, 131.5, 128.9, 128.2, 127.8, 127.3, 126.7, 126.6, 125.7, 125.6, 123.6, 115.0, 109.1, 104.5, 104.4, 89.1, 64.3, 64.2, 47.7, 41.9, 41.3, 41.2, 36.0, 35.9, 32.8, 23.6, 22.9; LRMS (APCI) *m/z* calculated for $C_{30}H_{26}NO_5S$ $[M–H]^-$: 512.16; Found: 512.17.

Compound 6s

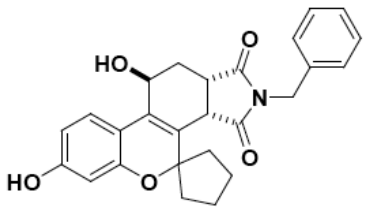

Yellowish solid (37% from compound **5s**); ^{1}H-NMR (500 MHz, $CDCl_3$): δ 7.33–7.23 (m, 5H), 7.03 (d, J = 9.0 Hz, 1H), 6.51 (bs, 1H), 6.32 (s, 1H), 6.31 (d, J = 9.0 Hz, 1H), 4.70 (s, 1H), 4.64–4.56 (AB q, J_{AB} = 14.0 Hz, 2H), 3.58 (d, J = 7.0 Hz, 1H), 3.17–3.13 (m, 1H), 2.86 (bs, 1H), 2.32–2.29 (m, 1H), 2.24–2.17 (m, 1H), 2.02–1.94 (m, 2H), 1.91–1.82 (m, 3H), 1.76–1.73 (m, 2H), 1.47 (td, J = 13.5 and 3.0 Hz, 1H); ^{13}C-NMR (125 MHz, $CDCl_3$): δ 179.5, 175.0, 157.6, 154.7, 135.9, 130.9, 129.0, 128.8, 128.3, 124.7, 123.3, 115.2, 109.1, 105.0, 89.4, 61.0, 42.9, 42.6, 36.6, 35.7, 33.1, 32.7, 23.3, 22.6; LRMS (APCI) *m/z* calculated for $C_{26}H_{24}NO_5$ $[M–H]^-$: 430.17; Found: 430.18.

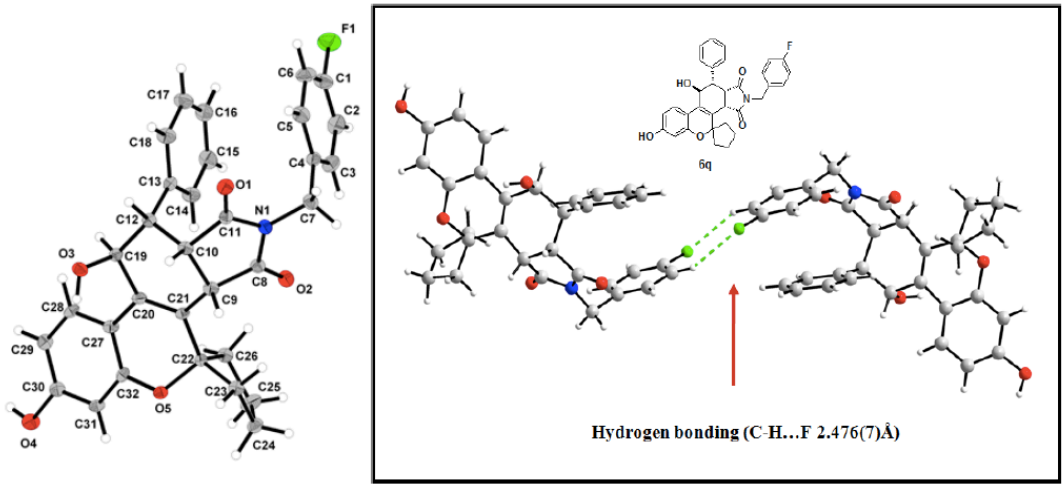

Figure S3. X-ray crystal structure of compound 6q.

Reference

[1] O. Brinkmann, J. Trapman, *Nat. Med*. **2000**, *6*, 628.

[2] Y. Chen, C. L. Sawyers, H. I. Scher, *Curr. Opin. Pharmacol*. **2008**, *8*, 440.

[3] G. Andriole, N. Bruchovsky, L. W. K. Chung, A. M. Matsumoto, R. Rittmaster, C. Roehrborn, D. Russell, D. Tindall, *J. Urol.* **2004**, *172*, 1399.

[4] C. Ntais, A. Polycarpou, A. Tsatsoulis, *Eur. J. Endocrinol*. **2003**, *149*, 469.

[5] H. Koch, *Drugs Today* **1984**, *20*, 561.

[6] Y. Fradet, *Expert Rev. Anticancer Ther.* **2004**, *4*, 37.

[7] H. Miyamoto, E. M. Messing, C. S. Chang, *Prostate* **2004**, *61*, 332.

[8] M. Urushibara, J. Ishioka, N. Hyochi, K. Kihara, S. Hara, P. Singh, J. T. Isaacs, Y. Kageyama, *Prostate* **2007**, *67*, 799.

[9] a) J. Veldscholte, C. Ris-Stalpers, G. G. J. M. Kuiper, G. Jenster, C. Berrevoets, E. Claassen, H. C. J. van Rooij, J. Trapman, A. O. Brinkmann, E. Mulder, *Biochem. Biophys. Res. Commun*. **1990**, *173*, 534; b) J. Veld- scholte, C. A. Berrevoets, A. O. Brinkmann, J. A. Grootegoed, E. Mulder, *Biochemistry* **1992**,

31, 2393; c) J. Veldscholte, C. A. Berrevoets, E. Mulder, *J. Steroid Biochem. Mol. Biol*. **1994**, *49*, 341.

[10] T. Hara, J. Miyazaki, H. Araki, M. Yamaoka, N. Kanzaki, M. Kusaka, M. Miyamoto, *Cancer Res*. **2003**, *63*, 149.

[11] C. E. Bohl, W. Gao, D. D. Miller, C. E. Bell, J. T. Dalton, *Proc. Natl. Acad. Sci. USA* **2005**, *102*, 6201.

[12] P. L. McGinley, J. T. Koh, *J. Am. Chem. Soc*. **2007**, *129*, 3822.

[13] C. Tran, S. Ouk, N. J. Clegg, Y. Chen, P. A. Watson, V. Arora, J. Wongvipat, P. M. Smith-Jones, D. Yoo, A. Kwon, T. Wasielewska, D. Welsbie, C. D. Chen, C. S. Higano, T. M. Beer, D. T. Hung, H. I. Scher, M. E. Jung, C. L. Sawyers, *Science* **2009**, *324*, 787.

[14] J. J. Li, D. M. Iula, M. N. Nguyen, L.-Y. Hu, D. Dettling, T. R. Johnson, D. Y. Du, V. Shanmugasundaram, J. A. Van Camp, Z. Wang, W. G. Harter, W. -S. Yue, M. L. Boys, K. J. Wade, E. M. Drummond, B. M. Samas, B. A. Lefker, G. S. Hoge, M. J. Lovdahl, J. Asbill, M. Carroll, M. A. Meade, S. M. Ciotti, T. Krieger-Burke, *J. Med. Chem.* **2008**, *51*, 7010.

[15] S. K. Ko, H. J. Jang, E. Kim, S. B. Park, *Chem. Commun.* **2006**, 2962.

[16] a) H. An, S. -J. Eum, M. Koh, S. K. Lee, S. B. Park, *J. Org. Chem*. **2008**, *73*, 1752; b) R. Sagar, S.B. Park, *J. Org. Chem*. **2008**, *73*, 3270; c) Y. Kim, J. Kim, S. B. Park, *Org. Lett*. **2009**, *11*, 17.

[17] a) S. -C. Lee, S. B. Park, *J. Comb. Chem*. **2006**, *8*, 50; b) S. -C. Lee, S. B. Park, *J. Comb. Chem.* **2007**, *9*, 828; c) S. -C. Lee, S. B. Park, *Chem. Commun.* **2007**, 3714; d) S. O. Park, J. Kim, M. Koh, S. B. Park, *J. Comb. Chem.* **2009**, *11*, 315.

[18] F. A. G. El-Essawy, S. M. Yassin, I. A. El-Sakka, A. F. Khattab, I. Søtofte, J. Ø. Madsen, A. Senning, *J. Org. Chem.* **1998**, *63*, 9840.

Chapter 2. Discovery and Target Identification of an Antiproliferative Agent in Live Cells Using Fluorescence Difference in Two-Dimensional Gel Electrophoresis

- *Angew. Chem. Int. Ed.* **2012**, doi: 10.1002/anie.201200609.

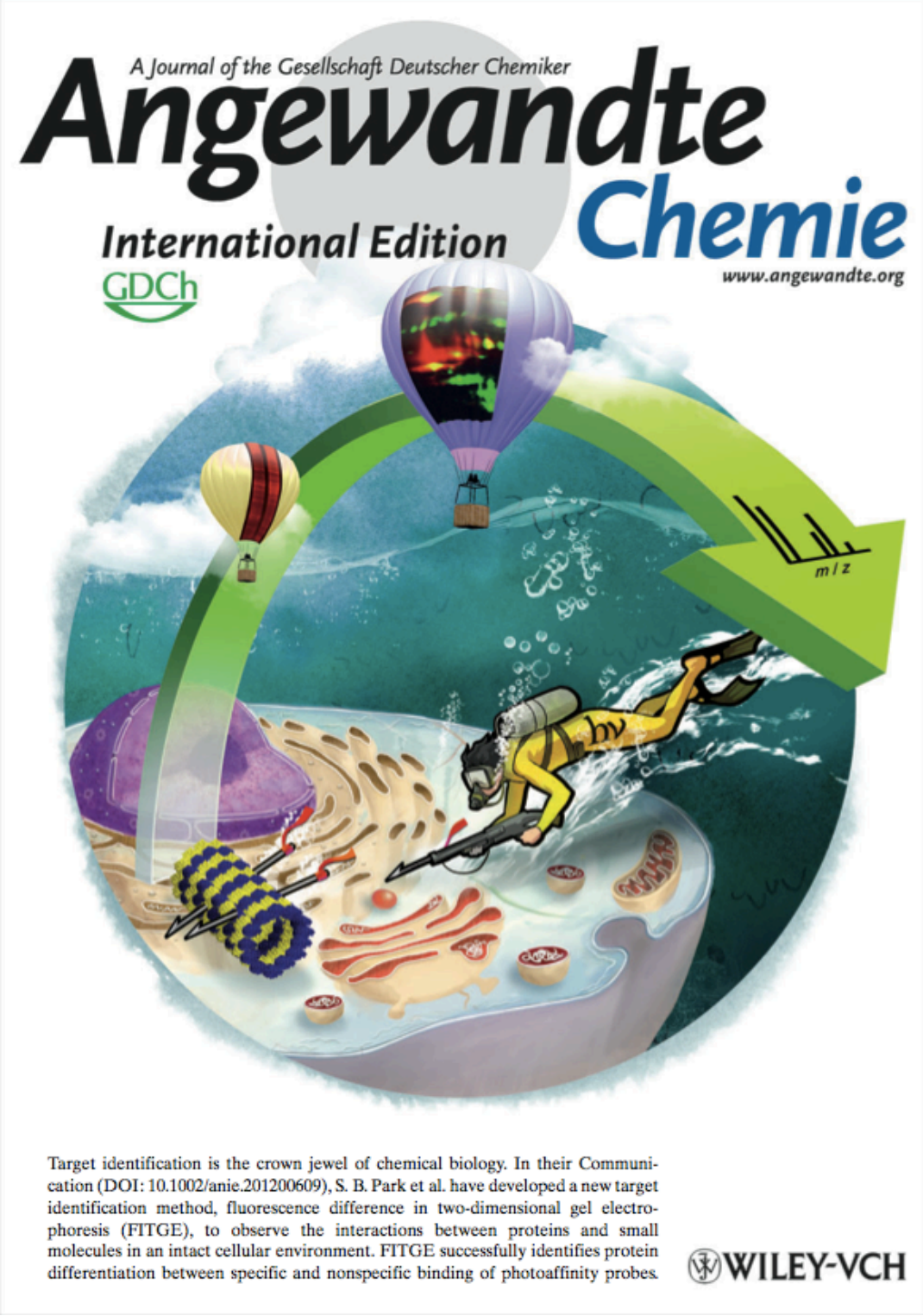

Introduction

Phenotype-based screening has been recognized as a key approach to the discovery of novel therapeutic agents because of the recent withdrawal of marketed drugs developed by conventional target-based medicinal chemistry.[1a] Furthermore, the identification of small molecules that control nonconventional drug targets has become increasingly important for curing diseases that are resistant to existing drugs, for the development of regenerative medicines, and for the treatment of incurable diseases.[1b,c] Phenotype-based assays facilitate the use of efficiency-based evaluations for the discovery of a small-molecule modulator for unknown drug targets, which leads to the development of novel classes of drugs or the discovery of new drugable protein targets. For this approach, it is essential to identify the mode of action of small-molecule modulators. However, understanding their mechanism, the target identification process in particular, is time-consuming, difficult to implement, and does not provide clear results. Therefore, there is a great demand for the development of new and robust methods for target identification.[2]

The conventional affinity-based pull-down method is hampered by nonspecific binding events owing to the large size of the probe and the use of solid beads. Also, the experimental buffer conditions can yield completely different patterns for the interactions between proteins and small molecules, which limits the robustness of this method.[3] Several research groups have addressed these issues by using photoaffinity activation and bioorthogonal transformation.[2g, 4] Photoaffinity groups in bioactive small molecules can generate covalent linkages to adjacent target proteins upon irradiation, which can be suitable for target identification under various experimental conditions (for example, cell lysate labeling, live cell labeling, and ex vivo labeling) without being affected by buffers or salt concentrations. Bioorthogonal

moieties allow the selective labeling of small-molecule bound target proteins for visualization. Despite these advantages, nonspecific labeling on various proteins, especially on abundant and sticky proteins, as well as on actual target proteins, has been a major problem for the photoaffinity-based crosslinking method.[5] Furthermore, the differentiation of actual binding events from nonspecific binding is essential for the successful application of photoaffinity groups to target identification. To address this limitation, we have developed a new method called fluorescence difference in two-dimensional gel electrophoresis (FITGE), and employed it in the target identification of a new antitumor agent screened from our in-house small-molecule library.

Results and Discussion

After identification of hit compounds from the cell-based phenotype assay and subsequent structure–activity relationship study, a bioactive small-molecule probe derived from a hit compound, and a corresponding negative probe can be prepared. Each probe bears a photoaffinity group and a bioorthogonal acetylene moiety to attach to and visualize binding events. As shown in Figure 1, the resulting probe and negative probe are separately incubated with live cells to induce specific binding events between proteins and small molecules. The subsequent UV irradiation of live cells allows the in situ generation of radical species on the photoaffinity group, which crosslinks the adjacent proteins with covalent bonds. After lysis of the treated cells, proteins labeled with probes can be visualized with fluorescent dyes using a bio-orthogonal click reaction.[6] Owing to the high nonspecific labeling of photoaffinity

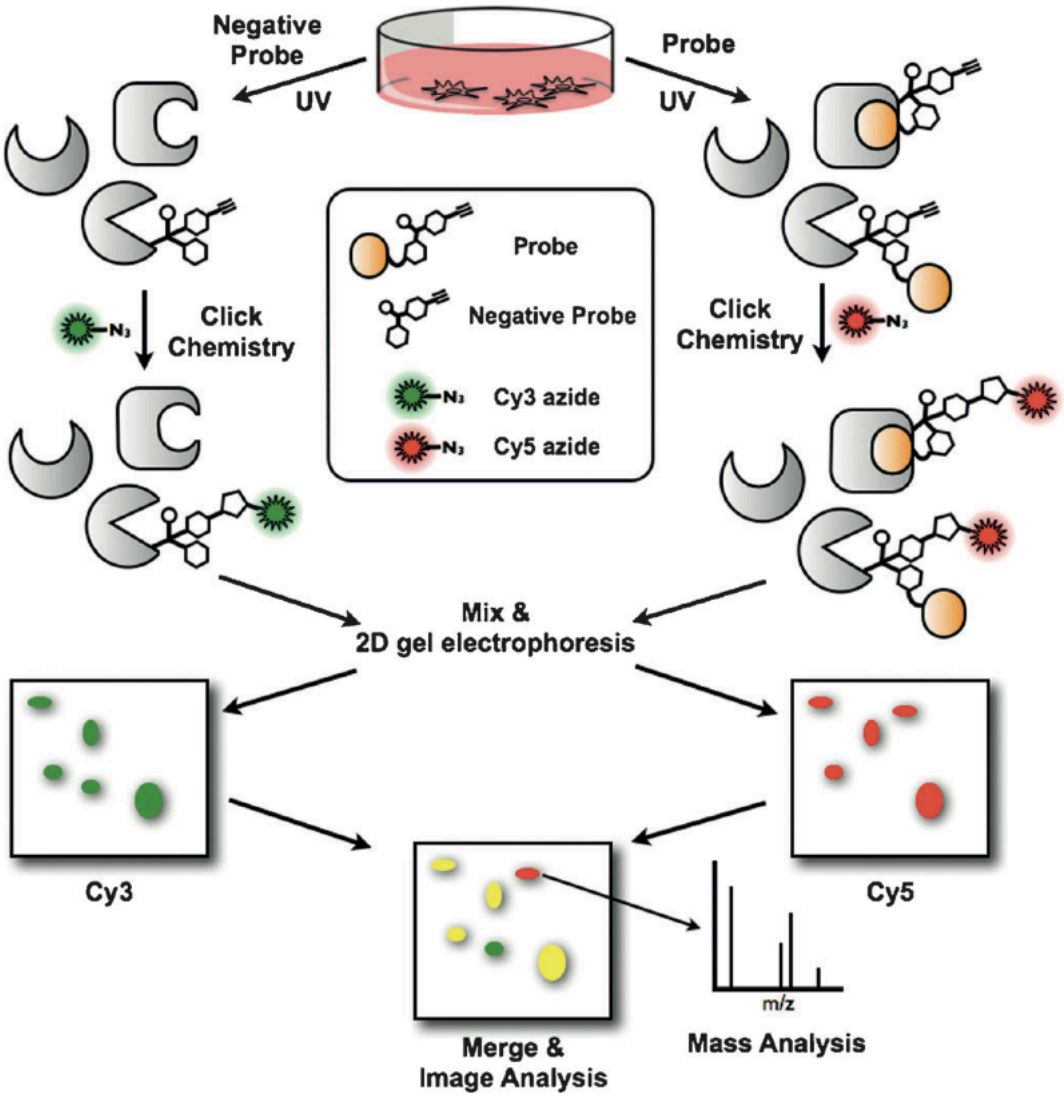

Figure 1. Outline of the FITGE method for identification of the targets of bioactive small molecules in live cells.

groups,[5] the side by side comparison of labeling patterns between probe-labeled and negative- probe-labeled proteins is a critical step in the FITGE method; however, this comparison is difficult and misleading because of gel-to-gel inconsistency.[7] Researchers in the field of proteomics have addressed this issue by running two different samples with two different fluorescent dyes in a single gel in a procedure known as difference gel electrophoresis (DIGE).[8] Inspired by the DIGE strategy, probe-labeled and negative-probe-labeled proteomes are crosslinked to two different fluorescent dyes, pooled in a single sample, and separated by two-dimensional gel

electrophoresis (2DGE). As probe-labeled and negative-probe-labeled proteomes are labeled with Cy5 and Cy3, respectively, nonspecific binding events can be ruled out by direct comparison of the labeling patterns of whole proteomes in 2DGE. Following fluorescent gel image analysis, the desired protein spots are cut out and subjected to mass analysis for the identification of potential target proteins.

We also noticed that most studies in the field of target identification have been conducted using cell lysates, as these are more easily handled. However, the specific interactions between bioactive small molecules and target proteins in cell lysates can differ from those in live cells as a result of the extremely high concentration of proteins inside live cells, as well as the nonspecific attractive and repulsive interactions that occur in live cells with many macromolecules, including proteins, nucleotides, lipids, and metabolites.[9] Chang and co-workers reported the environment-dependent covalent labeling of an organic fluorophore to target proteins, but they did not focus on the functional modulation of target proteins.[10] Yao and co-workers successfully demonstrated the in vitro and in cell target identification of known bioactive small molecules.[11] Herein, we report the target identification of a novel bioactive small molecule discovered by phenotype-based screening using the FITGE method along with a systematic comparison of live cells with cell lysates. In particular, we aimed to demonstrate the importance of efficient high-resolution differentiation between specific and nonspecific binding.

We initiated probe design on the basis of an anticancer agent, which was identified using a cell-based proliferation assay against our 3000 member library of small molecules, constructed by privileged-substructure-based diversity-oriented synthesis (pDOS). The pDOS synthetic strategy employs the divergent recombination

of polyheterocycles embedded with privileged substructures to maximize the molecular diversity of the drug-like small-molecule library.[12]

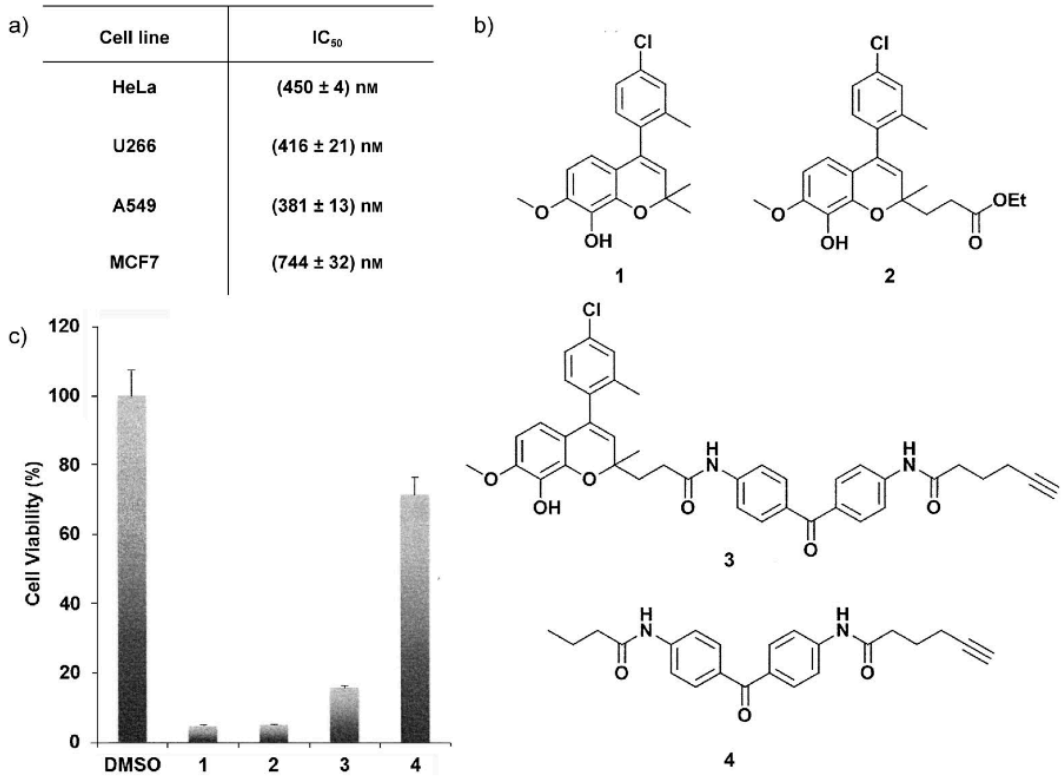

Figure 2. Biological activity of antiproliferative agents discovered by a pDOS chemical library screen. a) IC_{50}(± standard deviation) values of 1 in HeLa, U266, A549, and MCF7 cell lines. Each cell line was treated with 1 in various concentrations for 72 h. Cell cytotoxicity was measured with WST-1. b) Chemical structure of hit compound 1 and derivatives 2–4, for target identification. c) Viability of HeLa cells after 72 h of treatment with compounds 1–4 (10 μM).

As shown in Figure 2 a, compound 1 was antiproliferative toward HeLa (human cervical cancer cell line) with an IC50 of 450 nm, as well as U266 (human myeloma cell line), A549 (human lung cancer cell line), and MCF7 (human breast cancer cell line). Based on analogue activity patterns, we successfully introduced a long aliphatic chain at the C2 position of the benzopyran moiety and produced compound 2 without deterioration of biological activity (Figure 2 c). This functional handle was used as the starting point of probe design for FITGE-based target identification. The desired probe 3 was synthesized with benzophenone and acetylene

moieties at the C2 position of 1 to enable the temporal crosslinking of the target proteins upon UV irradiation and the fluorescence-based visualization of target proteins by a bioorthogonal click reaction, respectively. We also designed a negative probe 4 to eliminate nonspecific protein labeling. Prior to their application in target identification, the cellular activities of probe 3 and negative probe 4 were tested. As shown in Figure 2 c, we confirmed that probe 3 still has antiproliferative activity, but negative probe 4 does not; therefore, these probes possess the essential criteria for use in target identification.

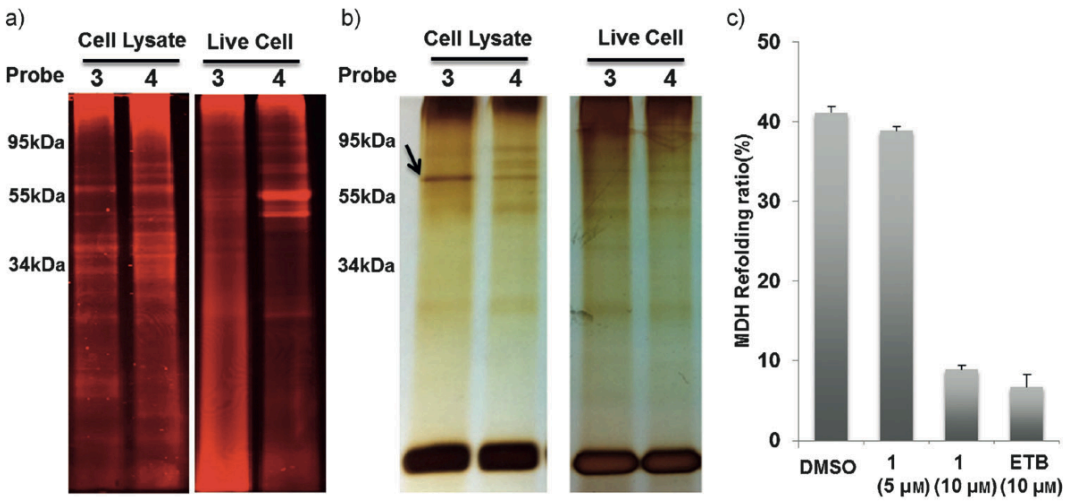

Figure 3. Target identification and validation. a) 3 and 4 were separately covalently linked to proteomes from cell lysates and live cells. The labeled proteomes were visualized with Cy5–azide and analyzed by 1DGE. b) The labeled proteomes were covalently linked with biotin–azide, enriched by affinity pull-down, separated by 1DGE, and visualized by silver staining. The arrow indicates a potential target protein. c) Malate dehydrogenase (MDH) refolding assay. Epolactaene tert-butyl ester (ETB) is a known inhibitor of MDH refolding by HSP60.

Probe 3 and negative probe 4 were incubated separately with cell lysates and live cells. During incubation, UV irradiation at 365 nm was used to induce covalent crosslinking of probes with adjacent proteins. Proteomes from each condition were then modified with a Cy5–azide fluorescent label by a click reaction and analyzed by sodium dodecyl sulfate polyacrylamide gel electrophoresis (SDS-PAGE). However, we did not observe any significant difference in bands based on the fluorescence

labeling pattern (Figure 3 a). We suspected that the amount of target proteins was too small to distinguish changes in bands by one-dimensional gel electrophoresis (1DGE). Therefore, we enriched the target proteins using a traditional pull-down method in conjunction with UV-induced crosslinking. Proteomes covalently linked to 3 and 4 were labeled with a biotin–azide linker by a click reaction, after which the labeled proteins were enriched by an affinity pull-down method using a streptavidin bead. The enriched proteomes were eluted, separated by 1DGE, and visualized by silver staining. Interestingly, we observed different protein patterns after enrichment, and a single labeled protein band (Figure 3 b, indicated by an arrow) in the cell lysate appeared to be the target protein of antiproliferative agent 1, which was identified as heat shock protein 60 (HSP 60) by MS analysis. For target validation, we performed a malate dehydrogenase (MDH) refolding assay to measure the enzymatic activity of HSP60.[4a] As shown in Figure 3 c, MDH refolding by HSP60 was inhibited by 1 at 10 mm, which is similar to epolactaene tert-butyl ester (ETB), a known HSP60 inhibitor. However, the drastic concentration-dependent reduction of the inhibition activity of 1 on HSP60, even at 5 mm, suggested that HSP60 can not be a major target protein of 1, which exhibits excellent antiproliferative activity with a submicromolar IC50 value.

Undaunted by a series of failures in target identification, we pursued the possibility that the analysis of the entire proteome display using 2DGE could address the poor resolution of 1DGE. To address the intrinsically high nonspecific labeling obtained when using the benzophenone moiety as a photocrosslinker, the proteomes labeled with probe 3 and negative probe 4 were also visualized with Cy5 and Cy3, respectively. To compare the images from two fluorescence channels and eliminate the nonspecifically labeled proteins, proteomes labeled with 3 and Cy5 or 4 and Cy3

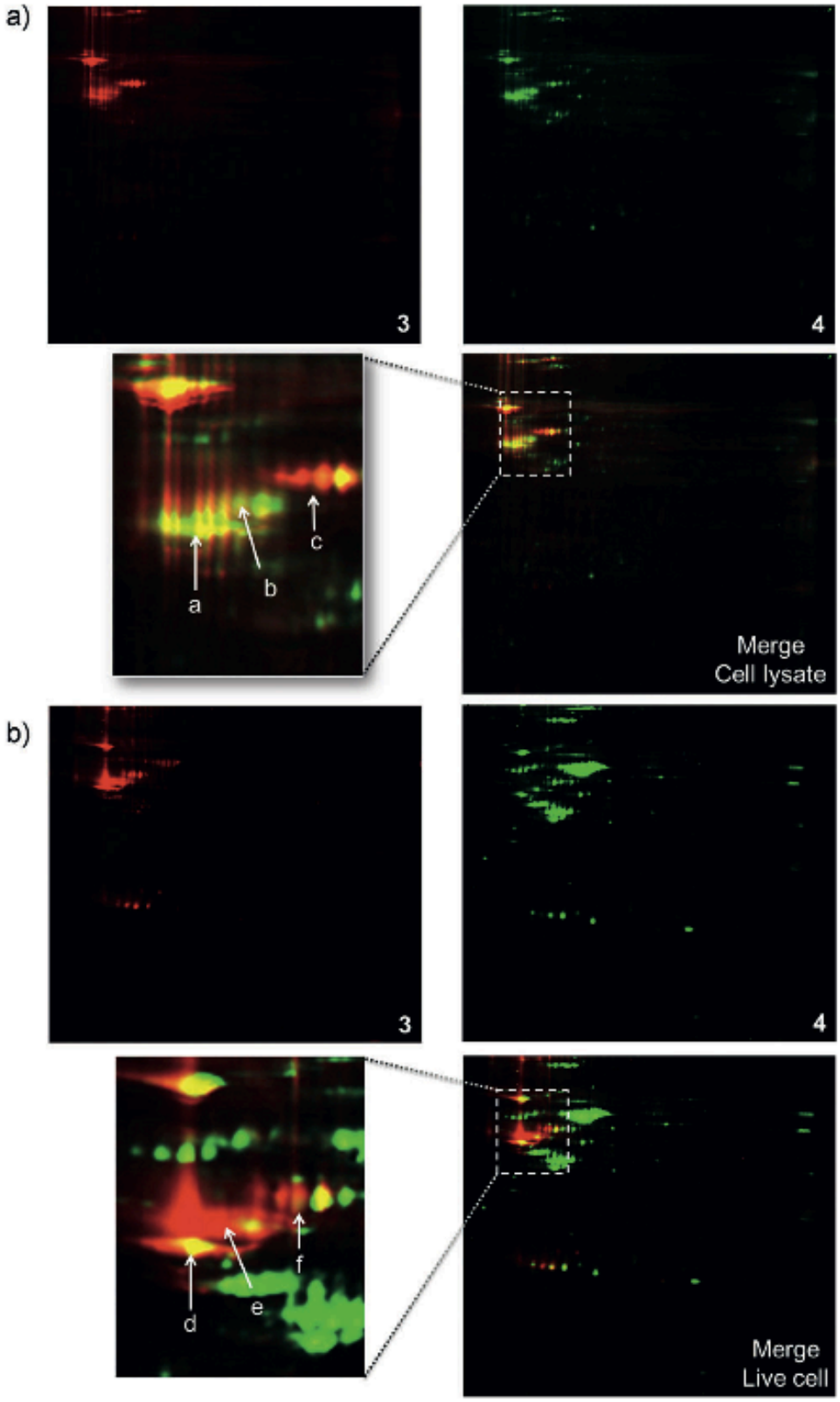

Figure 4. Target identification using the FITGE method. Cy5 channel image (proteome labeled with 3) and Cy3 channel image (proteome labeled with 4) are merged into one image for analysis. a) Cell lysate proteome labeling image. b) Live cell proteome labeling image.

were subjected to a single round of 2DGE and the merged images of the Cy5 and Cy3 channels were then analyzed. The merged image revealed three fluorescent colors, red and green spots from proteins preferentially labeled with probe 3 and negative probe 4, respectively, and yellow spots from proteins dual-labeled with 3 and 4. Surprisingly, we also clearly observed some red spots among a large collection of green and yellow spots, which we ruled out as proteins labeled nonspecifically by negative probe 4 (Figure 4). We believe that the higher resolution obtained by 2DGE over 1DGE enables the discrimination of the actual target proteins from nonspecifically labeled proteins.

Furthermore, the labeling pattern using the FITGE method in cell lysates was different from that in live cells. This finding demonstrates the importance of the environment during target identification. As shown in Figure 4 a, FITGE-based labeling under cell lysate conditions revealed a single red spot c that was selectively labeled by 3, but not by 4. The merged image showed the proteins dual-labeled by 3 and 4 in yellow, such as spots a and b, which helps to deprioritize them for further mass analysis. Based on this labeling pattern in cell lysate, red spot c represented a strong target protein candidate. Subsequent mass analysis revealed that this spot was HSP60, which was identical to the results obtained using our previous pull-down enrichment. As HSP60 is not a major target protein of 1 and was confirmed to be inhibited by com- pound 1 only at high concentrations, we further investigated the FITGE method in live cells. As shown in Figure 4 b, negative probe 4 labels more proteins in live cells than in the cell lysate, which is probably a result of the high protein concentration in live cells. The number of spots labeled by probe 3 was similar under both conditions, but the size of individual red spots was slightly different. In live cells, spots e and f were preferentially labeled by 3, but not by 4.

Interestingly, spots d, e, and f are similar to spots a, b, and c in terms of molecular weight and isoelectric point (pI) value, but their labeling patterns are different; unlike spots a and d or spots c and f, which are consistently labeled in yellow or red, respectively, spots b and e were labeled in red in live cells, but labeled in yellow in the cell lysate. Subsequent MS analysis revealed that spot f is HSP60, but spot e is tubulin, which can be a potential target protein of 1. These results suggest that the FITGE method allows significantly simplified protein mass analysis, as compared to the 1D pull-down enrichment method, through sensitive detection in the labeling preference of active and negative probes, and thus provides a potential solution to overcome the current limitation of extensive nonspecific binding of photoaffinity probes.

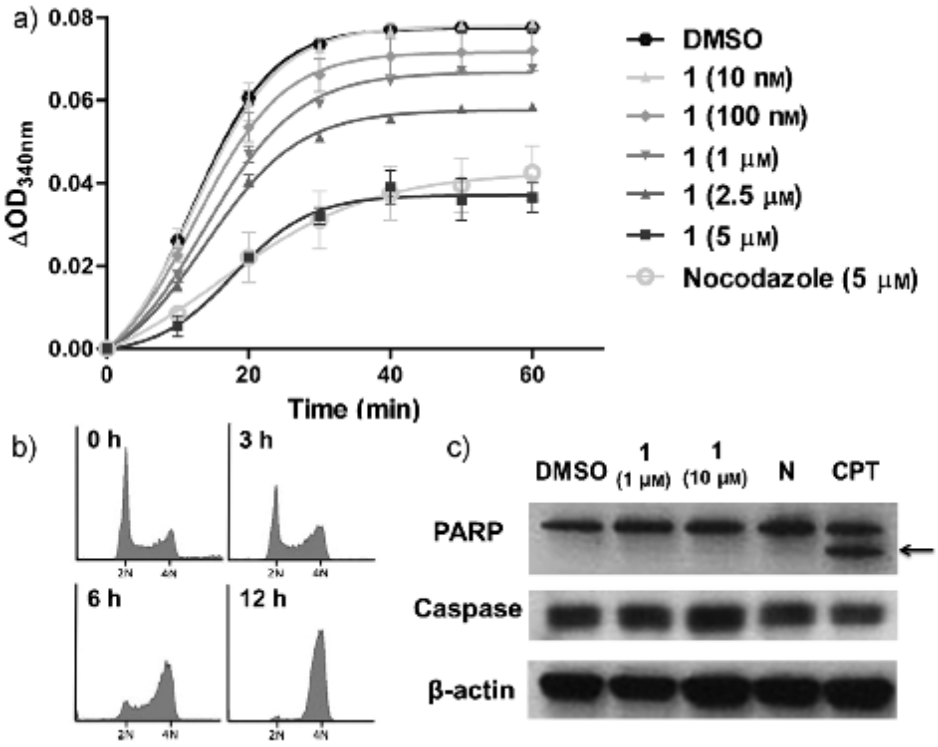

Figure 5. Validation of tubulin as a target protein of 1. a) An in vitro tubulin polymerization assay showing dose-dependent inhibition by 1. ΔOD_{340nm} = optical density difference at 340 nm b) Flow cytometry cell cycle analysis of HeLa cells treated with 1 (1 μM). c) Western blot analysis of the apoptotic pathway. N = nocodazole (10 μM), CPT = camptothecin (10 μM). The arrow indicates cleaved PARP.

Target validation was then performed using an in vitro tubulin polymerization assay. As shown in Figure 5 a, compound 1 inhibited tubulin polymerization in a dose-dependent manner and showed a similar activity to nocodazole,[13] a known tubulin polymerization inhibitor. Even at 100 nm, compound 1 still showed some inhibition of tubulin polymerization. Considering the antiproliferative activity of 1, this result strongly supports tubulin as the target protein of 1. As the hallmark of cellular response toward tubulin polymerization inhibitors is a cell-cycle arrest,[14] we tested whether 1 triggers cell-cycle arrest using flow cytometry. As shown in Figure 5 b, the cell cycle of HeLa cells was arrested upon treatment with 1 at 1 mm in a time-dependent manner, and the cell cycle completely stopped after 12 h. However, western blot analysis showed that neither caspase 3 nor poly(ADP–ribose)polymerase (PARP) were activated after 12h of treatment with 1, which is similar to nocodazole. Instead, a different type of anticancer agent, camptothecin (a DNA topoisomerase I inhibitor),[15] triggered the apoptotic pathway (Figure 5 c). We also confirmed the inhibition of tubulin polymerization upon treatment of 1 by cell-based fluorescent imaging through the visualization of tubulin and its microtubules (Figure S1–2 in the Supporting Information). Therefore, we have concluded that 1 is a potent antitumor agent that functions by the inhibition of tubulin polymerization.

Conclusion

We have developed a new target identification method, FITGE, which aims to observe interactions between proteins and small molecules in an intact cellular environment. After a series of failures using conventional target identification methods, we successfully identified the protein target of anti-proliferative compound 1 with FITGE only in live cells, and observed the environment-dependent binding

events of a functional small molecule by direct comparison between live cells and cell lysates. Even though it still requires the synthesis of bioactive probes with a photo-crosslinker moiety, the FITGE method can address the current limitations of conventional target identification methods and can significantly enhance the possibility of target identification through the combination of the covalent capturing of target proteins in an intact cellular environment and the efficient exclusion of nonspecific protein labeling using two-color 2DGE. We believe our FITGE method provides a unique means of target identification in live cells.

Supporting Information

Trypsin in-gel digestion of proteins : Excise protein spot/band and dehydrate in CH_3CN for 10 min. Remove CH_3CN and SpeedVac until dry. For mass analysis, the resulting gel pieces were re-swelled at 4 °C for 45 min in buffer containing trypsin and 50 mM NH_4CO_3 and incubated overnight at 37 °C for tryptic digestion. The samples with gel pieces were centrifuged and the supernatant was collected for mass analysis. The residual peptides in gel pieces were further extracted with 50% CH_3CN containing 20 mM NH_4CO_3 and 5% formic acid three times at room temperature. The combined peptide samples were condensed down in SpeedVac until the desired sample concentration was reached.[16]

LC-MS/MS analysis : LC-MS/MS experiments were performed essentially as described in the previous report.[17] In brief, we used a hybrid quadrupole-TOF LC-MS/MS spectrometer (Q-Star Elite) [Applied Biosystems, USA] that had a nanoelectrospray ionization source and was fitted with a fused silica emitter tip [New

Objective, USA]. For each LC-MS/MS run, 1–2 µg of fractionated peptides was injected into the LC-MS/MS system, and the peptides were trapped and concentrated on an Agilent Zorbax 300SB-C18 column (300 µm i.d. x 50 mm, 5 µm, 100 Å) [Agilent Technologies, USA]. The peptide mixture was separated on an Agilent Zorbax 300SB nanoflow C18 column (75 µm i.d. x 150 mm, 3.5 µm, 100 Å) [Agilent Technologies, USA] at a flow rate of 300 nL/min, and eluted peptides were electrosprayed through a coated silica tip (ion spray voltage at 2300 eV).

Mass spectrometric data analysis : ProteinPilot Software 2.0.1 (Software Revision Number: 67476) [Applied Biosystems, USA] was used to identify peptides and proteins and quantify differentially expressed proteins. To process an MS or MS/MS spectrum, a thorough search was performed against a NCBI or IPI database using the Paragon and Pro Group algorithms [Applied Biosystems, USA]. Peptides detected for each protein were colored in the Protein Sequence Coverage pane (Table S1).

Color	Peptide Confidence
Gray	No match
Red	> 0 and < 50
Yellow	≥ 50 and < 95
Green	≥ 95

Table S1. Peptide color in the Protein Sequence Coverage pane

Mass analysis of protein bands from affinity pull-down method :

Identified Proteins from pull-down method with active probe **(3)** in Figure 3(b)

N	Unused	Total	%Cov	%Cov(50)	%Cov(95)	Accession	Name
1	19.41	19.41	44.8757768	22.9813665	15.9937888	IPI:IPI00220327.3	Gene_Symbol=KRT1 Keratin, type II cytoskeletal 1
2	15.79	15.79	53.8461566	31.4903855	29.3269217	IPI:IPI00792677.1	Gene_Symbol=TUBA1B 46 kDa protein
2	0	15.79	49.6674061	29.0465623	27.0509988	IPI:IPI00387144.4	Gene_Symbol=TUBA1B Tubulin alpha-1B chain
2	0	15.79	42.9844111	29.1759461	27.1714926	IPI:IPI00218343.4	Gene_Symbol=TUBA1C Tubulin alpha-1C chain
2	0	13.79	49.6674061	25.9423494	23.9467844	IPI:IPI00180675.4	Gene_Symbol=TUBA1A Tubulin alpha-1A chain
3	14.11	14.11	38.5232747	25.8426964	19.4221511	IPI:IPI00019359.3	Gene_Symbol=KRT9 Keratin, type I cytoskeletal 9
4	8.64	8.64	45.2702701	20.7207203	10.5855852	IPI:IPI00011654.2	Gene_Symbol=TUBB Tubulin beta chain
4	0	8.64	43.6619729	21.596244	11.0328637	IPI:IPI00645452.1	Gene_Symbol=TUBB Tubulin, beta polypeptide
4	0	7.87	37.0786518	18.6516851	10.5617978	IPI:IPI00013475.1	Gene_Symbol=TUBB2A Tubulin beta-2A chain
4	0	7.87	33.4831446	18.6516851	10.5617978	IPI:IPI00031370.3	Gene_Symbol=TUBB2B Tubulin beta-2B chain
5	8.27	8.88	24.7892067	13.1534576	6.74536228	IPI:IPI00009865.2	Gene_Symbol=KRT10 Keratin, type I cytoskeletal 10
5	0	7.86	21.7468813	10.3386812	7.13012442	IPI:IPI00884222.1	Gene_Symbol=- Similar to Keratin, type I cytoskeletal 10
6	8.14	8.14	64.2233849	15.3577656	12.2164048	IPI:IPI00784154.1	Gene_Symbol=HSPD1 60 kDa heat shock protein, mitochondrial p
6	0	7.48	71.2446332	30.0429195	30.0429195	IPI:IPI00790763.1	Gene_Symbol=HSPD1 Putative uncharacterized protein HSPD1 (Fr
7	7.67	7.67	34.9206358	7.40740746	6.45502657	IPI:IPI00219994.2	Gene_Symbol=CSE1L Isoform 3 of Exportin-2
7	0	7.67	33.985582	7.20906258	6.28218353	IPI:IPI00022744.5	Gene_Symbol=CSE1L Isoform 1 of Exportin-2
7	0	7.67	30.0546438	7.65027329	6.66666701	IPI:IPI00219762.2	Gene_Symbol=CSE1L Cellular apoptosis susceptibility protein varia
8	7.24	7.24	39.0015602	9.82839316	4.83619347	IPI:IPI00845339.1	Gene_Symbol=HSPA1A;HSPA1B heat shock 70kDa protein 1A
8	0	7.24	33.2293302	9.82839316	4.83619347	IPI:IPI00847536.1	Gene_Symbol=HSPA1A;HSPA1B heat shock 70kDa protein 1B
8	0	7.24	33.2293302	9.82839316	4.83619347	IPI:IPI00304925.5	Gene_Symbol=HSPA1A;HSPA1B Heat shock 70 kDa protein 1
9	7.23	7.23	52.0202041	23.7373739	23.7373739	IPI:IPI00795676.1	Gene_Symbol=RAB11A 22 kDa protein
9	0	7.23	47.6851851	21.7592597	21.7592597	IPI:IPI00429190.3	Gene_Symbol=RAB11A Ras-related protein Rab-11A
9	0	7.23	40.8256888	21.5596333	21.5596333	IPI:IPI00020436.4	Gene_Symbol=RAB11B Ras-related protein Rab-11B
10	2.92	2.92	33.9826852	7.5757578	5.19480519	IPI:IPI00396485.3	Gene_Symbol=EEF1A1 Elongation factor 1-alpha 1
10	0	2.92	35.6009066	7.93650821	5.44217676	IPI:IPI00025447.8	Gene_Symbol=EEF1A1 Elongation factor 1-alpha
10	0	2.92	32.6839834	7.5757578	5.19480519	IPI:IPI00472724.1	Gene_Symbol=- Elongation factor 1-alpha
10	0	2.77	49.779737	15.4185027	10.5726875	IPI:IPI00382804.1	Gene_Symbol=EEF1A1 EEF1A protein (Fragment)
11	2.42	2.42	30.6629837	3.45303863	1.65745858	IPI:IPI00414676.6	Gene_Symbol=HSP90AB1 Heat shock protein HSP 90-beta
11	0	2.19	24.2388755	2.92740054	1.40515221	IPI:IPI00382470.3	Gene_Symbol=HSP90AA1 heat shock protein 90kDa alpha (cytoso
11	0	2.19	25.5102038	3.18877548	1.53061226	IPI:IPI00789847.1	Gene_Symbol=- Protein
11	0	2.19	24.5901644	3.4153007	1.63934417	IPI:IPI00784295.2	Gene_Symbol=HSP90AA1 Isoform 1 of Heat shock protein HSP 90-
11	0	1.94	38.0614668	5.91016561	2.83687934	IPI:IPI00455599.3	Gene_Symbol=HSP90AB2P Heat shock protein 90Bb
11	0	1.94	54.1935503	16.1290318	7.74193555	IPI:IPI00411633.3	Gene_Symbol=HSP90AB1 Heat shock protein beta
11	0	1.94	16.3461536	8.01282078	3.84615399	IPI:IPI00031523.3	Gene_Symbol=HSP90AA2 Heat shock protein 90 kDa alpha class A
11	0	1.94	15.0259063	12.9533678	6.21761642	IPI:IPI00795108.1	Gene_Symbol=HSP90AA1 21 kDa protein
12	2	4.09	25.2713174	3.72093022	3.72093022	IPI:IPI00021304.1	Gene_Symbol=KRT2 Keratin, type II cytoskeletal 2 epidermal
12	0	1.76	35.4609936	2.12765951	2.12765951	IPI:IPI00299145.9	Gene_Symbol=KRT6C Keratin, type II cytoskeletal 6C
12	0	1.76	35.4609936	2.12765951	2.12765951	IPI:IPI00293665.8	Gene_Symbol=KRT6B Keratin, type II cytoskeletal 6B
12	0	1.76	35.9929085	2.12765951	2.12765951	IPI:IPI00300725.7	Gene_Symbol=KRT6A Keratin, type II cytoskeletal 6A
12	0	1.75	54.1401267	7.64331222	7.64331222	IPI:IPI00796330.1	Gene_Symbol=KRT6A 18 kDa protein
12	0	1.72	33.3333343	2.11640205	2.11640205	IPI:IPI00796776.1	Gene_Symbol=KRT5 60 kDa protein
12	0	1.7	25.6074756	2.24299058	2.24299058	IPI:IPI00241841.9	Gene_Symbol=KRT79 Keratin, type II cytoskeletal 79
12	0	1.7	18.8747734	2.17785835	2.17785835	IPI:IPI00005859.3	Gene_Symbol=KRT75 Keratin, type II cytoskeletal 75
12	0	1.7	19.0045252	5.4298643	5.4298643	IPI:IPI00795197.1	Gene_Symbol=KRT5 24 kDa protein
12	0	1.7	59.3220353	10.1694912	10.1694912	IPI:IPI00794362.1	Gene_Symbol=KRT5 Protein
12	0	1.7	30.6122452	6.12244904	6.12244904	IPI:IPI00793849.1	Gene_Symbol=KRT5 Protein
12	0	1.7	68.1818187	13.636364	13.636364	IPI:IPI00793778.1	Gene_Symbol=KRT5 Keratin
13	2	2	8.42391327	1.03260865	1.03260865	IPI:IPI00470917.2	Gene_Symbol=KIAA1529 Isoform 2 of Uncharacterized protein KIA
13	0	2	9.41676795	1.15431352	1.15431352	IPI:IPI00292836.4	Gene_Symbol=KIAA1529 Isoform 1 of Uncharacterized protein KIA
14	2	2	33.7016582	6.07734807	6.07734807	IPI:IPI00219518.7	Gene_Symbol=ARL1 ADP-ribosylation factor-like protein 1
15	2	2	24.5614037	14.0350878	14.0350878	IPI:IPI00008527.3	Gene_Symbol=RPLP1 60S acidic ribosomal protein P1

Identified Proteins from pull-down method with negative probe (**4)** in Figure 3(b)

N	Unused	Total	%Cov	%Cov(50)	%Cov(95)	Accession	Name
1	13.51	13.51	37.422359	14.1304344	12.8881991	IPI:IPI00220327.3	Gene_Symbol=KRT1 Keratin, type II cytoskeletal 1
2	9.01	9.01	38.4976536	15.2582154	15.2582154	IPI:IPI00645452.1	Gene_Symbol=TUBB Tubulin, beta polypeptide
2	0	9.01	36.9369358	14.6396399	14.6396399	IPI:IPI00011654.2	Gene_Symbol=TUBB Tubulin beta chain
2	0	8.84	28.3146054	14.6067411	14.6067411	IPI:IPI00013475.1	Gene_Symbol=TUBB2A Tubulin beta-2A chain
2	0	8.84	24.7191012	14.6067411	14.6067411	IPI:IPI00031370.3	Gene_Symbol=TUBB2B Tubulin beta-2B chain
2	0	7.51	35.7526869	13.4408608	13.4408608	IPI:IPI00647896.1	Gene_Symbol=TUBB Tubulin, beta
2	0	7.5	27.64045	11.2359554	11.2359554	IPI:IPI00007752.1	Gene_Symbol=TUBB2C Tubulin beta-2C chain
3	7.1	7.1	39.9038464	15.384616	12.0192304	IPI:IPI00792677.1	Gene_Symbol=TUBA1B 46 kDa protein
3	0	7.1	36.807096	14.1906872	11.0864744	IPI:IPI00387144.4	Gene_Symbol=TUBA1B Tubulin alpha-1B chain
3	0	7.1	36.9710475	14.253898	11.1358576	IPI:IPI00218343.4	Gene_Symbol=TUBA1C Tubulin alpha-1C chain
3	0	6.73	33.7028831	11.0864744	11.0864744	IPI:IPI00180675.4	Gene_Symbol=TUBA1A Tubulin alpha-1A chain
3	0	6.73	41.1042958	15.337424	15.337424	IPI:IPI00166768.3	Gene_Symbol=TUBA1C TUBA1C protein
3	0	5.79	36.1194044	16.4179102	12.2388057	IPI:IPI00793930.1	Gene_Symbol=TUBA1B TUBA1B protein
4	5.82	5.82	28.5491407	8.11232477	4.2121686	IPI:IPI00847536.1	Gene_Symbol=HSPA1A;HSPA1B heat shock 70kDa protein 1B
4	0	5.82	27.6131034	8.11232477	4.2121686	IPI:IPI00845339.1	Gene_Symbol=HSPA1A;HSPA1B heat shock 70kDa protein 1A
4	0	5.82	27.6131034	8.11232477	4.2121686	IPI:IPI00304925.5	Gene_Symbol=HSPA1A;HSPA1B Heat shock 70 kDa protein 1
4	0	5.01	20.8398134	6.22083992	4.19906676	IPI:IPI00339269.1	Gene_Symbol=HSPA6 Heat shock 70 kDa protein 6
5	3.53	3.53	44.9494958	17.6767677	6.56565651	IPI:IPI00795676.1	Gene_Symbol=RAB11A 22 kDa protein
5	0	3.53	41.2037045	16.203703	6.01851866	IPI:IPI00429190.3	Gene_Symbol=RAB11A Ras-related protein Rab-11A
5	0	3.53	40.8256888	16.055046	5.96330278	IPI:IPI00020436.4	Gene_Symbol=RAB11B Ras-related protein Rab-11B
6	3.29	3.29	32.9842925	10.1221643	2.09424086	IPI:IPI00784154.1	Gene_Symbol=HSPD1 60 kDa heat shock protein, mitochondrial p
6	0	1.99	41.2017167	14.1630903	5.15021458	IPI:IPI00790763.1	Gene_Symbol=HSPD1 Putative uncharacterized protein HSPD1 (Fr
6	0	1.97	53.1645596	20.8860755	7.59493634	IPI:IPI00795445.1	Gene_Symbol=HSPD1 Short heat shock protein 60 Hsp60s1
6	0	1.55	15.4017851	2.67857146	2.67857146	IPI:IPI00880053.1	Gene_Symbol=- 49 kDa protein
7	2.89	2.89	21.0272878	5.1364366	3.69181372	IPI:IPI00019359.3	Gene_Symbol=KRT9 Keratin, type I cytoskeletal 9
8	2.5	2.5	17.3693091	3.54131535	2.0236088	IPI:IPI00009865.2	Gene_Symbol=KRT10 Keratin, type I cytoskeletal 10
8	0	2.5	8.73440281	3.74331549	2.13903747	IPI:IPI00884222.1	Gene_Symbol=- Similar to Keratin, type I cytoskeletal 10
9	2.48	2.48	14.0394092	3.69458124	3.69458124	IPI:IPI00871852.1	Gene_Symbol=EIF4A1 46 kDa protein
9	0	2.48	14.0394092	3.69458124	3.69458124	IPI:IPI00025491.1	Gene_Symbol=EIF4A1 Eukaryotic initiation factor 4A-I
9	0	2.28	13.6000007	3.99999991	3.99999991	IPI:IPI00555602.1	Gene_Symbol=EIF4A1 CD68 antigen variant (Fragment)
9	0	2.2	8.66807625	3.17124724	3.17124724	IPI:IPI00386604.1	Gene_Symbol=EIF4A1 Putative uncharacterized protein (Fragmen
10	2.13	2.13	17.9723501	2.76497696	2.76497696	IPI:IPI00465248.5	Gene_Symbol=ENO1 Isoform alpha-enolase of Alpha-enolase
10	0	2	12.2270741	2.62008738	2.62008738	IPI:IPI00013769.1	Gene_Symbol=- Alpha-enolase, lung specific
10	0	2	17.0087978	3.51906158	3.51906158	IPI:IPI00759806.1	Gene_Symbol=ENO1 Isoform MBP-1 of Alpha-enolase

The comparison of identified proteins from pull-down method with active probe (**3**) and negative probe (**4**) in Figure 3(b). The highlighted proteins are identified by both probes (**3** and **4**), which means that most of proteins, even target proteins (i.e. tubulin and Hsp60), are nonspecifically bound to negative probe (**4**). Therefore, the affinity pull-down-based mass analysis might cause the misleading toward the false negatives in target identification.

N	Unused	Total	%Cov	%Cov(50)	%Cov(95)	Accession	Name
1	19.41	19.41	44.8757768	22.9813665	15.9937888	IPI:IPI00220327.3	Gene_Symbol=KRT1 Keratin, type II cytoskeletal 1
2	15.79	15.79	53.8461566	31.4903855	29.3269217	IPI:IPI00792677.1	Gene_Symbol=TUBA1B 46 kDa protein
2	0	15.79	49.6674061	29.0465623	27.0509988	IPI:IPI00387144.4	Gene_Symbol=TUBA1B Tubulin alpha-1B chain
2	0	15.79	42.9844111	29.1759461	27.1714926	IPI:IPI00218343.4	Gene_Symbol=TUBA1C Tubulin alpha-1C chain
2	0	13.79	49.6674061	25.9423494	23.9467844	IPI:IPI00180675.4	Gene_Symbol=TUBA1A Tubulin alpha-1A chain
3	14.11	14.11	38.5232747	25.8426964	19.4221511	IPI:IPI00019359.3	Gene_Symbol=KRT9 Keratin, type I cytoskeletal 9
4	8.64	8.64	45.2702701	20.7207203	10.5855852	IPI:IPI00011654.2	Gene_Symbol=TUBB Tubulin beta chain
4	0	8.64	43.6619729	21.596244	11.0328637	IPI:IPI00645452.1	Gene_Symbol=TUBB Tubulin, beta polypeptide
4	0	7.87	37.0786518	18.6516851	10.5617978	IPI:IPI00013475.1	Gene_Symbol=TUBB2A Tubulin beta-2A chain
4	0	7.87	33.4831446	18.6516851	10.5617978	IPI:IPI00031370.3	Gene_Symbol=TUBB2B Tubulin beta-2B chain
5	8.27	8.88	24.7892067	13.1534576	6.74536228	IPI:IPI00009865.2	Gene_Symbol=KRT10 Keratin, type I cytoskeletal 10
5	0	7.86	21.7468813	10.3386812	7.13012442	IPI:IPI00884222.1	Gene_Symbol=- Similar to Keratin, type I cytoskeletal 10
6	8.14	8.14	64.2233849	15.3577656	12.2164048	IPI:IPI00784154.1	Gene_Symbol=HSPD1 60 kDa heat shock protein, mitochondrial p
6	0	7.48	71.2446332	30.0429195	30.0429195	IPI:IPI00790763.1	Gene_Symbol=HSPD1 Putative uncharacterized protein HSPD1 (Fr
7	7.67	7.67	34.9206358	7.40740746	6.45502657	IPI:IPI00219994.2	Gene_Symbol=CSE1L Isoform 3 of Exportin-2
7	0	7.67	33.985582	7.20906258	6.28218353	IPI:IPI00022744.5	Gene_Symbol=CSE1L Isoform 1 of Exportin-2
7	0	7.67	30.0546438	7.65027329	6.66666701	IPI:IPI00219762.2	Gene_Symbol=CSE1L Cellular apoptosis susceptibility protein varia
8	7.24	7.24	39.0015602	9.82839316	4.83619347	IPI:IPI00845339.1	Gene_Symbol=HSPA1A;HSPA1B heat shock 70kDa protein 1A
8	0	7.24	33.2293302	9.82839316	4.83619347	IPI:IPI00847536.1	Gene_Symbol=HSPA1A;HSPA1B heat shock 70kDa protein 1B
8	0	7.24	33.2293302	9.82839316	4.83619347	IPI:IPI00304925.5	Gene_Symbol=HSPA1A;HSPA1B Heat shock 70 kDa protein 1
9	7.23	7.23	52.0202041	23.7373739	23.7373739	IPI:IPI00795676.1	Gene_Symbol=RAB11A 22 kDa protein
9	0	7.23	47.6851851	21.7592597	21.7592597	IPI:IPI00429190.3	Gene_Symbol=RAB11A Ras-related protein Rab-11A
9	0	7.23	40.8256888	21.5596333	21.5596333	IPI:IPI00020436.4	Gene_Symbol=RAB11B Ras-related protein Rab-11B
10	2.92	2.92	33.9826852	7.5757578	5.19480519	IPI:IPI00396485.3	Gene_Symbol=EEF1A1 Elongation factor 1-alpha 1
10	0	2.92	35.6009066	7.93650821	5.44217676	IPI:IPI00025447.8	Gene_Symbol=EEF1A1 Elongation factor 1-alpha
10	0	2.92	32.6839834	7.5757578	5.19480519	IPI:IPI00472724.1	Gene_Symbol=- Elongation factor 1-alpha
10	0	2.77	49.779737	15.4185027	10.5726875	IPI:IPI00382804.1	Gene_Symbol=EEF1A1 EEF1A protein (Fragment)
11	2.42	2.42	30.6629837	3.45303863	1.65745858	IPI:IPI00414676.6	Gene_Symbol=HSP90AB1 Heat shock protein HSP 90-beta
11	0	2.19	24.2388755	2.92740054	1.40515221	IPI:IPI00382470.3	Gene_Symbol=HSP90AA1 heat shock protein 90kDa alpha (cytoso
11	0	2.19	25.5102038	3.18877548	1.53061226	IPI:IPI00789847.1	Gene_Symbol=- Protein
11	0	2.19	24.5901644	3.4153007	1.63934417	IPI:IPI00784295.2	Gene_Symbol=HSP90AA1 Isoform 1 of Heat shock protein HSP 90-
11	0	1.94	38.0614668	5.91016561	2.83687934	IPI:IPI00455599.3	Gene_Symbol=HSP90AB2P Heat shock protein 90Bb
11	0	1.94	54.1935503	16.1290318	7.74193555	IPI:IPI00411633.3	Gene_Symbol=HSP90AB1 Heat shock protein beta
11	0	1.94	16.3461536	8.01282078	3.84615399	IPI:IPI00031523.3	Gene_Symbol=HSP90AA2 Heat shock protein 90 kDa alpha class A
11	0	1.94	15.0259063	12.9533678	6.21761642	IPI:IPI00795108.1	Gene_Symbol=HSP90AA1 21 kDa protein
12	2	4.09	25.2713174	3.72093022	3.72093022	IPI:IPI00021304.1	Gene_Symbol=KRT2 Keratin, type II cytoskeletal 2 epidermal
12	0	1.76	35.4609936	2.12765951	2.12765951	IPI:IPI00299145.9	Gene_Symbol=KRT6C Keratin, type II cytoskeletal 6C
12	0	1.76	35.4609936	2.12765951	2.12765951	IPI:IPI00293665.8	Gene_Symbol=KRT6B Keratin, type II cytoskeletal 6B
12	0	1.76	35.9929085	2.12765951	2.12765951	IPI:IPI00300725.7	Gene_Symbol=KRT6A Keratin, type II cytoskeletal 6A
12	0	1.75	54.1401267	7.64331222	7.64331222	IPI:IPI00796330.1	Gene_Symbol=KRT6A 18 kDa protein
12	0	1.72	33.3333343	2.11640205	2.11640205	IPI:IPI00796776.1	Gene_Symbol=KRT5 60 kDa protein
12	0	1.7	25.6074756	2.24299058	2.24299058	IPI:IPI00241841.9	Gene_Symbol=KRT79 Keratin, type II cytoskeletal 79
12	0	1.7	18.8747734	2.17785835	2.17785835	IPI:IPI00005859.3	Gene_Symbol=KRT75 Keratin, type II cytoskeletal 75
12	0	1.7	19.0045252	5.4298643	5.4298643	IPI:IPI00795197.1	Gene_Symbol=KRT5 24 kDa protein
12	0	1.7	59.3220353	10.1694912	10.1694912	IPI:IPI00794362.1	Gene_Symbol=KRT5 Protein
12	0	1.7	30.6122452	6.12244904	6.12244904	IPI:IPI00793849.1	Gene_Symbol=KRT5 Protein
12	0	1.7	68.1818187	13.636364	13.636364	IPI:IPI00793778.1	Gene_Symbol=KRT5 Keratin
13	2	2	8.42391327	1.03260865	1.03260865	IPI:IPI00470917.2	Gene_Symbol=KIAA1529 Isoform 2 of Uncharacterized protein KIA
13	0	2	9.41676795	1.15431352	1.15431352	IPI:IPI00292836.4	Gene_Symbol=KIAA1529 Isoform 1 of Uncharacterized protein KIA
14	2	2	33.7016582	6.07734807	6.07734807	IPI:IPI00219518.7	Gene_Symbol=ARL1 ADP-ribosylation factor-like protein 1
15	2	2	24.5614037	14.0350878	14.0350878	IPI:IPI00008527.3	Gene_Symbol=RPLP1 60S acidic ribosomal protein P1

Mass analysis of protein spots identified by FITGE method

Protein spot **c**, **e**, and **f** from FITGE were excised from the gel for mass analysis.

Protein spot c mass analysis result

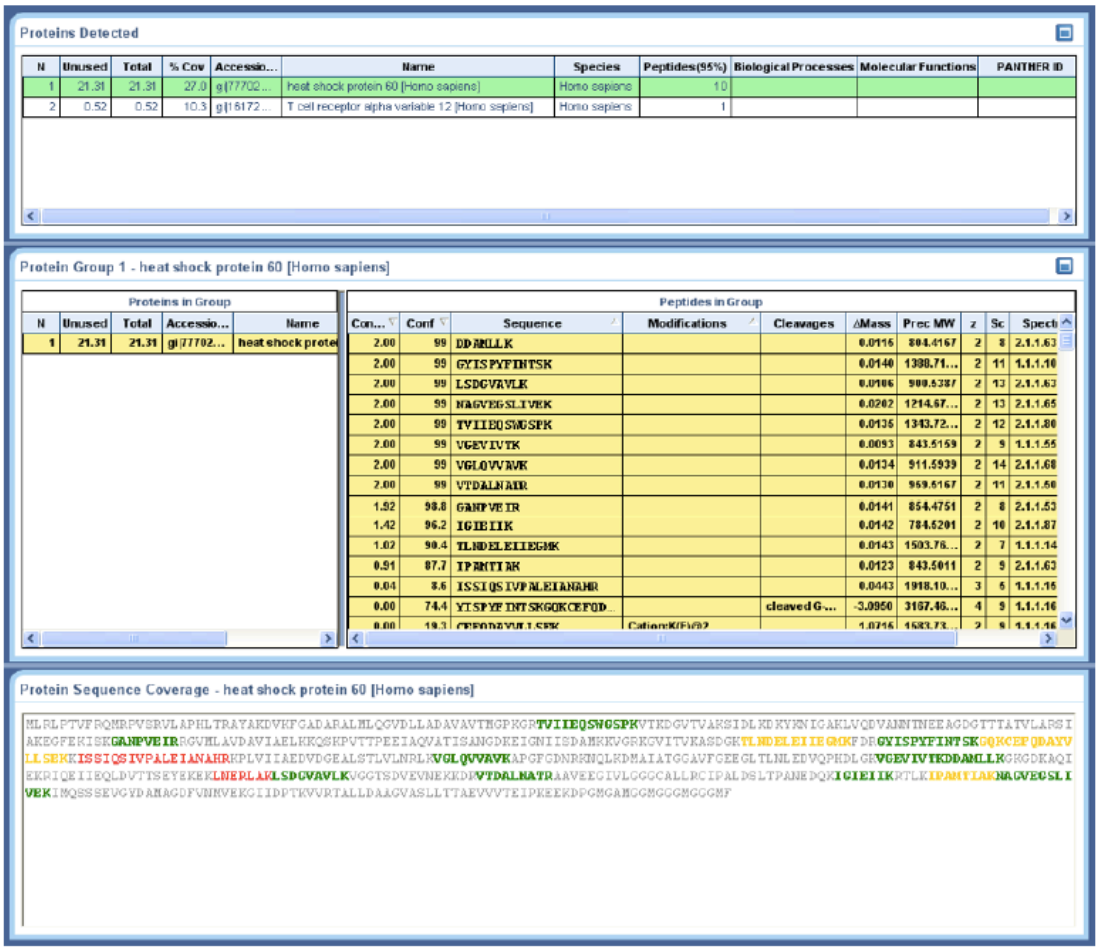

Protein spot e mass analysis result

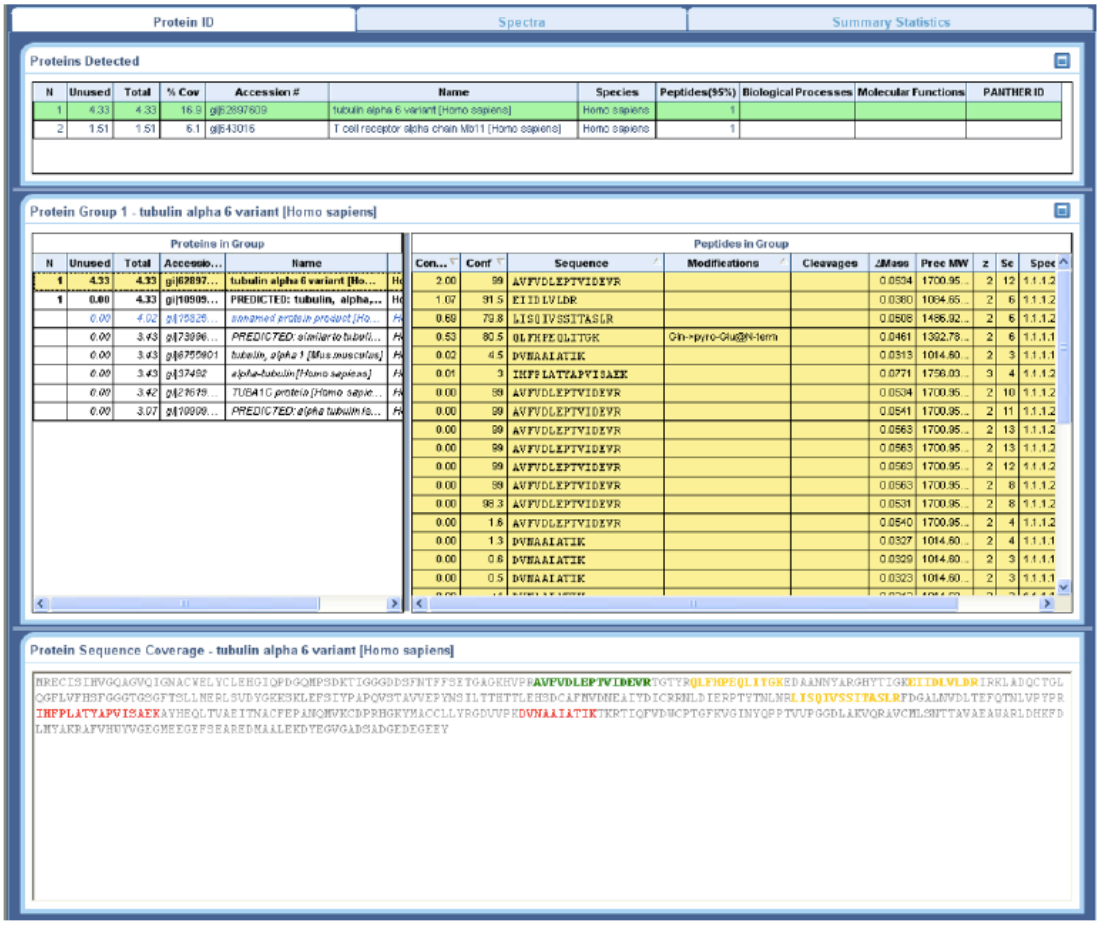

Protein spot f mass analysis result

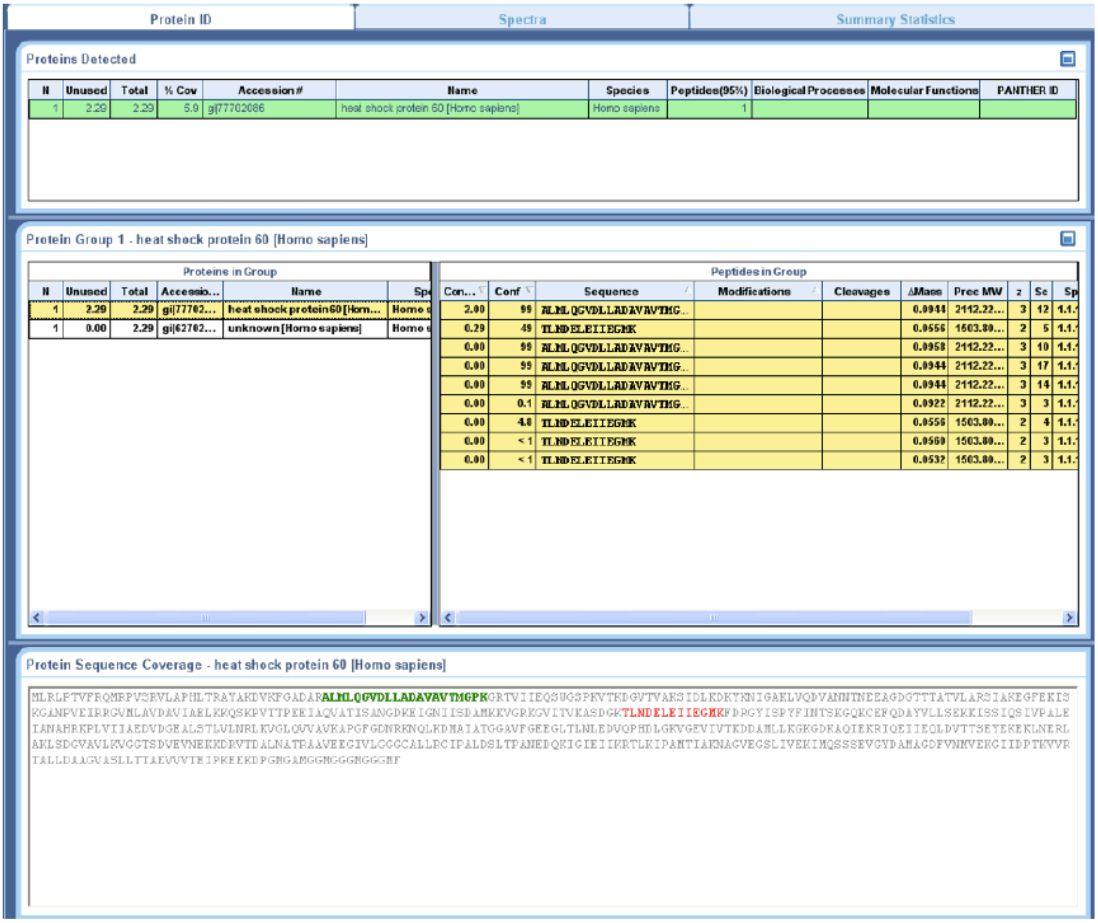

MDH refolding assay : The chaperone activity of HSP60 was determined using malate dehydrogenase (MDH) from porcine heart [Sigma, USA]. Denaturation of MDH (17.1 μM) was performed for 2 h at room temperature in 10 mM HCl. A mixture of HSP60 (4 μM) and HSP10 (8 μM) [Assay Designs, USA] was incubated for 90 min at 30 °C with or without **1** or epolactaene *tert*-butyl ester (ETB)[Wako, Japan] in reconstitution buffer (50 mM Tris, pH 7.6, 300 mM NaCl, 20 mM KCl, 20 mM $Mg(CH_3COO)_2$ and 4 mM ATP). The MDH folding reaction was performed in folding assay buffer (100 mM Tris, pH 7.6, 7 mM KCl, 7 mM MgCl2, 10 mM DTT, and 2 mM ATP) and the final concentrations of MDH, HSP60, and HSP10 were 1.71 μM, 1 μM, and 2 μM, respectively. After incubation for 30 min at 42 °C, the aggregation level of MDH was measured by the absorbance at 340 nm using Synergy HT [Bio-Tek, USA] as the turbidity level of MDH solution.

Tubulin polymerization assay : In vitro tubulin polymerization assay was performed using tubulin polymerization assay kit [Cytoskelecton, USA] and followed by manufacturer's manual.

Cell cycle arrest analysis : Cells were treated with compounds as indicated in the manuscript in a time-dependent manner. Cells were harvested and prepared to cell suspension in buffer (PBS + 0.1% BSA). The cells were washed and resuspended with same buffer. 1 mL of resulting cells at 1 x 10^6 cell/mL were aliquoted in a 15-mL polypropylene tube and added 3 mL of cold ethanol. Cells were fixed overnight at 4 °C and washed with PBS. Propidium iodide (50 mg/mL) [Sigma, USA] staining solution was added to the resulting cells and mixed properly. RNase A [Qiagen, USA] was added and incubated 3 h at 4 °C. The samples were analyzed by FACSCalibur

[Becton Dickinson, USA].

Western blot : Proteins samples were separated by SDS-PAGE and transferred to PVDF membrane [BioRad, USA]. Caspase-3 antibody [#9662, Cell signaling, USA], β-actin antibody [#4970, Cell signaling, USA] and PARP antibody [#9542, Cell signaling, USA] were used as primary antibodies. Anti-rabit IgG HRP-linked antibody [#7074, Cell signaling, USA] was used as a secondary antibody.

Immunocytochemisty : Cells were treated with compounds for 12 h. Cells were fixed with 3.7% formaldehyde in PBS for 15 min. The cells were washed with PBS twice times. To the fixed cells, a solution of 0.5 % Triton X-100 in PBS was added. The cells were incubated at 4 °C for 15 min and washed with ice-cold PBS three times. The cells were incubated with 1% BSA in TBST for 60 min. α-Tubulin antibody [#3873, Cell signaling, USA] in TBST with 1% BSA was added to cells under different experimental conditions overnight at 4 °C. The cells were washed with TBST three times. Anti-mouse IgG FITC-linked antibody [ab6717, Abcam, UK] in TBST with 1% BSA was added to the cells at room temperature for 1 h. The cells were washed with TBST three times and observed with fluorescent microscope [IX71, Olympus, Japan].

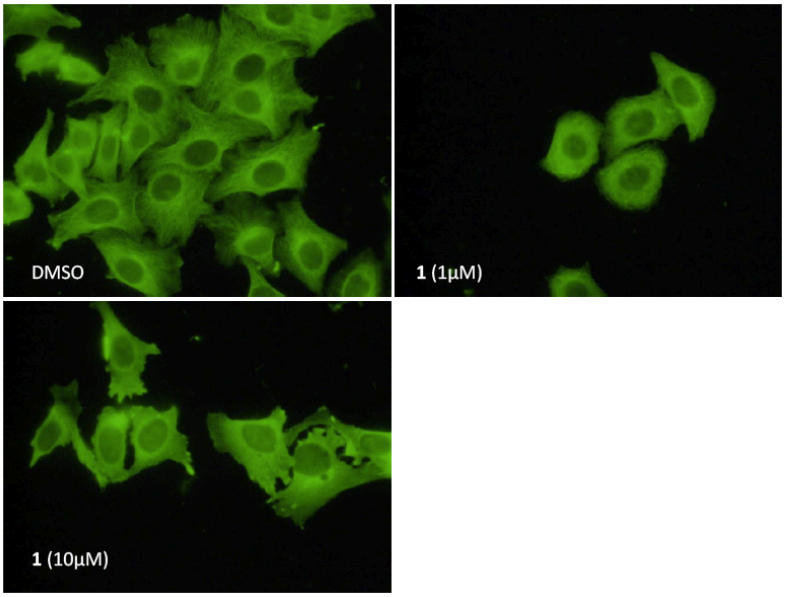

Figure S1. Dose-dependent inhibition of 1 toward cellular tubulin polymerization visualized by a-tubulin antibody. As shown in DMSO condition, a-tubulin antibody can visualize the microtubule as fibers. Upon treatment of compound 1, the formation of fiber-like tubulin microtubule was dose-dependently inhibited. However, the a-tubulin antibody can still visualize monomers or oligomers of a-tubulin, which allows the greenish colors in all experimental conditions.

Cellular microtubule imaging : Cells were treated with compounds for 12 h. Cells were fixed with 3.7 % formaldehyde in PBS for 15 min. The cells were washed with PBS twice times. To the fixed cells, a solution of 0.5 % Triton X-100 in PBS was added. The cells were incubated at 4 °C for 15 min and washed with ice-cold PBS three times. The cells were incubated with 1% BSA in TBST for 60 min. 1 mM taxol-oregon green 488 [Invitrogen, USA] in PBS was added to the cells at room temperature for 1 h. The cells were washed with PBS three times and observed with fluorescent microscope [IX71, Olympus, Japan].

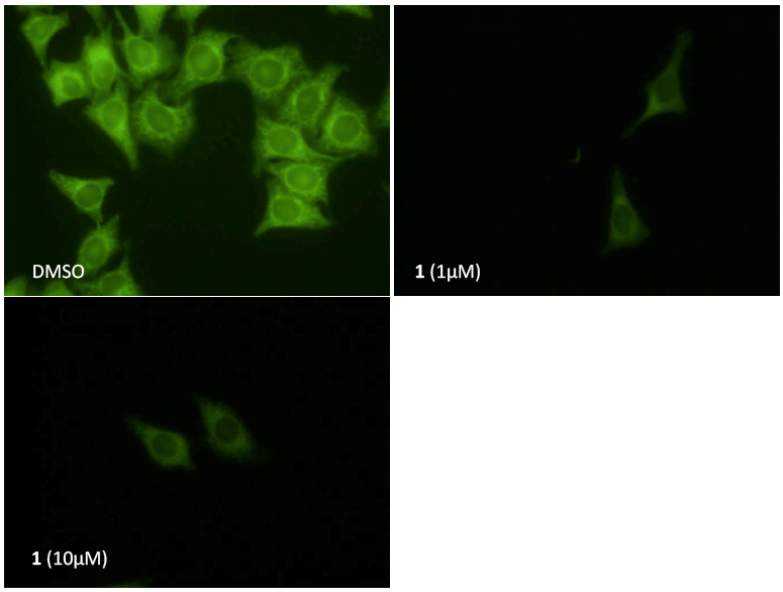

Figure S2. Dose-dependent inhibition of 1 toward tubulin microtubule formation in live cells visualized by selective staining of microtubule with taxol-oregon green 488 (1 mM). Unlike a-tubulin antibody, taxol-oregon green 488 can selectively visualize tubulin microtubule, not monomers or oligomers of tubulin. Therefore, the direct inhibition of microtubule formation upon treatment of compound 1 can be visualized with taxol-oregon green 488.

Target Identification with 1DGE Fluorescent Imaging

Cell lysate labeling : HeLa cell (150ϕ dish x 3) was scrapped with cold Ca^{2+}- and Mg^{2+}-free phosphate buffered saline (PBS) [WelGENEc, S. Korea] and centrifuged. The supernatant was discarded and cell pellet was kept at —80 °C until use. RIPA buffer containing 50 mM Tris(pH 7.5), 150 mM NaCl, 1% NP-40, 0.5% deoxycholate, protease inhibitor [Roche, Switzerland] was added to the cells for lysis. The cells were incubated for 15 min on ice. The cell lysate was centrifuged at 4 °C, 13000 rpm for 15 min. The protein concentration of supernatant was measured with BCA assay kit [Thermo, USA] and the protein concentration was adjusted to 1 mg/mL. The protein and compounds was mixed. The mixture was incubated at room temperature for 30 min. 365 nm UV light from BLAK-Ray (B-100AP) UV lamp [UVP, USA] was irradiated to the mixture for 30 min on ice. The mixture was under click chemistry with Cy5-azide [Lumiprobe, USA] (40 mM), tris[(1-benzyl-1H-1,2,3-triazol-4-yl)methyl]- amine (TBTA) [Sigma, USA] (100 mM), $CuSO_4$ [Sigma, USA] (1 mM), tris(2-carboxyethyl)-phosphine (TCEP) [TCI, Japan] (1 mM) and *t*BuOH [Sigma, USA] (5%) for 1 h. 5 x Laemmli buffer was added and incubated at 95 °C for 5 min. The protein samples were separated by 1DGE and scanned with Typhoon Trio [Amersham Bioscience, USA].

Live cell labeling : HeLa cells were seeded on 6-well plate. Compounds were treated for 3 h. 356-nm UV light was irradiated to the mixture for 30 min on ice. The cells were washed with PBS and kept at —80 °C until use. RIPA buffer was added to the cells for lysis. The cells were incubated for 15 min on ice. The cell lysate was scrapped and centrifuged at 4 °C, 13000 rpm for 15 min. Supernatant was taken and

the protein concentration was measured with BCA assay and protein concentration was adjusted to 1 mg/mL. The mixture was under click chemistry with Cy5-azide (40 mM), TBTA (100 mM), $CuSO_4$ (1 mM), TCEP (1 mM) and *t*BuOH (5%) for 1 h. 5 x Laemmli sample buffer was added and incubated at 95 °C for 5 min. The protein samples were separated by 1DGE and scanned with Typhoon Trio.

Fluorescence detection and quantification : The *in-gel* fluorescence signal was visualized at the Cy3 (532 nm excitation) or Cy5 (633 nm excitation) channel by Typhoon Trio and analyzed by ImageQuant TL program [Amersham Bioscience, USA].

Target Identification with Affinity Pull-down Method

Cell lysate labeling : HeLa cell (150ϕ dish x 3) was scrapped in cold PBS and centrifuged. The supernatant was discarded and cell pellet was kept at —80 °C until use. RIPA buffer was added to the cells for lysis. The cells were incubated for 15 min on ice. The cell lysate was centrifuged at 4 °C, 13000 rpm for 15 min. The protein concentration of supernatant was measured with BCA assay and the protein concentration was adjusted to 1 mg/mL. The protein and compounds was mixed. The mixture was incubated at room temperature for 30 min. 356-nm UV light was irradiated to the mixture for 30 min on ice. The mixture was under click chemistry with Biotin-azide [Invitrogen, USA] (100 mM), TBTA (100 mM), $CuSO_4$ (1 mM), TCEP (1 mM) and *t*BuOH (5%) for 1 h. Acetone was added to the mixture for precipitation and the mixture was kept at —20°C for 20 min. The mixture was centrifuged at 4°C, 14000 rpm for 10 min. Supernatant was discarded and the pellet was washed with cold acetone two times. PBS with 1.2% SDS was added to the pellet. The sample was sonicated and incubated at 80°C for 5 min. The protein solution was diluted with PBS to 0.2% SDS solution. 50 ml avidin-agarose bead [Sigma, USA] was added and rotated at room temperature for 3 h. The beads were washed with PBS (0.2% SDS) x 3, PBS x 3 and ddH_2O x 3. Then, 2 x Laemmli sample buffer (50 ml) was added. The beads were incubated at 95 °C for 5 min. The protein samples were separated by SDS-PAGE and visualized with silver staining.

Live cell labeling : HeLa cells were seeded on 6-well plate. Compounds were treated for 3 h. 356-nm UV light was irradiated to the mixture for 30 min on ice. The cells were washed with PBS and kept at —80 °C until use. RIPA buffer was added to the

cells for lysis. The cells were incubated for 15 min on ice. The cell lysate was scrapped and centrifuged at 4 °C, 13000 rpm for 15 min. The protein concentration of supernatant was measured with BCA assay and the protein concentration was adjusted to 1 mg/mL. The mixture was under click chemistry with biotin-azide (100 mM), TBTA (100 mM), $CuSO_4$ (1 mM), TCEP (1 mM) and *t*BuOH (5%) for 1 h. Acetone was added to the mixture for precipitation and the mixture was kept at —20 °C for 20 min. The mixture was centrifuged at 4 °C, 14000 rpm for 10 min. Supernatant was discarded and the pellet was washed twice with cold acetone. PBS with 1.2% SDS was added to the pellet. The sample was sonicated and incubated at 80 °C for 5 min. The protein solution was diluted with PBS to 0.2% SDS solution. 50 ml avidin-agarose bead was added and rotated at room temperature for 3 h. The beads were washed with PBS (0.2% SDS) x 3, PBS x 3 and ddH_2O x 3. Then, 2 x Laemmli sample buffer (50 ml) was added. The beads were incubated at 95 °C for 5 min. The protein samples were separated by SDS-PAGE and visualized with silver staining.

Target Identification with FITGE Strategy

Cell lysate labeling : HeLa cell (150ϕ dish x 3) was scrapped in cold PBS and centrifuged. The supernatant was discarded and cell pellet was kept at —80 °C until use. RIPA buffer was added to the cells for lysis and incubated for 15 min on ice. The cell lysate was centrifuged at 4 °C, 13000 rpm for 15 min. The protein concentration of supernatant was measured with BCA assay and the protein concentration was adjusted to 1 mg/mL. The protein and probes were mixed. The mixture was incubated at room temperature for 30 min. Then, 356-nm UV light was irradiated to the mixture for 30 min on ice. The mixture was under click chemistry with Cy5-azide or Cy3-azide [Lumiprobe, USA] (40 mM), TBTA (100 mM), $CuSO_4$ (1 mM), TCEP (1 mM) and *t*BuOH (5%) for 1 h. Acetone was added to the resulting mixture for precipitation. The mixture was kept at —20 °C for 20 min and centrifuged at 4 °C, 14000 rpm for 10 min. Supernatant was discarded and the pellet was washed twice with cold acetone. The pellet was resolved with rehydration buffer [7 M urea, 2 M thiourea, 2% CHAPS (3-[(3-cholamidopropyl)dimethylammonio]-1-propanesulfonate, w/v), 40 mM DTT, IPG buffer (5 ml/mL) in ddH_2O]. The proteomes labeled with probe **3** (labeled with Cy5-azide) and negative probe **4** (labeled with Cy3-azide) were mixed in equal quantity. The resulting proteomes were separated by 2DGE and scanned with Typhoon Trio.

Live cell labeling : HeLa cells were seeded on 6-well plate. Compounds were treated for 3 h. 356-nm UV light was irradiated to the mixture for 30 min on ice. The cells were washed with PBS and kept at —80 °C until use. RIPA buffer was added to the cells for lysis and incubated for 15 min on ice. The cell lysate was scrapped and

centrifuged at 4 °C, 13000 rpm for 15 min. The protein concentration of supernatant was measured with BCA assay and the protein concentration was adjusted to 1 mg/mL. The mixture was under click chemistry with Cy5-azide or Cy3-azide (40 mM), TBTA (100 mM), $CuSO_4$ (1 mM), TCEP (1 mM) and *t*BuOH (5%) for 1 h. Acetone was added to the mixture for precipitation and the mixture was kept at —20 °C for 20 min. The mixture was centrifuged at 4 °C, 14000 rpm for 10 min. Supernatant was discarded and the pellet was washed twice with cold acetone. The pellet was resolved with rehydration buffer. The proteomes labeled with active probe **3** (labeled with Cy5-azide) and negative probe **4** (labeled with Cy3-azide) were mixed in equal quantity. The resulting proteomes were separated by 2DGE and scanned with Typhoon Trio.

2 dimensional gel electrophoresis (2DGE) : Isoelectric focusing (IEF) was performed with 24-cm pH 3-10 Immobiline^{TM} Drystrip gel [GE healthcare, USA] using Ettan IPGphor3 IEF system [GE healthcare, USA]. The Drystrip was loaded to 12% SDS-PAGE gel and proteins were separated by Ettan Daltsix [GE healthcare, USA].

General Information for Chemical Synthesis : ^{1}H and ^{13}C NMR spectra were recorded on a Varian Inova-500 [Varian Assoc., Palo Alto, USA], and chemical shifts were measured in ppm relative to internal tetramethylsilane (TMS) standard or specific solvent signal. Multiplicity was indicated as follows: s (singlet); d (doublet); t (triplet); q (quartet); m (multiplet); dd (doublet of doublet); dt (doublet of triplet); td (triplet of doublet); bs (broad singlet), etc. Coupling constants were reported in Hz. The HRMS analyses were conducted at the Mass Spectrometry Laboratory of Seoul National University by direct injection on JEOL JMS AX505WA spectrometer using fast atom bombardment (FAB) method and electron spray ionization (ESI) method. All reagents in this synthetic procedure were purchase from Sigma-Aldrich [MO, USA] and TCI [Japan].

All reagents in this synthetic procedure were purchase from Sigma-Aldrich [MO, USA] and TCI [Japan]. The progress of reaction was monitored using thin-layer chromatography (TLC) (silica gel 60 F_{254} 0.25 mm), and components were visualized by observation under UV light (254 and 365 nm) or by treating the TLC plates with anisaldehyde staining solution followed by heating. Silica gel 60 (40–63 mm) used in flash column chromatography was purchased from Merck [Germany]. All reactions were conducted in oven-dried glassware under dry argon atmosphere, unless otherwise specified. CH_2Cl_2 was distilled from CaH_2 immediately prior to use. Other solvents and organic reagents were purchased from commercial venders and used without further purification unless otherwise mentioned.

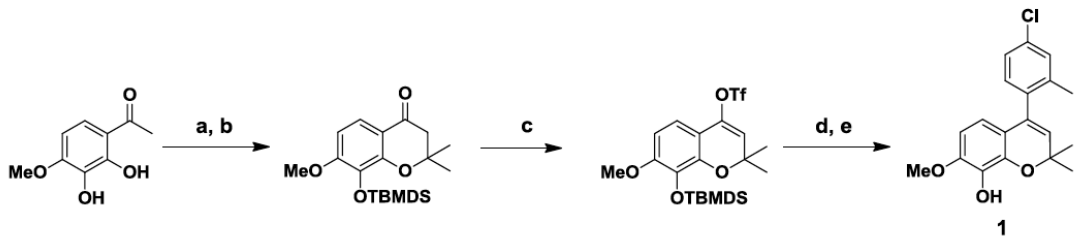

Scheme S1. Synthetic scheme of the novel benzopyran-embedded compound **1**[a]

[a] Reagents and conditions: (a) acetone, pyrrolidine (2.0 equiv.), EtOH, reflux, overnight stirring, 75%; (b) TBDMSCl (1.2 equiv.), imidazole (1.5 equiv.), room temperature, 3 h, 98%; (c) trifluoromethanesulfonic anhydride (1.2 equiv.), 2,6-di-*tert*-butyl-4-methylpyridine (1.4 equiv.), CH_2Cl_2, 0 °C, 30 min, 79%; (d) 4-chloro-2-methylphenylboronic acid (1.1 equiv.), $Pd(PPh_3)_4$ (5 mol%), Na_2CO_3 (2.0 equiv.), toluene / EtOH / H_2O, 70 °C, 3 h, 83%; (e) TBAF (1.1 equiv.), THF, room temperature, 30 min, 93%.

4-(4-chloro-2-methylphenyl)-7-methoxy-2,2-dimethyl-2*H*-chromen-8-ol (1).

Synthetic procedure was followed by previous study.[18] Slightly yellow solid (77% from vinyl triflate intermediate)

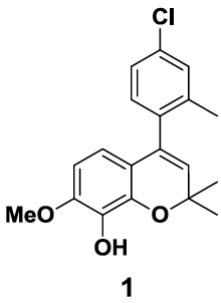

1

^{1}H-NMR (500 MHz, $CDCl_3$): d 7.22 (d, J = 2.0 Hz, 1H), 7.18 (dd, J = 8.0 and 2.0 Hz, 1H), 7.07 (d, J = 8.0 Hz, 1H), 6.32 (d, J = 8.5 Hz, 1H), 6.08 (d, J = 8.5 Hz, 1H), 5.44 (s, 1H), 5.38 (s, 1H), 3.85 (s, 3H), 2.13 (s, 3H), 1.56 (s, 3H), 1.52 (s, 3H); ^{13}C-NMR (125 MHz, $CDCl_3$): 148.1, 140.2, 138.9, 136.6, 134.4, 133.5, 131.2, 130.1, 130.0, 127.8, 127.7, 126.1, 116.6, 116.0, 115.9, 103.6, 77.2, 56.4, 56.3, 28.3, 27.8, 19.8; HRMS (FAB+) *m/z* calculated for $C_{19}H_{20}ClO_3$ [M+H]+ 331.1101, found *m/z* 331.1099

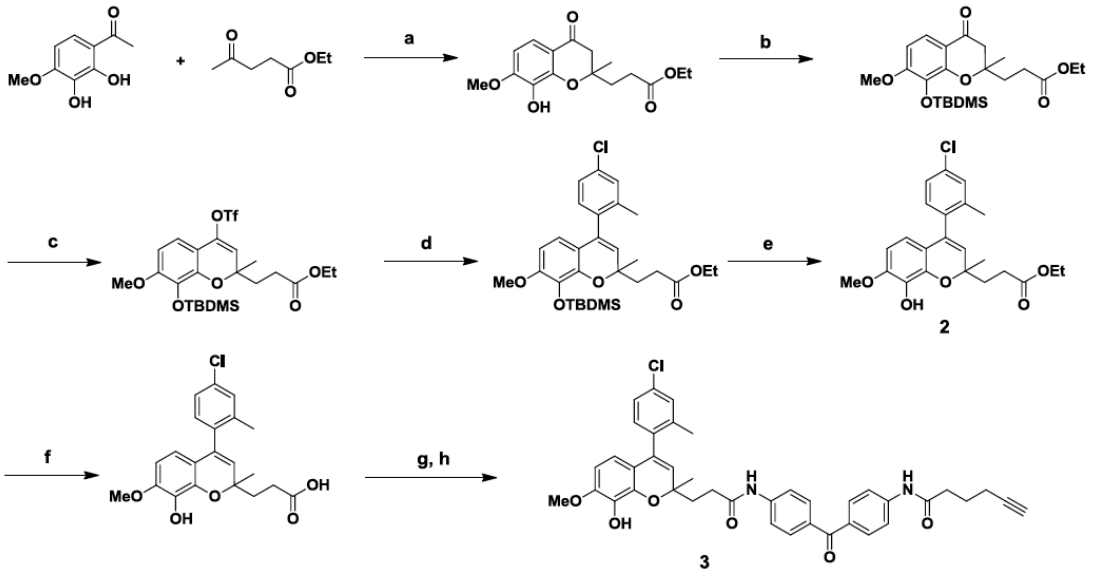

Scheme S2. Synthetic scheme for the compounds of target identification[a]

[a] Reagents and conditions: (a) pyrrolidine (2.0 equiv.), EtOH, reflux, 3 days, 61%; (b) TBDMSCl (1.2 equiv.), imidazole (1.5 equiv.), room temperature, 5 h, 94%; (c) trifluoromethanesulfonic anhydride (1 equiv.), 2,6-di-*tert*-butyl-4-methylpyridine (1.4 equiv.), CH_2Cl_2, 0 °C, 30 min, 79%; (d) 4-chloro-2-methylphenylboronic acid (1.1 equiv.), $Pd(PPh_3)_4$ (5 mol%), Na_2CO_3 (3.0 equiv.), toluene / EtOH / H_2O, 70 °C, 85%; (e) TBAF (1.1 equiv.), THF, 0 °C, 30 min, 91%; (f) NaOH (3.0 equiv.), EtOH / H_2O, 0 °C, 1 h, 96%; (g) oxalyl chloride (2.0 equiv.), CH_2Cl_2, 0 °C, 1 h; (h) *N*-(4-(4-aminobenzoyl)phenyl)hex-5-ynamide (in Scheme 3), DIPEA (1.5 equiv.)′, THF, 0 °C, 1 h, 43% of two step yield.

Ethyl 3-(8-hydroxy-7-methoxy-2-methyl-4-oxochroman-2-yl)propanoate

[Reagents and conditions: (a)]**.**

A solution of 2′,3′-dihydroxy-4′-methoxyacetophenone hydrate (1.0 equiv.) in EtOH was treated with pyrrolidine (3.0 equiv.) and ethyl levulinate (3.0 equiv.) and then heated at reflux for about 3 days. After the completion of reaction monitored by TLC, the reaction mixture was concentrated *in vacuo*. Evaporated residue was redissolved in ethyl acetate and washed several times with 1N HCl solution. After washing with brine, the combined organic layer was dried over anhydrous MgSO4, filtrated, and evaporated *in vacuo*. Purification by silica-gel flash column chromatography (EA /

hexane) gave the desired compound, ethyl 3-(8-hydroxy-7-methoxy-2-methyl-4-oxochroman-2-yl)propanoate (colorless crystral, 61%).

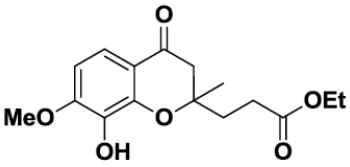

^{1}H-NMR (500 MHz, $CDCl_3$): d 7.46 (d, J = 8.8 Hz, 1H), 6.62 (d, J = 9.1 Hz, 1H), 5.59 (s, 1H), 4.14 (q, J = 7.2 Hz, 2H), 3.95 (s, 3H), 2.79 (d, J = 16.5 Hz, 1H), 2.64 (d, J = 16.5, 1H), 2.51 (m, 2H), 2.25 (m, 1H), 2.06 (m, 1H), 1.45 (s, 3H), 1.24 (t, J = 7.1 Hz, 3H) ; ^{13}C-NMR (125 MHz, $CDCl_3$): d 190.9, 173.6, 152.7, 147.2, 134.2, 118.4, 115.4, 105.0, 81.723, 61.0, 56.5, 47.8, 34.9, 29.3, 23.8, 14.4.

Ethyl 3-(8-(*tert*-butyldimethylsilyloxy)-7-methoxy-2-methyl-4-oxochroman-2-yl)propanoate

[Reagents and conditions: (b)]**.**

To a solution of this purified ethyl 3-(8-hydroxy-7-methoxy-2-methyl-4-oxochroman-2-yl)propanoate (1.0 equiv.) and imidazole (1.5 equiv.) dissolved in CH_2Cl_2, *tert*-butyldimethylsilyl chloride (TBDMSCl, 1.2 equiv.) was added and then stirred for about 5 h at room temperature. After the reaction completion monitored by TLC, the reaction mixture was diluted with ethylacetate and then washed with brine. The separated organic layer was dried over anhydrous $MgSO_4$, filtrated and evaporated *in vacuo*. The resulting mixture was purified with silica-gel flash column chromatography (EA / hexane) to provide desired product, ethyl 3-(8-(*tert*-butyldimethylsilyloxy)-7-methoxy-2-methyl-4-oxochroman-2-yl)propanoate (colorless crystal, 94%).

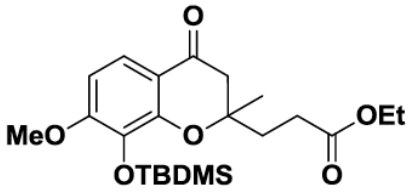

^{1}H-NMR (500 MHz, $CDCl_3$): d7.46 (d, J = 8.8 Hz, 1H), 6.52 (d, J = 8.8 Hz, 1H), 4.07 (q, J = 7.1Hz, 2H), 3.80(s, 1H), 2.67 (d, J = 16.5 Hz, 1H), 2.55

(d, J = 16.5 Hz, 1H), 2.44 (m, 2H), 2.11 (m, 1H), 1.97 (m, 1H), 1.36 (s, 3H), 1.19 (t, J = 7.2 Hz, 3H), 0.98 (s, 9H), 0.11 (d, J = 2.9, 6H); ^{13}C-NMR (125 MHz, $CDCl_3$): d 191.3, 172.9, 157.1, 151.7, 133.3, 119.7, 115.5, 104.7, 80.6, 60.6, 55.6, 47.1, 34.2, 28.9, 25.9, 24.0, 18.7, 14.3, —4.3.

Ethyl 3-(8-(*tert*-butyldimethylsilyloxy)-7-methoxy-2-methyl-4-(trifluoromethyl sulfonyl oxy)-2*H*-chromen-2-yl)propanoate

[Reagents and conditions: (c)]**.**

A solution of ethyl 3-(8-(*tert*-butyldimethylsilyloxy)-7-methoxy-2-methyl-4-oxochroman-2-yl)propanoate (1.0 equiv.) and 2,6-di-*tert*-butyl-4-methylpyridine (DTBMP, 1.3 equiv.) in anhydrous CH_2Cl_2 at 0 °C was treated with triflic anhydride (Tf_2O, 1.2 equiv.) under N_2 atmosphere. The reaction was stirred for 30 min at the same temperature. The reaction mixture was filtered to remove any solid and the filtrate was concentrated *in vacuo*. The residue was redissolved in ethyl acetate and washed with sat. $NaHCO_3$ solution and brine. The combined organic layer was dried over anhydrous $MgSO_4$, filtrated, and evaporated *in vacuo*. Purification by silica-gel flash column chromatography (EA / hexane) gave the desired compound ethyl 3-(8-(*tert*-butyldimethylsilyloxy)-7-methoxy-2-methyl-4-(trifluoromethylsulfonyloxy)-2*H*-chromen-2-yl)propanoate (colorless liquid, 79%).

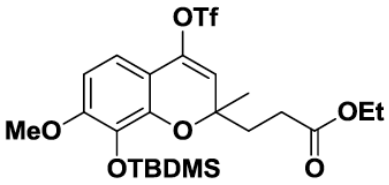

^{1}H-NMR (500 MHz, $CDCl_3$): d 6.82 (d, J = 8.5 Hz, 1H), 6.46 (d, J = 8.5 Hz, 1H), 5.43 (s, 1H), 4.11 (q, J = 7 Hz, 2H), 3.8 (s, 3H), 2.49 (m, 2H), 2.10 (m, 2H), 1.47 (s, 3H), 1.23 (t, J =7 Hz, 3H), 1.01 (s, 9H), 0.15 (s, 6H); ^{13}C-NMR (125 MHz, $CDCl_3$) : 173.3, 154.2, 145.7, 143.5, 133.7, 120.0, 117.5, 114.2, 110.3, 104.1, 80.2, 60.8, 55.6, 36.3, 29.4, 26.8, 25.9, 18.9, 14.3, —4.2.

Ethyl 3-(4-(4-chloro-2-methylphenyl)-8-hydroxy-7-methoxy-2-methyl-2*H*-chromen-2-yl) propanoate

[Reagents and conditions: (d)]**.**

Ethyl 3-(8-(*tert*-butyldimethylsilyloxy)-7-methoxy-2-methyl-4-(trifluoromethyl sulfonyloxy)-2*H*-chromen-2-yl)propanoate (1.0 equiv.), 4-chloro-2-methylphenyl boronic acid (1.1 equiv.), $Pd(PPh_3)_4$ (5 mol%) and Na_2CO_3 (3.0 equiv.) were suspended in solvent mixture of EtOH:toluene:H_2O (1:1:0.5) and the reaction mixture was stirred at 70 °C for about 3 h. After reaction completion monitored by TLC, the resulting mixture was diluted with ethyl acetate and then washed with brine. The organic layer was dried over anhydrous $MgSO_4$, filtrated, and evaporated *in vacuo*. Purification by silica-gel flash column chromatography (EA / hexane) gave the desired compound (slightly yellow solid, 85%).

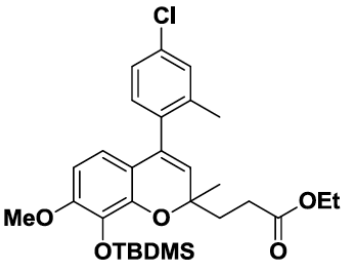

^{1}H-NMR (500 MHz, $CDCl_3$): d 7.21–7.16 (m, 2H), 7.07 (dd, *J* = 12 and 8.1 Hz, 1H), 6.26 (dd, *J* = 8.5 and 3.1 Hz, 1H), 6.09 (dd, *J*= 8.5 and 3.1 Hz, 1H), 5.26 (d, 1H), 4.10 (m, 2H), 3.7 (s, 3H), 2.55 (m, 2H), 2.12 (m, 5H), 1.46 (d, 3H), 1.22 (q, *J*= 7 Hz, 3H), 1.05 (s, 9H), 0.18 (m, 6H); ^{13}C-NMR (125 MHz, $CDCl_3$): d 173.8, 152.6, 144.9, 138.8, 136.9, 135.0, 133.4, 131.2, 130.0, 126.0, 125.3, 117.6, 116.3, 103.5, 78.2, 60.6, 55.6, 36.3, 29.8, 26.9, 26.6, 26.1, 19.8, 19.0, 14.4, —4.14.

Ethyl 3-(4-(4-chloro-2-methylphenyl)-8-hydroxy-7-methoxy-2-methyl-2*H*-chromen-2-yl) propanoate [**2,** Reagents and conditions: (e)]**.**

To a solution of purified Ethyl 3-(4-(4-chloro-2-methylphenyl)-8-hydroxy-7-methoxy-2-methyl-2*H*-chromen-2-yl) propanoate (1.0 equiv.) dissolved in

tetrahydrofuran (THF), tetrabutylammonium fluoride (1 M solution in THF, 1.5 equiv.) was added at 0 °C and then stirred for about 30 min at the same temperature. After the reaction completion monitored by TLC, the reaction mixture was diluted with ethylacetate and then washed with brine. The separated organic layer was dried over anhydrous $MgSO_4$, filtrated and evaporated *in vacuo*. Purification by silica-gel flash column chromatography (EA / hexane) gave the desired compound **2** (slightly yellow solid, 91%).

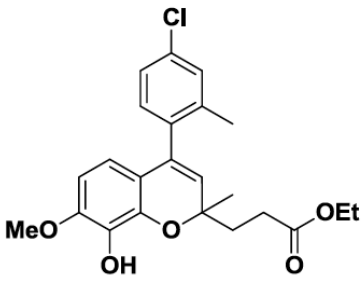

2

^{1}H-NMR (500 MHz, $CDCl_3$): d 7.23–7.22 (m, 1H), 7.20–7.18 (m, 1H), 7.07 (dd, *J* = 10.5 and 8.0 Hz, 1H), 6.32 (d, *J* = 8.5 Hz, 1H), 6.07 (d, *J* = 8.5 Hz, 1H), 5.46 (s, 1H), 5.30 (d, 1H), 4.14–4.09 (m, 2H), 3.85 (s, 3H), 2.64–2.47 (m, 2H), 2.26–2.08 (m, 2H), 2.14 (d, 3H), 1.51 (d, 3H), 1.24–1.19 (m, 3H); ^{13}C-NMR (125 MHz, $CDCl_3$): d 173.8, 148.3, 140.1, 139.9, 138.8, 138.7, 136.5, 136.4, 135.0, 134.7, 134.3, 134.2, 133.6, 133.5, 131.2, 131.1, 130.1, 126.1, 125.7, 116.2, 116.1, 103.8, 103.7, 79.1, 78.9, 60.8, 56.3, 36.5, 36.2, 31.1, 30.0, 29.8, 26.7, 26.4, 20.0, 19.7, 14.4; HRMS (FAB$^+$) *m/z* calculated for $[M+H]^+$ $C_{23}H_{26}ClO_5$ 417.1469, found *m/z* 417.1471.

3-(4-(4-Chloro-2-methylphenyl)-8-hydroxy-7-methoxy-2-methyl-2*H*-chromen-2-yl)propanoic acid [Reagents and conditions: (f)]**.**

To a solution of compound **2** (1.0 equiv.) in EtOH and water was added NaOH (3.0 equiv.) at 0 °C. The reaction was stirred for 1 h at the same temperature. After the reaction completion monitored by TLC, the reaction mixture was acidified by 1N HCl solution until pH 3.0 and then extracted by ethyl acetate twice. The combined organic layer was dried over anhydrous $MgSO_4$, filtrated, and evaporated *in vacuo*.

Purification by silica-gel flash column chromatography (MeOH / MC) gave the desired compound 3-(4-(4-chloro-2-methylphenyl)-8-hydroxy-7-methoxy-2-methyl-2*H*-chromen-2-yl)propanoic acid (slightly yellow solid, 96%).

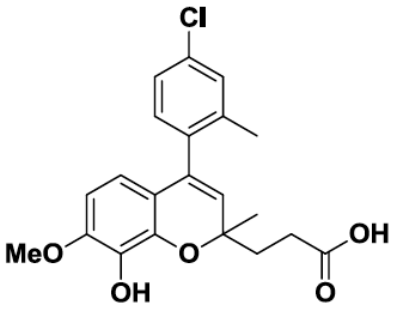

^{1}H-NMR (500 MHz, $CDCl_3$): d 7.22 (s, 1H), 7.19 (m, 1H), 7.06 (m, 1H), 6.32 (d, *J* = 8.5 Hz, 1H), 6.07 (d, *J* =8.5 Hz, 1H), 5.30 (d, 1H), 3.84 (s, 3H), 2.66–2.56 (m, 2H), 2.23–2.08 (m, 5H), 1.52 (d, 3H); ^{13}C-NMR (125 MHz, $CDCl_3$): d 179.7, 148.3, 140.0, 138.7, 136.4, 135.0 134.2, 133.6, 131.1, 130.0, 126.1, 125.5, 116.2, 103.8, 78.9, 56.3, 36.0, 29.7, 26.6, 19.9.

_N_-(4-(4-(3-(4-(4-Chloro-2-methylphenyl)-8-hydroxy-7-methoxy-2-methyl-2*H*-chromen-2-yl)propanamido)benzoyl)phenyl)hex-5-ynamide

[**3,** Reagents and conditions: (g) and (h)]**.**

To a solution of 3-(4-(4-chloro-2-methylphenyl)-8-hydroxy-7-methoxy-2-methyl-2*H*-chromen-2-yl)propanoic acid (1.0 equiv.) in anhydrous CH_2Cl_2 was added oxalyl chloride (2.0 equiv.) at 0 °C. The reaction was stirred for 1 h at the same temperature and then evaporated *in vacuo*. This evaporated residue was dissolved in anhydrous THF again. To this solution was added a solution of *N*-(4-(4-aminobenzoyl)phenyl)hex-5-ynamide (see **Scheme 3**, 1.0 equiv.) and DIPEA (1.5 equiv.) in anhydrous THF at 0 °C and then stirred for 1 h at the same temperature. After the reaction completion monitored by TLC, the reaction mixture was diluted by ethyl acetate and then and then washed with brine. The separated organic layer was dried over anhydrous $MgSO_4$, filtrated and evaporated *in vacuo*. Purification by silica-gel flash column chromatography (EA / hexane) gave the desired compound **3**

(slightly yellow solid, 43% overall two steps).

^{1}H-NMR (500 MHz, $CDCl_3$): d 8.08 (d, 1H), 7.80 (s, 1H), 7.20 (t, *J* = 9.0 Hz, 4H), 7.63 (d, *J* = 9.0 Hz, 4H), 7.21–6.96 (m, 3H), 6.33 (dd, *J* = 8.0 and 6.0 Hz, 1H), 6.09 (t, *J* = 8.0 Hz, 1H), 5.74 (bs, 1H), 5.35 (d, 1H), 3.85 (d, 3H), 2.72–2.60 (m, 2H), 2.56 (t, *J* = 7.0 Hz, 2H), 2.32 (td, *J* = 7.0 and 2.5 Hz, 2H), 2.26–2.21 (m, 2H), 2.11 (d, 3H), 2.01 (t, *J* = 2.5 Hz, 1H), 1.99–1.93 (m, 2H), 1.52 (d, 3H); ^{13}C-NMR (125 MHz, $CDCl_3$): d 194.8, 171.8, 148.3, 142.2, 141.9, 138.7, 133.5, 133.2, 133.0, 131.6, 131.2, 131.0, 130.1, 126.2, 126.1, 119.1, 116.5, 116.4, 113.9, 103.8, 103.7, 83.6, 79.1, 69.8, 56.3, 36.6, 36.5, 36.2, 26.9, 26.3, 24.0, 19.7, 18.0; HRMS (ESI^+) *m/z* calculated for $[M+H]^+$ $C_{40}H_{38}ClO_6N_2$ 677.2423, found *m/z* 677.2413.

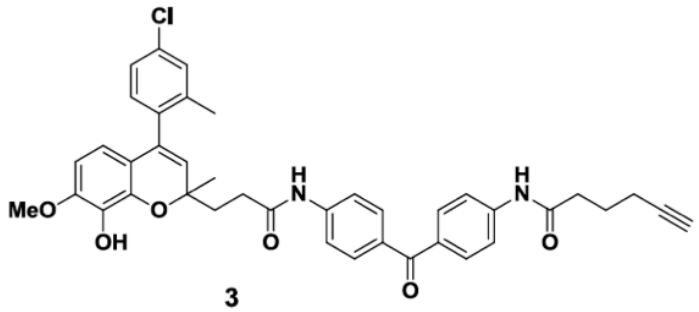

3

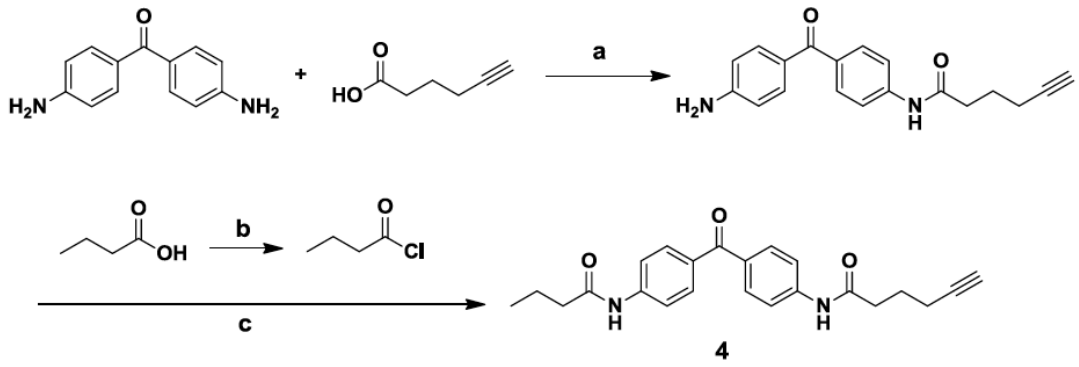

Scheme S3. Synthetic scheme for the compounds of target identification[a]

[a] Reagents and conditions: (a) 5-hexanoic acid (2.0 equiv.), EDC (2.0 equiv.), HOBt (2.3 equiv.), DMF, room temperature, 5 h, 74%; (b) excess amount of oxalyl chloride, room temperature, 1 h, distilled purification; (c) TEA (1.2 equiv.), CH_2Cl_2, 30 min, 67%.

***N*-(4-(4-Aminobenzoyl)phenyl)hex-5-ynamide** [Reagents and conditions: (a)]**.**

To a solution of 5-hexanoic acid (2.0 equiv.), EDC (2.0 equiv.) and HOBt (2.3 equiv.) dissolved in DMF, 4,4′-diaminobenzophenone (1.0 equiv.) was added and then stirred for about 5 h at room temperature. After the reaction completion monitored by TLC, the reaction mixture was diluted with ethylacetate and then washed with brine. The separated organic layer was dried over anhydrous $MgSO_4$, filtrated and evaporated *in vacuo*. The resulting mixture was purified with silica-gel flash column chromatography (EA / hexane) to provide desired product, *N*-(4-(4-aminobenzoyl)phenyl)hex-5-ynamide (white solid, 74%).

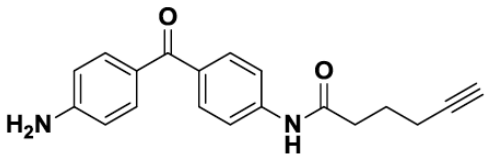

^{1}H-NMR (500 MHz, $(CD_3)_2CO$): δ 8.01 (s, 1H), 7.76 (m, 2H), 7.68 (dd, *J* = 8.5 and 2 Hz, 2H), 7.63 (dd, *J* = 8.5 and 2 Hz, 2H), 6.69 (dd, *J* = 8.5 and 2 Hz, 2H), 5.11 (bs, 2H), 2.85 (m, 1H), 2.55 (m, 2H), 2.29 (m, 2H), 1.92 (m, 2H); ^{13}C-NMR (125 MHz, $(CD_3)_2CO$): δ 192.9, 171.1, 153.2, 142.5, 134.1, 132.6, 130.6, 126.1, 118.3, 113.1, 83.7, 69.8, 35.6, 24.3, 17.7.

***N*-(4-(4-Butyramidobenzoyl)phenyl)hex-5-ynamide** [**4,** Reagents and conditions: (b) and (c)]**.**

Butyric acid (3.0 equiv.) was mixed with excess amount of oxalyl chloride and then stirred for 1 h at room temperature. This reaction mixture was purified by distillation method and then desired product, butyryl chloride, was finally obtained at around 95 °C (theoretical bp 102 °C) as a colorless liquid.

To a solution of *N*-(4-(4-aminobenzoyl)phenyl)hex-5-ynamide (1.0 equiv.) and TEA (1.2 equiv.) dissolved in CH_2Cl_2, butyryl chloride was added and then stirred for about 30 min at room temperature. After the reaction completion monitored by TLC, the reaction mixture was diluted with ethylacetate and then washed with brine. The separated organic layer was dried over anhydrous $MgSO_4$, filtrated and evaporated *in vacuo*. The resulting mixture was purified with silica-gel flash column chromatography (EA / hexane) to provide desired product **4** (white solid, 67%).

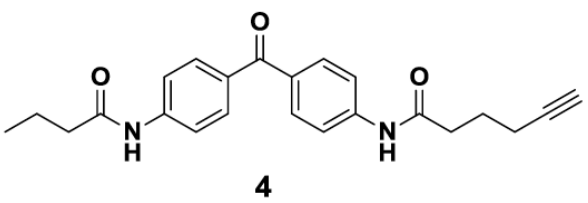

4

^{1}H-NMR (500 MHz, $(CD_3)_2SO$): δ 10.30 (s, 1H), 10.23 (s, 1H), 7.77–7.75 (m, 4H), 7.70–7.67 (m, 4H), 2.81 (t, J = 2.5 Hz, 1H), 2.48 (t, J = 7.5 Hz, 2H), 2.34 (t, J = 7.5 Hz, 2H), 2.24 (td, J = 7 and 2.5 Hz, 2H), 1.78 (tt, J = 7 Hz, 2H), 1.63 (qt. J = 7.5 Hz, 2H), 0.92 (t, J = 7.5 Hz, 3H); ^{13}C-NMR (125 MHz, $(CD_3)_2SO$): δ 193.4, 171.8, 171.2, 143.1, 143.0, 131.7, 131.7, 130.9, 118.2, 118.2, 83.9, 71.7, 38.4, 35.2, 23.8, 18.5, 17.3, 13.6; HRMS (ESI^+) *m/z* calculated for $[M+H]^+$ $C_{23}H_{25}O_3N_2$ 377.1863, found *m/z* 377.1860.

Cell culture : HeLa (human cervical adenocarcinoma cells), U266 (human myeloma cell line), A549 (human lung cancer cell line), and MCF7 (human breast cancer cell line) were obtained from American Type Culture Collection [ATCC, USA]. HeLa, U266, and A549 cells were cultured in RPMI 1640 [GIBCO, USA] supplemented with 10% (v/v) fetal bovine serum [GIBCO, USA] and 1% (v/v) antibiotic-antimycotic solution [GIBCO, USA]. MCF7 cells were cultured in high glucose DMEM [GIBCO, USA] supplemented with 10% (v/v) fetal bovine serum [GIBCO, USA] and 1% (v/v) antibiotic-antimycotic solution [GIBCO, USA]. The cells were maintained in a humidified atmosphere of 5 % CO_2 and 95 % air at 37 °C, and cultured in T75 Flask [Nalgene Nunc International, USA] according to manufacturers' instruction. The growth medium was changed every 2 to 3 days. Cells were grown to confluence prior to the experiment.

Antiproliferative agent screening : Cell viability was measured to determine the cytotoxicity of our probe using the WST–1 [Daeil Science, S. Korea], and the experimental procedure is based on the manufacturer's manual. HeLa cells were cultured into 96-well plates at a density of 2×10^3 cells/well for 24 h, followed by the treatment of 3000 membered pDOS chemical library (10 μM). After 72 h incubation with compounds (10 μM), 10 μL of WST–1 solution was added to each well, and plates were incubated for additional 1 h at 37 °C. The absorbance of each well at 450 nm was measured using Synergy HT [Bio-Tek, USA]. The percentage of cell viability was calculated by following formula: % cell viability = (mean absorbance in test wells) / (mean absorbance in control well) × 100. Each experiment was performed in triplicate experiments.

Reference

[1] D. C. Swinney, J. Anthony, *Nat. Rev. Drug Discovery* **2011**, *10*, 507; b) J. Zuberetal., *Nature* **2011**, 478, 524; c) C. A. Lyssiotis, L. L. Lairson, A. E. Boitano, H. Wurdak, S. Zhu, P. G. Schultz, *Angew. Chem., Int. Ed.* **2011**, *50*, 200.

[2] a) S. Sato, Y. Kwon, S. Kamisuki, N. Srivastava, Q. Mao, Y. Kawazoe, M. Uesugi, *J. Am. Chem. Soc.* **2007**, *129*, 873; b) H. Lim, D. Cai, C. T. Archer, T. Kodadek, *J. Am. Chem. Soc*. **2007**, *129*, 12936; c) S. Tsukiji, M. Miyagawa, Y. Takaoka, T. Tamura, I. Hamachi, *Nat. Chem. Biol.* **2009**, *5*, 341; d) C. C. Hughes, Y. Yang, W. Liu, P. C. Dorrestein, J. J. L. Clair, W. Fenical, *J. Am. Chem. Soc*. **2009**, *131*, 12094; e) B. Lomenick, et al., *Proc. Natl. Acad. Sci. USA* **2009**, *106*, 21984; f) L. Li, Q. Zhang, A. Liu, X. Li, H. Zhou, Y. Liu, B. Yan, *J. Am. Chem. Soc.* **2011**, *133*, 6886; g) S. A. Wacker, S. Kashyap, X. Li, T. M. Kapoor, *J. Am. Chem. Soc.* **2011**, *133*, 12386; h) M. Kita, Y. Hirayama, M. Sugiyama, H. Kigoshi, *Angew. Chem. Int. Ed.* **2011**, *50*, 9871.

[3] U. Rix, G. Superti-Furga, *Nat. Methods* **2009**, *5*, 616.

[4] a) H. S. Ban, K. Shimizu, H. Minegishi, H. Nakamura, *J. Am. Chem. Soc.* **2010**, *132*, 11870; b) K. Koteva, H. Hong, X. D. Wang, I. Nazi, D. Hughes, M. J. Naldrett, M. J. Buttner, G. D. Wright, *Nat. Chem. Biol.* **2010**, *6*, 327; c) J. Eirich, R. Orth, S. A. Sieber, *J. Am. Chem. Soc*. **2011**, *133*, 12144.

[5] a) H. Wu, J. Ge, P. Yang, J. Wang, M. Uttamchandani, S. Q. Yao, *J. Am. Chem. Soc.* **2011**, *133*, 1946; b) H. Wurdak, et al., *Proc. Natl. Acad. Sci. USA* **2010**, *107*, 16542.

[6] a) A. E. Speers, G. C. Adam, B. F. Cravatt, *J. Am. Chem. Soc.* **2003**, *125*, 4686; b) A. E. Speers, B. F. Cravatt, *Chem. Biol.* **2004**, *11*, 535.

[7] R. Tonge, J. Shaw, B. Middleton, R. Rowlinson, S. Rayner, J. Young, F. Pognan, E. Hawkins, I. Currie, M. Davison, *Proteomics* **2001**, *1*, 377.

[8] M. Ünlü, M. E. Morgan, J. S. Minden, *Electrophoresis* **1997**, *18*, 2071.

[9] H. Zhou, G. Rivas, A. P. Minton, *Annu. Rev. Biophys.* **2008**, *37*, 375.

[10] Y.K. Kim, J. Lee, X. Bi, H. Ha, S.H. Ng, Y. Ahn, J. Lee, B.K. Wagner, P. A. Clemons, Y. T. Chang, *Angew. Chem. Int. Ed.* **2011**, *50*, 2761.

[11] a) H. Shi, X. Cheng, S. K. Sze, S. Q. Yao, *Chem. Commun.* **2011**, *47*, 11306; b) P. -Y. Yang, M. Wang, C. Y. He, S. Q. Yao, *Chem. Commun.* **2012**, *48*, 835; c) H. Shi, C. -J. Zhang, G. Y. J. Chen, S. Q. Yao, *J. Am. Chem. Soc.* **2012**, *134*, 3001.

[12] S. Oh, S. B. Park, *Chem. Commun.* **2011**, *47*, 12754.

[13] T. Cupido, P. G. Rack, A. J. Firestone, J. M. Hyman, K. Han, S. Sinha, C. A. Ocasio, J. K. Chen, *Angew. Chem. Int. Ed.* **2009**, *48*, 2321.

[14] a) A. L. Blajeski, *J. Clin. Invest.* **2002**, *110*, 91; b) Y. K. Kim, H. Ha, J. Lee, X. Bi, Y. Ahn, S. Hajar, J. Lee, Y. T. Chang, *J. Am. Chem. Soc.* **2010**, *132*, 576.

[15] P. B. Arimondo, C. Bailly, A. S. Boutorine, V. A. Ryabinin, A. N. Syniakov, J. S. Sun, T. Garestier, C. Helene, *Angew. Chem. Int. Ed.* **2001**, *40*, 3045.

[16] A. Shevchenko, M. Wilm, O. Vorm, M. Mann, *Anal. Chem.,* **1996**, *68*, 850.

[17] J. Jin, J. Park, K. Kim, Y. Kang, S. G. Park, J. H. Kim, K. S. Park, H. Jun, Y. Kim, *J. Proteome Res.* **2009**, *8*, 1393.

[18] S. Oh, S. W. Cho, J. Y. Yang, H. J. Sun, Y. S. Chung, C. S. Shin, S. B. Park, *Med. Chem. Commun.,* **2011***, 2,* 76.

국문초록

박종민

서울대학교 자연과학대학 대학원 화학부

기존의 표적기반 신약 개발을 통해 개발된 약물들이 예측하지 못했던 부작용때문에 최근 시장에서 퇴출되는 예가 생기고 있다. 이에 최근 새로운 접근 방식을 통해 신약을 개발하려는 연구가 활발히 진행되고 있다. 또한 최근 기존의 약물에 저항성을 가지는 질병이나, 재생의학, 난치병등을 치료하는데 있어서 기존의 신약 타겟이 아닌 비전통적인 신약타겟을 조절하는 새로운 저분자 물질을 찾아내는 것이 주목 받고 있다. 따라서 본 연구에서는 새로운 신약 개발 접근방식을 개발하기 위한 플랫폼의 개발에 촛점을 맞추고 있다. 생명현상을 모니터링 하기 위한 새로운 바이오프로브(Bioprobe)의 개발, 새로운 생리활성 저분자 물질의 스크리닝, 그리고 발굴된 새로운 생리활성 저분자 물질의 작용기전을 밝히기 위한 표적 단백질 동정법 개발이 본 연구에서 다루고 있는 핵심 내용이다.

Part I 에서는 글루코스 바이오프로브 (Chapter 1-4), 불소 프로브 (Chapter 5), 그리고 Zidovudine 프로브 (Chapter 6) 의 개발에 대해서 다루고 있다. 처음으로 개발된 글루코스 바이오 프로브는 Cy3-Glc-α로 명명되었으며 기존의 글루코스 바이오 프로브인 2-NBDG 에 비해서 월등은 물성을 보였다. 이 연구를 기반으로 암세포내의 글루코스 흡수 정도를 Cy3-Glc-α를 이용하여 측정하고 항암제를 스크리닝 할 수 있는 시스템을 구축하였다. (Chapter 1) Cy3-Glc-α의 성공을 바탕으로 Chapter 2 에서는 새로운 글루코스 바이오프로브의

유사체들의 합성에 대해 다루었다. 그중에서 기존의 2-NBDG 는 물론 첫번째 글루코스 바이오프로브인 Cy3-Glc-α에 비해서도 더 좋은 물성을 가지는 GB2-Cy3 로 명명된 새로운 바이오프로브를 발굴 해내었다. GB2-Cy3 는 암세포 뿐만 아니라 대사질환에 중요한 연구 모델인 C2C12 근육 세포에서도 글루코스를 잘 모니터링 할 수 있었다. (Chapter 2) 이렇게 개발된 GB2-Cy3 는 대사질환에 중요한 역할을 하는 AMPK 를 조절하는 저분자 화합물의 작용기전을 연구하는데 이용되었다. (Chapter 3) 일광자 글루코스 바이오프로브의 성공은 조직 이미징이 가능한 이광자 글루코스 바이오프로브의 개발을 가능하게 하였다. GB2-Cy3 의 구조를 기반으로 하여 개발된 이광자 글루코스 바이오프로브는 AG2 로 명명 되었으며 암세포에서 뿐만아니라 대장암 조직에서의 글루코스 모니터링을 가능하게 하였다. (Chapter 4) 글루코스 바이오프로브 이외에도 본 연구에서는 세계 최초로 세포에 사용가능한 새로운 불소 프로브인 TBPCA 의 개발에 성공하였다. TBPCA 를 이용하여 폐암세포인 A549 세포 안의 불소를 이미징하고 그 농도를 측정 가능하였다. (Chapter 5) Chapter 6 에서는 AIDS 치료제인 zidovudine (ZDV) 을 모니터링 할수 있는 프로브에 관한 내용을 다루고 있다. ZDV 는 AIDS 치료제로 널리 사용되고 있으므로 그 부작용에 관한 연구가 매우 중요하다고 할수 있다. 따라서 본 연구에서는 ZDV 에 존재하는 azide 작용기가 Bioorthogonal 한 반응인 Click Chemistry 가 가능하다는 점을 이용하여 ZDV 를 모니터링 할 수 있는 새로운 방법을 개발하였다.

Part II 에서는 생리활성 저분자 물질의 스크리닝 (Chapter 1) 과 표적 단백질을 동정하는 새로운 방법의 개발 (Chapter 2)에 관한 내용을 다루고 있다. Part

I 에서의 바이오프로브 개발경험을 바탕으로 본 연구에서는 비스테로이드 계열의 안드로젠 수용체 길항제를 스크리닝 하였다. 벤조파이란 구조를 기반으로 한 새로운 안드로젠 수용체 길항제 6 f는 전립선 암을 효과적으로 억제하는 것으로 밝혀졌다. 또한 기존의 치료제에 저항성을 가지는 전립선 암의 경우도 성공적으로 억제가 가능한 것으로 밝혀졌다. 이러한 새로운 전립선암 치료제 후보 물질 6 f 는 추후 효과적인 전립선 치료를 위한 새로운 방향을 제시할 것으로 기대하고 있다. (Chapter 1) 위와 같은 방식으로 발굴된 새로운 생리활성 저분자 물질의 작용기전을 연구하기 위하여 본 연구에서는 새로운 표적 단백질 동정방법인 FITGE 를 개발하였다. FITGE 방법은 손상을 주지 않은 살아있는 세포 상태에서 표적 단백질의 동정이 가능하다. 이러한 점은 기존의 방법으로는 성공하지 못했던 표적 단백질 동정이 FITGE 방법에 의해서만 성공할 수 있었다. FITGE 방법은 기존의 표적 단백질 동정 방법의 한계를 극복 할수 있는 새로운 방법으로 제시 되었으며 살아있는 세포상에서의 표적 단백질 동정의 효과적인 수단이 될 것으로 기대하고 있다. (Chapter 2)

색인어 : 글루코스 바이오프로브, AMPK, 대사질환, 이광자 글루코스 바이오프로브, 불소, Zidovudine, 안드로젠 수용체, 항암제, 표적 단백질 동정.

학번 : 2005-23208

Appendix

Part I

Development of Novel Bioprobes and Its Applications in Biological Systems

Chapter 1. Development of a Cy3-Labeled Glucose Bioprobe and Its Application in Bioimaging and Screening for Anticancer Agents

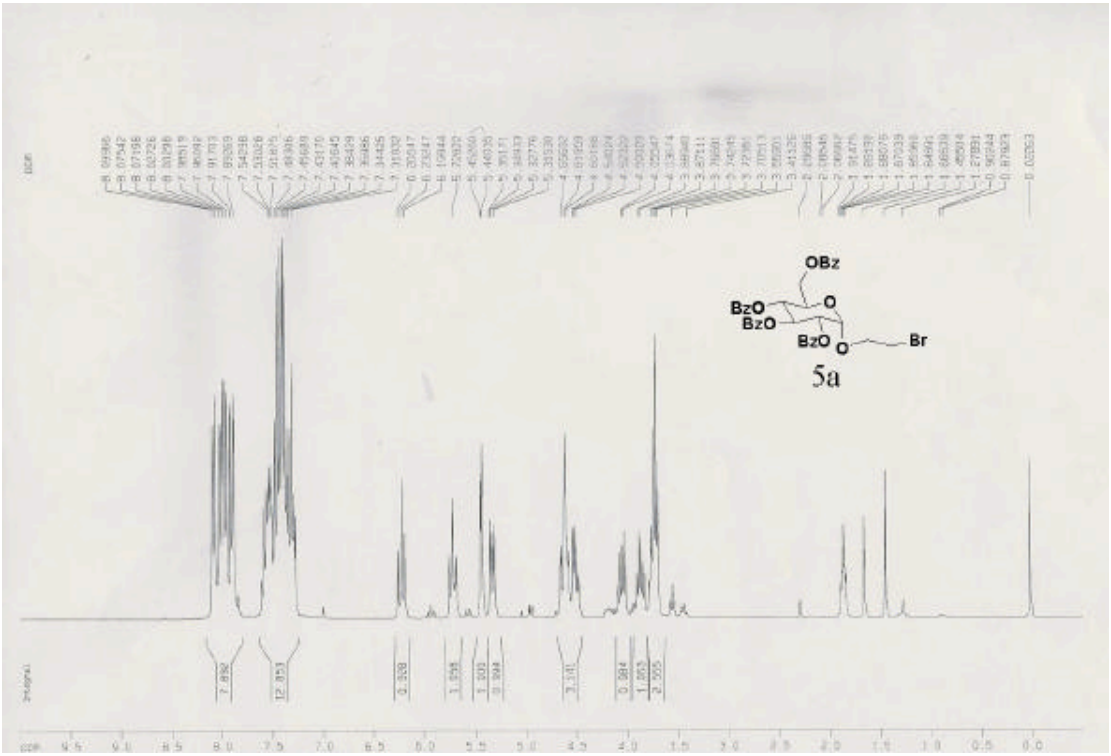
OBz
BzO
BzO
O
BzO
O
Br
5a

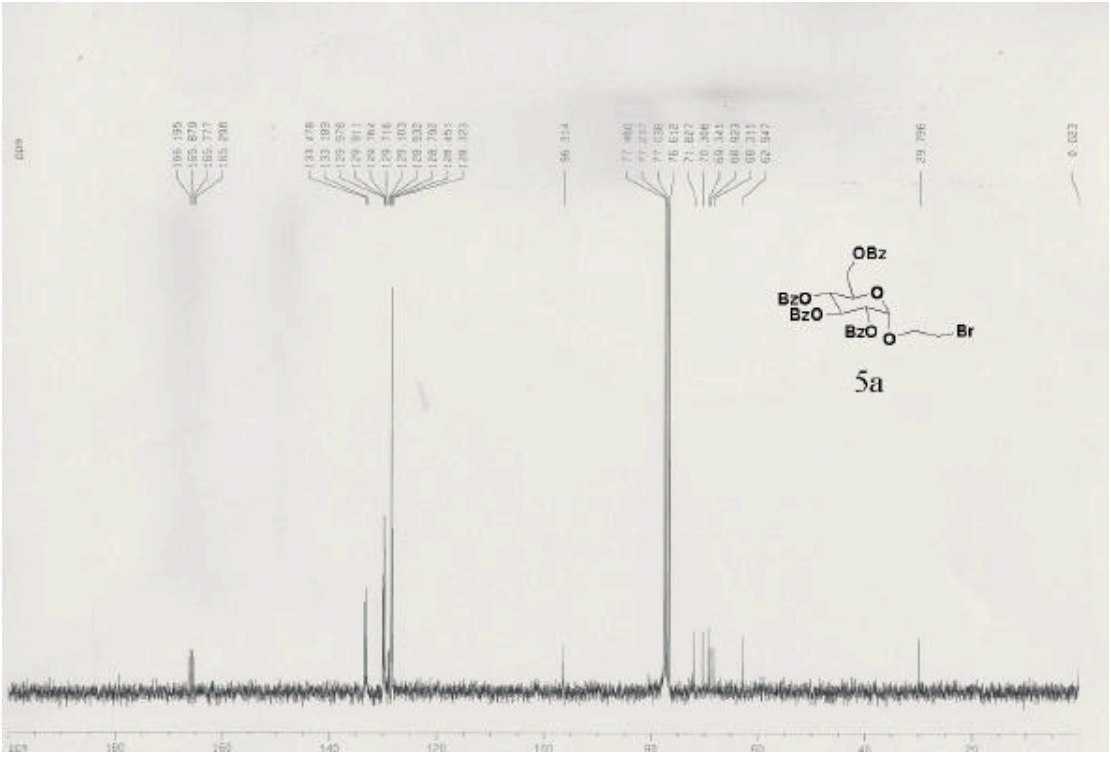
OBz
BzO
BzO
O
BzO
O
Br
5a

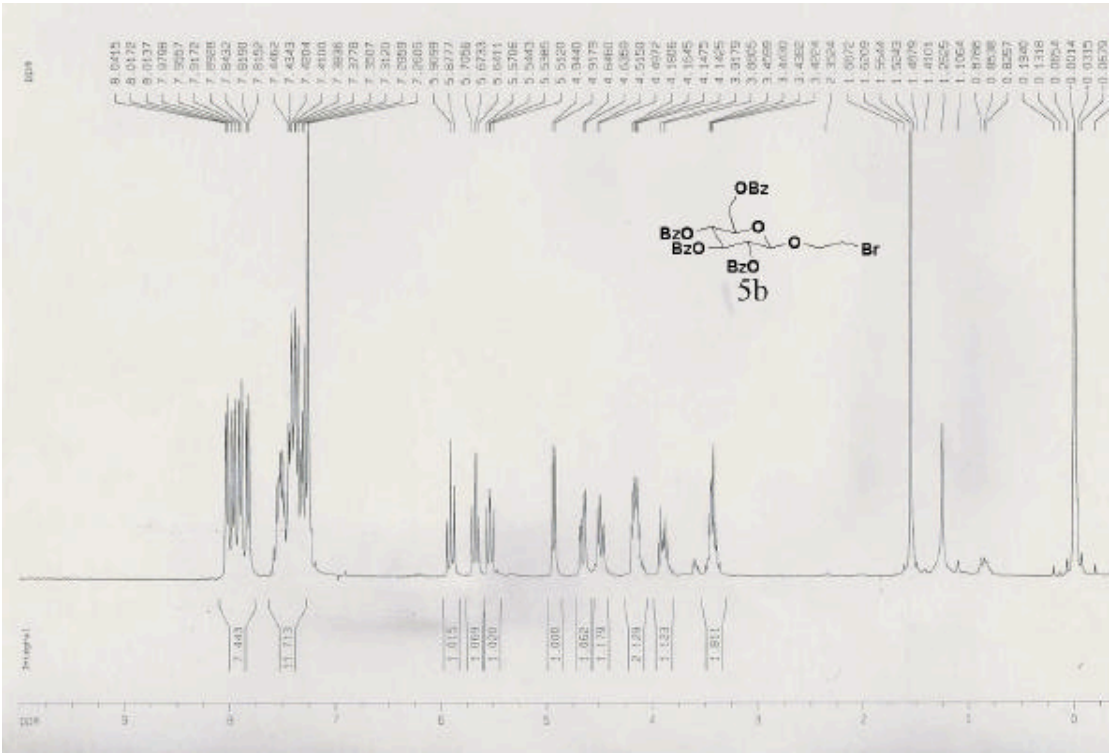
OBz
BzO
BzO
BzO
O
O
Br
5b

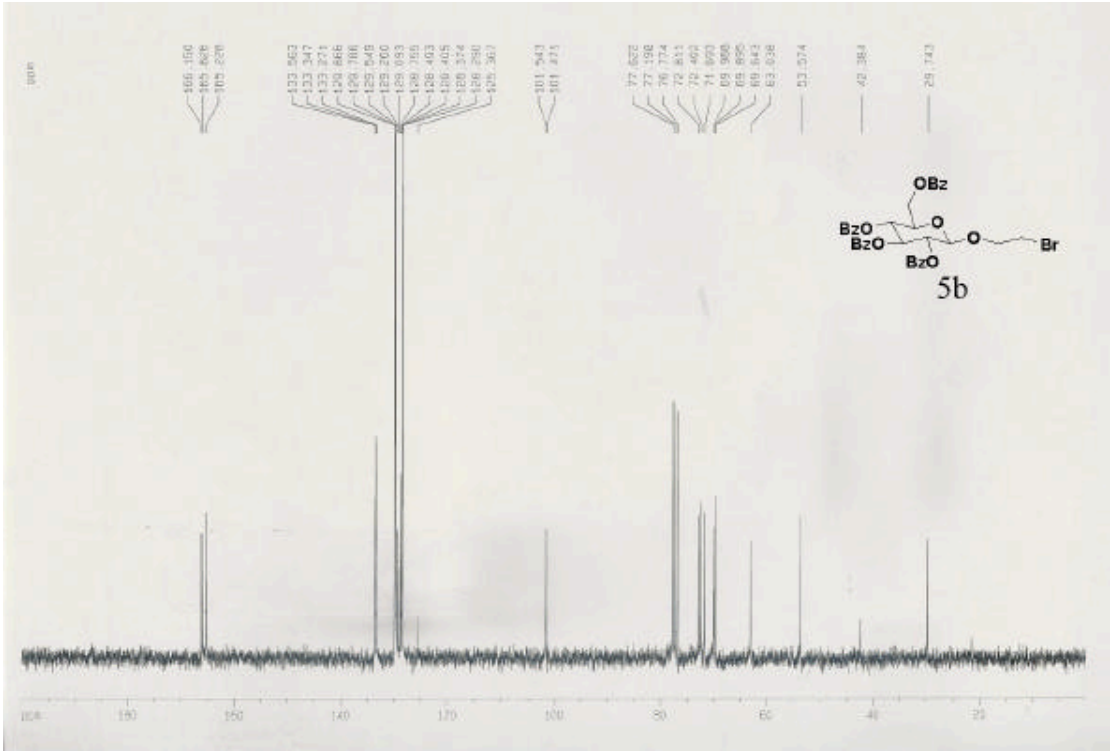
OBz
BzO
BzO
BzO
O
O
Br
5b

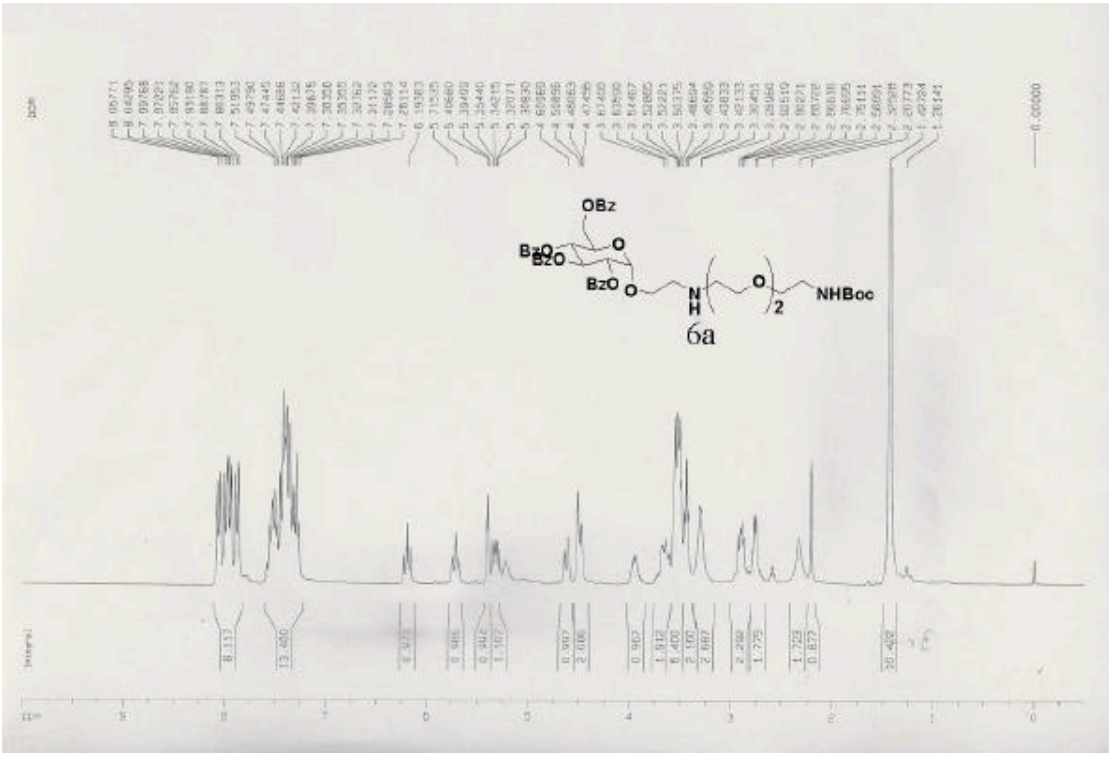

6a

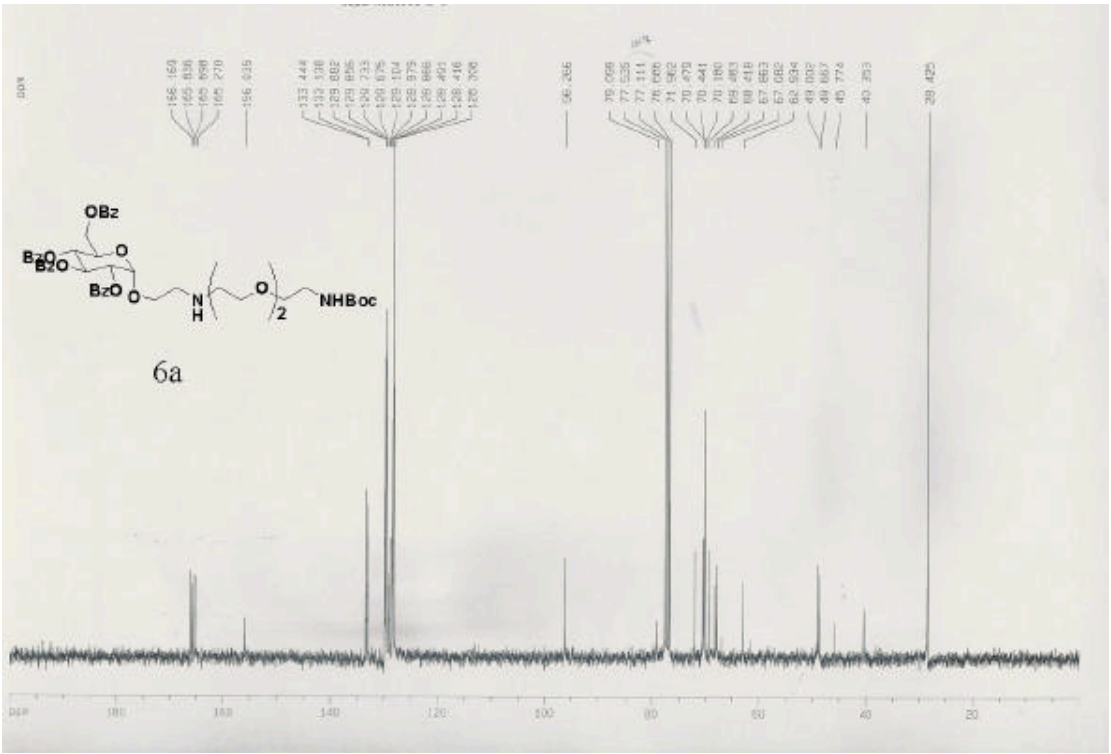

6a

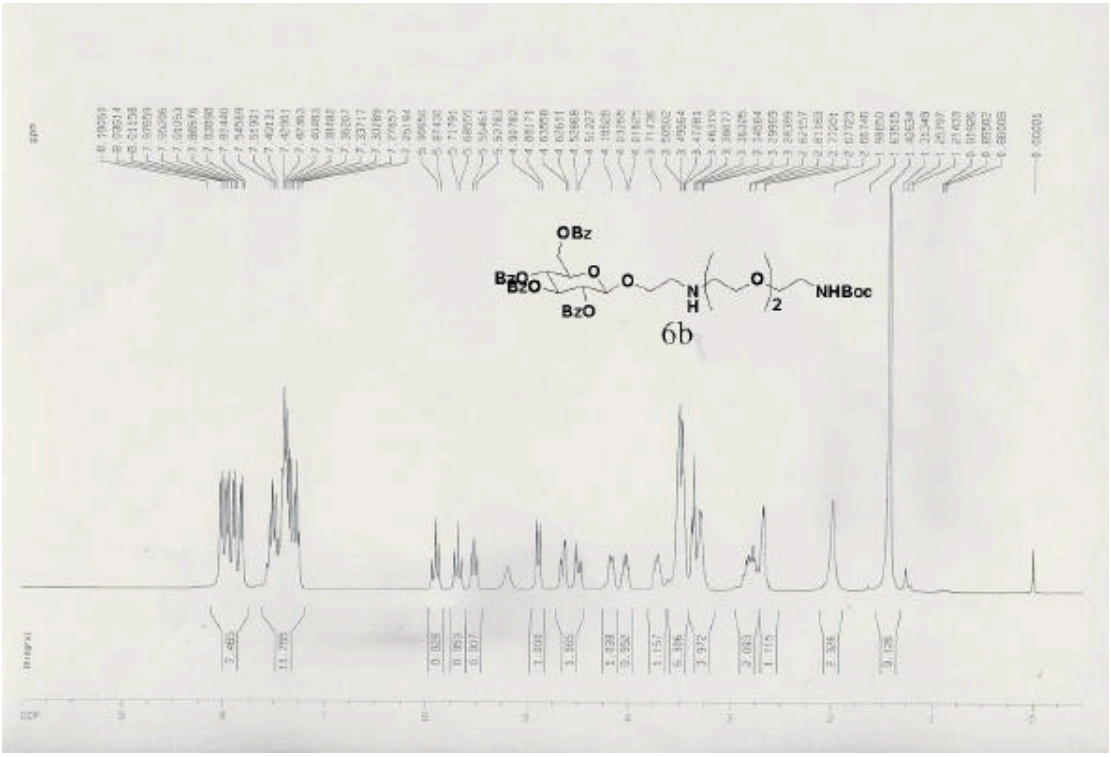
OBz
BzO
BzO
BzO
O
O
N
H
O
2
NHBoc
6b

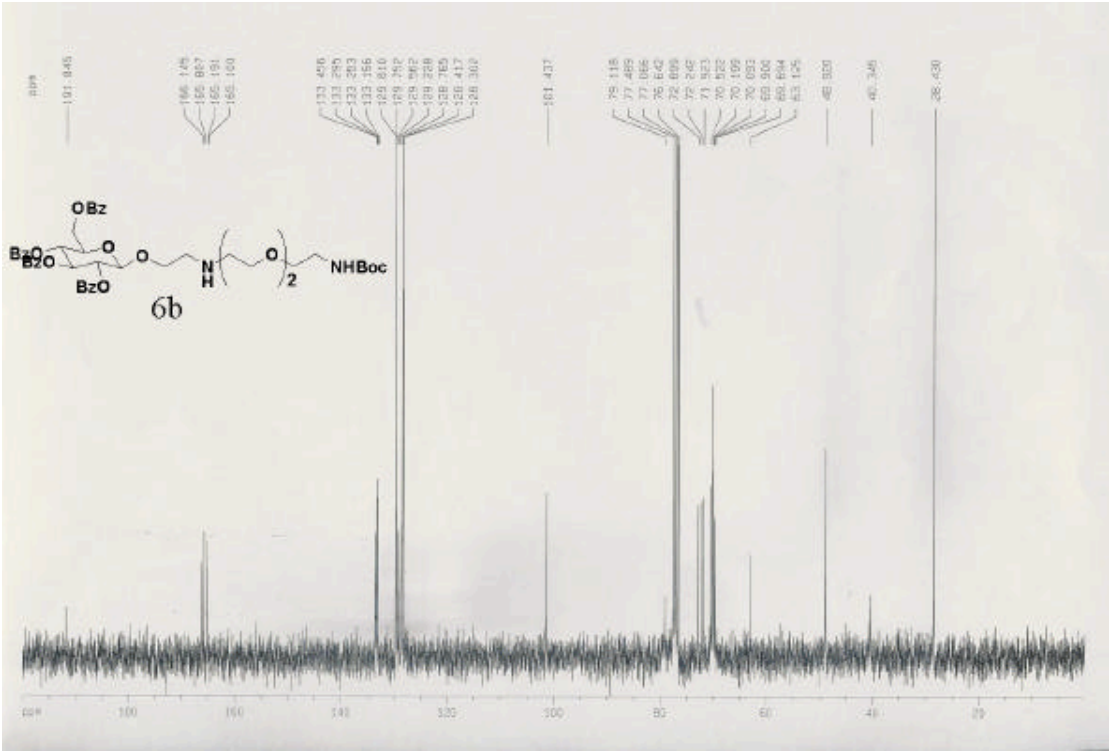
OBz
BzO
BzO
BzO
O
O
N
H
O
2
NHBoc
6b

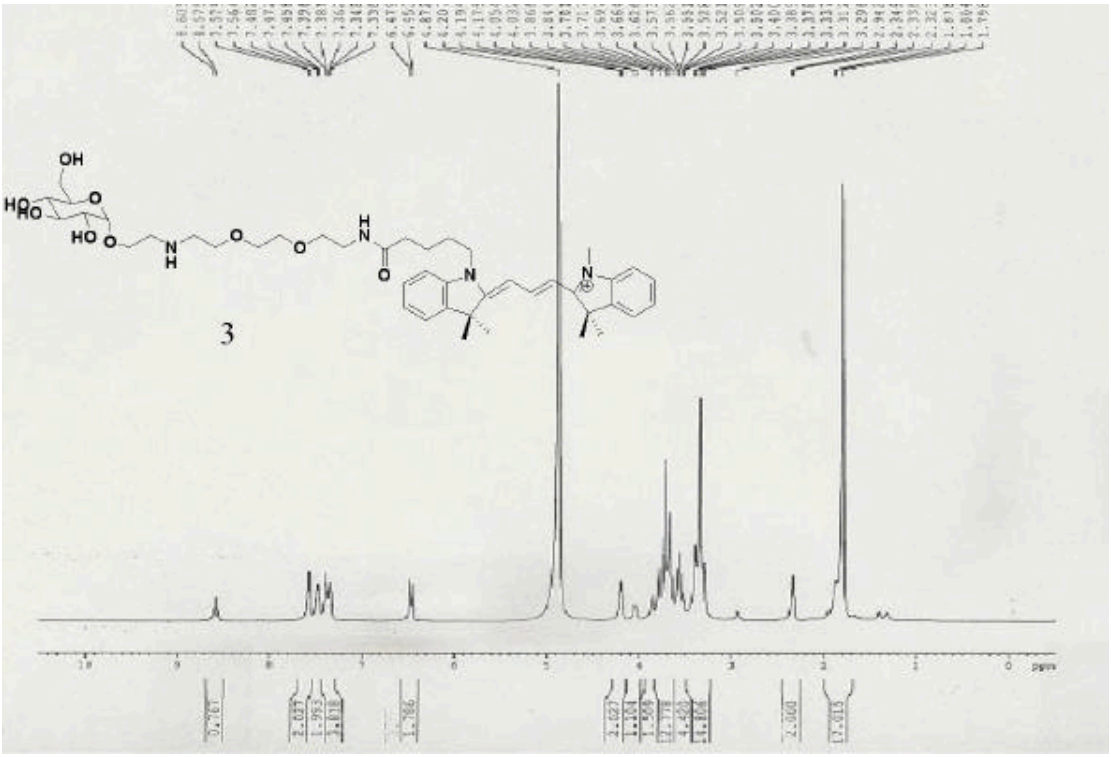
OH
HO
HO
HO
O
N
H
O
N
O
3

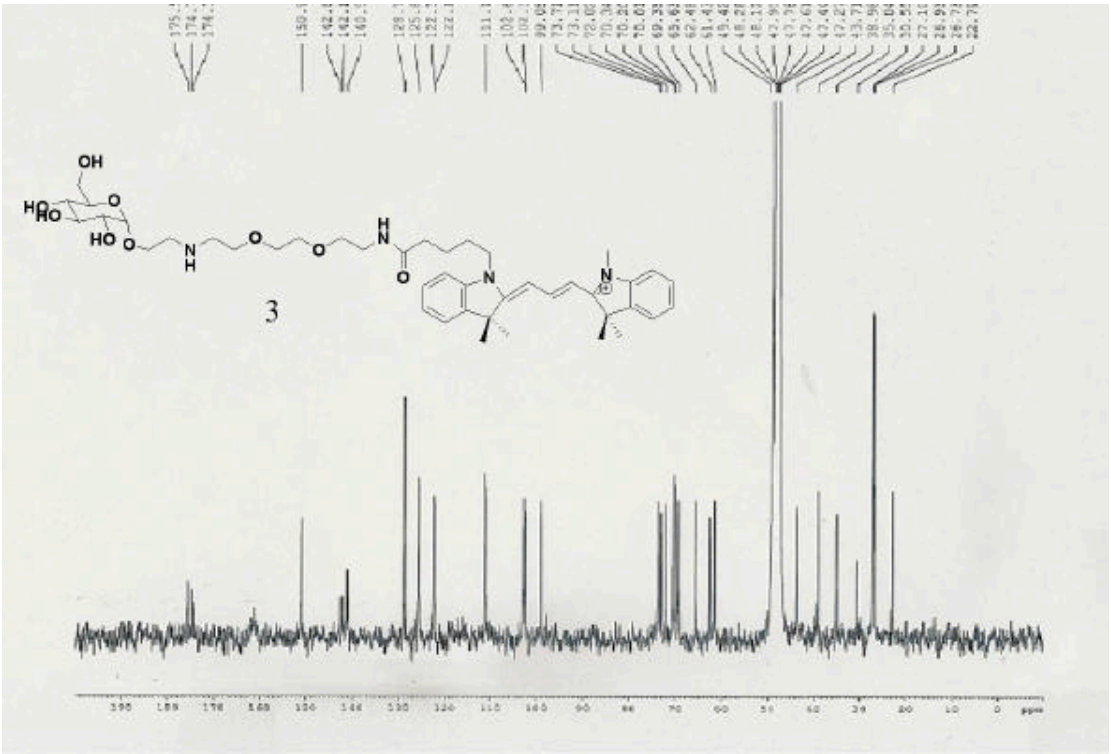
OH
HO
HO
HO
O
N
H
O
N
O
3

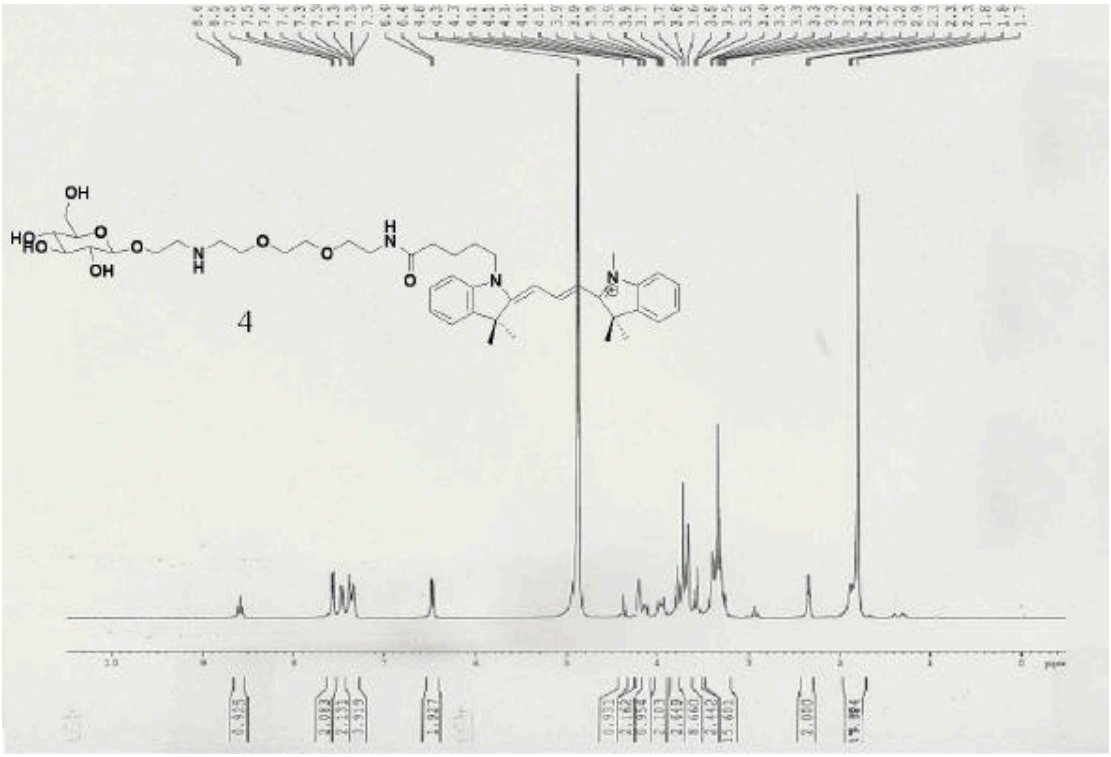
OH
HO
HO
O
OH
O
N
H
O
O
H
N
O
N
N
4

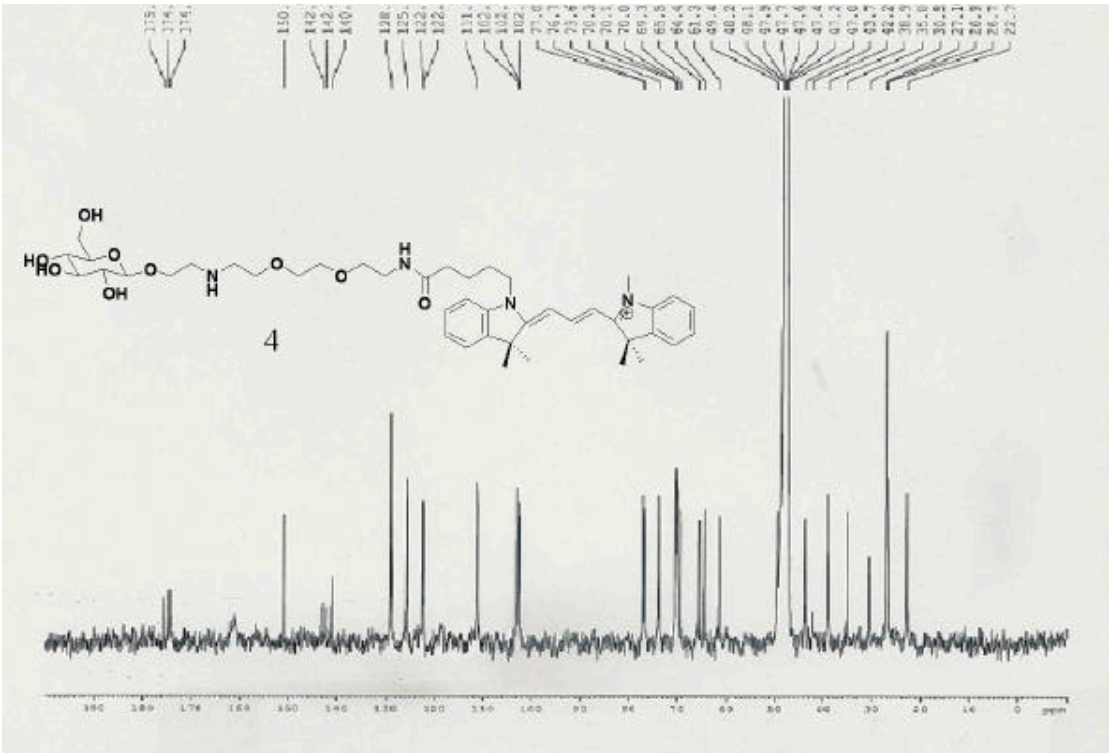
OH
HO
HO
O
OH
O
N
H
O
O
H
N
O
N
N
4

Chapter 2. Development of a New Series of Fluorescent Glucose Bioprobes and Their Application on Real-Time and Quantitative Monitoring of Glucose Uptake in Living Cells

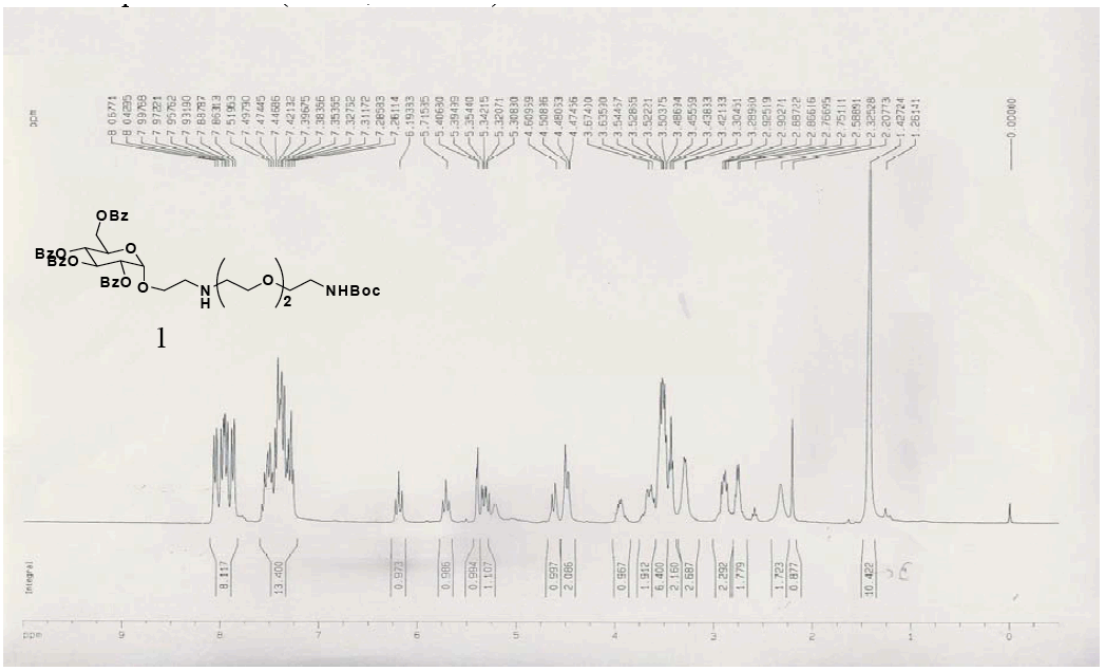
OBz
BzO
BzO
BzO
O
N
H
O
2
NHBoc
1

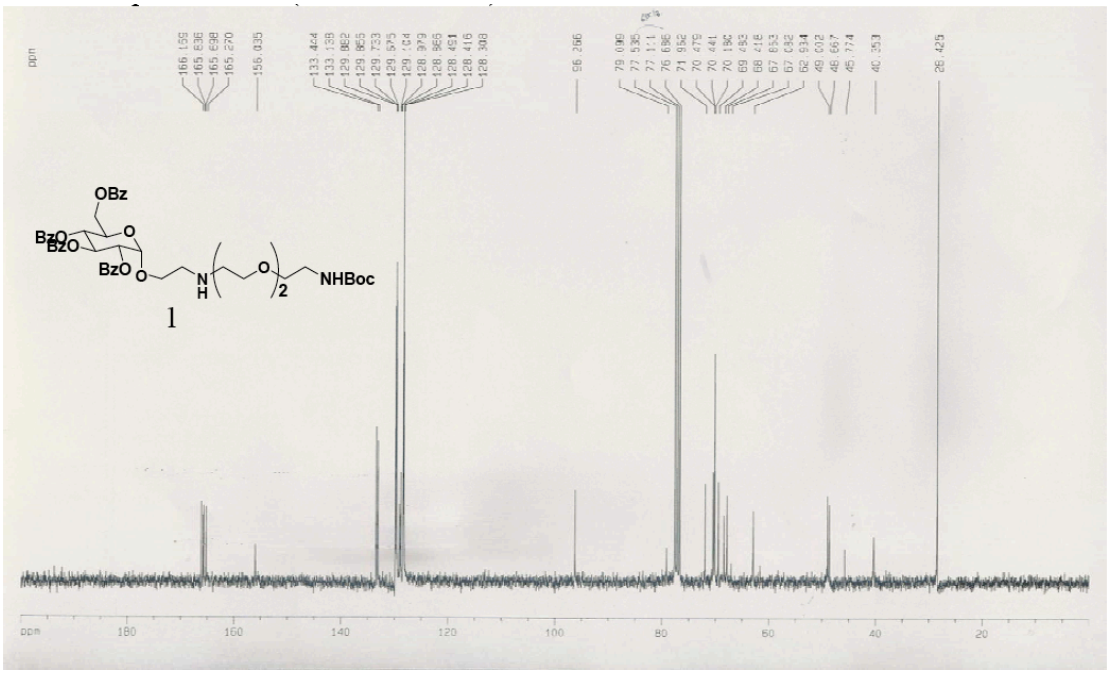
OBz
BzO
BzO
BzO
O
N
H
O
2
NHBoc
1

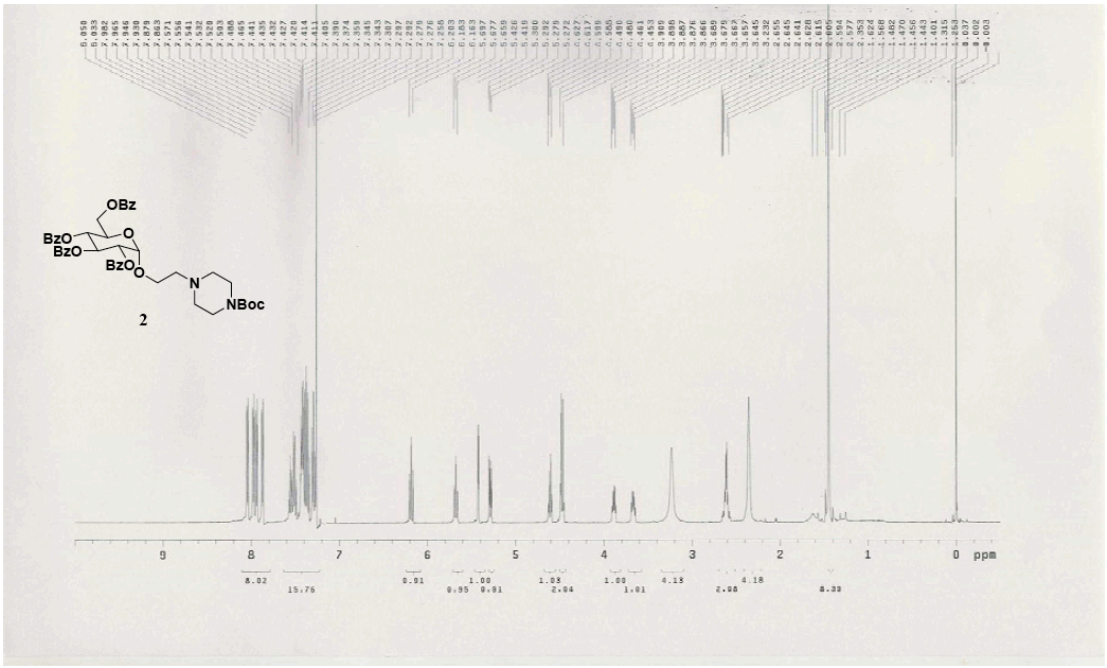
OBz
BzO
BzO
BzO
O
N
NBoc
2
9
8
7
6
5
4
3
2
1
0 ppm

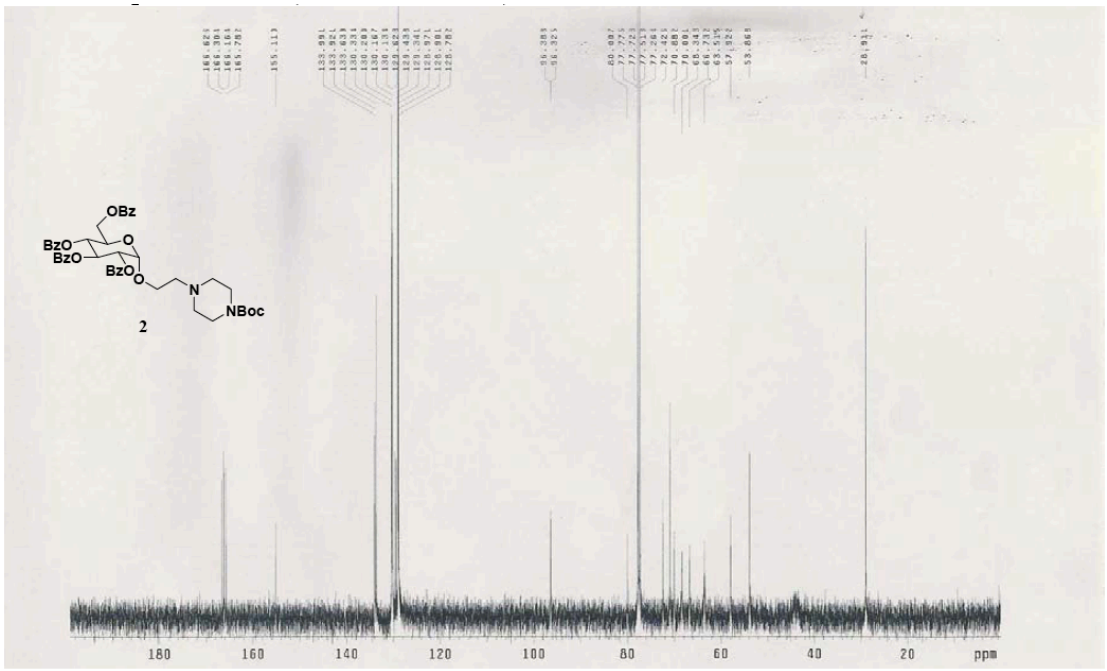
OBz
BzO
BzO
BzO
O
N
NBoc
2
180
160
140
120
100
80
60
40
20
ppm

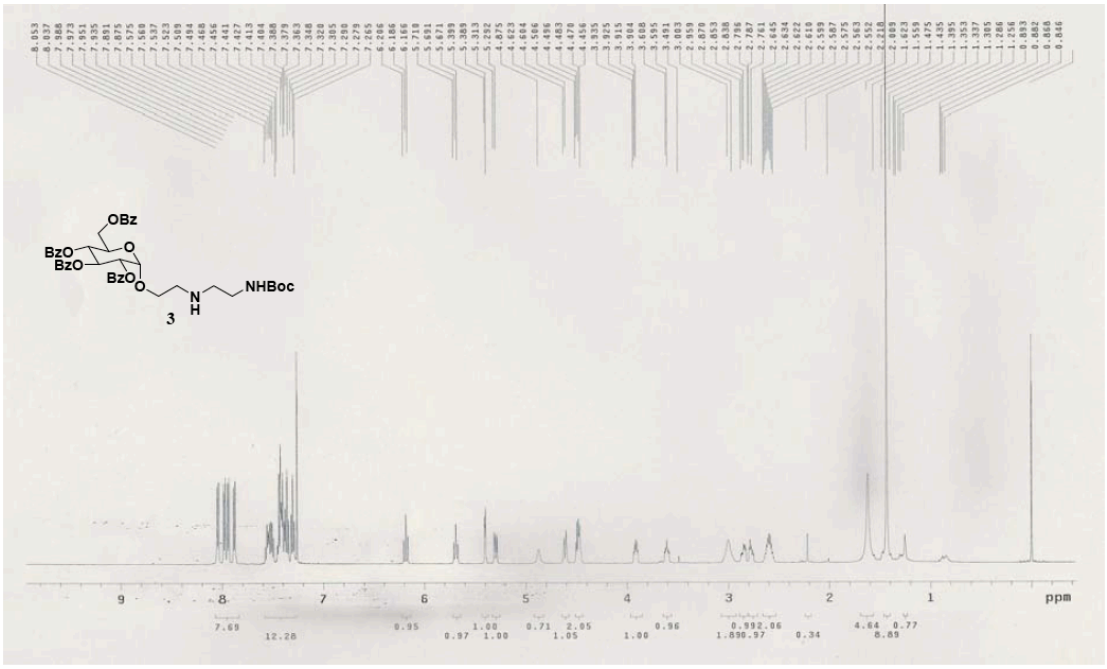
OBz
BzO
BzO
BzO
O
O
N
H
3
NHBoc
ppm

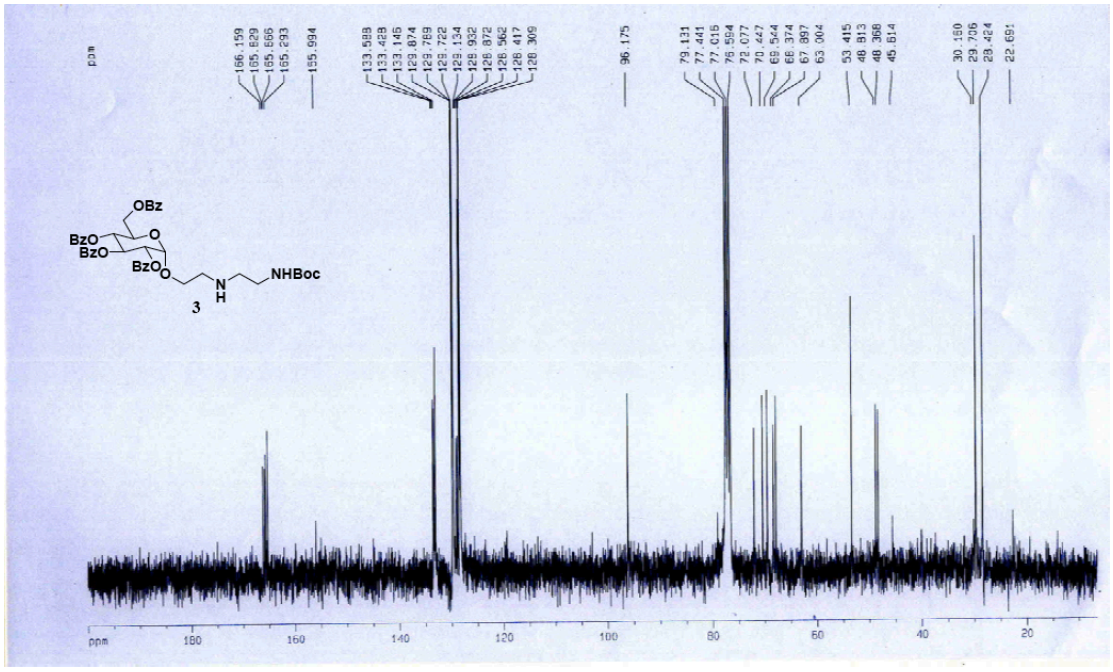
OBz
BzO
BzO
BzO
O
O
N
H
3
NHBoc
ppm

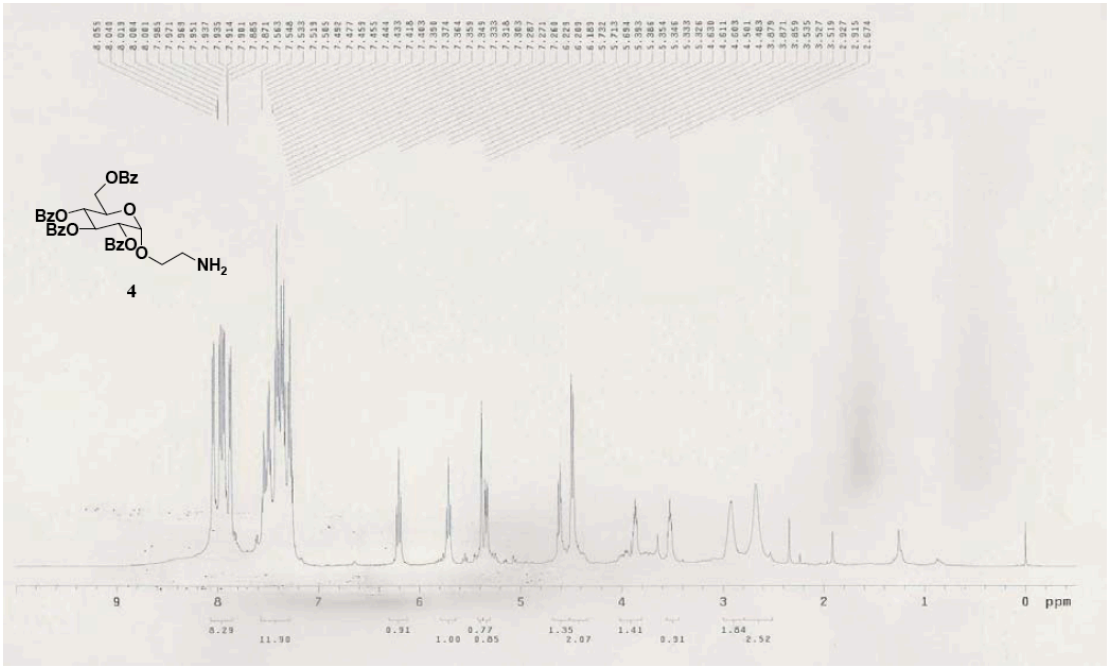
OBz
BzO
BzO
BzO
O
O
NH2
4
9
8
7
6
5
4
3
2
1
0 ppm

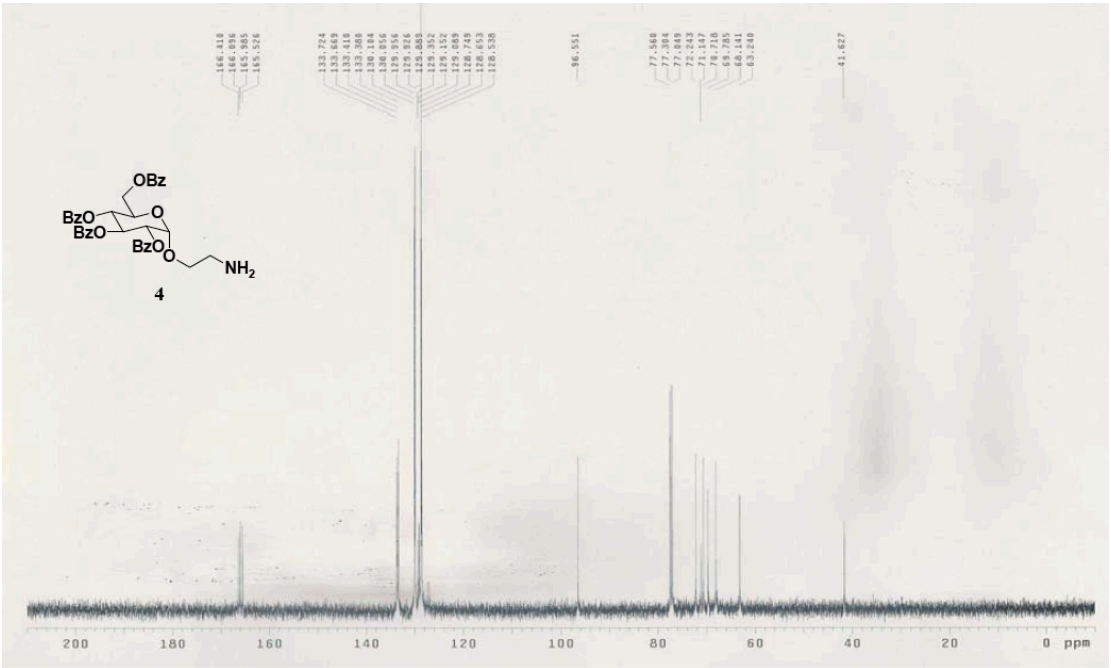
OBz
BzO
BzO
BzO
O
O
NH2
4
200
180
160
140
120
100
80
60
40
20
0 ppm

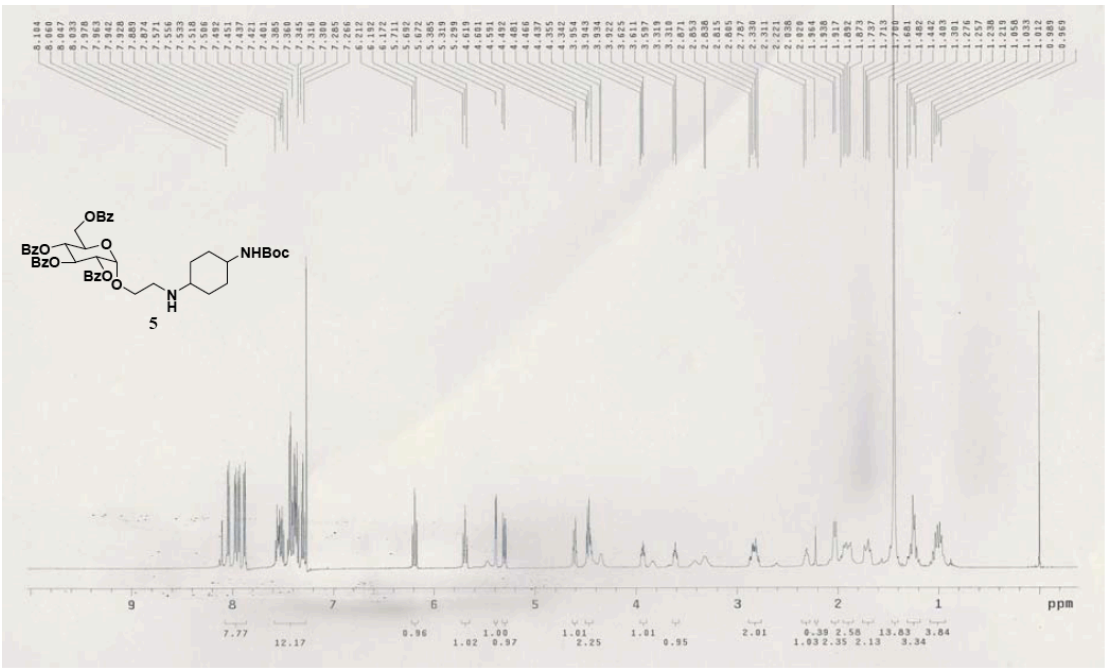
OBz
BzO
BzO
BzO
O
O
NHBoc
N
H
5
9
8
7
6
5
4
3
2
1
ppm
7.77
12.17
0.96
1.00
1.02
0.97
1.01
2.25
1.01
0.95
2.01
0.39
2.58
13.83
3.84
1.03
2.35
2.13
3.34

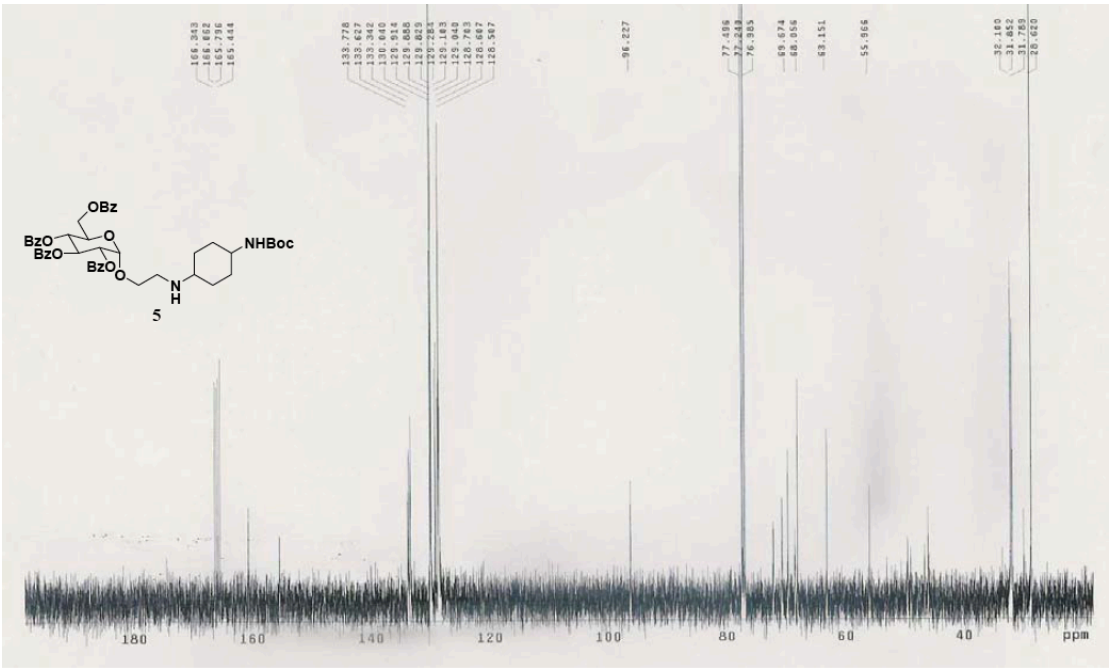
OBz
BzO
BzO
BzO
O
O
NHBoc
N
H
5
180
160
140
120
100
80
60
40
ppm

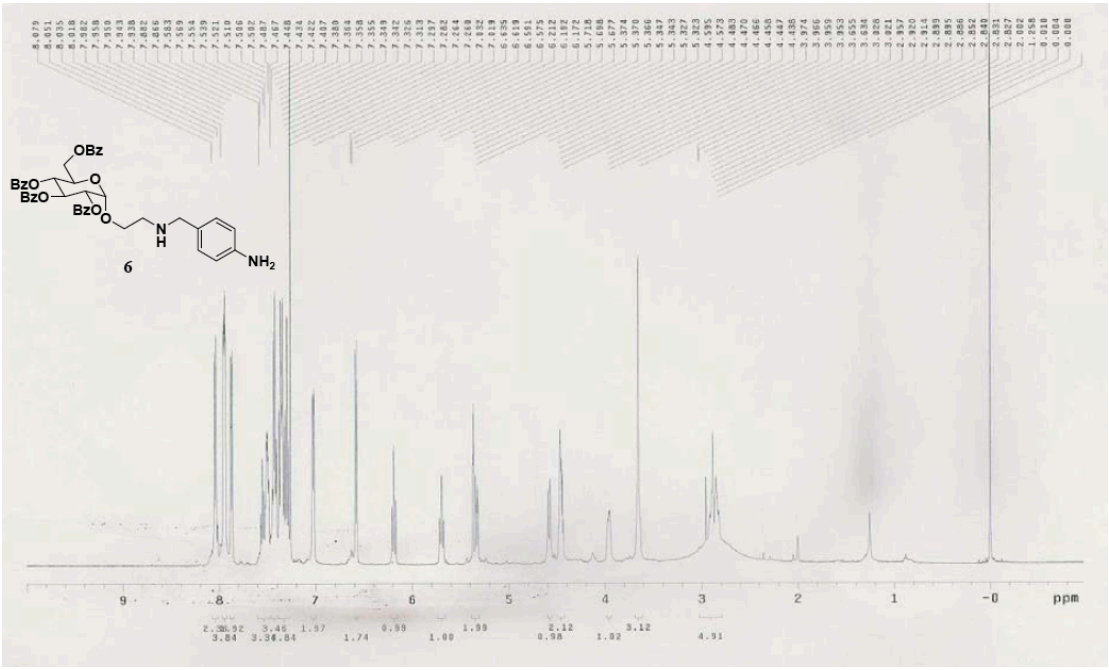
OBz
BzO
BzO
BzO
O
O
N
H
NH2
6
ppm

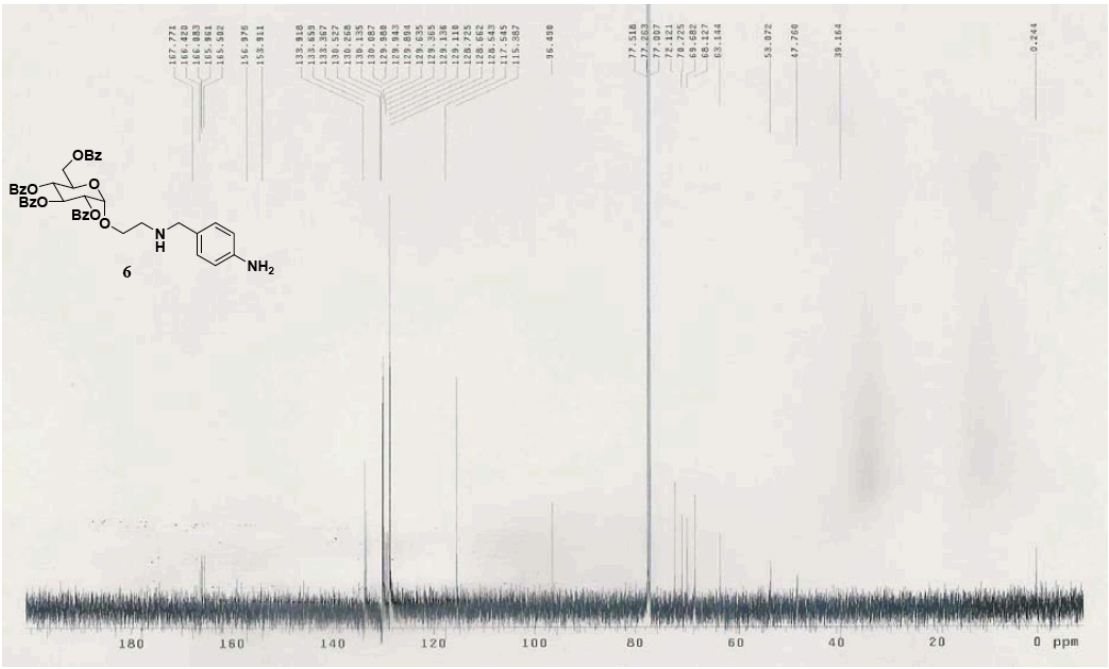
OBz
BzO
BzO
BzO
O
O
N
H
NH2
6
ppm

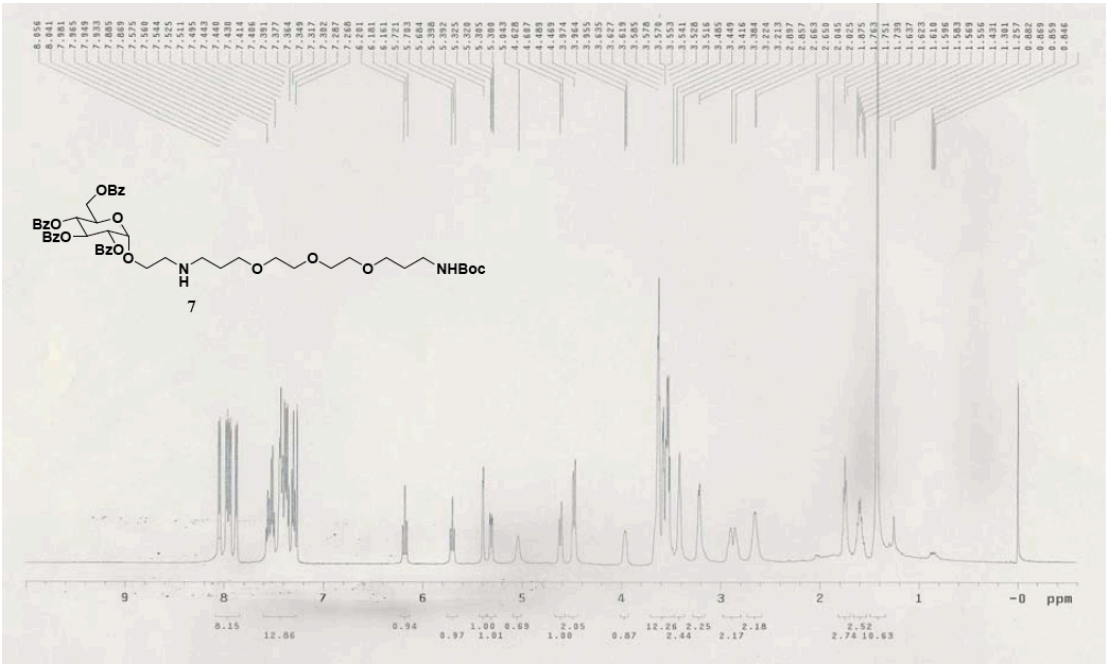
OBz
BzO
BzO
BzO
O
N
H
NHBoc
7
9
8
7
6
5
4
3
2
1
-0
ppm

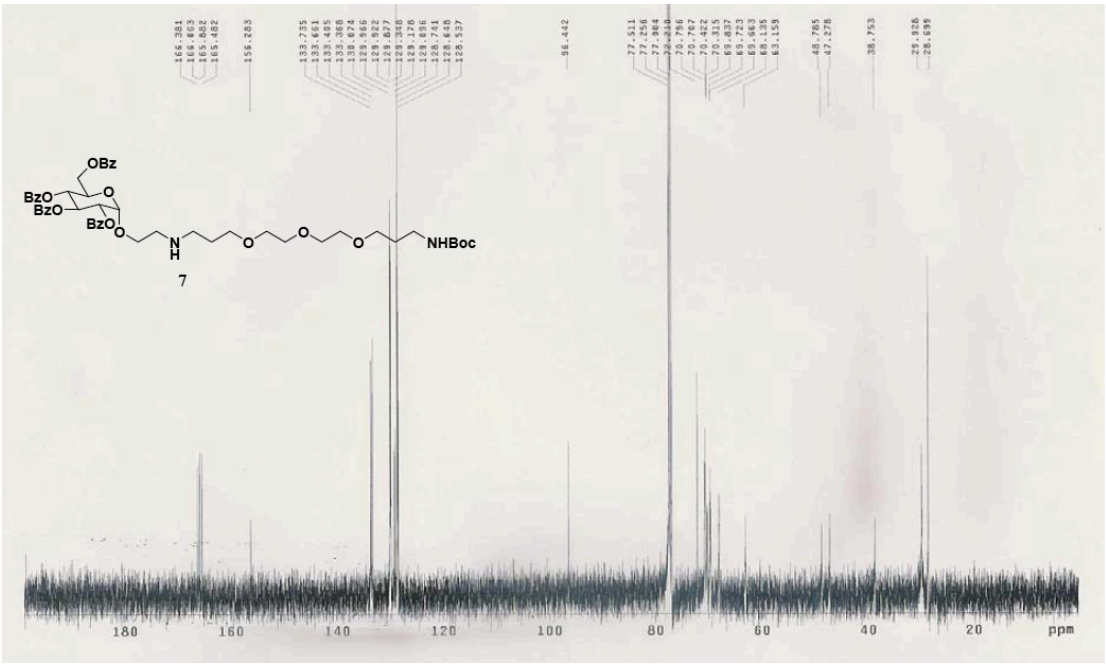
OBz
BzO
BzO
BzO
O
N
H
NHBoc
7
180
160
140
120
100
80
60
40
20
ppm

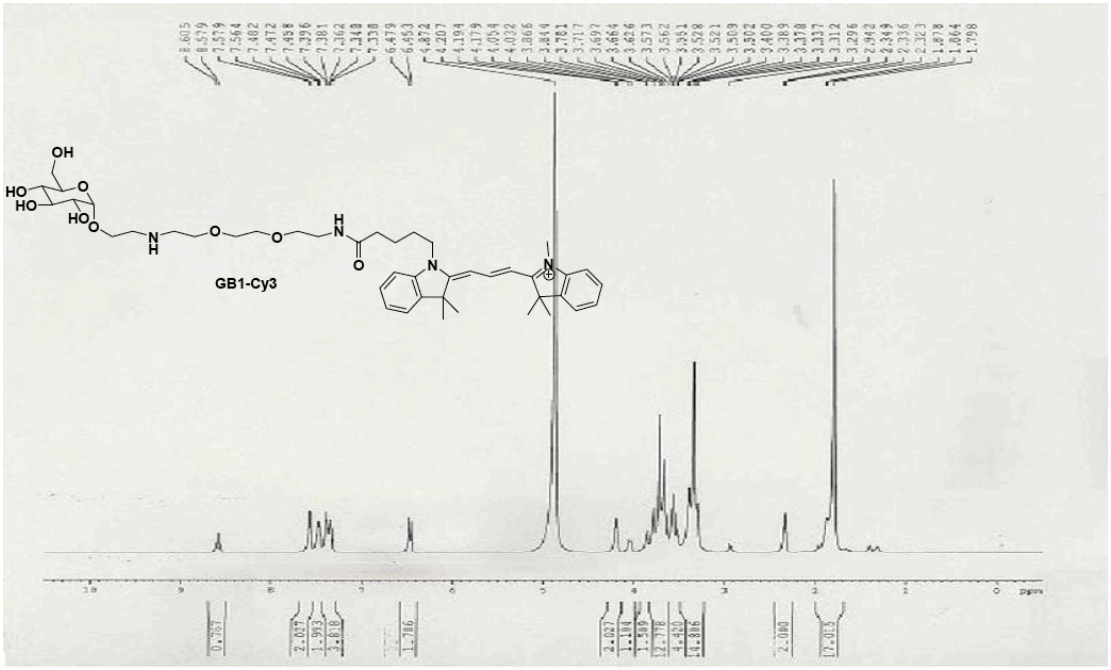
GB1-Cy3

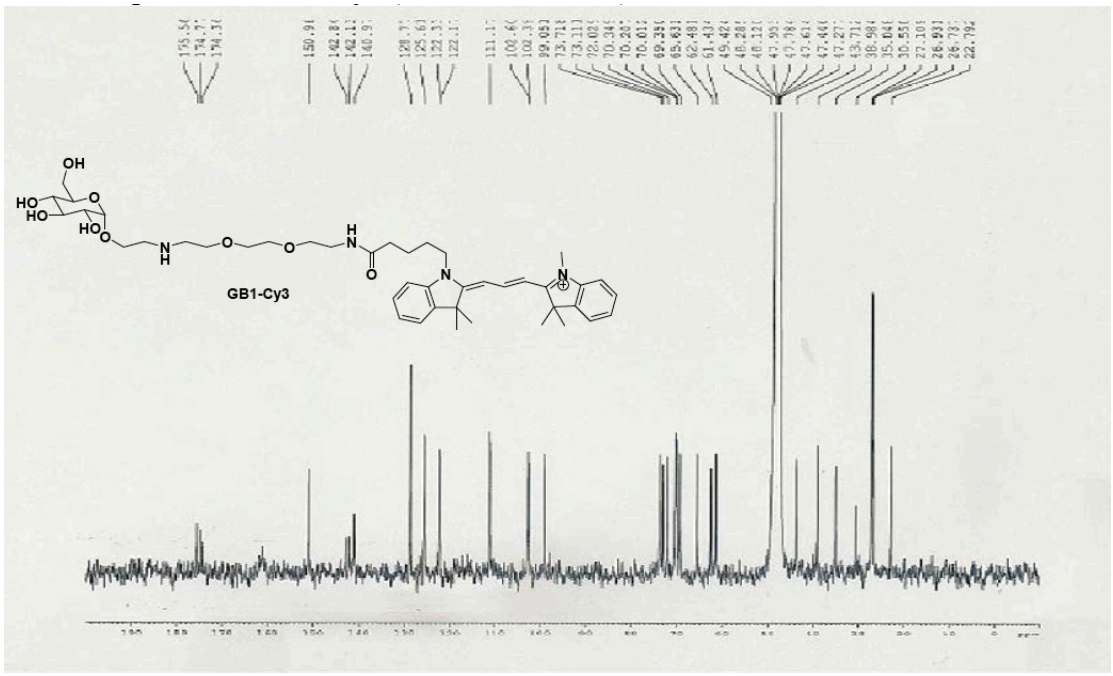
GB1-Cy3

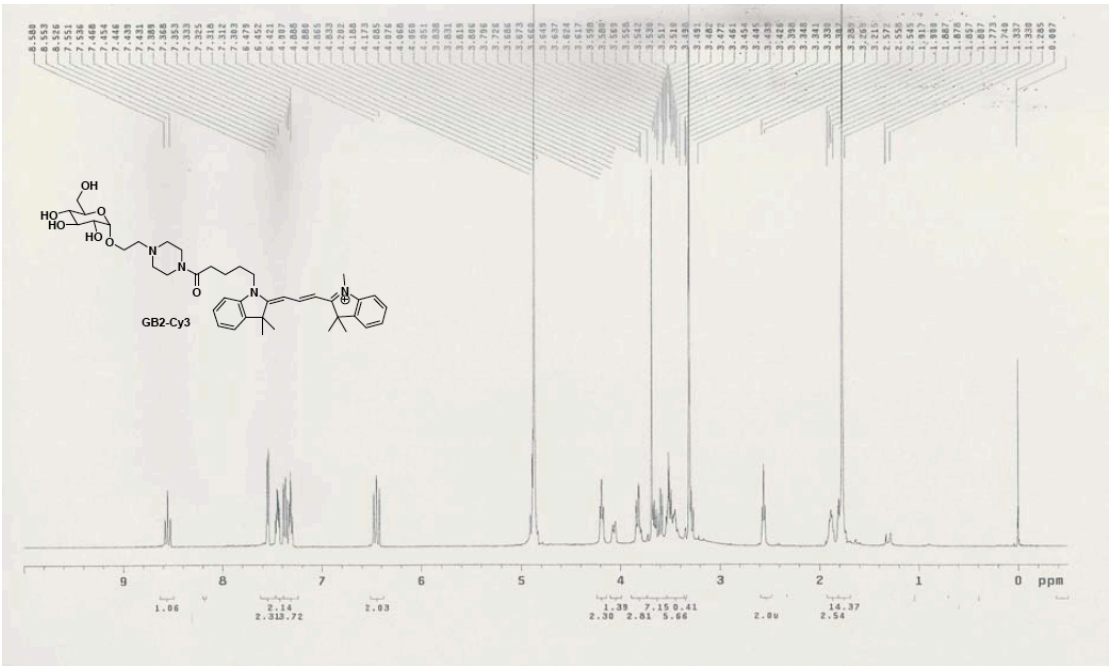
GB2-Cy3
9
8
7
6
5
4
3
2
1
0
ppm


GB2-Cy3
180
160
140
120
100
80
60
40
20
ppm

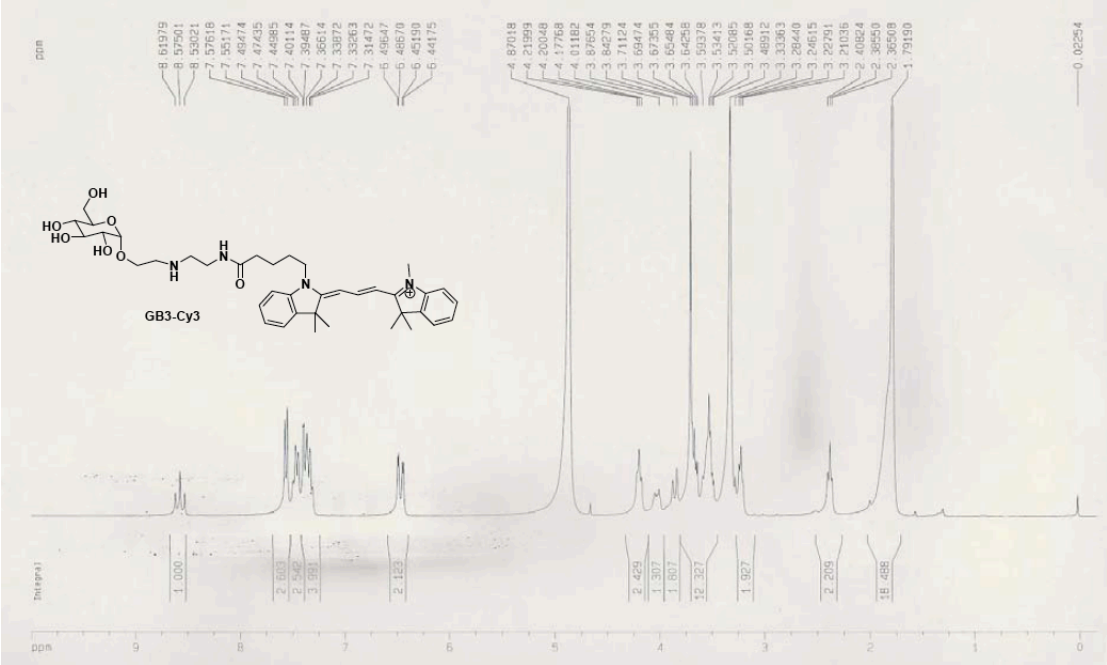
GB3-Cy3

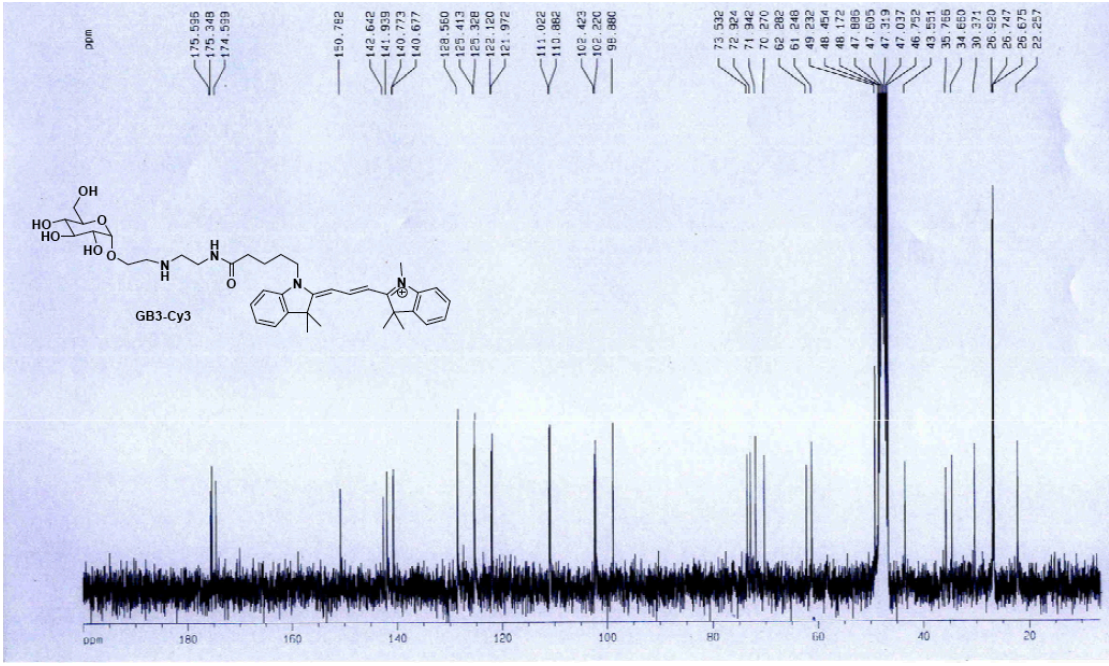
GB3-Cy3

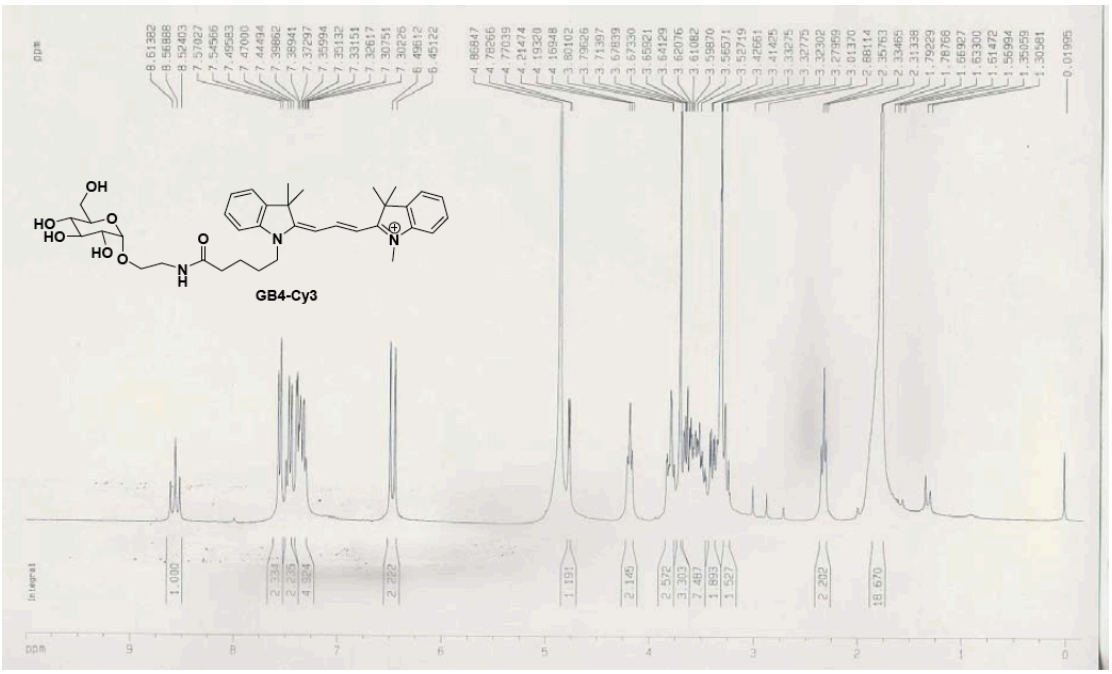
GB4-Cy3

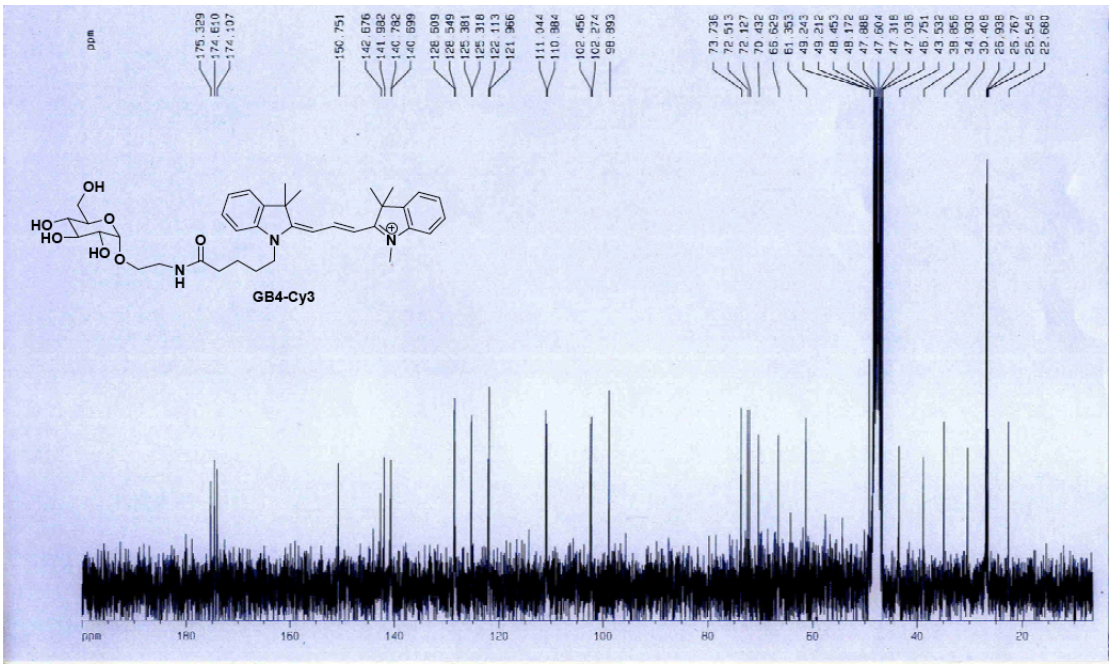
GB4-Cy3

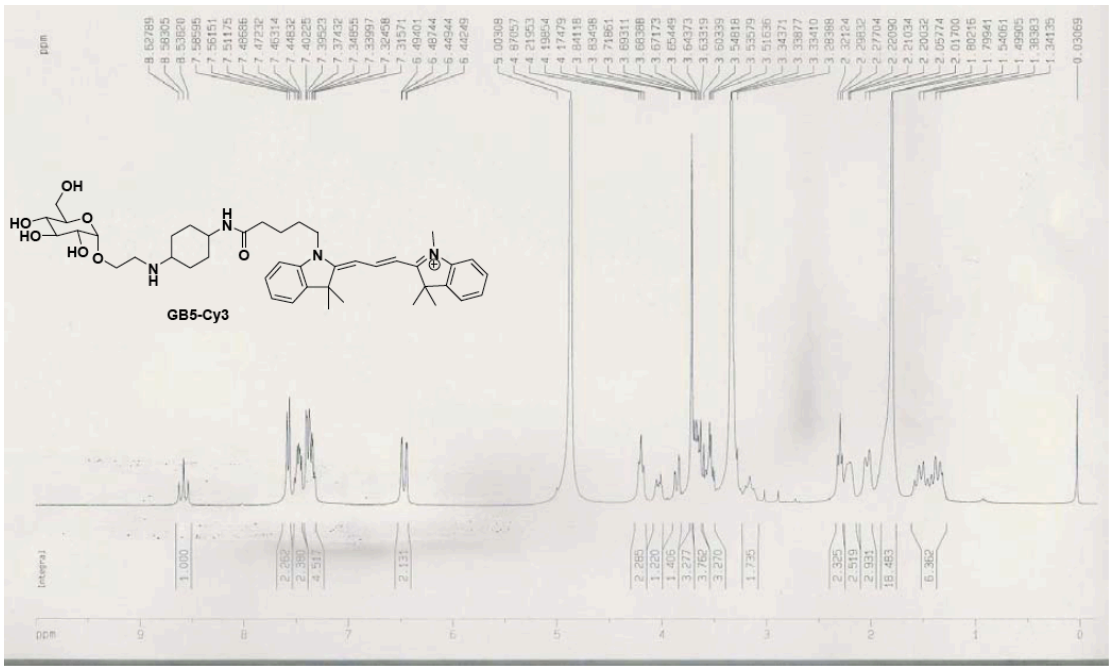
GB5-Cy3

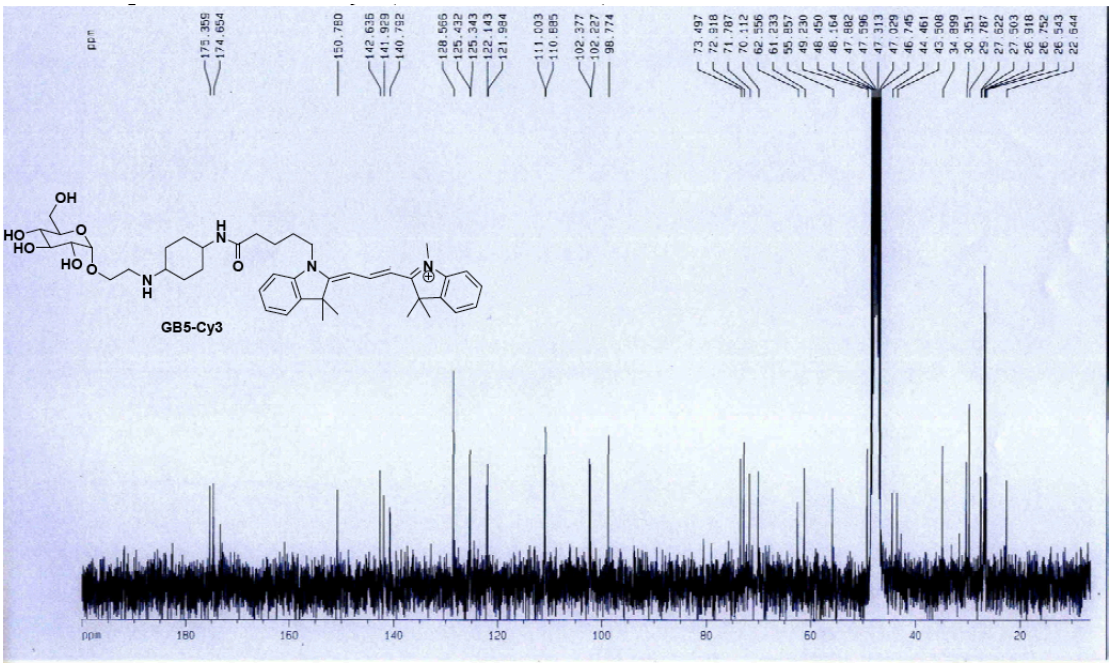
GB5-Cy3

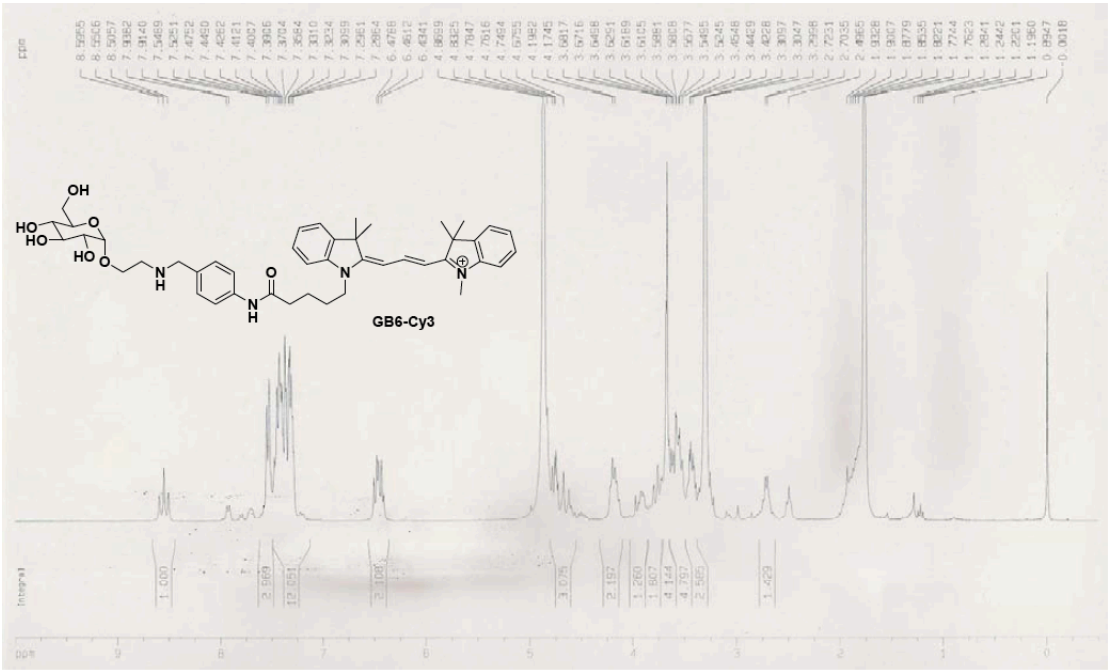
GB6-Cy3

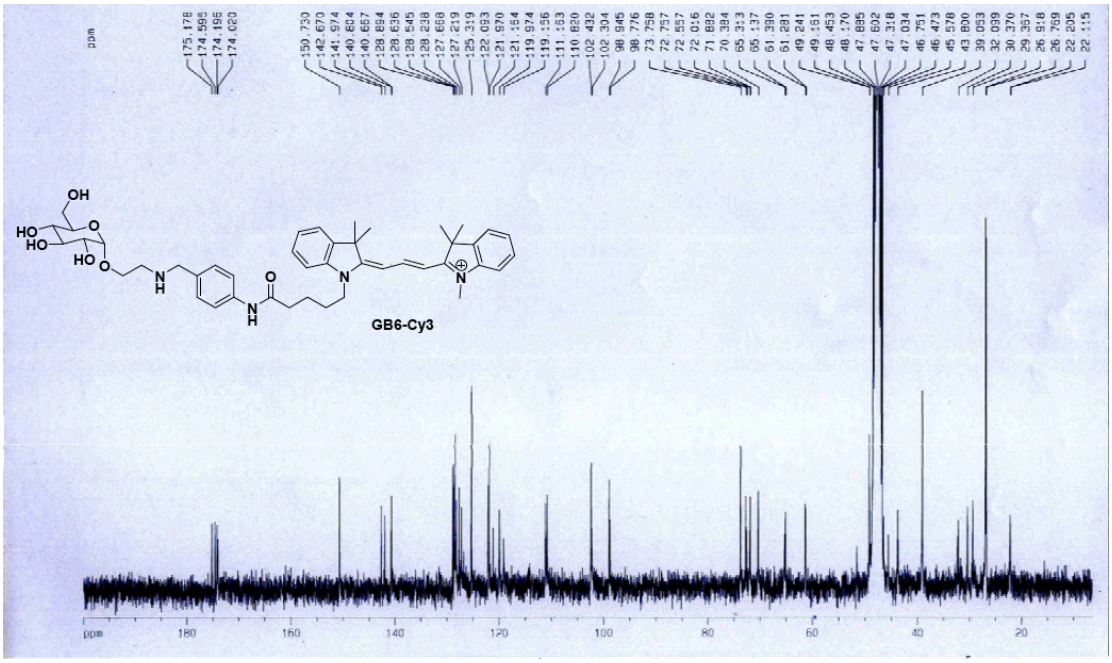
GB6-Cy3

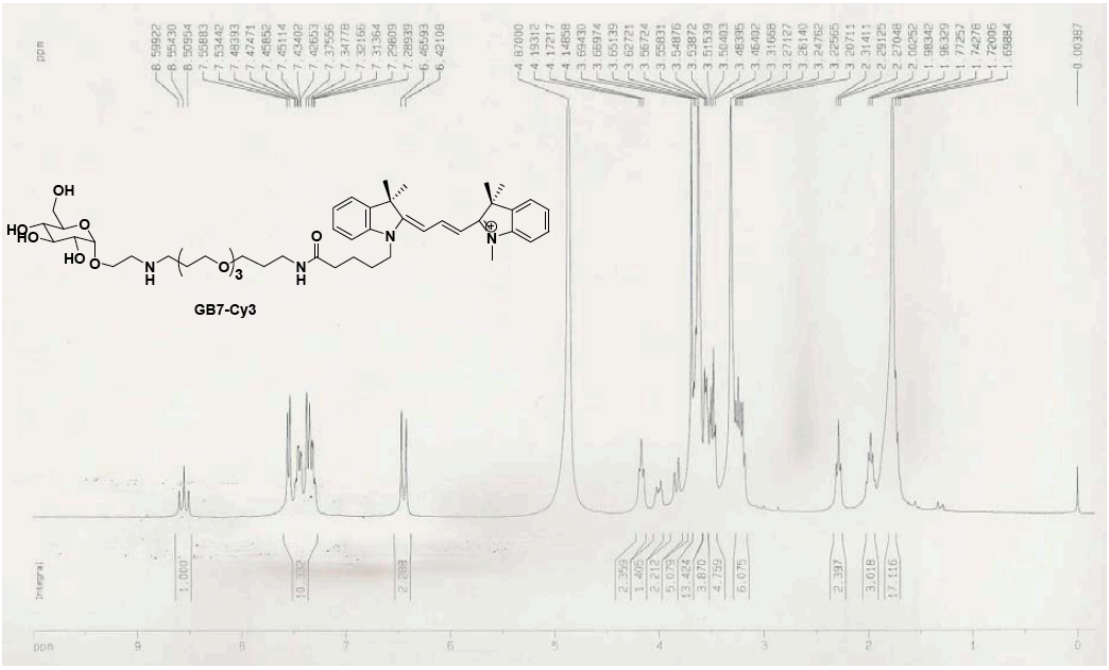
GB7-Cy3

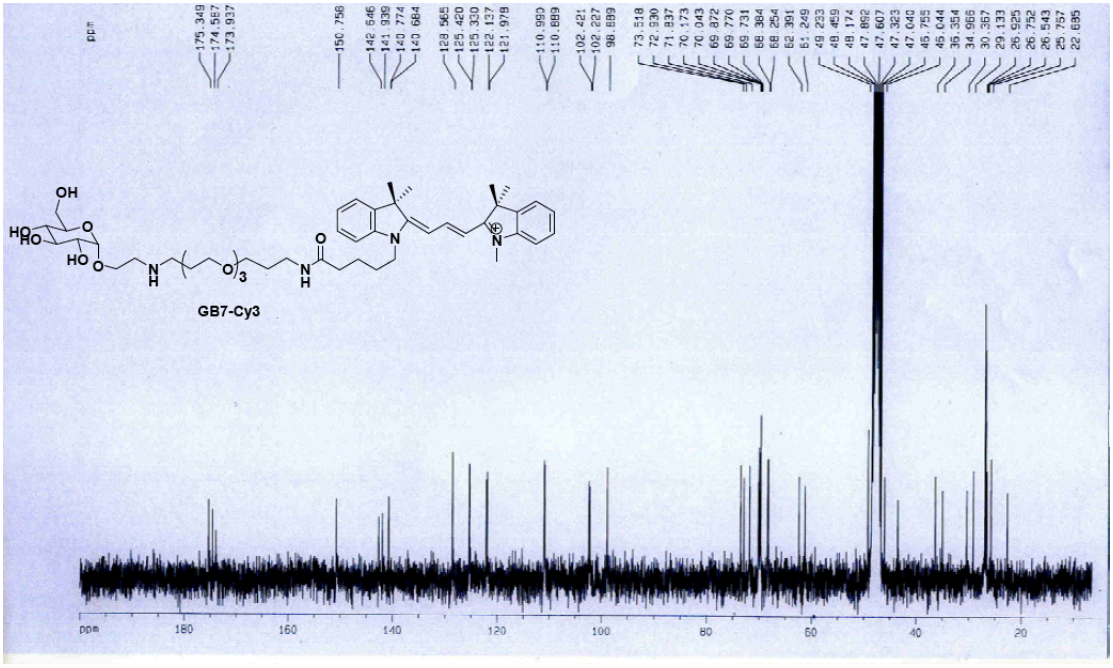
GB7-Cy3

Chapter 4. Development of a Two-Photon Tracer for Glucose Uptake and its application in live tissues

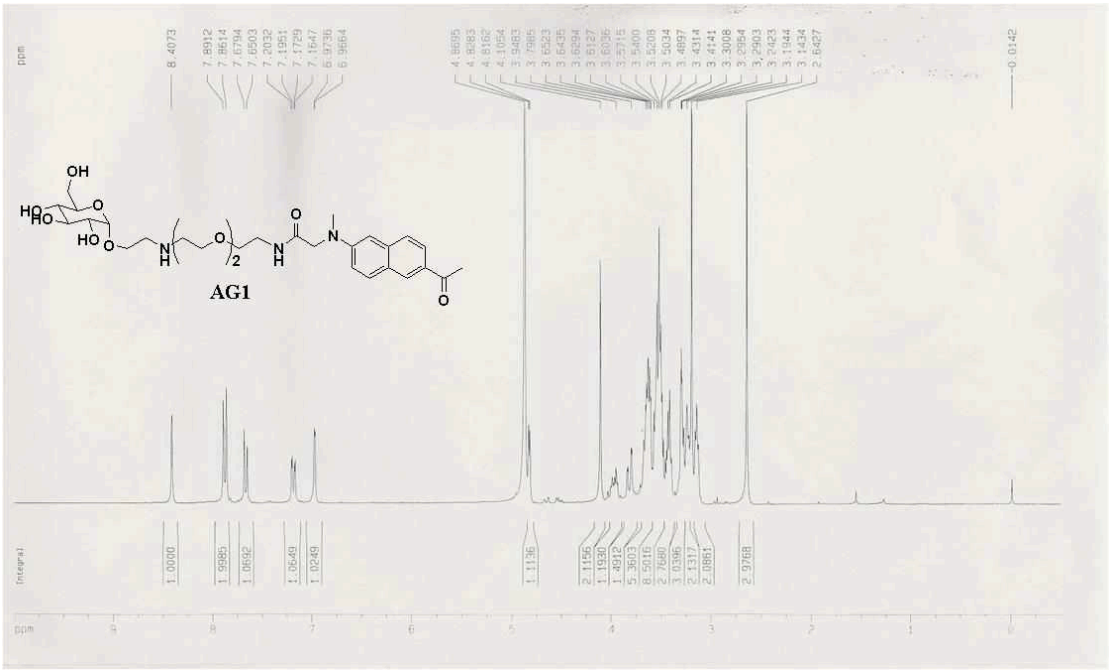
AG1

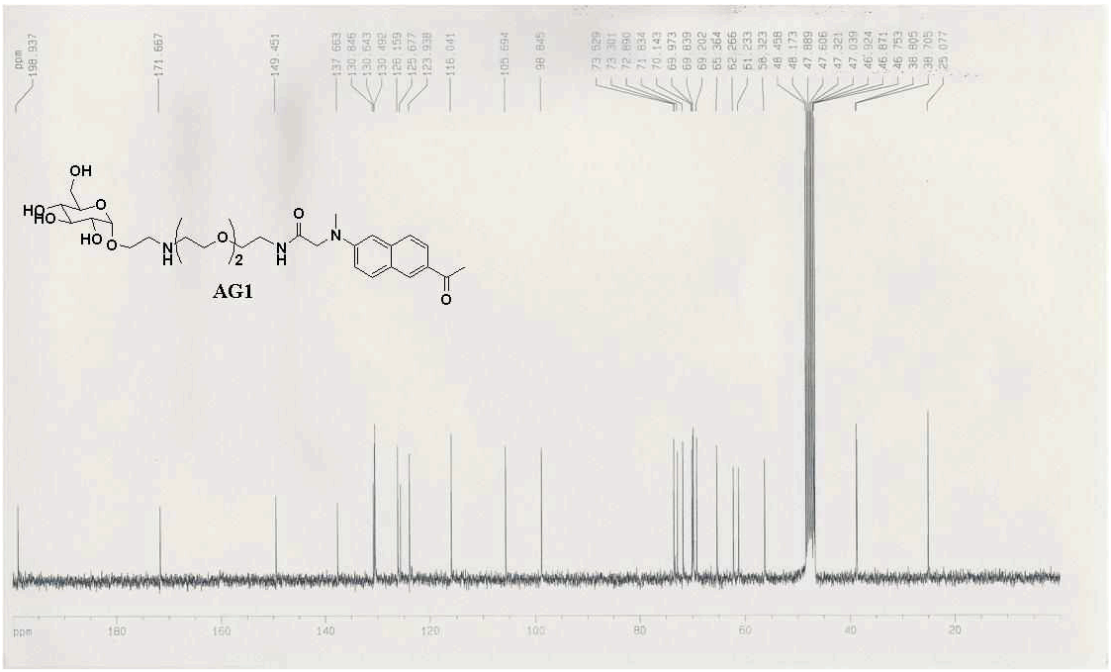
AG1

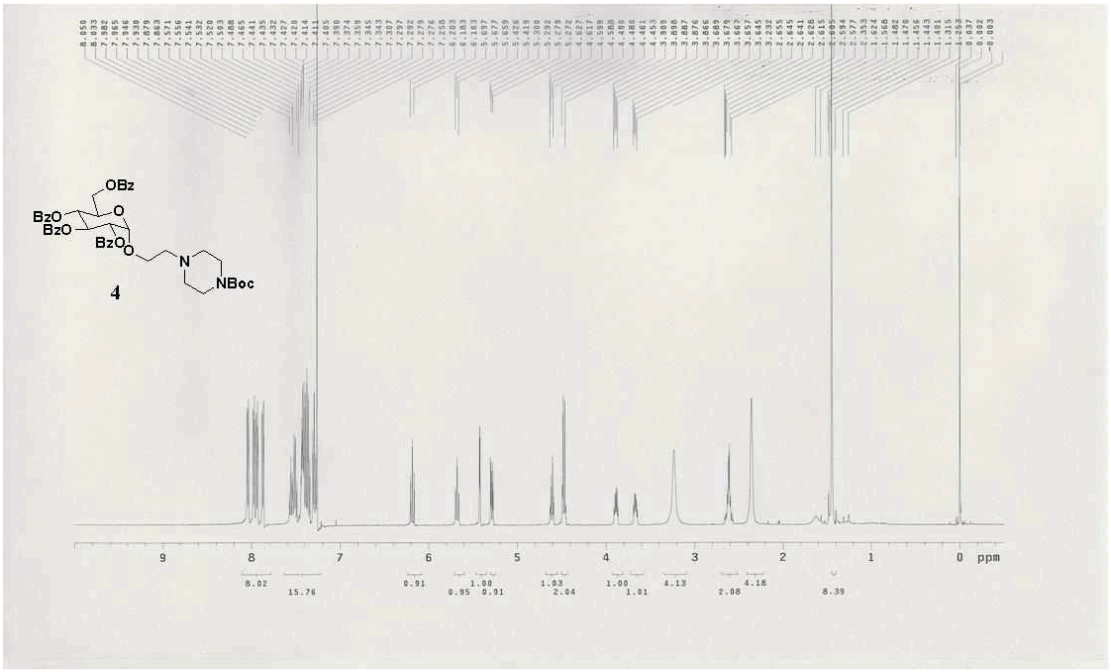
OBz
BzO
BzO
BzO
O
N
NBoc
4
ppm

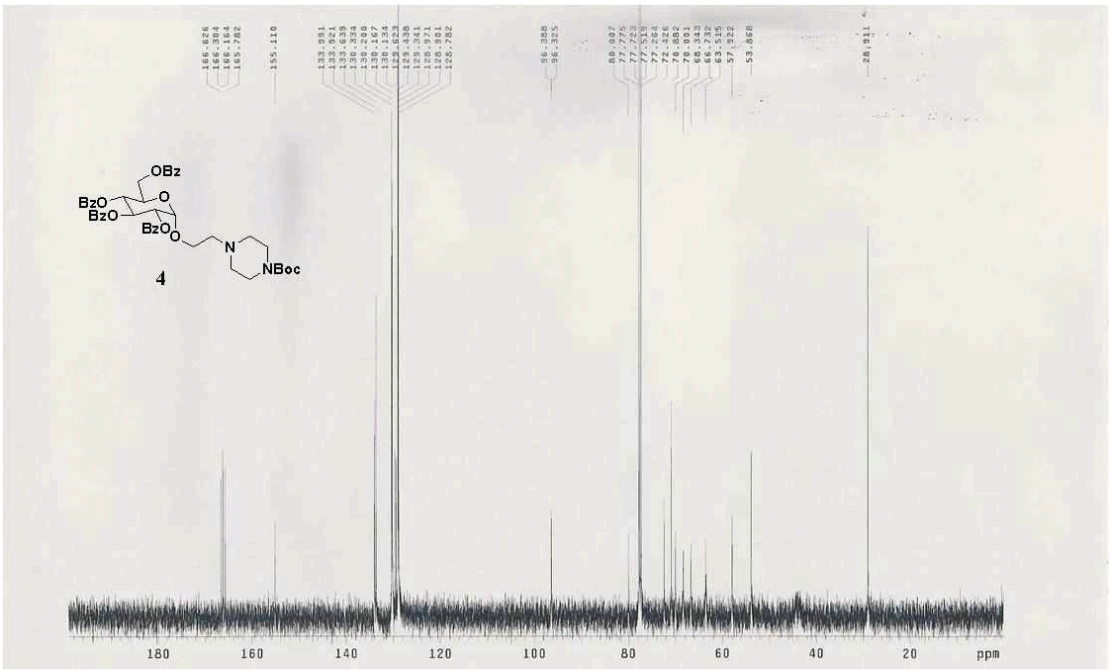
OBz
BzO
BzO
BzO
O
N
NBoc
4
ppm

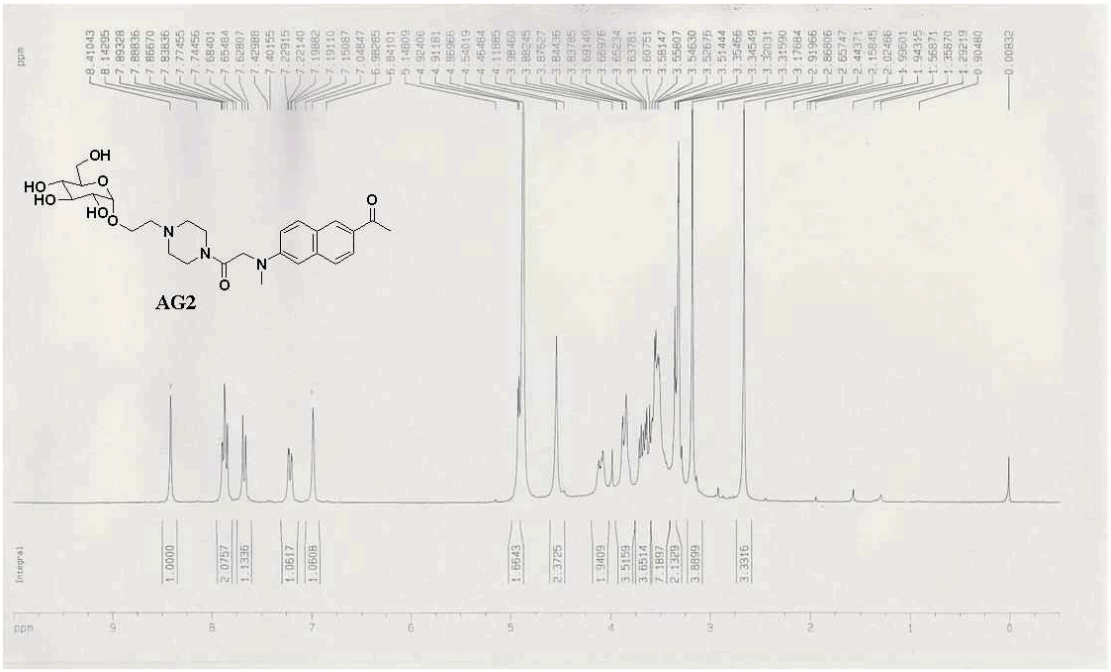
AG2

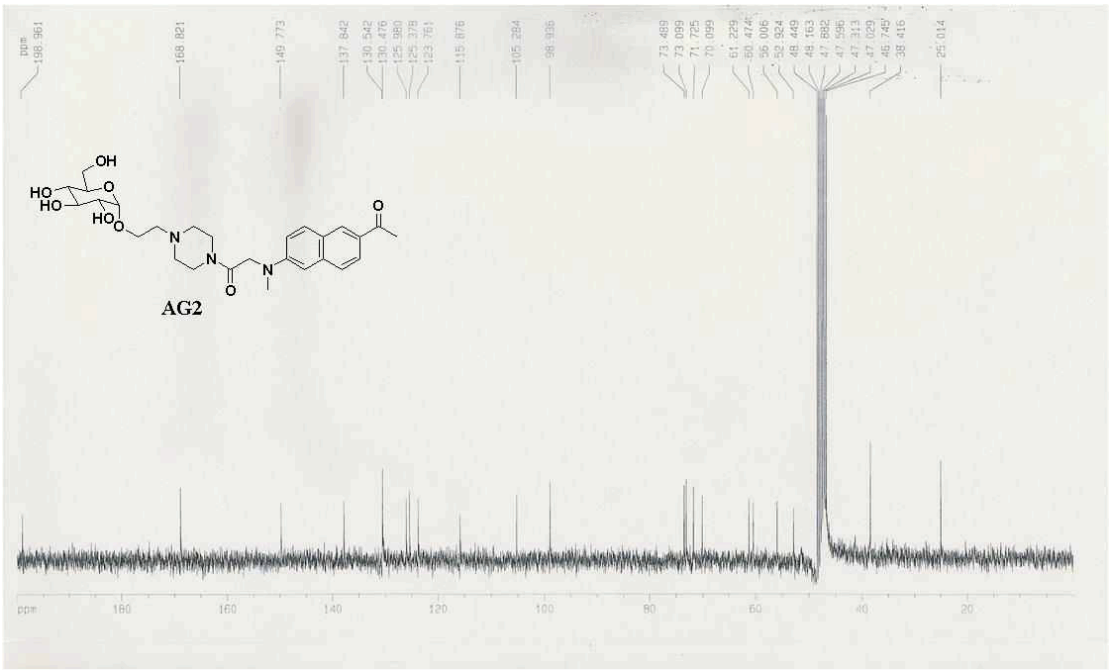
AG2

Part II

Screening and Target Identification of Bioactive Small molecules

Chapter 1. Screening of a Benzopyran-Containing Androgen Receptor Antagonist to Treat Antiandrogen-Resistant Prostate Cancer

6a

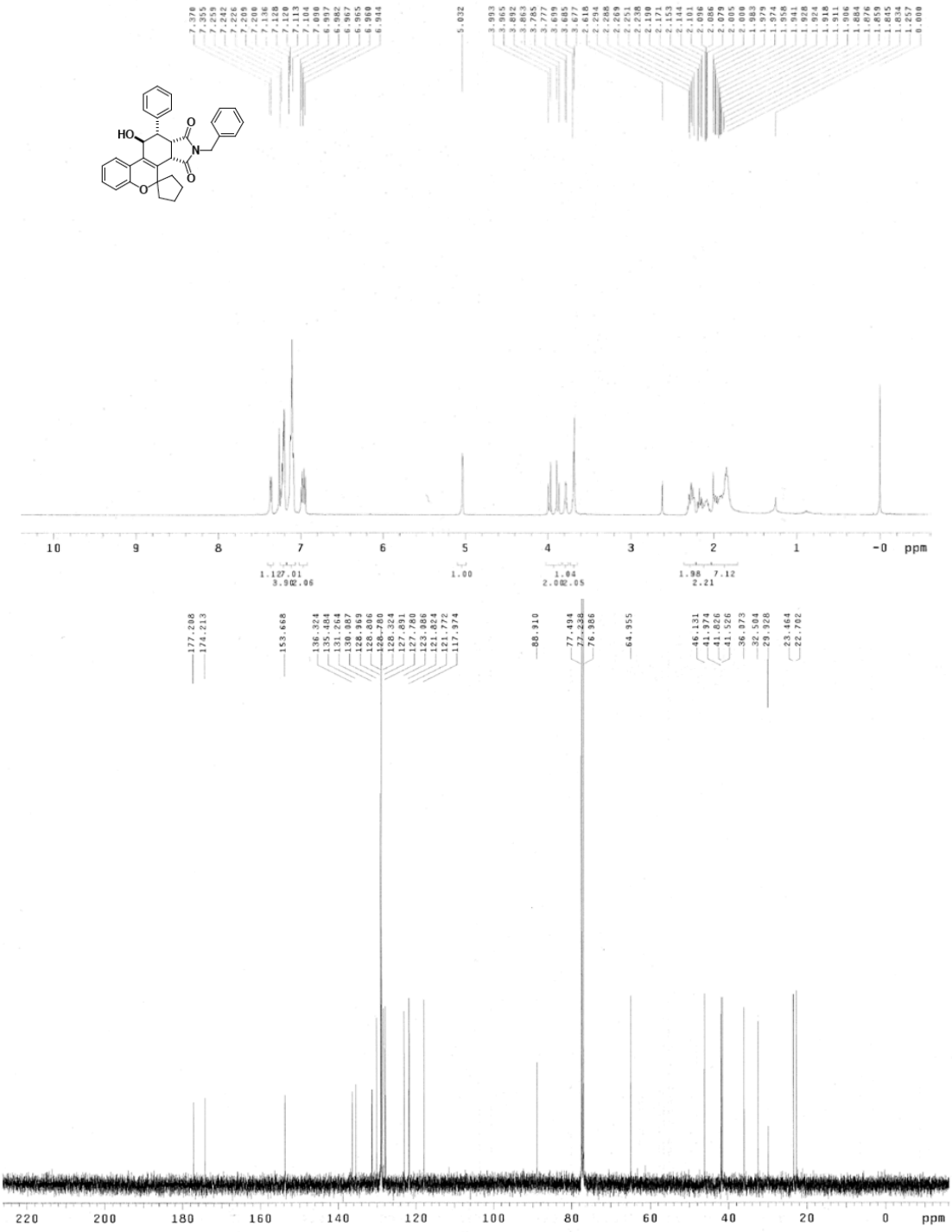
HO
O
N
O
O
10
9
8
7
6
5
4
3
2
1
-0
ppm
220
200
180
160
140
120
100
80
60
40
20
0
ppm

6b

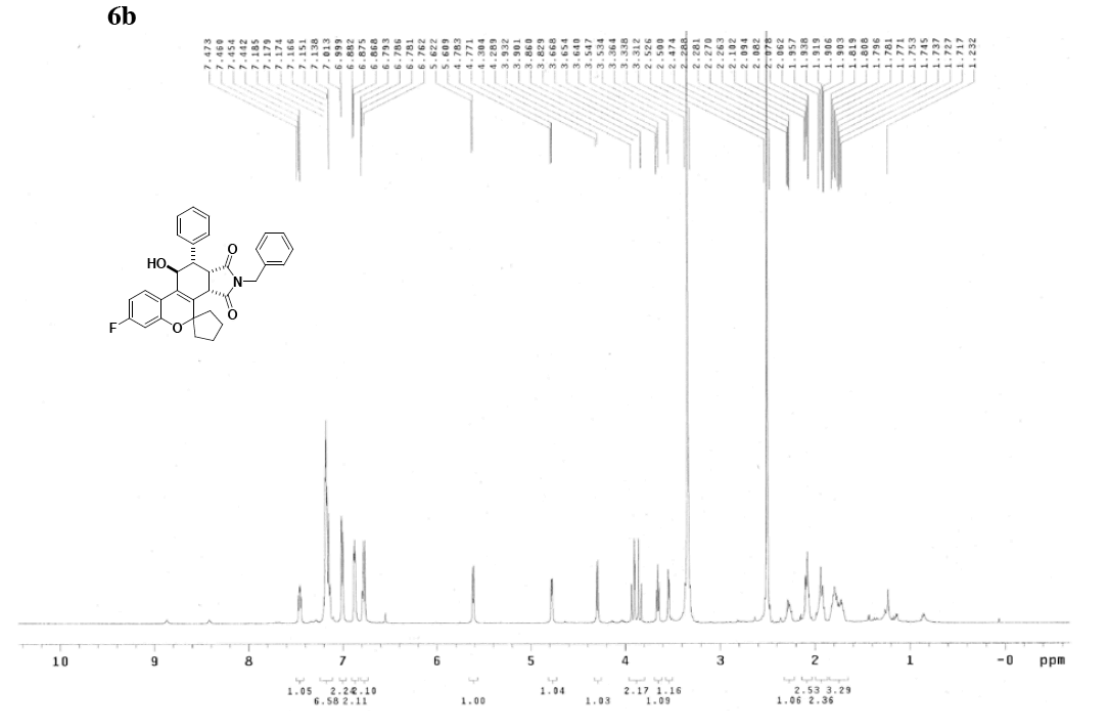
HO
O
N
O
F
O
10
9
8
7
6
5
4
3
2
1
-0
ppm

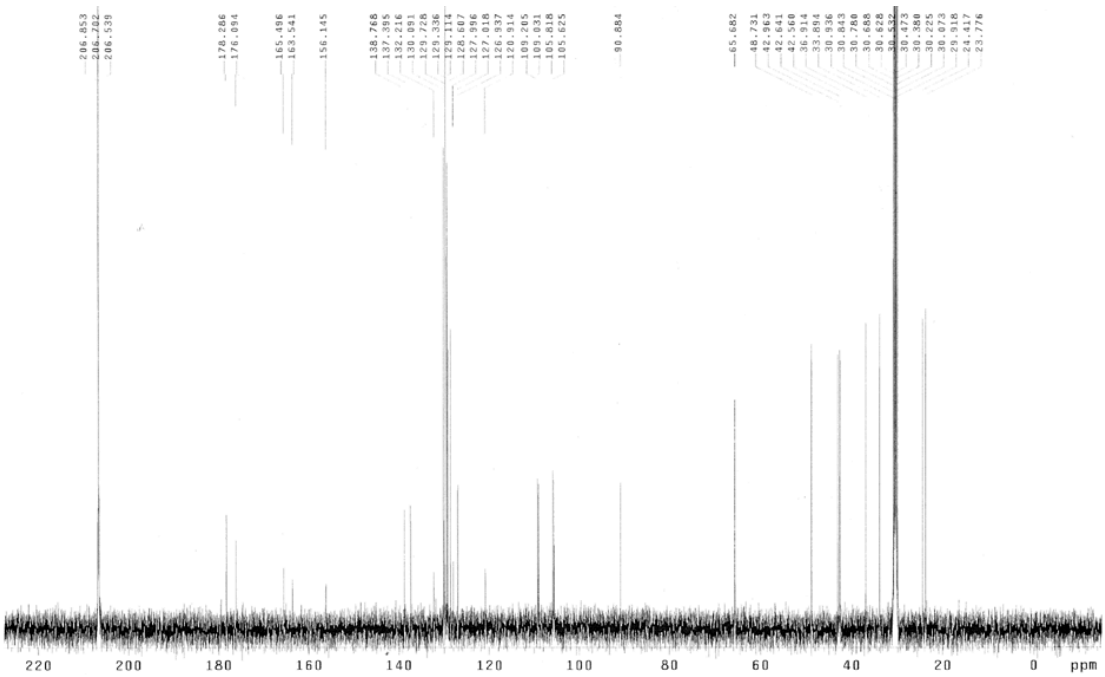
220
200
180
160
140
120
100
80
60
40
20
0
ppm

6c

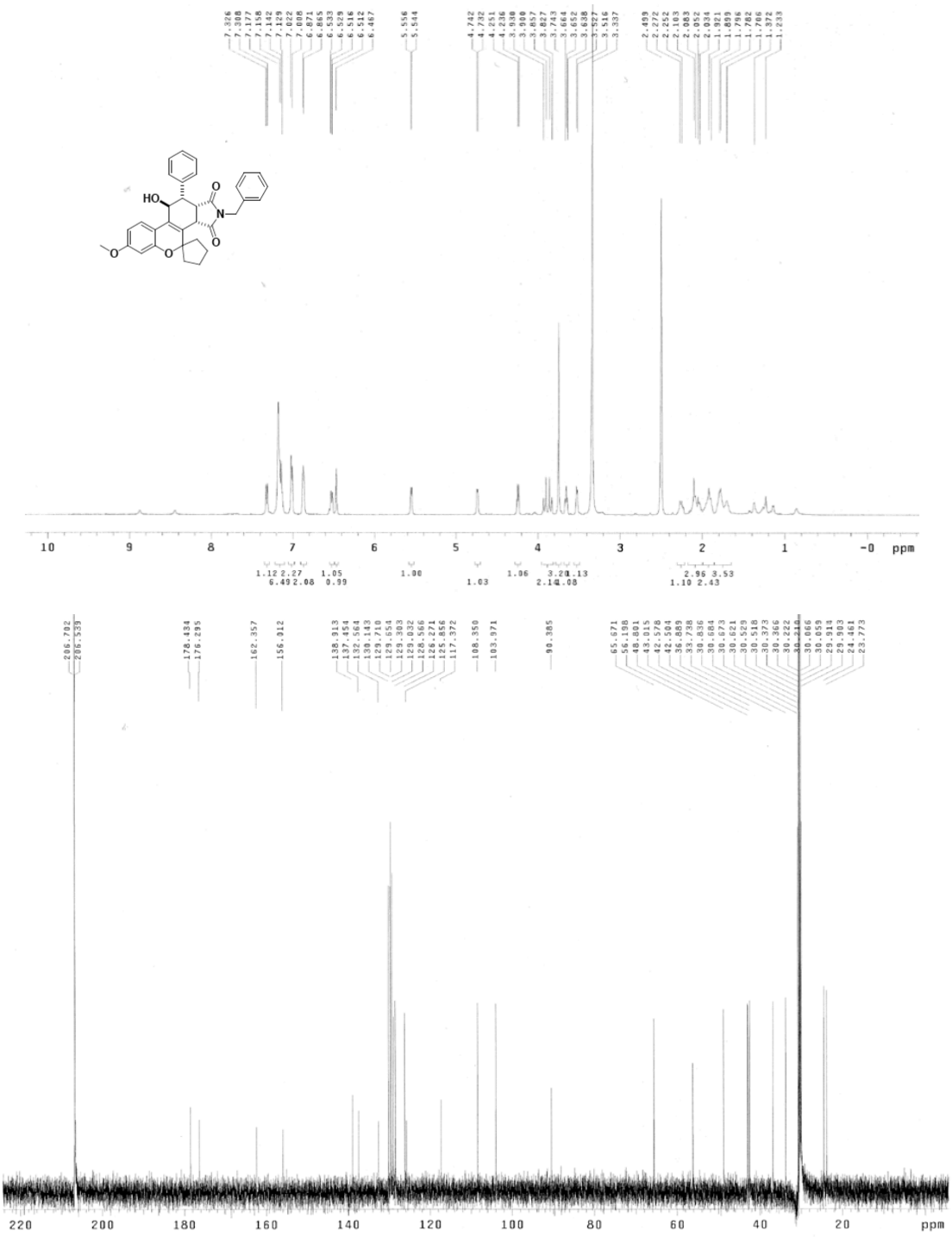
HO
O
N
O
O
O
10
9
8
7
6
5
4
3
2
1
-0
ppm
220
200
180
160
140
120
100
80
60
40
20
ppm

6d

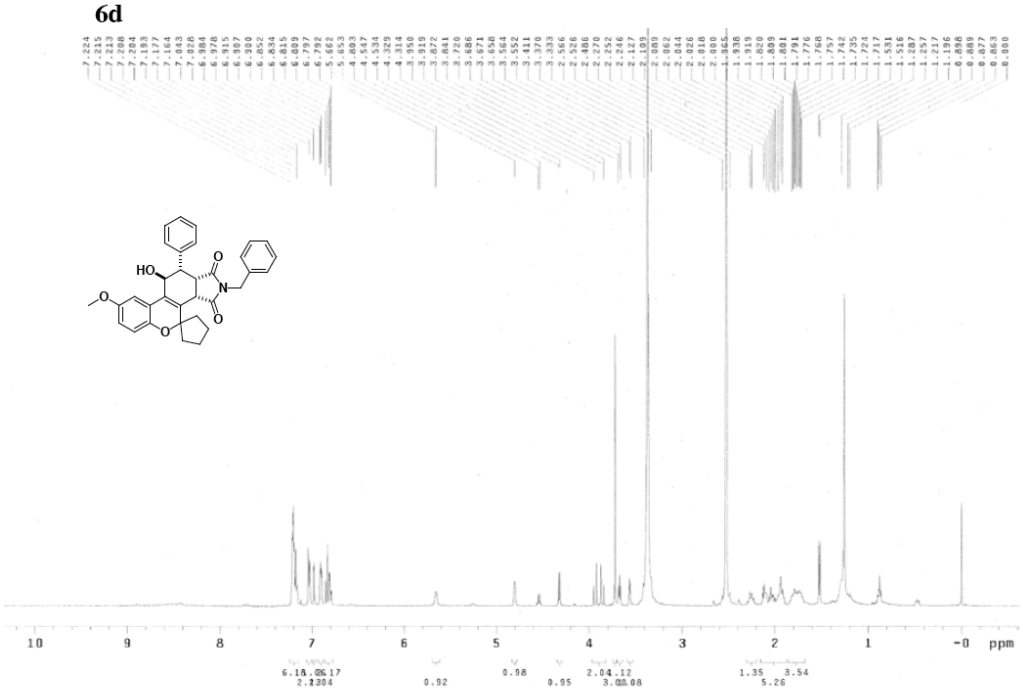
HO
O
N
O
O
O
10
9
8
7
6
5
4
3
2
1
0
ppm

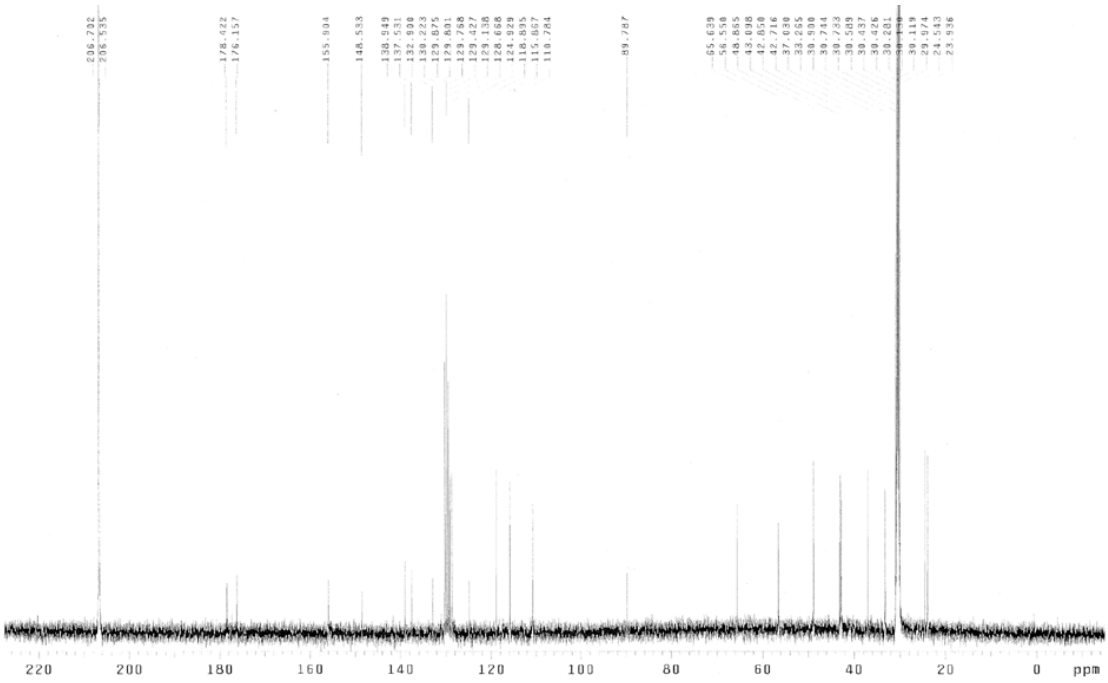
220
200
180
160
140
120
100
80
60
40
20
0
ppm

6e

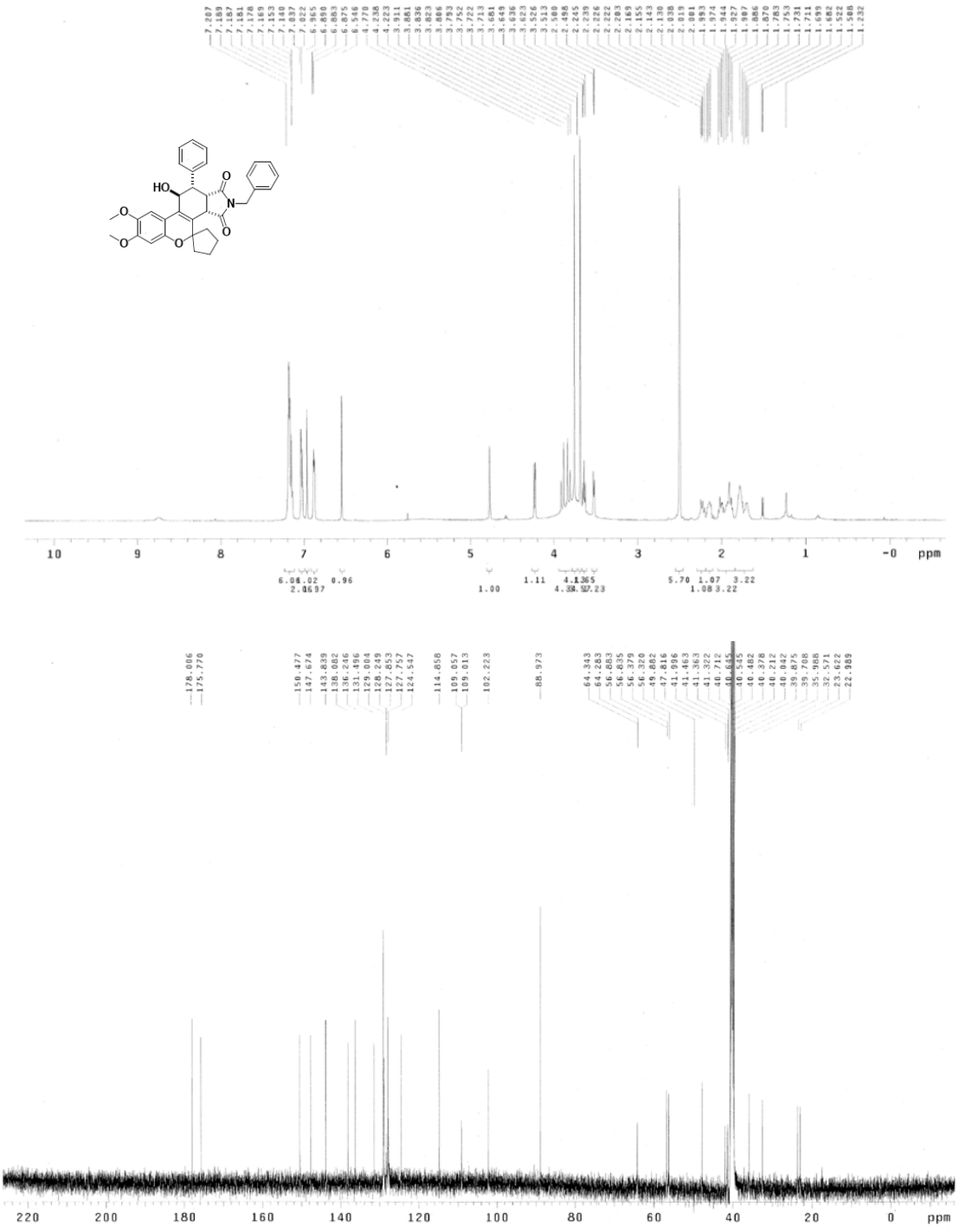

6f

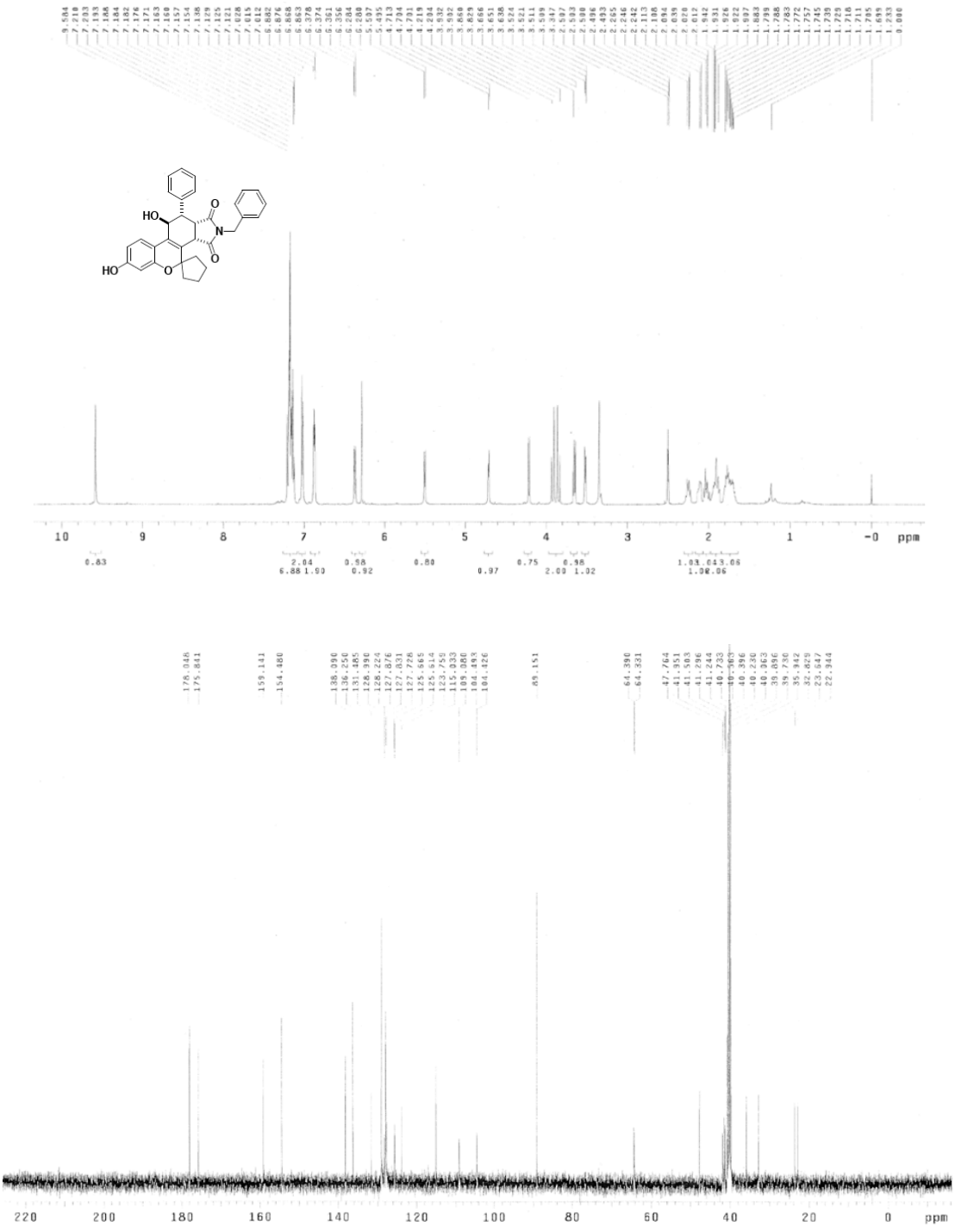

6g

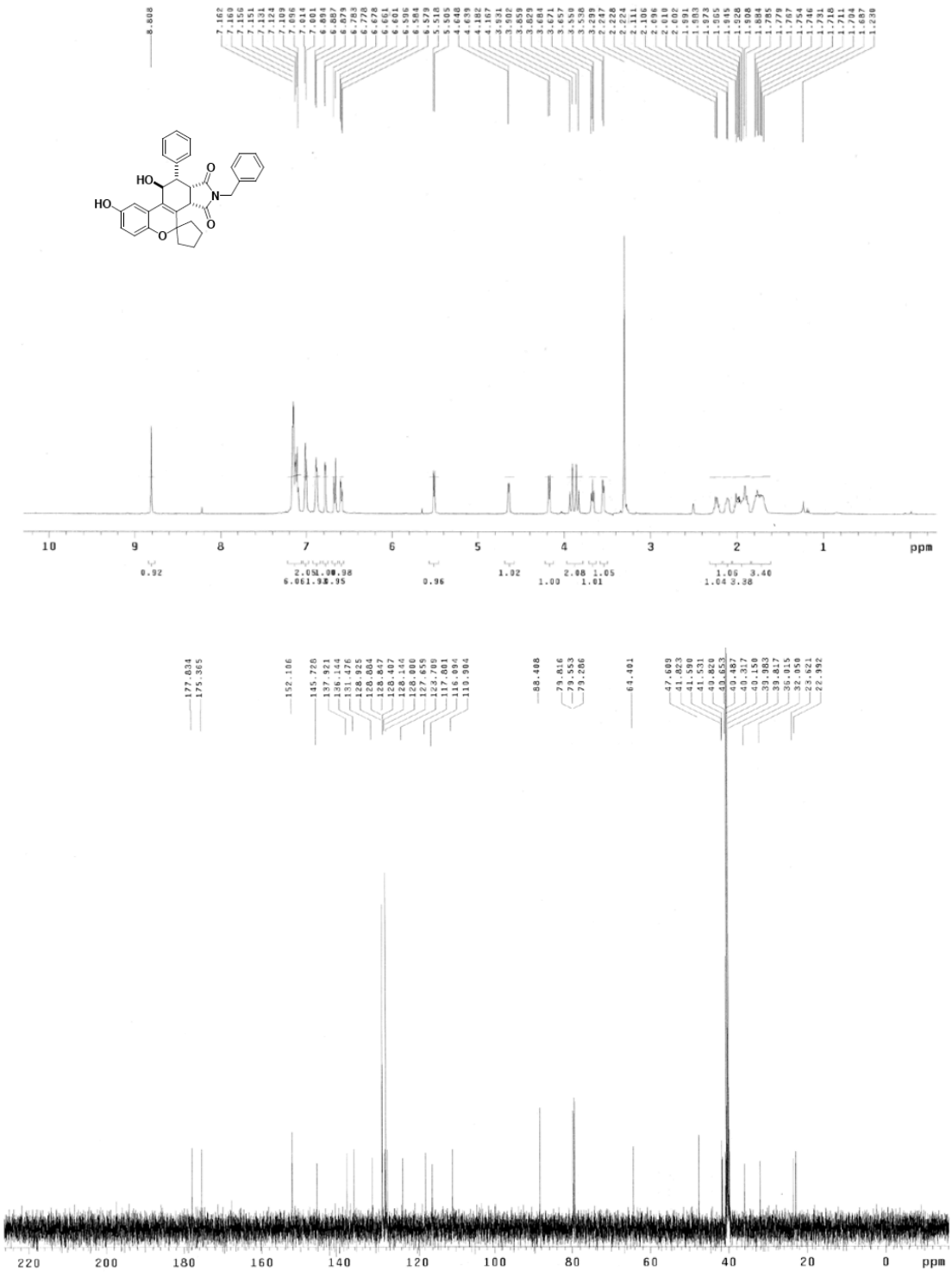

6h

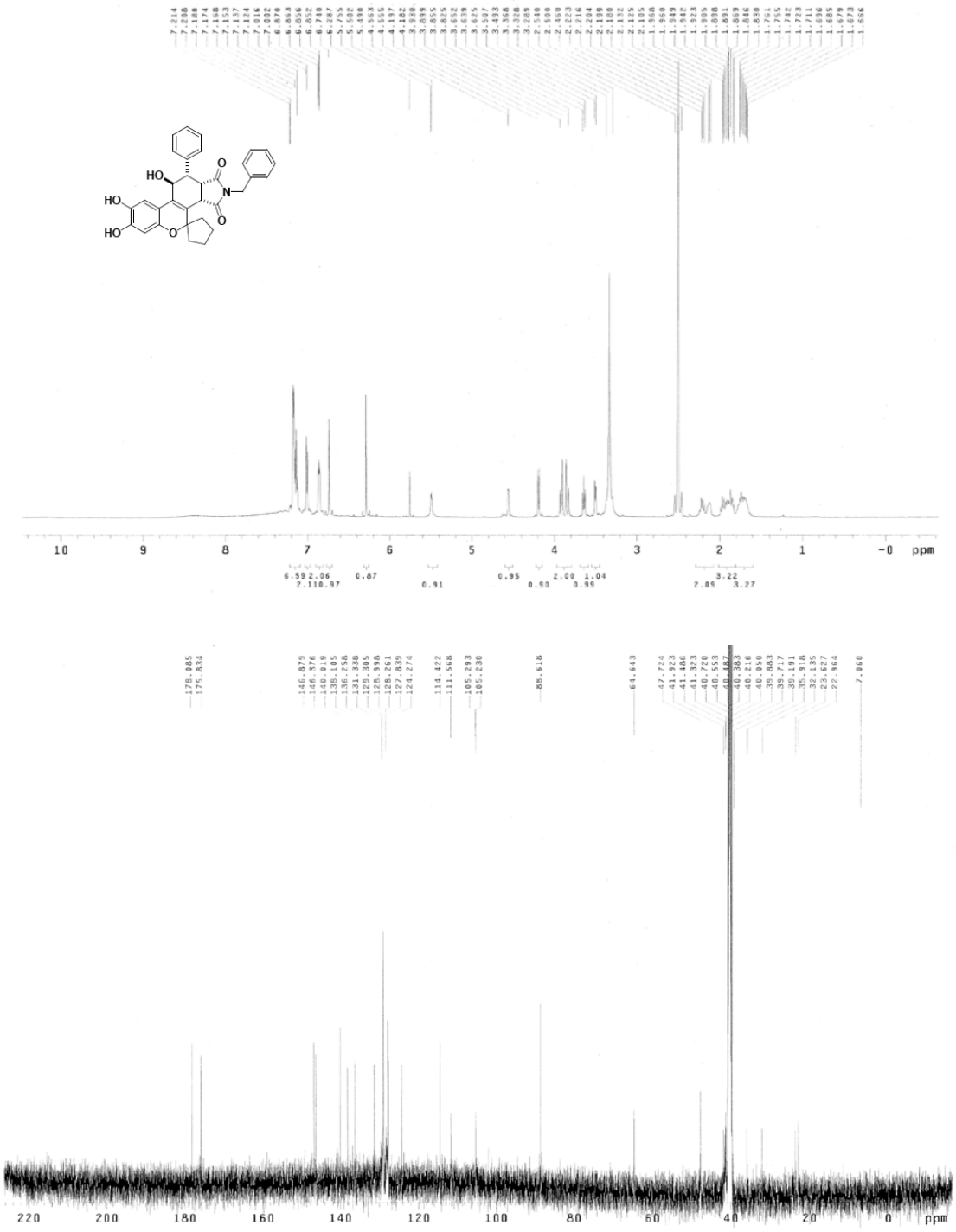

6i

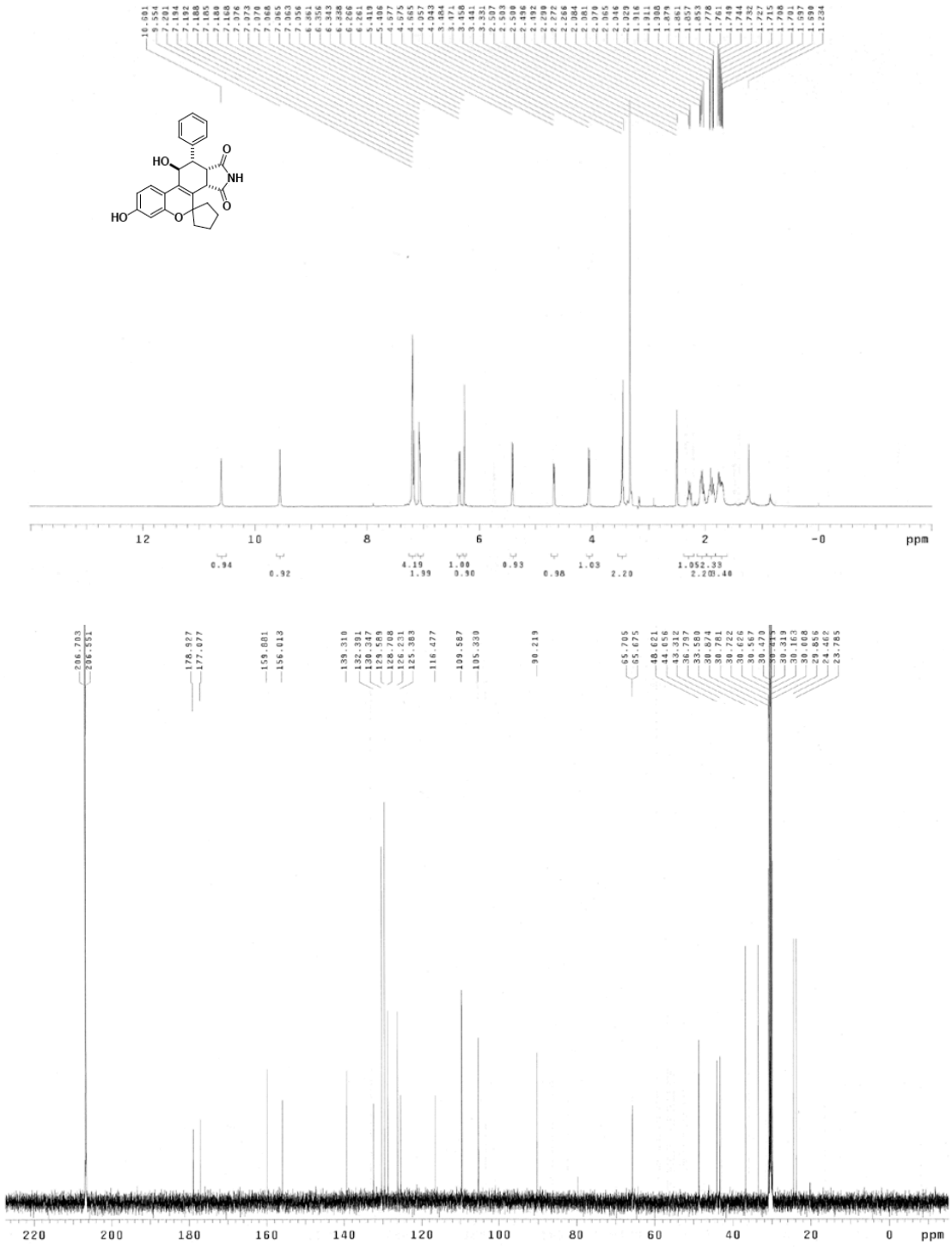
HO
O
NH
O
HO
O
12
10
8
6
4
2
-0
ppm
220
200
180
160
140
120
100
80
60
40
20
0
ppm

6j

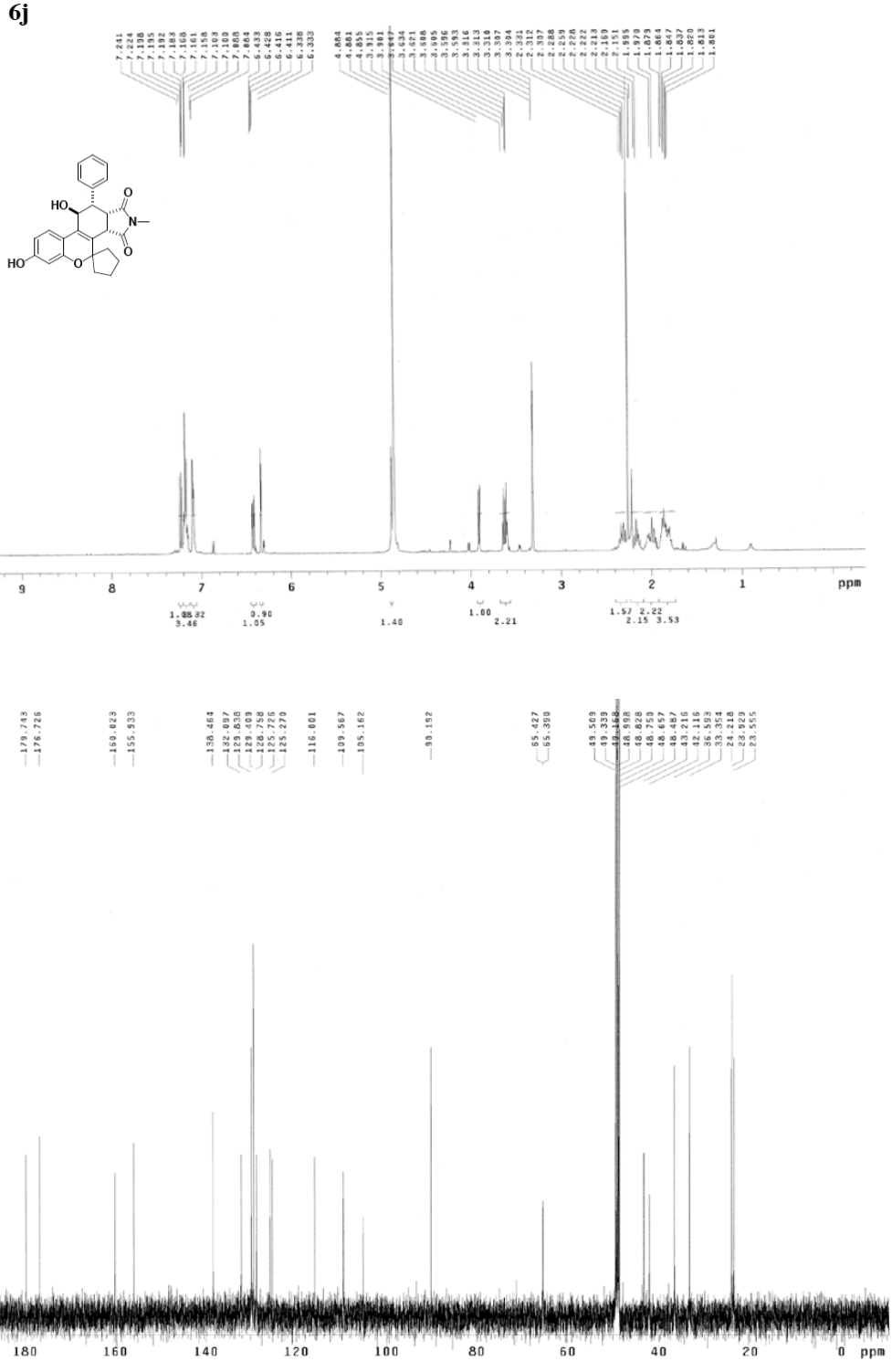

6k

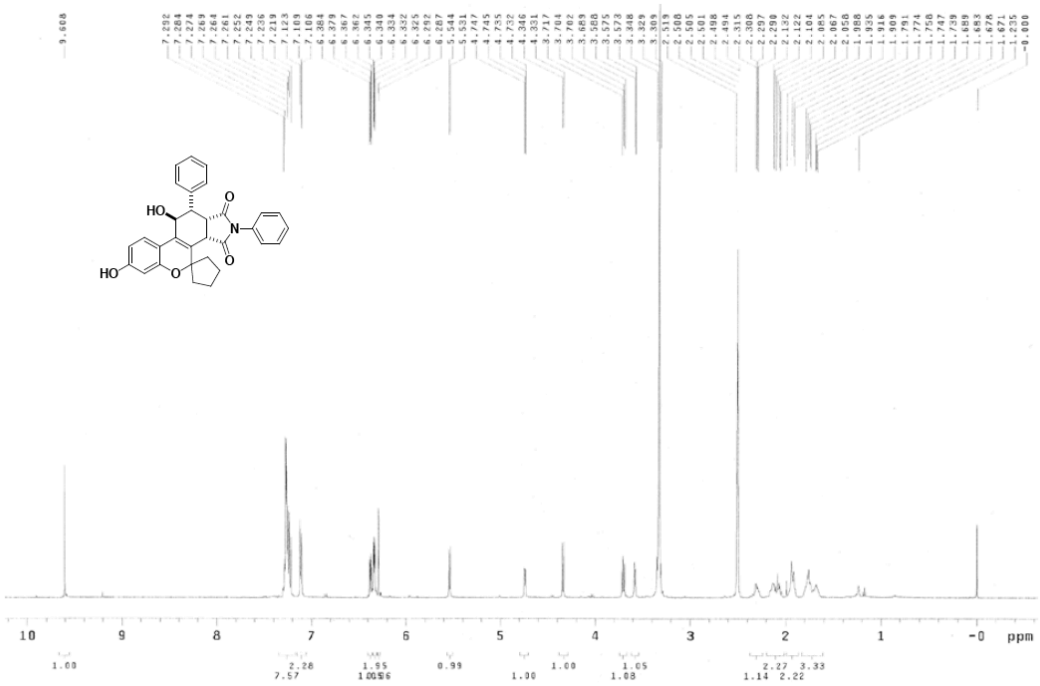
HO
O
N
O
HO
O
10
9
8
7
6
5
4
3
2
1
-0
ppm

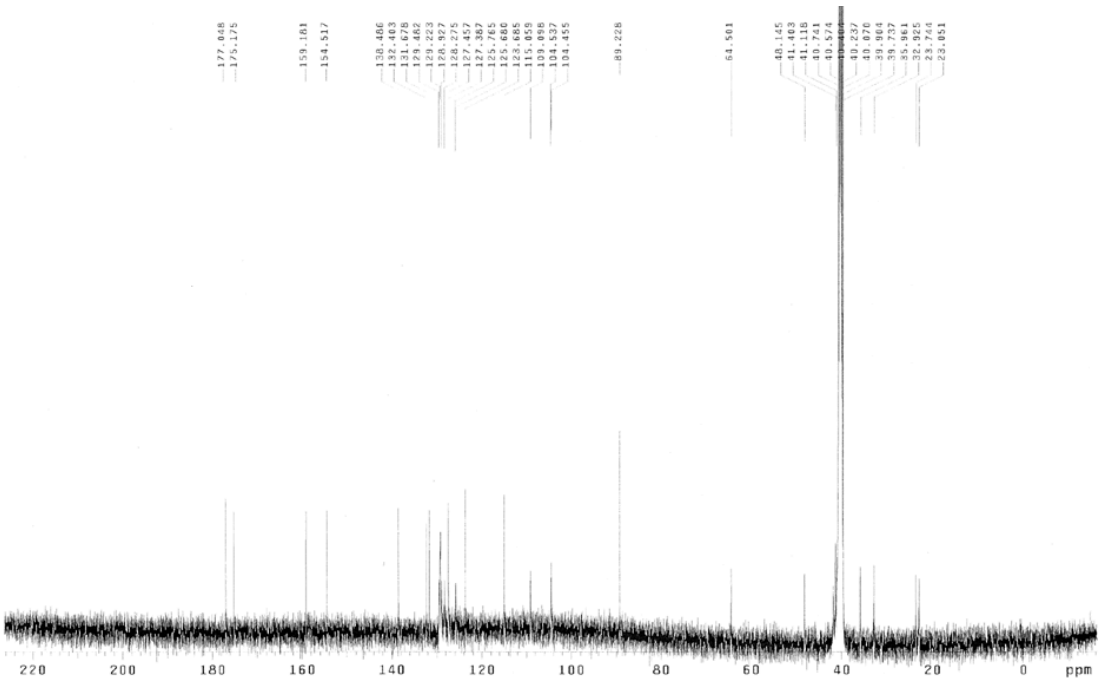
220
200
180
160
140
120
100
80
60
40
20
0
ppm

6l

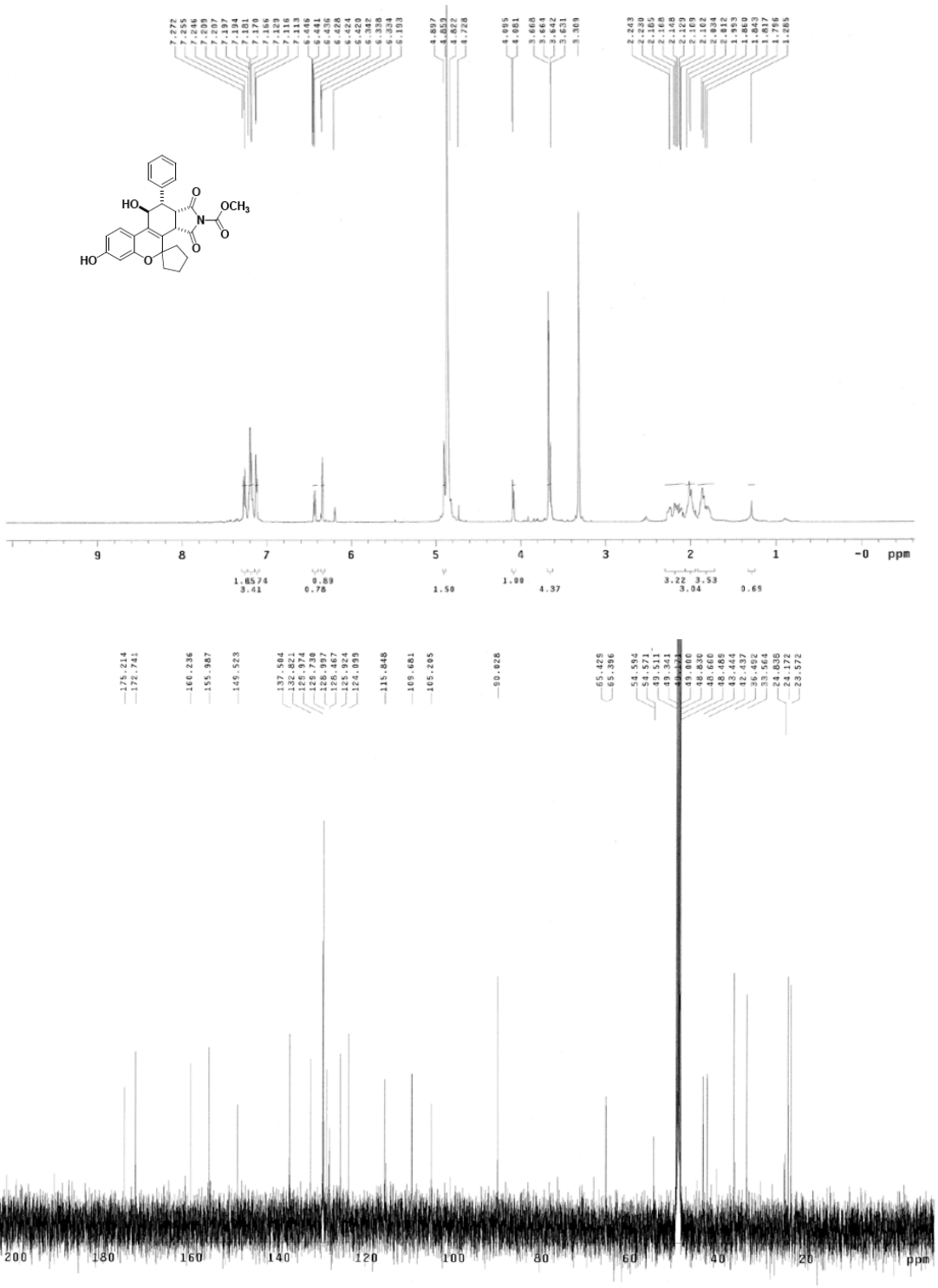

6m

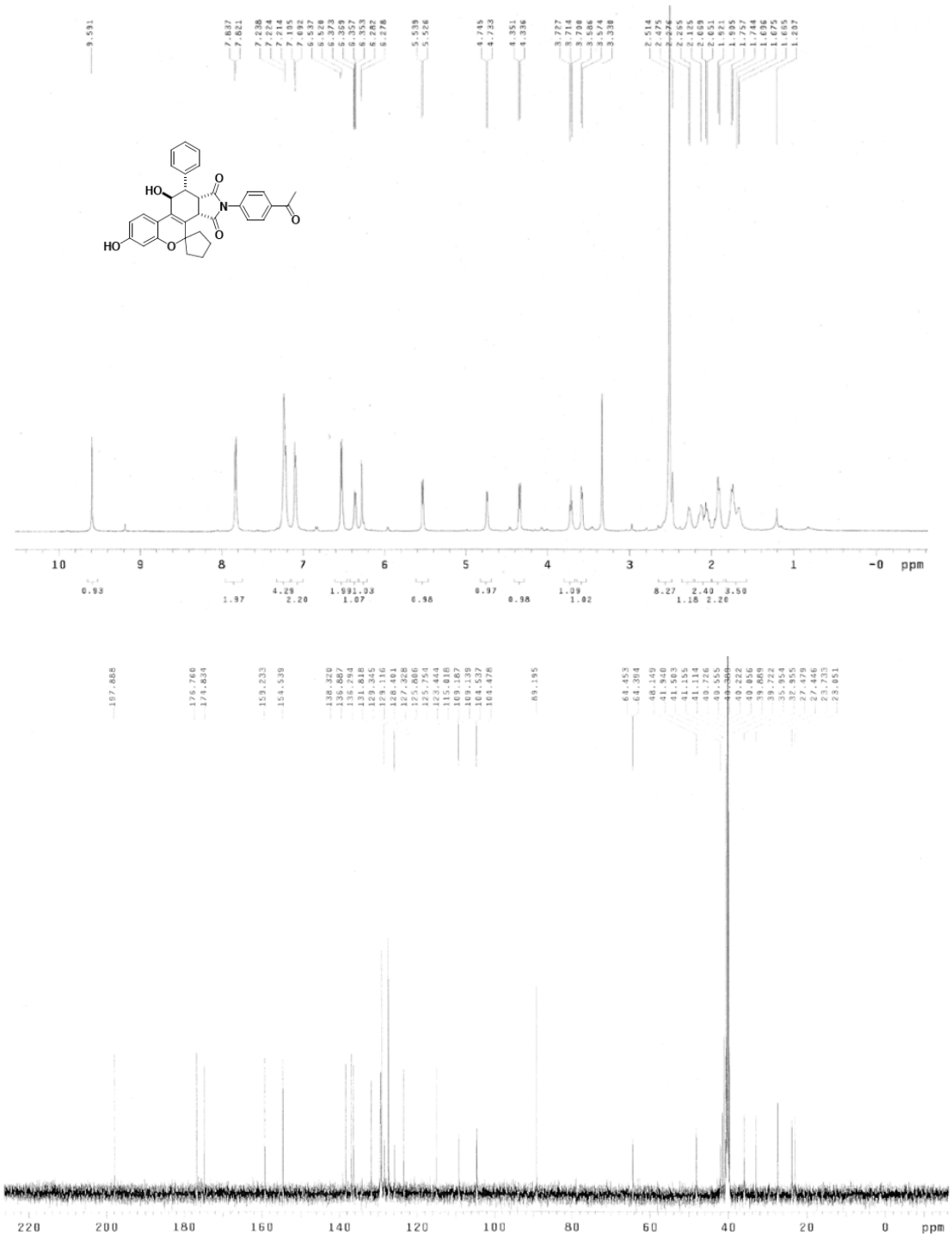

6n

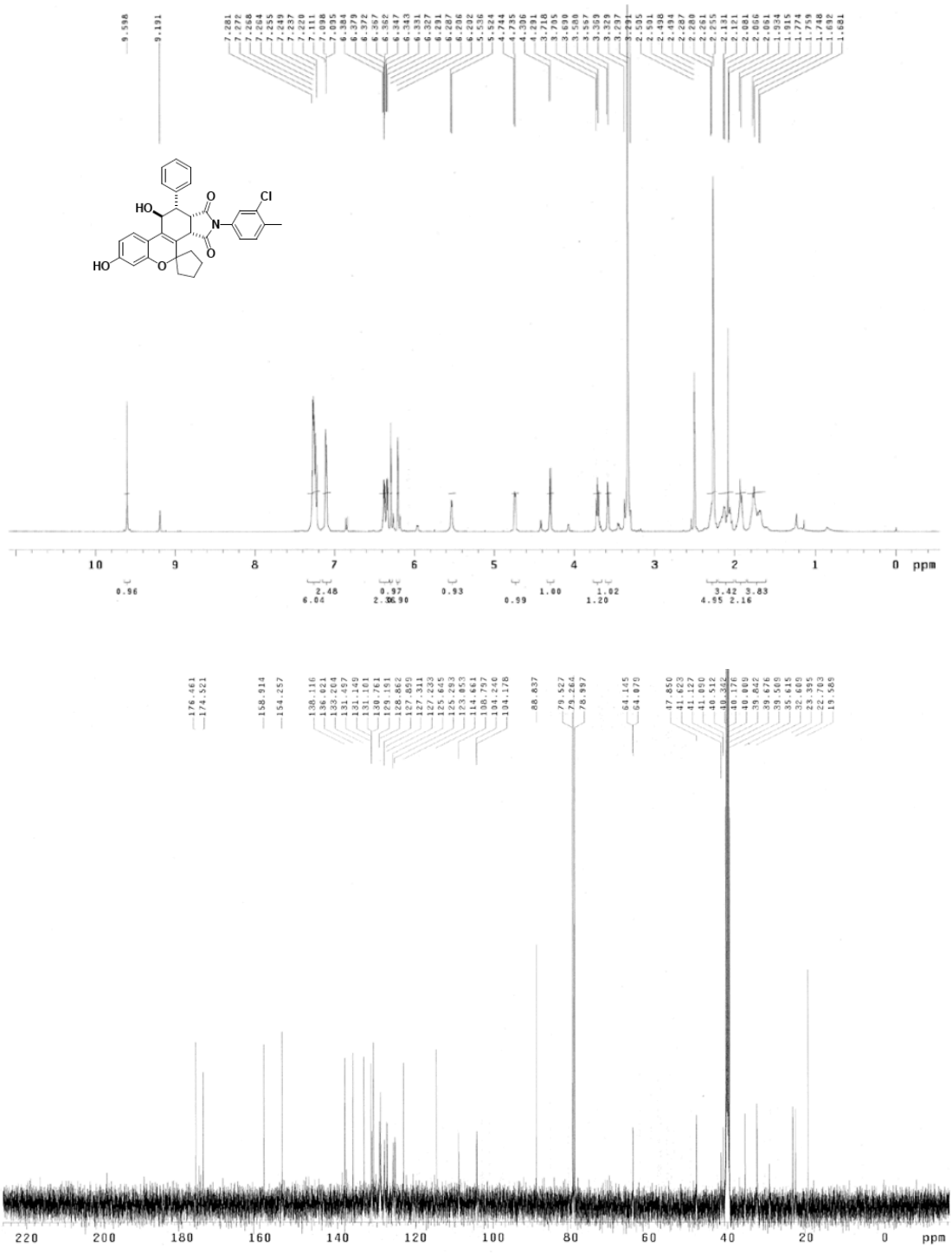

6o

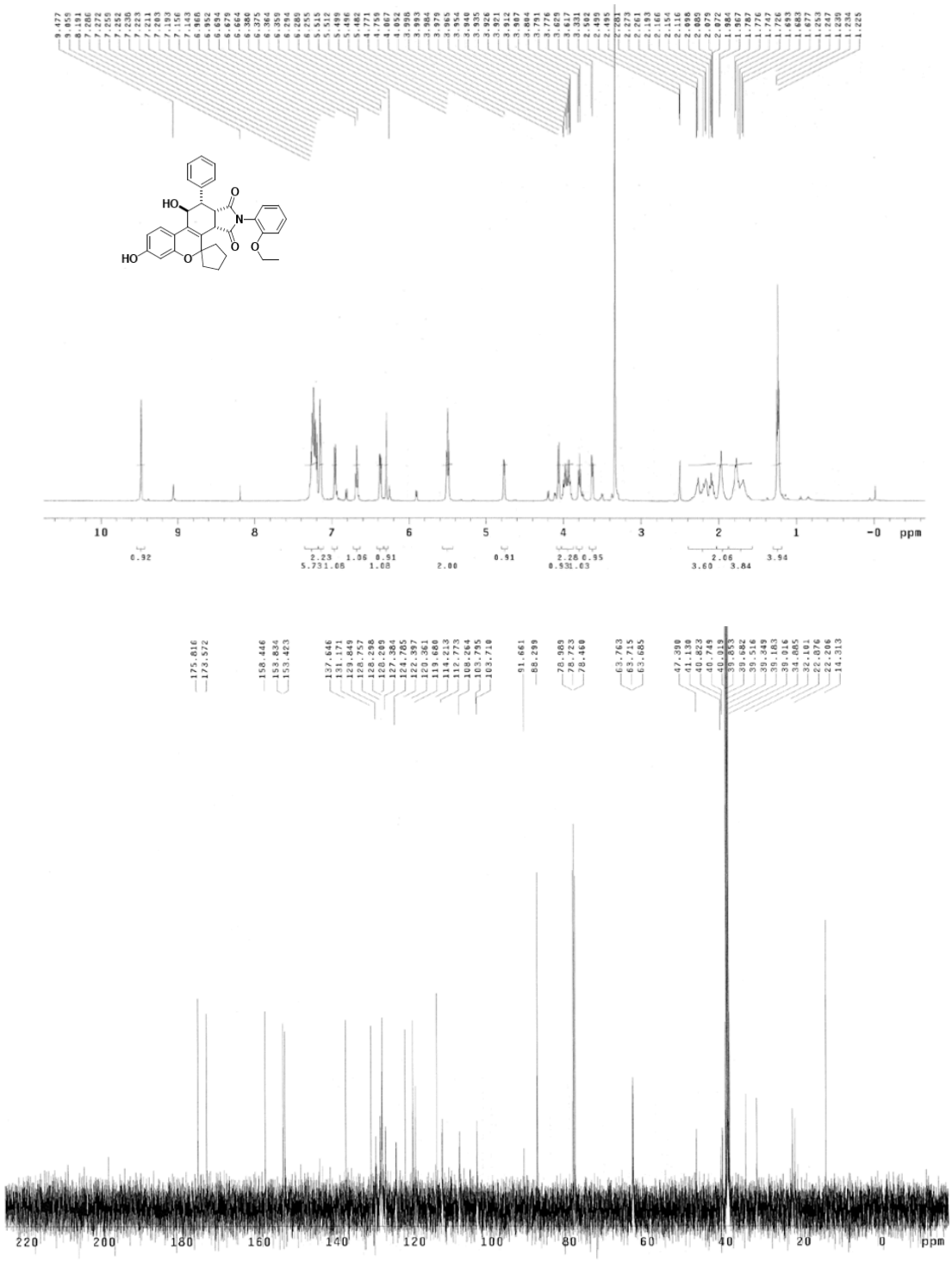

6p

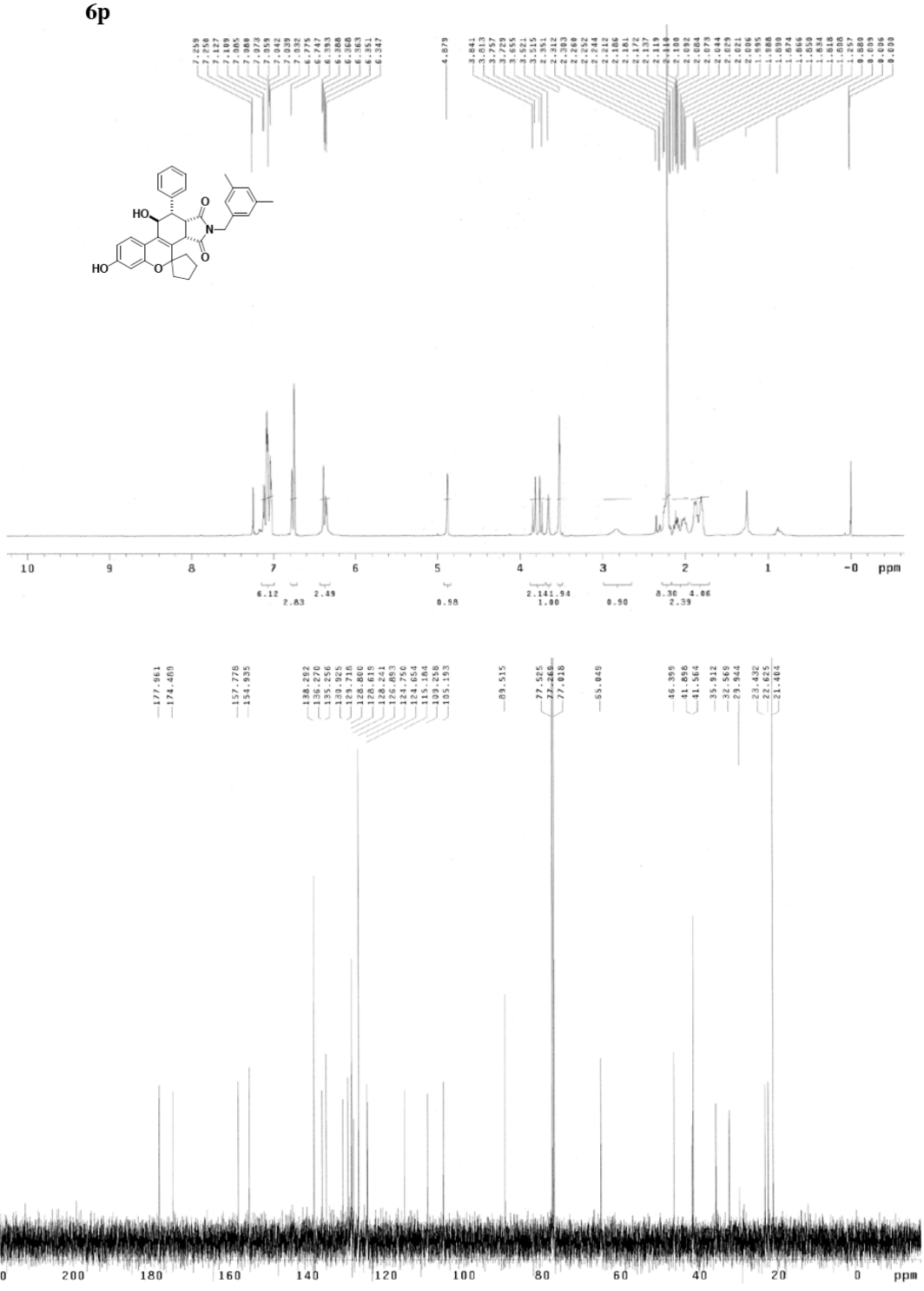

6q

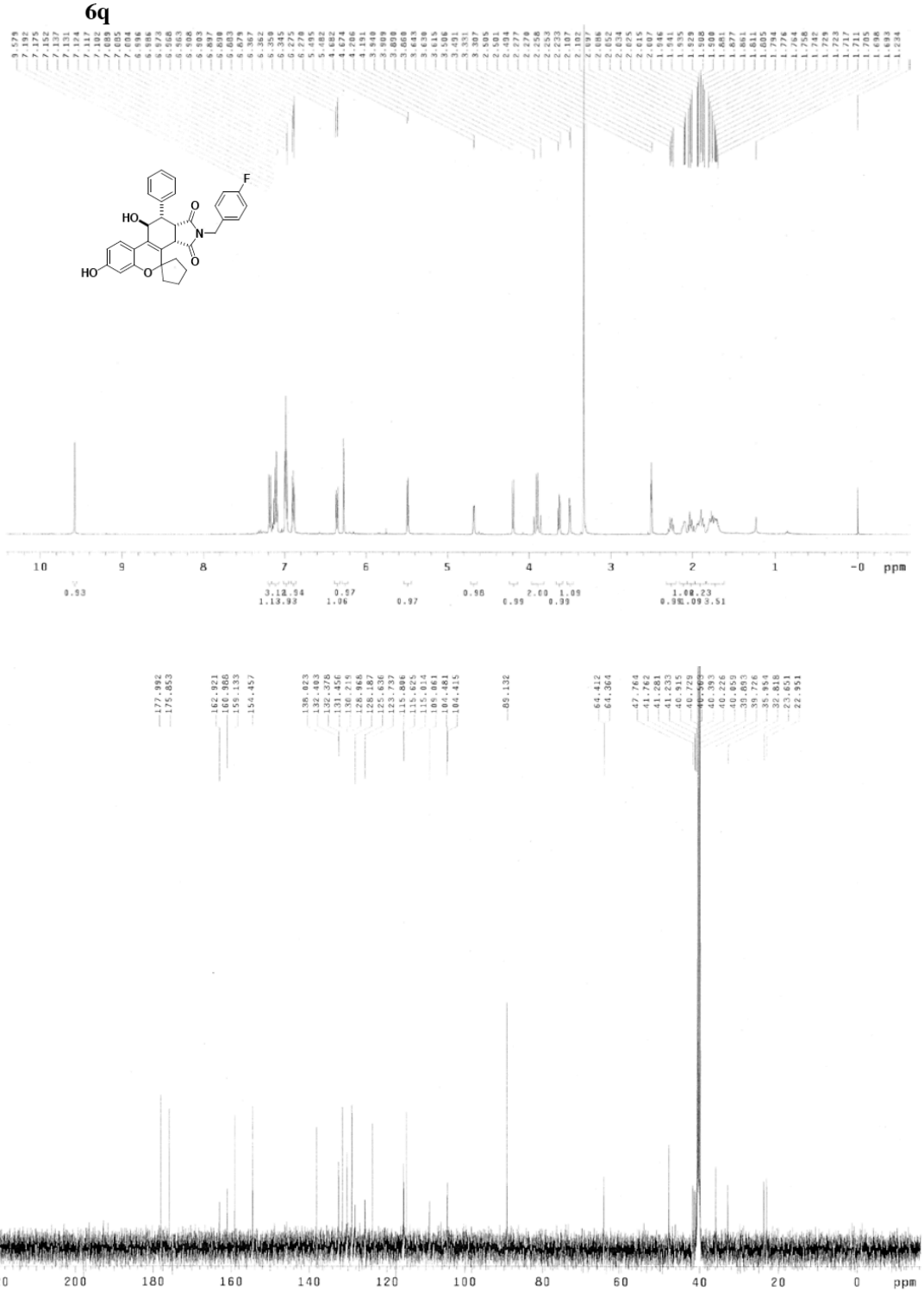

6r

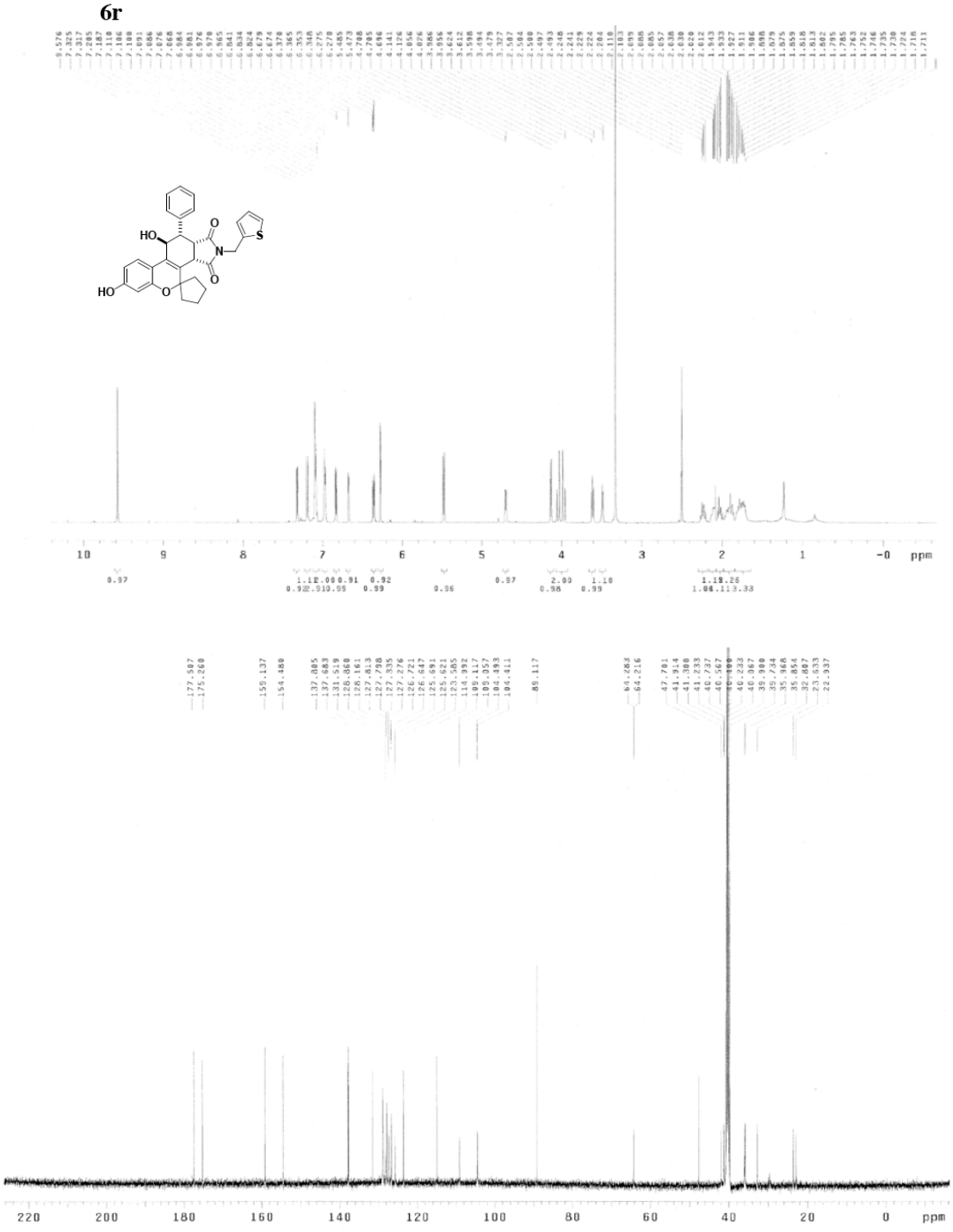

6s